Structural Analysis of Metal and Semimetal Adsorption on Cu{100} by Low Energy Electron Diffraction

Ehab M. AlShamaileh

School of Chemical Sciences
Dublin City University

A thesis submitted to Dublin City University

for the Degree of Doctor of Philosophy

Research Supervisor

Dr. Colin J. Barnes

January 2002

Declaration

I hereby certify that this material, which I now submit for assessment on the programme of study leading to the award of Doctor of Philosophy is entirely my own work and has not been taken from the work of others to the extent that such work has been cited and acknowledged within the text of my work.

Signed: Ehab AlShamaileh I.D. No.: 98970445

Ehab M. AlShamaileh

Date: 28th Jun 2012

Acknowledgements

I would like to thank my research supervisor Dr. Colin Barnes for his help.

My thanks to all whom supported me.

Dublin, 2002

Ehab M. AlShamaileh

Publications

This thesis is based on the following papers which have been published, submitted or are to be submitted for publication:

1. "Early stages of surface alloy formation: a diffuse LEED *I(V)* study", C.J. Barnes, **E. AlShamaileh**, T. Pitkänen and M. Lindroos, *Surface Science, **482** (2001) 1425.*

2. "The kinetics of formation and structure of an underlayer alloy: the Cu{100}-c(2×2)-Pd system", C. J. Barnes, **E. AlShamaileh**, T. Pitkänen, P. Kaukasoina and M. Lindroos, S*urface Science **492** (2001) 55.*

3. "Structural analysis of Cu{100}-Palladium monolayer surface alloys", K. Pussi, M. Lindroos, **E. AlShamaileh** and C. J. Barnes (submitted to *Surface Science).*

4. "Formation of a Cu-capped Cu{100}-c(2x2)-Pt Underlayer Alloy: a SATLEED analysis", E. AlShamaileh and C. J. Barnes (to be submitted).

5. "A Tensor LEED Determination of the Structure and Compositional Profile of a Cu{100}-c(2x2)-Pt Surface Alloy", **E. AlShamaileh**, H. Younis, C. J. Barnes, K. Pussi and M. Lindroos (submitted to *Surface Science*).

6. "LEED investigation of the alloying/dealloying transition in the Cu{100}/Bi system", **E. AlShamaileh** and C.J. Barnes (to be submitted to J. Chem. Phys.).

7. "A re-interpretation of the Cu{100}/Sn surface phase diagram", E. McLoughlin, A. A. Cafolla, **E. AlShamaileh** and C. J. Barnes, *Surface Science, **482** (2001) 1431.*

I have performed the experimental work for papers 1,2,3 and 6 and for the majority of papers 4,5 and 7 including collecting and preparing data for analysis. Moreover, I have performed the LEED I(V) analysis including performing the full structural solutions for papers 4 and 6. My contribution extends to the writing of papers 4 and 6.

Contents

Abstract

The structures formed by growing a range of metals and semimetals on Cu{100} single crystal are investigated by quantitative low-energy electron-diffraction (LEED). Symmetrized Automated Tensor LEED (SATLEED) calculations are used to determine the structure of the surface alloys and overlayers formed.

The Cu{100}/Pd system has been studied in the Pd coverage range 0.1-1.0 ML using SATLEED and Diffuse LEED (DLEED). Palladium atoms adsorb in the coverage range $0.1 \leq \theta_{Pd} \leq 0.5$ ML primarily by substitutional replacement of top layer copper atoms forming a two-dimensional Cu_xPd_{1-x} surface alloys leading to formation of an ordered Cu{100}-c(2x2)-Pd two-dimensional alloy at $\theta_{Pd} = 0.5$ ML The kinetics and mechanism of an irreversible overlayer to underlayer transition in the Cu{100}-c(2x2)-Pd surface alloy ($\theta_{Pd} = 0.5$ ML) has been investigated. The activation energy for Pd site switching from the outermost layer to sub-surface (second layer) sites has been found to be 109±12 kJ mol^{-1} (1.13±0.12 eV). The structure of the underlayer alloy has been determined by SATLEED. Substitution of 0.5 ML of Pd into subsurface sites leads to significant expansion of the outermost two interlayer spacings $\Delta dz_{12} = +3.3 \pm 3.3$ %, $\Delta dz_{23} = +6.6 \pm 2.8$ %. At monolayer coverage, Pd forms a double layer ordered c(2x2) CuPd alloy with p(2x2)-p2gg symmetry introduced into the outermost layer via clock rotation of the CuPd monolayer with the p(2x2) vertices centred over second layer Pd atoms. Lateral shifts of the top layer Cu and Pd atoms are determined to be 0.25±0.12Å.

The room temperature deposition of 0.5 ML Pt on Cu{100} followed by annealing to 525 K results an ordered c(2x2) Cu-Pt second layer capped with a pure Cu layer. The first and second interlayer spacings are found to be expanded by +5.1±1.7 % and +3.5±1.7%, respectively (relative to the bulk Cu interlayer spacing of 1.807 Å) due to the insertion of the 8% larger Pt atoms into the second layer with Pt atoms rippled outwards towards the solid-vacuum interface by 0.08±0.06 Å.

A Cu{100}-c(2x2)-Pt surface alloy structure formed by deposition of 1 ML Pt and thermal processing to 550 K is shown to correspond to a copper capped bimetallic surface localised alloy with an ordered c(2x2) CuPt monolayer in layer 2. The selvedge structure within the LEED probing depth strongly resembles the {100} surface of the $L1_2$ phase of

the bulk Cu_3Pt alloy. Excess Pt is distributed in layers 3 (20±20at.%) and layer 4(30±30at.%). Substitution of platinum into the selvedge results in a significant expansion in the surface interlayer spacings relative to clean Cu{100} due to the larger metallic radius of Pt and switches the weak oscillatory relaxation of clean Cu{100} to a strongly and non-uniformly expanded interlayer separation. A small rippling in the first CuPt underlayer with Pt atoms rippled outwards towards the vacuum interface within the composite layer occurs.

The surface structures formed by deposition of 0.25 ML and 0.50 ML Bi on Cu{100} at room temperature have been determined. At θ_{Bi}=0.25 ML, Bi forms a partially ordered p(2x2) surface alloy with the Bi atoms located 0.56±0.06 Å above the surface Cu atoms. At higher Bi coverage, de-alloying of Bi atoms occurs until a well ordered c(2x2) overlayer at θ_{Bi}=0.50 ML is formed. LEED calculations show that Bi atoms occupy four-fold hollow sites with a vertical Bi-Cu interlayer separation of d_{Bi-Cu}=2.17±0.06 Å above a slightly perturbed substrate.

The Cu{100}/Sn bimetallic system has been re-examined by double scattering LEED simulation as a function of adsorbate coverage for a range of model structures. A model for a low coverage ordered phase (θ_{Sn}=0.21 ML) has been suggested based on a "light" antiphase domain wall p(2×2) (θ_{Sn}=0.37 ML) structure. We have suggested alternative explanations for the structures of phases II (p(2x6)) and III (p(3√2×√2)R45°) which yield better agreement with the relative intensities of superlattice beams in the LEED patterns compared to previous explanations. A possible explanation of the transition to the p(2×6) structure has been suggested involving formation of narrow domains of c(2×2) CuSn structure of two unit cells width separated by a p(2×2) unit cell yielding sixth order periodicity in [011] and $[01\bar{1}]$ directions. The p(3√2×√2)R45° phase is suggested to have its origin in a c(2×2) structure with elastic strain due to the large metallic diameter of Sn leading to displacive reconstruction within the outer layer(s). The transition between phases occurs by nucleation of domains of the higher coverage phase within the lower coverage structure with concomitant density modulations across the surface. Further quantitative structural work both by LEED I-V analysis and STM are required to validate the proposed models and to differentiate between surface alloy and overlayer structures in this case.

CHAPTER 1

Introduction

A ***surface*** may be defined as the interface between a condensed phase of matter (solid or liquid) and another phase (solid, liquid or gas). A ***single crystal*** surface is formed when a solid is cut parallel to a selected plane of atoms. Surface atoms' properties are expected to be different from the bulk of the solid due to the loss of neighbouring atoms. At the vacuum interface, rearrangement of atomic positions at the solid single crystal surface may take place such as atomic relaxation or reconstruction. Surface relaxation takes place in order for the surface to compensate for the loss of "bonding" in the form of an oscillatory change in the interlayer spacing. Surface reconstruction happens when simple truncation of the bulk crystal does not lead to the "expected" surface periodicity. Detailed discussion and examples on surface relaxation and reconstruction can be found in many reviews (see for example references [1-5]). The region over which atoms relax or reconstruct (usually few atomic layers deep) is often called the ***selvedge***.

The atoms of single crystals are arranged in a regular lattice structure. For example, table 1.1 shows some of the common types of close-packed crystal structures adopted by metals with some examples.

Table 1.1: Close-packed crystal structures adopted by metals.

Crystal structures	Abbreviation	Examples
Face-centered-cubic	Fcc	Cu, Pd, Pt, Au
Body-centered-cubic	Bcc	K, Cr, W, Fe
Hexagonal-closed-packed	Hcp	Co, Ti, Cd, Mg

1.1 Single Crystal Surfaces

Figure 1.1 illustrates the three planes corresponding to the simplest and most studied low Miller index surfaces of fcc metals {100}, {110} and {111}.

As shown in figure 1.1, compared to their normal bulk co-ordination number of 12, the {100} surface atoms have lost 4 nearest neighbours while the {110} and the {111} surface atoms have lost 5 and 3 nearest neighbours, respectively. This simple fact generally makes the {110} surfaces the most unstable in terms of surface relaxation and reconstruction and also the most reactive chemically, while the {111} is the most stable surface. The more stable the surface, the lower its surface energy which is attributed to the higher co-ordination induced by the increased bonding.

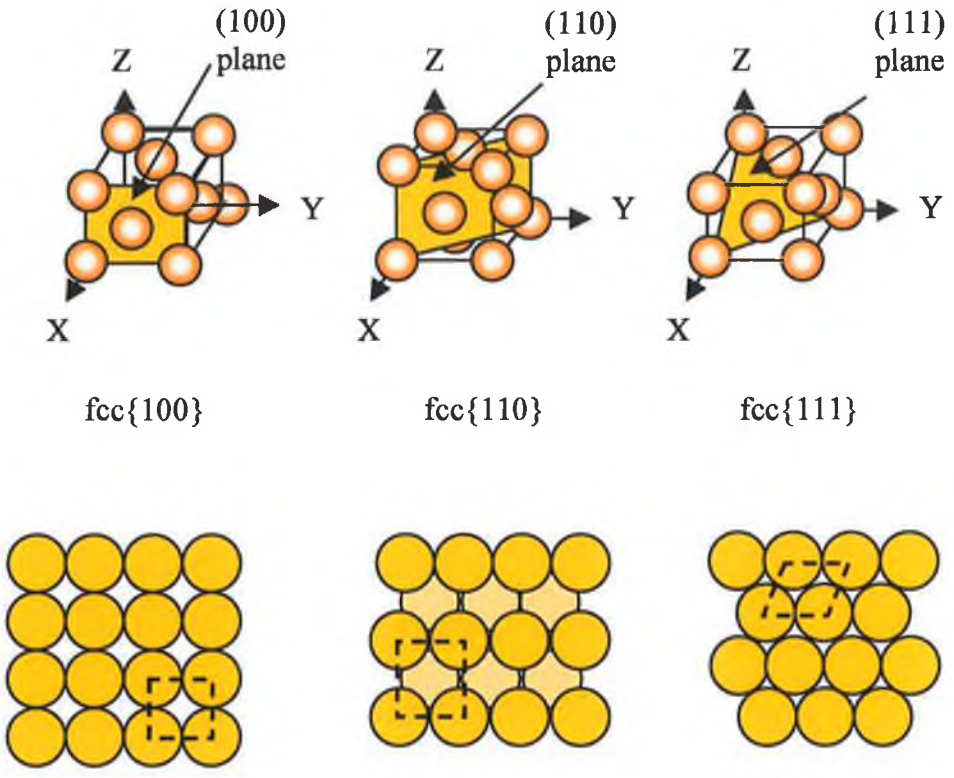

Figure 1.1: The {100}, {110} and the {111} planes of fcc metals and their corresponding real space atomic arrangement. The dotted lines indicate the two-dimensional unit cells.

(a) Surface Relaxation

The Cu{100} selvedge undergoes a relaxation in which the first interlayer spacing is contracted by between 1 and 2% relative to the bulk value (1%=0.018Å, 2%=0.036Å). This can be explained by considering the attractive forces between adjacent atomic layers before and after truncating the bulk crystal. Atoms of the

outermost layer contract towards the second layer to increase their co-ordination to compensate for loss of nearest neighbours at the vacuum interface. Third layer atoms respond by expanding away from second layer atoms to compensate for the over-coordination of the second layer. In the most recent analysis of Cu{100} structure by low energy electron diffraction (LEED) I(V), a contraction of –1.9% is found in the first interlayer spacing and an expansion of about +0.6% in the second interlayer spacing of Cu{100} compared to the bulk values at low temperature (80 K) [6].

(b) Surface Reconstruction

In the case of {110} surface where the surface energy is relatively large, in certain cases a surface reconstruction may take place to maximise surface atom co-ordination and to lower the surface energy. For example, the clean Au{110}-(1x1) surface forms the (1x2) missing-row reconstruction illustrated in figure 1.2 [7-9].

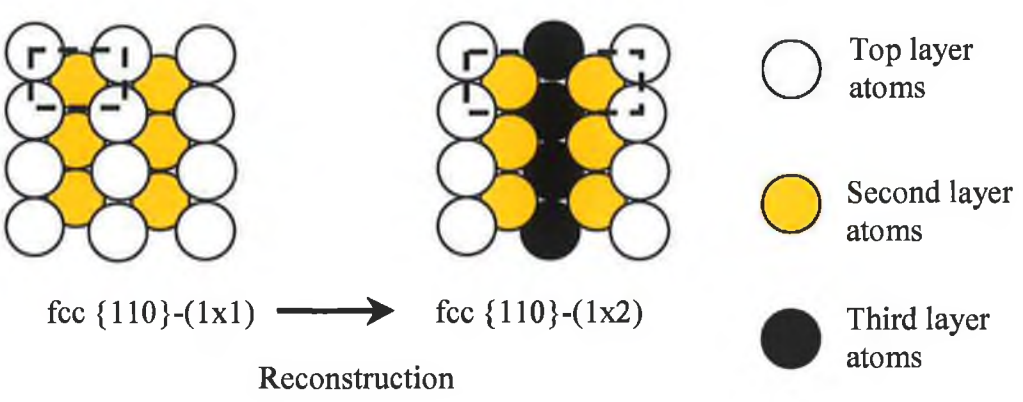

Figure 1.2: Reconstruction of the fcc{110} surface from a bulk truncated (1x1) structure to a (1x2) missing row surface. Dashed lines show the unit cell in each case.

1.2 Surface Alloys

An alloy is a mixture of the atoms of two or more metals. ***Surface alloys*** are made by the physical incorporation of usually submonolayer coverage of one or more metals within the selvedge of a different metal (the substrate). Physical Vapour Deposition (PVD) is a common technique used to make surface alloys by the

selective evaporation of metals onto the substrate [10]. Examples of surface alloy formation are discussed in the comprehensive review by Bardi [11].

From a chemist's point of view, surface alloys have the potential of being used as model heterogeneous catalysts. The importance of catalysts comes from their widespread use in many applications, for example: automobile exhaust control [16], polymerisation [17], ammonia [18] and methanol synthesis [19] and hydrocarbon reforming reactions [20]. Research in the field of steam reforming catalysis revealed that a two-dimensional gold-nickel alloy system formed by deposition of submonolayer coverge of Au on Ni{111} have lead to the invention of a new nickel based catalyst, which is much more resistant to poisoning via carbon formation than the conventional nickel catalysts [21]. This is one of the few examples of how fundamental research can lead to the invention of new catalysts.

The importance of copper as a heterogeneous catalyst is demonstrated by its use in large-scale industrial processes including the synthesis of methanol [19], higher alcohols, ethers and in phenol oxidation [22].

This thesis addresses surface alloy formation on Cu{100}. The first surface alloy corresponding to formation of two-dimensional mixed CuAu monolayer was suggested by Palmberg and Rhodin in 1968 [12] to explain the observation of a c(2x2) LEED pattern upon evaporation of 0.5 ML of Au. This was later confirmed by Jona and co-workers using LEED I(V) analysis [13]. Surface alloy formation on Cu{100} has been recently reviewed by Barnes [15].

The Cu{100} surface is a model substrate due its well-defined and stable surface structure. Model systems such as Cu{100}-based surface alloys may be studied to establish a link between the microscopic level of understanding the bonding and reactivity of adsorbates and the macroscopic measurements of kinetic rate and thermodynamic properties of the reacting system. The knowledge may then be exploited to create surfaces with the required microscopic structure to produce the desired catalytic properties.

Four elements were chosen as adsorbates in the course of this work: two open d-band metals with high catalytic activity: palladium (Pd) and platinum (Pt) and two less reactive sp-band metals: bismuth (Bi) and tin (Sn).

In this thesis, the surface structure of these four different systems was investigated as a function of adsorbate coverage.

Platinum and palladium catalysts, despite their high cost, have so far been found to be the best sufficiently durable catalysts for oxidising hydrocarbons and CO to produce acceptably low levels of these gases in automotive and factory effluent gas emissions [23]. Incorporating a small quantity of Pd or Pt within the surface of a cheaper metal such as Cu is receiving an increasing interest in the field of catalysis and environmental control. Such a catalyst could be tailored and manufactured to suit certain reaction requirements and it may in favourable circumstances lead to reduce catalyst poisoning and degradation.

In contrast, tin is an sp-band metal with little known catalytic reactivity. However, in the important catalytic conversion of CO to CO_2, studies have shown that the catalytic activity of the surface alloy Pd{100}-c(2x2)-Sn is significantly larger than that of the surface of pure Pd [24]. This result was attributed to the presence of SnO_x (x= 1-2). It was reported that Cu/Cu_xO surface clusters readily adsorb oxygen providing an enhanced coverage of reactive oxygen for CO oxidation [25]. Therefore, it is interesting to investigate the catalytic activity of Cu/Sn systems. At room temperature, Sn forms four different phases on Cu{100} depending on coverage. Structural determination of these phases is needed in order to interpret the results of any chemical reactions performed on such surfaces.

Bismuth is a well-established promoter of noble metal-based catalysts for the selective liquid phase oxidation of alcohols, aldehydes and carbohydrates with molecular oxygen [26]. In this thesis, the structure of the surface alloy formed by depositing Bi on Cu{100} and the structural effect of increasing Bi coverage are investigated.

References

[1] H. van Beijeren and I. Nolden, in W. Schommers and P. von Blanckenhagen (Eds.), Structures and Dynamics of Surfaces, Springer, Berlin, 1987; Erio Tosatti and Furio Ercolessi, Surface reconstruction of noble metals: models and consequences, Modern Physics Letters B **5** (1991) 413; J. Villain, J. L. Rouviere, and I. Vilfan, Phenomenology of surface reconstruction, *in* Phase transitions in surface films 2, Plenum Press, 1991.

[2] L.J. Clarke, Surface Crystallography, Wiley, New York, 1985.

[3] M. Prutton, Surface Physics, Oxford University Press, Oxford, 1985.

[4] K.P. Bohnen and K.M. Ho, Surf. Sci. Rep. 19 (1993) 99.

[5] M. Nijs, The Chemical Physics of Solid Surfaces and Heterogeneous Catalysis, (Editors: D. A. King and D.P. Woodruff), Vol. 7, Chapter 4, Elsevier, Amsterdam, 1994.

[6] S. Walter, V. Blum, L. Hammer, S. Muller, K. Heinz and M. Giesen, Surf. Sci. 458 (2000) 155.

[7] T. Gritsch, D. Coulman, R. J. Behm and G. Ertl, Surf. Sci. 257 (1991) 297.

[8] J.K. Gimzewski, R. Berndt and R.R. Schlittler, Phys. Rev. B 45 (1992) 6844.

[9] M. B. Hugenschmidt, A. Hitzke and R.J. Behm, Phys. Rev. Lett. 76 (1996) 2535.

[10] D. Mattox, Handbook of Physical Vapor Deposition (PVD) Processing, William Andrews/Noyes Publications, New Jersey, 1998.

[11] U. Bardi, Rep. Prog. Phys. 57 (1994) 939.

[12] P.W. Palmberg and T.N. Rhodin, J. Chem. Phys. 49 (1968) 134.

[13] Z.Q. Wang, C.K.C. Lok, J. Quinn, Y.S. Li and F. Jona, J. Phys. C , 21 (1988) 653; Z.Q. Wang, Y.S. Li, C.K.C. Lok, J. Quinn and F. Jona, Solid State Commun. 62 (1987) 181.

[14] F. Delamare and G.E. Rhead, Surf. Sci. 35 (1973) 172.

[15] C.J. Barnes, The Chemical Physics of Solid Surfaces and Heterogeneous Catalysis, (Editor: D.P. Woodruff)Vol. 15, Elsevier, Amsterdam, 2002.

[16] R. Heck and R. Farrauto, App. Catal. A, 221 (2001) 443 and references therein.

[17] B.C. Gates, J.R. Katzer and G.C.A. Shuit, Chemistry of Catalytic Processes, McGraw-Hill, New York, 1979.

[18] W.G. Frankenburg, in P.H. Emmett (Ed.), Catalysis, vol. 3, Reinhold, New York, 1955, p.171.

[19] G. Natta, in P.H. Emmett (Ed.), Catalysis, vol. 3, Reinhold, New York, 1955, p.349; J. Nerlov, S. Sckerl, J. Wambach and I. Chorkendorff, App. Catal. A 191 (2000) 97.

[20] F. Zaera, Prog. Surf. Sci. 69 (2001) 1 and references therein.

[21] J. Larsen and I. Chorkendorff, Surf. Sci. Rep. 35 (1999) 163.

[22] R.G. Herman, Catal. Today, 55 (2000) 233.

[23] G.A. Somorjai, Catal. Today, 18 (1993) 113; Kamil Klier et al, Catal. Today, 36 (1997) 3; G.A. Somorjai and P. Chen, Solid State Ionics, 141 (2001) 3.

[24] A.D. Logan and M.T. Paffett, J. Catal. 133 (1992) 179.

[25] J. Szanyi and D.W. Goodman, J. Catal. 15 (1994) 508.

[26] M. Besson and P. Gallezot, Catal. Today, 57 (2000) 127.

CHAPTER 2

Experimental Techniques

This chapter gives a description of the equipment used for collecting the data including the ultra-high-vacuum (UHV) chamber and metal/semimetal evaporation methods. The LEED experiment will be explained including the acquirement of LEED I(V) spectra, spot profile analysis (SPA) and how to prepare experimental data for analysis. Finally, an overview of the basic theory of desorption spectroscopy will be presented.

2.1 The UHV Chamber

All experiments were performed in an ion and titanium sublimation pumped stainless steel ultra-high-vacuum (UHV) chamber with a base pressure of 1×10^{-10} Torr. Figure 2.1 shows a photograph of the UHV chamber used to produce all the data reported in this thesis.

The Cu{100} sample was mounted on a high precision goniometer (manipulator) with facilities for sample rotation and incorporating a tilt mechanism, allowing an accurate attainment of such as normal incidence ($\pm$ 0.2°) required for LEED I-V spectra acquirement. The sample temperature was measured by means of a chromel-alumel thermocouple embedded in the sample.

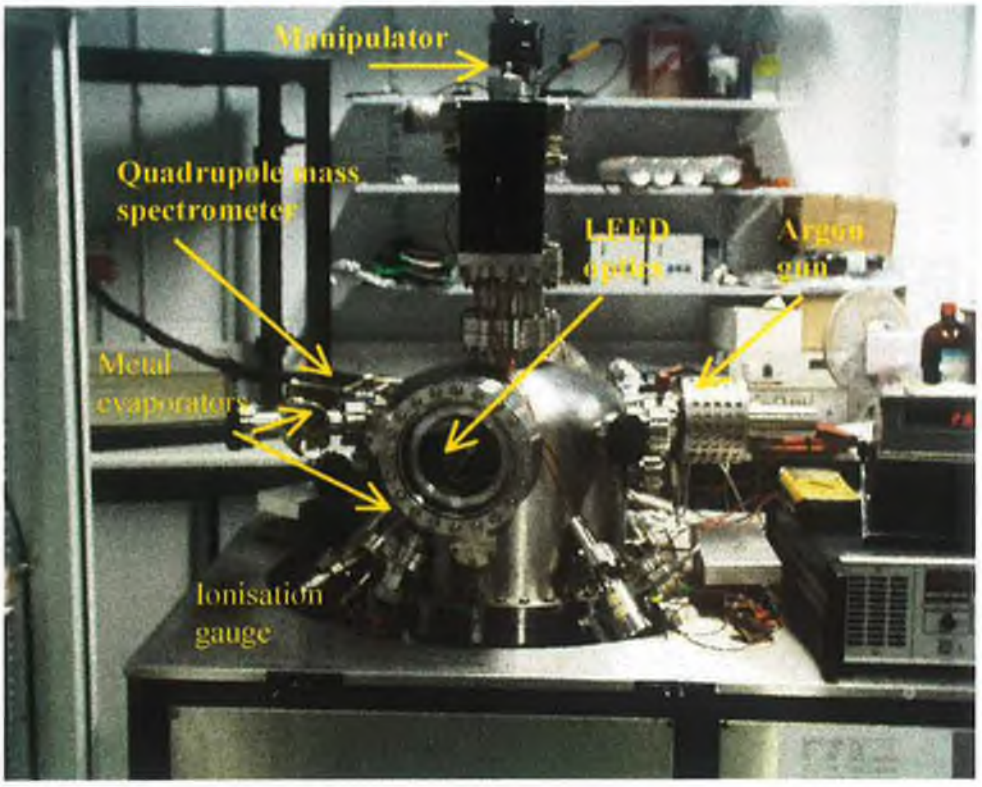

Figure 2.1: Photograph of the Dublin City University low energy electron diffractometer

There are two essential requirements needed to study the Cu{100} surface. Firstly preparing an atomically clean and well-defined surface and secondly keeping that surface clean over the period of the experiment that usually takes up-to a few hours. The former requirement may be achieved via the Ar^+ bombardment technique while the latter explains the need for UHV.

The crystal was cleaned in situ by Ar^+ bombardment in which the surface is bombarded with a beam of argon ions (or any other noble gas such as Krypton) of energies ranging between 500 eV to 5 keV. Upon striking the surface energy transfer from the argon ions to the substrate causes surface atoms to break their bonds with the substrate and desorb into the vacuum (this is called *sputtering*). The high-energy beam of Ar^+ is achieved by passing high-purity argon gas through high-voltage electrodes in an ion gun producing positive argon ions. The argon gas pressure needed for the ion gun to operate is between 10^{-5} and 10^{-6} Torr. Therefore, the chamber is pumped by a diffusion pump and not by the ion pump as the latter is not effective at pumping noble gases.

Annealing the surface after sputtering is required (typically to 700 K for 10 minutes) to restore the original surface structure and to desorb atomic argon embedded in the selvedge during sputtering.

2.2 The Need for UHV

For a clean surface, the rate of contamination depends on the rate of collision of gas molecules with the surface. From the kinetic theory of gases, the rate of surface bombardment (Z) by molecules is given by equation (2.1):

$$Z = p / (2\pi mkT)^{1/2} \quad m^{-2}\,s^{-1} \tag{2.1}$$

where p is the ambient pressure in Nm^{-2}; m is the molecular mass in kg $molecule^{-1}$; T is the temperature in K and k is the Boltzmann constant in JK^{-1} [1].

Assuming a sticking probability of unity (every molecule that collides with the surface sticks) and applying equation (2.1), a monolayer (full surface coverage) of CO gas will adsorb on a surface in approximately 2 seconds at a pressure of 10^{-6} Torr at room temperature. In comparison, at a pressure of 10^{-10} Torr, such a contamination requires longer than 7 hours to take place. For most solid-gas interface studies, and since sticking probabilities are usually lower than unity and decrease as a function of coverage, it is found that a base pressure of $1x\ 10^{-10}$ Torr is sufficient.

2.3 The Metal Evaporation Sources

Three types of evaporators were used in this work: (a) Tungsten-filament supported, (b) Tantalum boat crucibles and (c) a commercial Kundsen cell. Each type of evaporator will be briefly outlined.

(a) Tungsten-filament supported

Figure 2.2 shows a schematic diagram of the evaporator used for the deposition of palladium and platinum. A thin wire of Pd/Pt (0.125 mm diameter, Goodfellow Metals Ltd, UK) was wrapped onto a tungsten wire (0.3 mm diameter, Goodfellow Metals Ltd, UK). Electric current is passed through the W wire to resistively heat the W wire which itself heats the Pd/Pt wire by conduction and starts to sublime Pd/Pt as the temperature is raised. These evaporators were degassed at below their operational electric current for a significant time prior to use and a warm up time of 2 minutes was allowed prior to each evaporation process. Generally, a coverage calibration is performed by constructing a curve of evaporation time and the amount of Pd/Pt detected by AES and/or LEED.

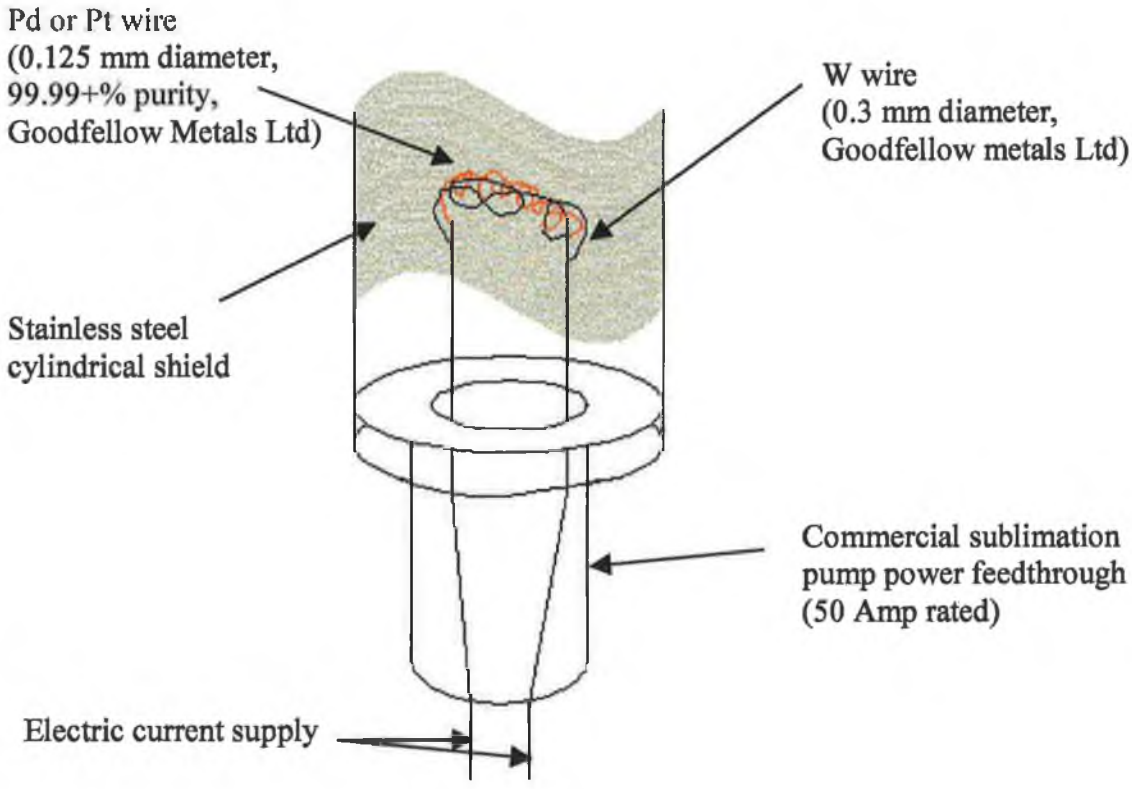

Figure 2.2: Schematic diagram of the home-made Pd and Pt evaporators.

(b) The Tantalum Crucible Evaporator

Deposition of bismuth was carried out using a tantalum crucible evaporator illustrated in figure 2.3. It consists of Ta boat-shaped crucible containing granules of high purity Bi. In this case, a boat is used instead of a wire because Bi evaporates well after its melting point hence is in the liquid phase during evaporation. The boat can be resistively heated by passing a direct current through Ta wires wrapped around the boat. The source was degassed for about 10 minutes prior to deposition. During Bi evaporation, a pressure of $<5\times10^{-10}$ Torr was maintained. For the calibration of the Bi source, a simple LEED calibration is applied which is highly accurate for the Cu{100}/Bi system (see Chapter 5).

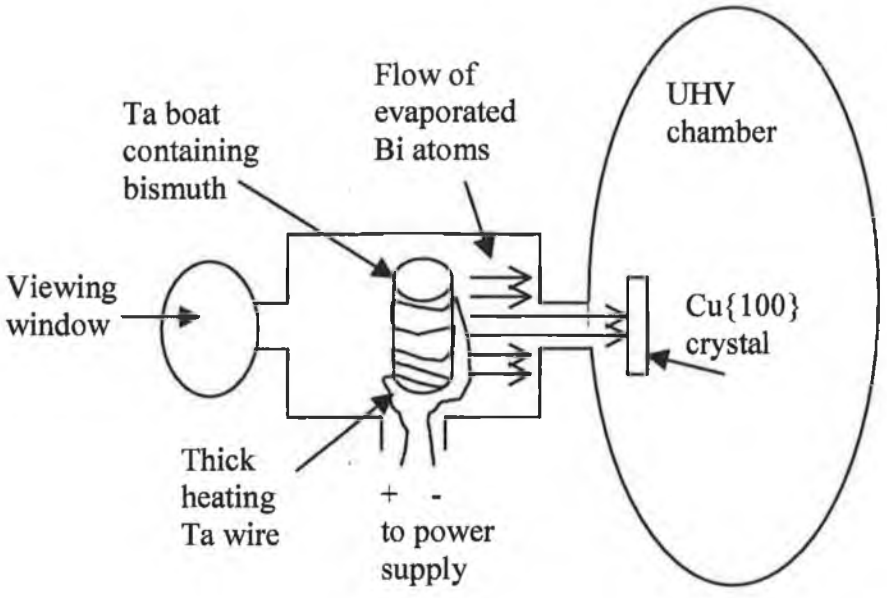

Figure 2.3: Schematic diagram of the Bi evaporator.

(c) Knudsen Cell

This cell (W.A. Technology) which is shown in figure 2.4 was used to deposit Sn onto the Cu{100} crystal. The Knudsen cell uses the molecular effusion principle introduced by Knudsen in 1909.

Sn granules are heated to provide a suitable vapour pressure in an isothermal graphite furnace. The furnace is designed as a removable cartridge that contains the crucible, heating element and heat shields. The heating filament is a tantalum foil isolated with pyrolytic boron nitride (PBN) shields and is water-cooled.

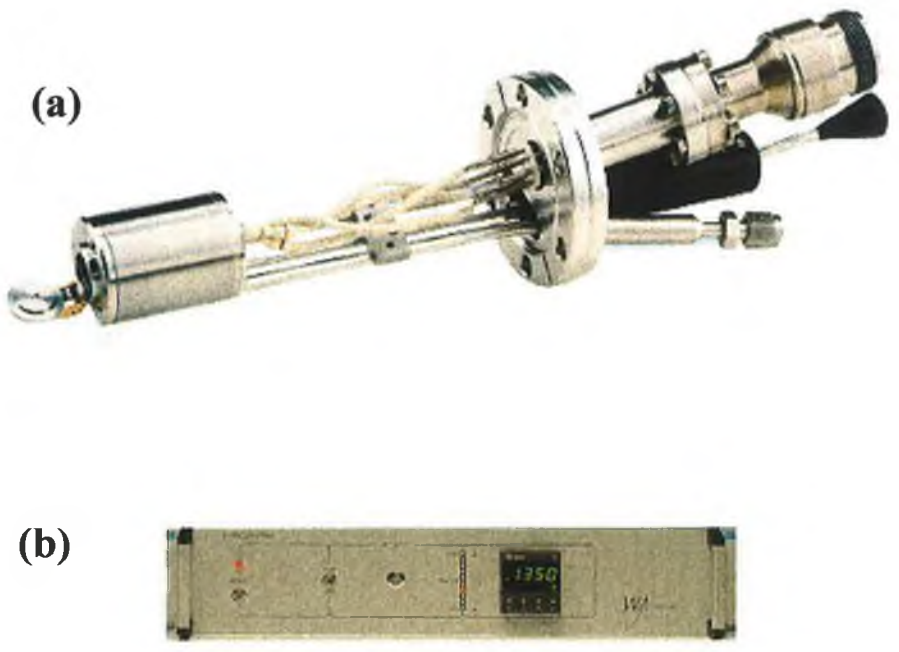

Figure 2.4: Photograph of (a) the Knudsen cell and (b) the Proportional Integral Derivative (PID) controller used for Sn evaporation.

The temperature of the furnace is monitored by a thermocouple carefully placed inside the graphite furnace in order to accurately reflect its internal temperature. The Sn is placed in a PBN crucible and planted inside the furnace. The deposition temperature can be held constant by means of a Proportional Integral Derivative (PID) controller that automatically controls the heating employing a built-in temperature feedback technology.

The temperature required for evaporation of Sn at a certain rate was judged from the relationship between vapour pressure and temperature. A flux rate of about 0.01 monolayer of Sn per minute was utilised experimentally.

2.4 Basic LEED Theory

LEED is one of the most widely used surface science techniques [2-4]. It is used to study the structure of crystalline surfaces [5-7]. In the LEED method, low-energy electrons are used to probe the crystal surface producing diffraction data which are analysed to provide the surface structural information. Monochromatic low-energy electrons, with energies ranging from 40 to 500 eV are incident upon the single crystal surface.

The electrons that are reflected (back-scattered) from the surface without energy loss are said to be *elastically scattered*. They represent a small fraction of the incident electrons while the majority of electrons exhibit kinetic energy losses and called *inelastically back-scattered*.

The depth that electrons may travel through the solid surface layers prior to energy loss is dependent on their kinetic energy. The inelastic mean free path (IMFP) is a measure of how far an electron can penetrate through a solid surface. It also depends on the material type.

For metals, a general formula to describe the IMFP was suggested by Seah and Dench [8]:

$$\frac{\lambda}{nm} = \frac{538}{E_p^2} + 0.41a^{\frac{3}{2}}(E_p)^{\frac{1}{2}} \qquad (2.2)$$

where a is the element's mean atomic diameter (nm) and E_p is the primary electron's kinetic energy (eV). Using this formula and for Cu{100} (a=0.255 nm), LEED electrons in the range between 40 and 500 eV will exhibit an IMFP in the range between 4 and 12Å as illustrated in figure 2.5. Knowing that the interlayer spacing of bulk Cu{100} is 1.807Å, electrons are expected to travel several atomic layers into the surface.

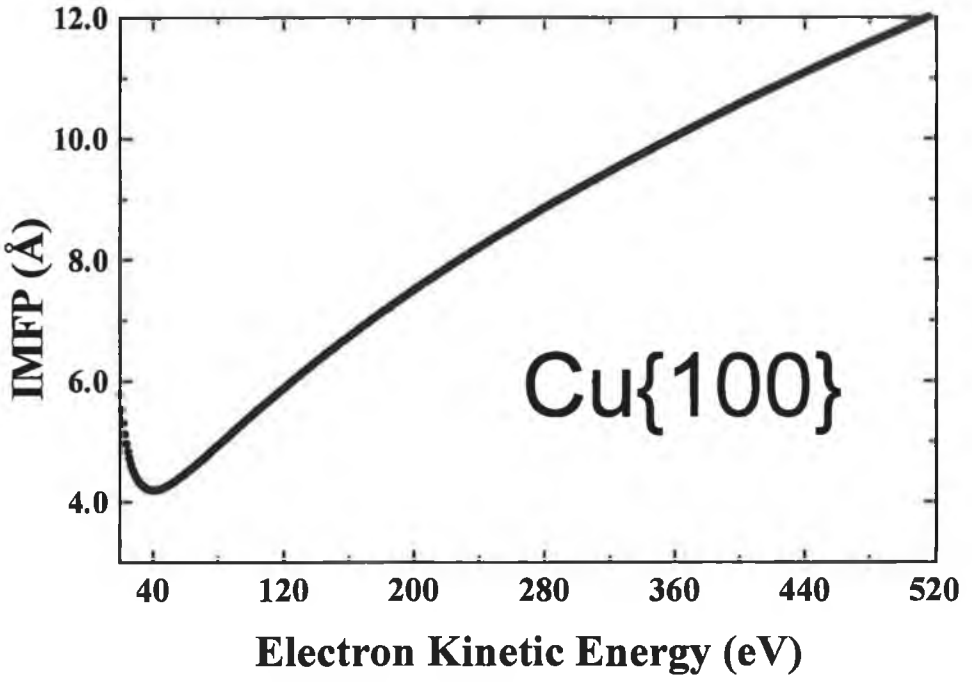

Figure 2.5: Inelastic mean free path (IMFP) for Cu{100} versus the incident electron energy.

The de Broglie wavelengths of LEED electrons are estimated to be in the range 2.74-0.39 Å for kinetic energies between 40 and 500 eV using the de Broglie equation:

$$\lambda = \sqrt{\frac{150.4}{E_p}} \qquad (2.3)$$

where λ is the electron's wavelength (Å) and E_p is the electron energy (eV).

The resulting order of wavelengths are comparable to the spacing between atoms both parallel and perpendicular to a metallic crystal surface, hence, the electrons may diffract (elastically backscatter) from the surface atoms. When a monochromatic beam of electrons hit a clean single crystal surface, at normal incidence, back-scattered (diffracted) electrons are produced satisfying the equation:

$$n\lambda = a\,sin\theta \qquad (2.4)$$

where n is the order of diffraction; a is an in-plane lattice spacing and θ is the diffraction angle of the backscattered electrons, measured from the surface normal.

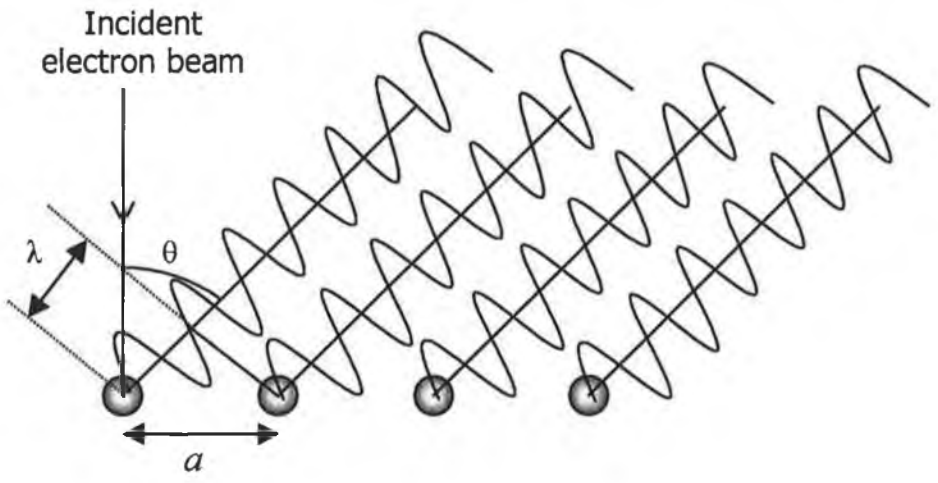

Figure 2.6: Diffraction from a one-dimensional periodic array of surface atoms.

The collection of these electrons takes place in the UHV chamber using a commercial LEED optics illustrated in figure 2.7. The diffracted electrons travel from the sample towards a series of four concentric hemispherical meshes or grids and a phosphor screen. The first grid (G1) and fourth grid (G4) and the sample are earthed to ensure that diffracted beams travel from the sample through a field-free region. The second (G2) and third (G3) grids are at potential several volts less than the electron-beam voltage. They filter out most of the inelastically scattered electrons coming from the sample. The elastically scattered electrons travel through the fourth grid and are accelerated towards the screen which is held at positive potentials (~5 keV). Beams appear on the hemispherical screen (S) as spots are called a *LEED pattern*. This pattern caused by electron diffraction is an image of the surface reciprocal-lattice.

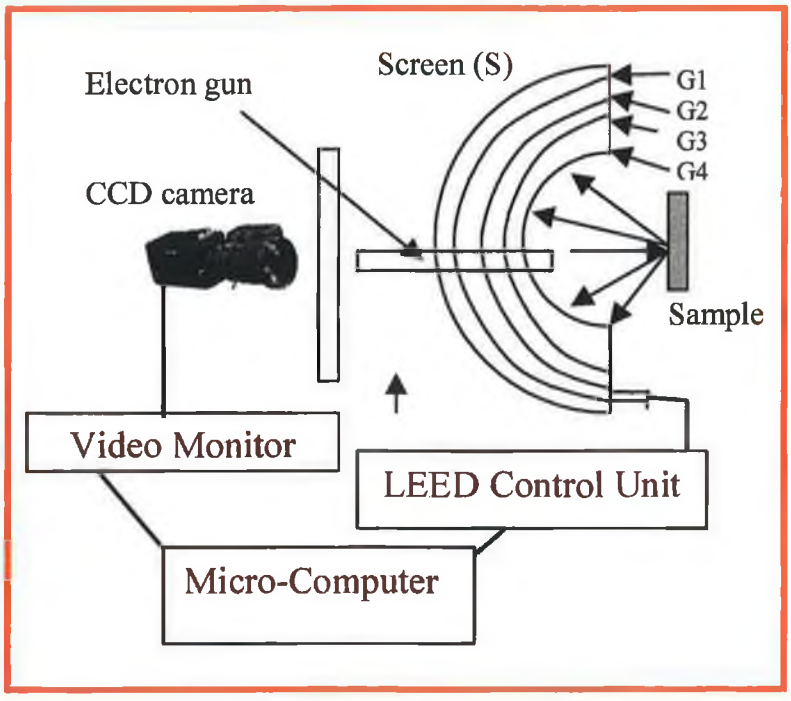

Figure 2.7: The LEED apparatus.

Qualitative information such as the surface symmetry, 2D unit-cell dimensions, and crystallographic "quality" of the surface layers is available from the LEED pattern. The two-dimensional surface unit cell periodicity may be deduced by the visual inspection of the positions of the diffracted beams. The size of regions with well-ordered surface structure can be predicted from the sharpness and the shape of the beams. Qualitative LEED is widely used in surface science research laboratories usually simply involving the visual inspection of the LEED pattern. However there is more much information that can be obtained from LEED patterns if quantitative measurements of LEED spot intensities is performed..

According to a survey covering the last 50 years, quantitative LEED has proved to be the most widely used technique for surface structure determination [2]. As the energy of a diffracted electron increases its wavelength and the diffraction angle decrease. Therefore, with increasing energy the beams move toward the specularly-reflected electron beam (0,0). Patterns not only compress with increasing energy, but the intensities of discrete beams are modulated. If single scattering and infinite penetration were exactly applicable, then the beams would only have intensity at discrete energies as in traditional X-ray diffraction. If single scattering occurs from one single layer was exactly applicable, then the beams would have constant intensity for all energies. However, this is not so, and the intensity modulation is a result of multiple scattering within the top few atomic layers thus a situation intermediate between X-ray diffraction and diffraction from a single periodic two-dimensional layer applies. The variation in the intensities of beams as a function of energy is a fingerprint of the surface structure. Hence, it is necessary to collect spectra of each beam's intensity as a function its energy I(V) curves. The spectra, however, cannot be Fourier transformed to reveal the atomic locations on the surface, instead, an indirect analysis of the LEED I(V) spectra is needed involving calculations of LEED I(V) for a guessed structure and comparison with measured LEED I(V) via reliability factors.

Kinematic diffraction theory which is based on the approximation of single scattering, and works well for higher-energy electrons and X-rays, is not applicable for LEED I(V) simulation. It generally produces incomplete and wrong structural results. Hence, the more complicated multiple-scattering theory must be used to model the experimental spectra.

The procedure adopted to solve a surface structure involves a series of steps: a surface structural model is first proposed. A range of structural parameters including a series of phase shifts to model the electron scattering properties of the atom types located within the selvedge. This model is used to produce theoretical LEED I(V) spectra. Several structural and non-structural parameters are systematically varied in order to obtain the "best-fit" between the theoretically calculated and the experimentally measured spectra. This is called the refinement process. Structural parameters include atomic interlayer spacing, in-plane atomic spacing and rippling and buckling in layers with atoms of two or more types. In addition to visual inspection, reliability factors (R-factors) are used to numerically evaluate the level of agreement between experiment and theory. The "correct structure2 corresponds to that yielding a minimum R-factor.

Because of both the small penetration depth of the electrons and the lack of a perfect periodicity in the perpendicular direction at the selvedge, the electron wave field does not see a perfect periodicity in the direction normal to the surface, but only in the parallel plane. The result is a quasi two-dimensional diffraction process that may be simplified to be corresponding to the three-dimensional case in which the lattice vector perpendicular to the surface is infinite. The perpendicular wave vector can have any value compatible with the kinetic energy, while only the parallel wave vector components have quantised values. The Laue conditions for diffraction are then

$$\Delta \boldsymbol{k}.\boldsymbol{a}=2\pi m, \quad \Delta \boldsymbol{k}.\boldsymbol{b}=2\pi n \tag{2.5}$$

where Δk is the change in the wave vector of the electron upon scattering while a and b are the basis vectors in the surface plane and m and n are integers. A two-dimensional reciprocal lattice is obtained:

$$G = ha^* + kb^* \tag{2.6}$$

where h and k are integers and the basis vectors a^* and b^* of the reciprocal lattice

are:

$$a^* = (2\pi N \times b) / A \; ; \quad b^* = (2\pi N \times a) / A \tag{2.7}$$

in which A is the area of the two-dimensional unit cell in the real space lattice, N is the surface normal vector.

Some of the incident electrons back-scatter elastically to form discrete beams (i.e., plane waves with well-defined wave-vectors) so that the total change in the wave-vector of the electron parallel to the surface is a vector of the reciprocal lattice:

$$\Delta k_{\parallel} = G \tag{2.8}$$

From observation of the diffraction pattern seen on the fluorescent screen, it is possible to find out directly the basis vectors **a** and **b** of the two-dimensional real space lattice. However, to obtain the information about exactly where the atoms are located, measurements of intensity variations as a function of energy (I(V) spectra) are required..

2.5 LEED I(V) Calculations

Several program libraries are available for the calculations of LEED I(V) spectra. In this section, the theoretical LEED spectra were calculated using the LEED package of Van Hove and Tong [10] modified to produce the Symmetrized Automated Tensor LEED (SATLEED) package of Van Hove and Barbieri [11]. In this thesis,

only a simplified synopsis of the LEED calculations theory will be given. The exact and detailed theory used is presented in reference [12], where the FORTRAN listings for the sub-routines are also discussed.

(a) The Inner Potential

In the vacuum, an electron beam is represented as a plane wave with a wave vector **k** and a kinetic energy E_o:

$$E_o = \hbar^2 \mathbf{k}^2 / 2m \tag{2.9}$$

When the electron penetrates a crystal, its kinetic energy increases to E:

$$E = E_o + V_{o,r} \tag{2.10}$$

where $V_{o,r}$ is the inner potential (or more precisely its real part). If we assume V_o to be energy independent then V_o may be regarded as a free fitting parameter.

The real part of the inner potential mainly moves the LEED IV spectra along the energy axis, i.e. it rigidly shifts the theoretical relative to the experimental spectra. The R-factor analysis then produces the final value of the real part of the inner potential, typically taking values in the range: 5-15 eV.

In LEED calculations, the inner potential V_o has also an imaginary part ($V_{o,i}$), which is used to mimic the damping of the electron wave field within the solid. Inelastic processes are the physical reason for the limited penetration depth of electrons, modelled using an exponentially damped intensity. In the studies carried out in this work, an energy independent value ($V_{o,i}$) was used as the imaginary part.

(b) Thermal Vibrations

The approximation is generally made that the atomic vibrations are independent: the momentary positions of atoms caused by vibrations are supposed uncorrelated. Furthermore, if the probability distribution of atomic displacements is supposed to be Gaussian, one obtains the Debye-Waller factor exp(-M):

$$\exp(-M) = [-(1/6)\,|\Delta\mathbf{k}|^2\ \langle\Delta r\rangle^2] \qquad (2.12)$$

where $\Delta\mathbf{k}$ is the momentum transfer in diffraction and $\langle\Delta r\rangle$ is the mean square amplitude of the vibrations [3].

There may be a connection between the vibrational amplitude of adsorbate atoms perpendicular to the surface and the precision of the obtained distance between that layer and the substrate. The information of the location of a layer originates from back-scattering from that layer. In case of forward scattering the diffracted electron wave does not depend on the location of the layer at all; it does depend on the fact that the layer exists but not on its location. The largest influence of the location is on the backscattered wave. Most observed LEED electrons have scattered several times in the forward direction but only once backwards. However, a large perpendicular vibrational amplitude of the adsorbate atoms decreases their back-scattering amplitude while not affecting the forward scattering nor the scattering from the substrate atoms. It follows that most LEED electrons have backscattered once from the substrate atoms and only a very small portion of the electrons have backscattered from the adsorbate atoms. Thus, in the case of large perpendicular vibrations, the effect on the LEED spectra caused by the perpendicular position of the adsorbate layer is very small compared to those of the substrate layers. On the other hand, the vibrational amplitude parallel to the surface can be large without affecting the obtained layer distances.

2.6 Acquirement of LEED I(V) Spectra

Figure 2.8(a) illustrates a photograph of a the LEED pattern of a Cu{100}-(1x1) surface measured at normal incidence at 147eV. The spots shown in the photograph are called the ``integral-order" beams and arise from scattering from the bulk-like surface planes. At normal incidence, the 4-fold rotation and mirror-plane symmetries of the surface creates degenerate beam-sets {(1,0},(0,1),(-1,0),(0,-1)}, {(1,1),(-1,1),(1,-1),(-1,-1)}, {(2,0),(0,2),(-2,0),(0,-2)}...etc. Additional beams (spots) may appear as a result of the addition/adsorption of different type of atoms. Figure 2.9 is a photograph of a the LEED pattern of Cu{100}-c(2x2)-Pd surface at normal incidence measured at 115 eV. Here, the bulk-like (Cu) and the superstructure (Pd) reciprocal beams are indicated. The additional beams, so called ``fractional-order" beams, are labelled with respect to the integral-order beams. Thus, the set of beams {a, b, c, d} is labelled {(1/2,1/2), (-1/2, 1/2), (1/2,-1/2), (-1/2,-1/2)}, respectively.

The LEED software consists of two main parts that can be run interactively. The former collects LEED I(V) spectra by the automatic tracking of diffraction spots whereas the latter measures line profiles through chosen diffraction spots.

A LEED I(V) spectrum reflects the intensity change of a chosen diffraction spot (y-axis) versus the incident beam energy (x-axis). As shown by the box in figure 2.8(a), the (1,0) diffraction spot is being tracked with a window size of 12x12 pixel. Figure 2.8(b) represents the output spectra of the tracked spot. More than one spot can be tracked simultaneously.

(a)

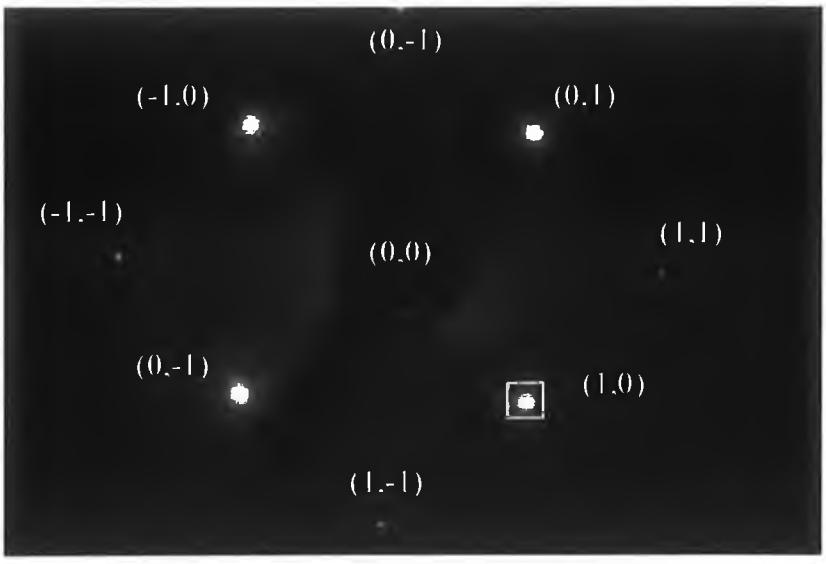

(b)

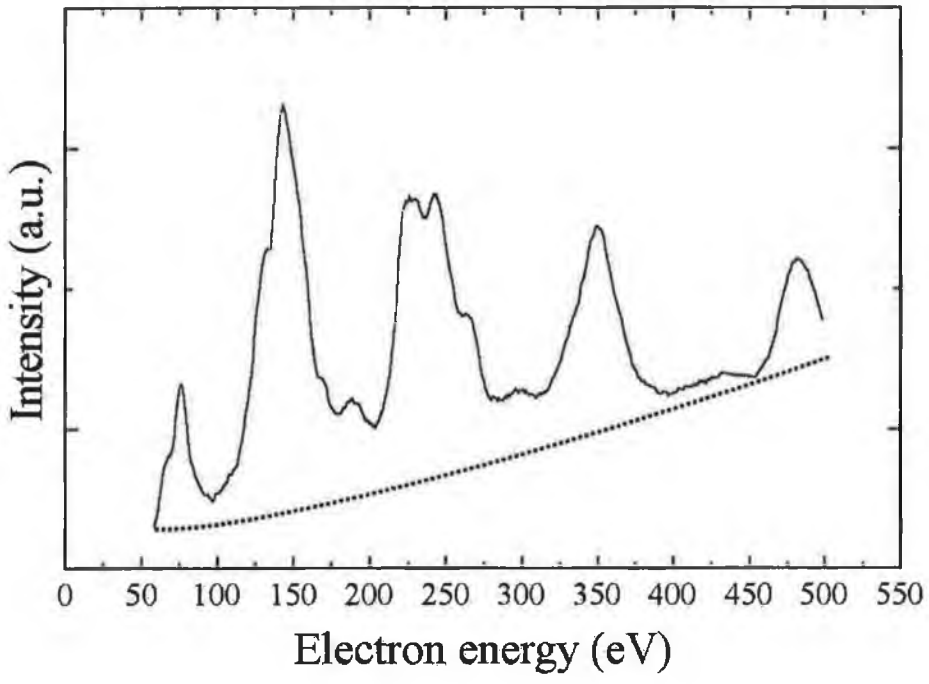

Figure 2.8: (a) Photograph of a the LEED pattern of Cu{100} at 147eV. The window size around the (1,0) diffraction spot is 12x12 pixel; (b) the output spectra of the tracked spot. A fitted background is represented by a dotted line.

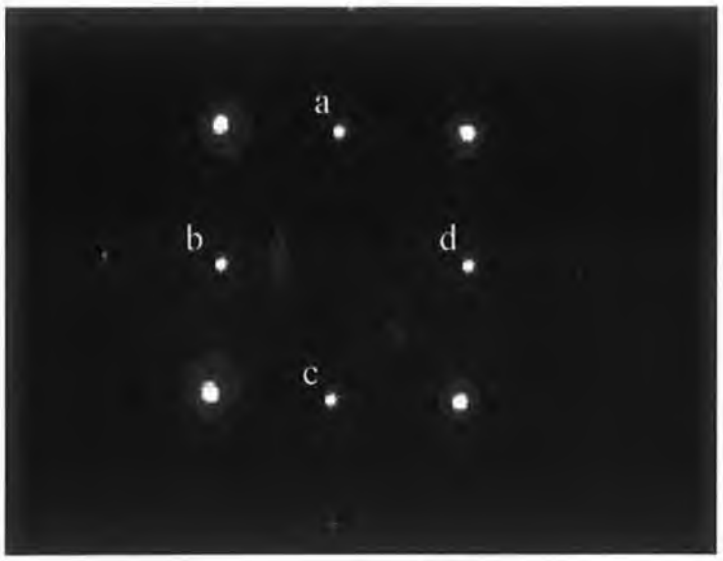

Figure 2.9: Photograph of a the LEED pattern of Cu{100}-c(2x2)-Pd at 115eV. The fractional-order beams are labelled a, b, c, and d which corresponds to (-1/2,1/2), (-1/2, -1/2), (1/2,-1/2), and (1/2,1/2) beams, respectively.

When measuring LEED-IV spectra, great attention should be paid to the energy axis which is automatically controlled and recorded by the computer software. It was found that a correction of the energy values requested by the software compared to the actual beam energy is required. Fortunately, a linear energy calibration proved to be sufficient and stable over long periods of time.

The correction equation used throughout this work is given as:

$$E_p = 0.963\ E_{measured} + 3.7 \qquad (2.12)$$

where $E_{measured}$ (eV) is the energy requested by the user via the computer software and E_p (eV) is the true energy.

2.7 Spot Profile Analysis (SPA)

A LEED line profile through different spots can be measured by locating a computer generated line passing through the chosen diffraction spots as shown in figure 2.10(a). The intensity along the line is recorded as y-axis while the x-axis reflects the reciprocal distance. Figure 2.10(b) represents the output spectrum (line profile).

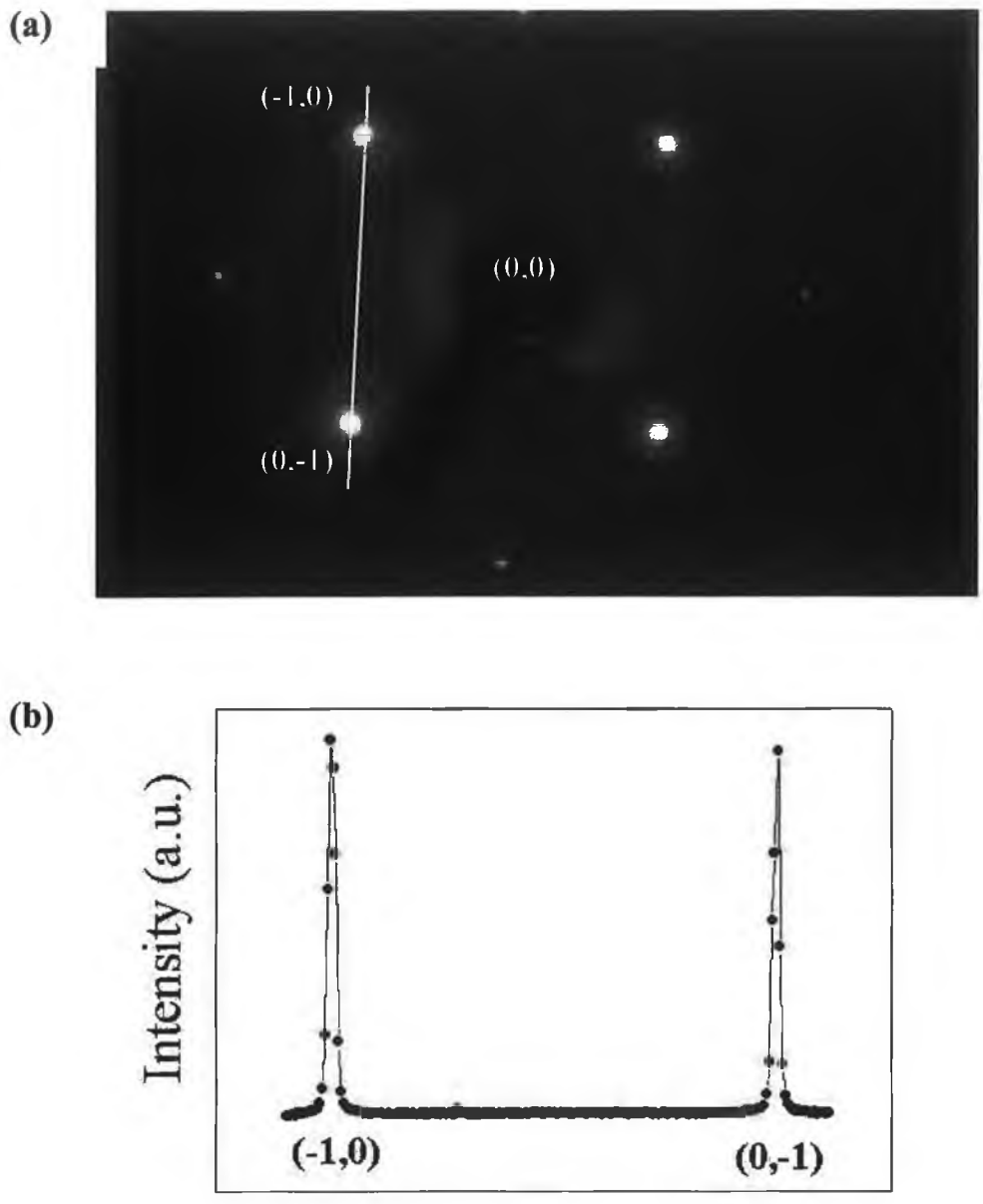

Figure 2.10: (a) A LEED photograph of the Cu{100}-(1x1) surface at 147eV with a line profile through the (-1,0) and the (0,-1) spots; (b) the output spectrum of the line drawn in (a).

SPA is very useful when new diffraction spots grow in intensity as a function of adsorbate coverage during adsorption. This technique may be used as a calibration method of adsorbate coverage especially when the transition from one diffraction pattern to another takes place over a narrow range of adsorbate coverage.

2.8 Preparation of Experimental LEED I(V) Spectra for Analysis

When tracked, the reflections (spots) of the LEED pattern represents the raw experimental data. To minimise the effect of external magnetic or electrostatic fields, to correct for any deviations from normal incidence and to improve the signal-to-noise ratio, an average of the four beams represents the best approximation to the actual (1,0) I(V) spectrum at normal incidence [13].

In the following example of a set of raw data will be treated to produce the final data that can be used in a subsequent LEED analysis.

Figure 2.11 illustrates the output of a tracking a set of four symmetrically equivalent (1,0) beams from the clean Cu{100} surface measured at close to normal incidence. As the energy is increased, inelastically scattered electrons add an increasing unwanted "background" to the spots. The background intensity is removed by the subtraction of a manually fitted background from the individual spectra measured for each spot. The fitting of the background is somewhat empirical as it relies on the experimentalist judgement of the points to fit which represent I(V) minima. Figure 2.12 shows the spectra after background correction.

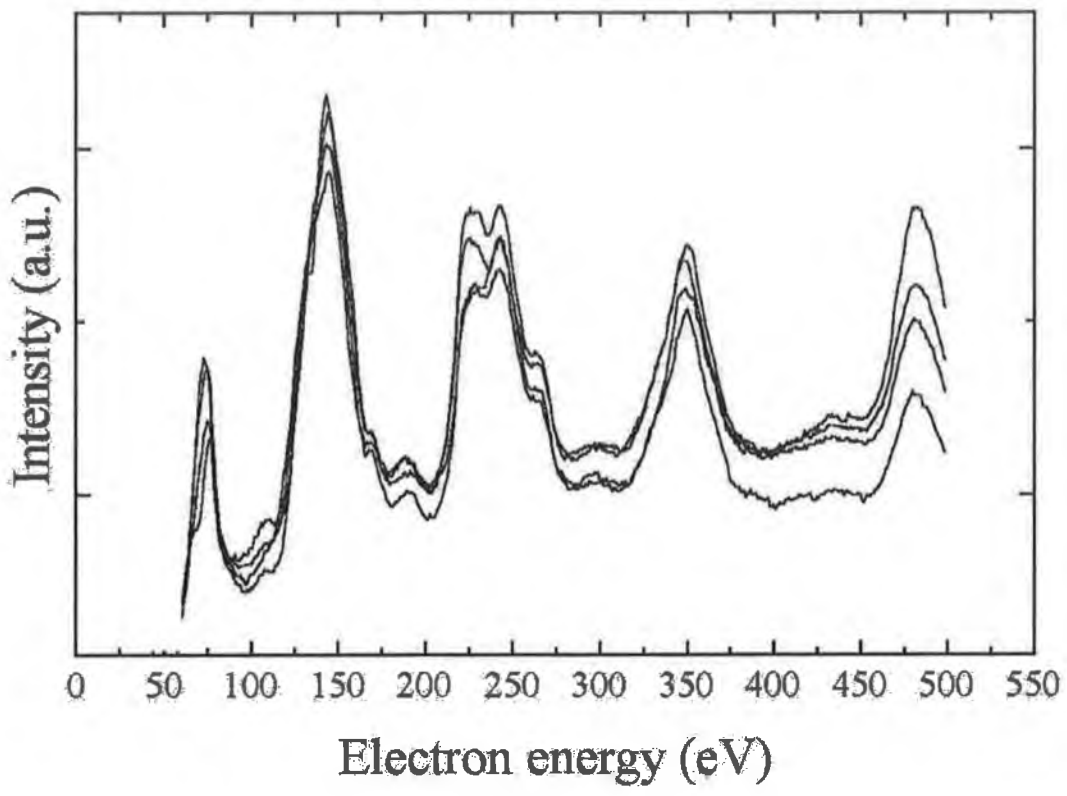

Figure 2.11: Raw experimental data from four symmetrically equivalent (1,0) beams of Cu{100} measured at close to normal incidence.

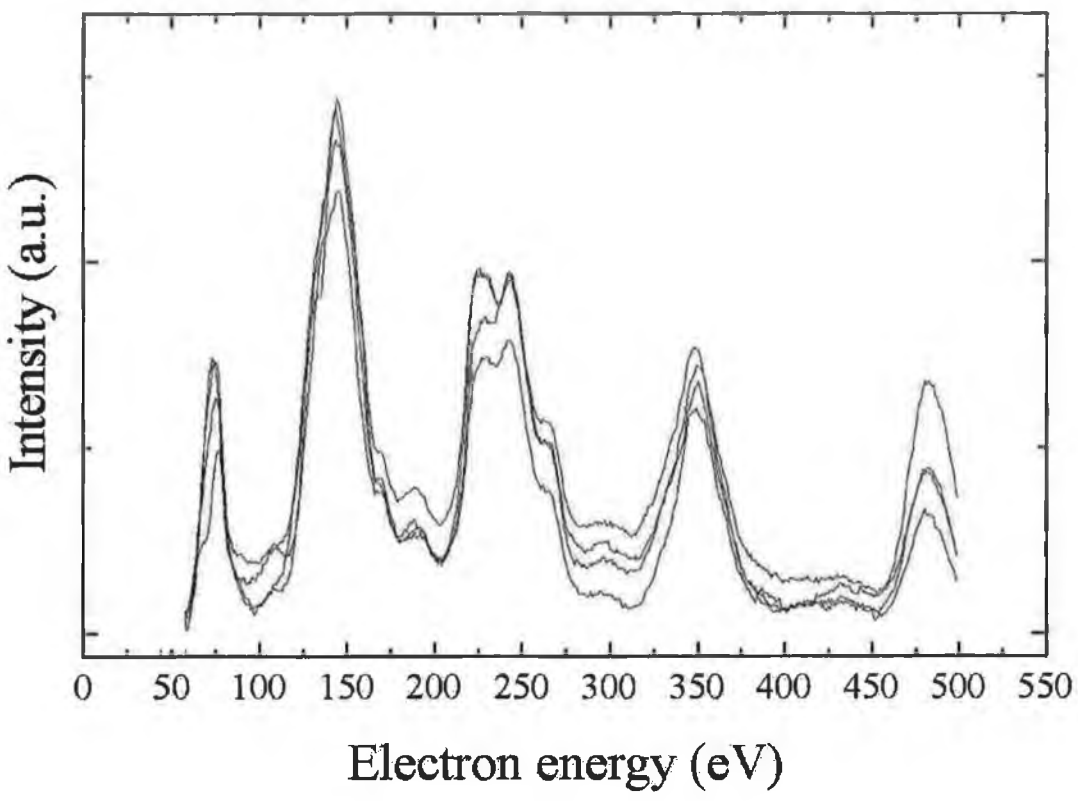

Figure 2.12: LEED I(V) spectra of the (1,0) beam after background correction

Smoothing of the averaged beams is usually required to reduce the noise in the spectra. Figure 2.13 shows the (1,0) beam after a 5-point adjacent averaging smoothing. Examining various extents of smoothing proved that a 5-point smoothing improved the spectra visually by removing most of the unwanted noise and at the same time retained features such as small peaks and shoulders. Hence, this value was chosen to be the optimum degree of smoothing.

Finally, since the incident beam-current varies with the beam energy (E_p), the spectra should be corrected to correspond to constant incoming beam-current. A function is fitted to the LEED I(V) spectrum of the (1,0) beam measured from the clean Cu{100} to bring the relative intensities of the different peaks in agreement with that reported by Davis and Noonan [14]. This function is then applied to all experimental spectra. The Figure 2.14 illustrates the "analysis-ready" LEED I(V) spectra of the {1,0} beam from clean Cu{100}. The full line in figure 2.14 illustrates the "analysis ready" normal incidence I(V) spectra from the (1,0) beam of clean Cu{100} measured using the Dublin City University electron diffractometer and the dotted line corresponds to that measured by Adams [15], illustrate the level of agreement obtainable between independent laboratories. Both spectra are also in excellent agreement with those measured by Davis and Noonan for a shorter energy range [14].

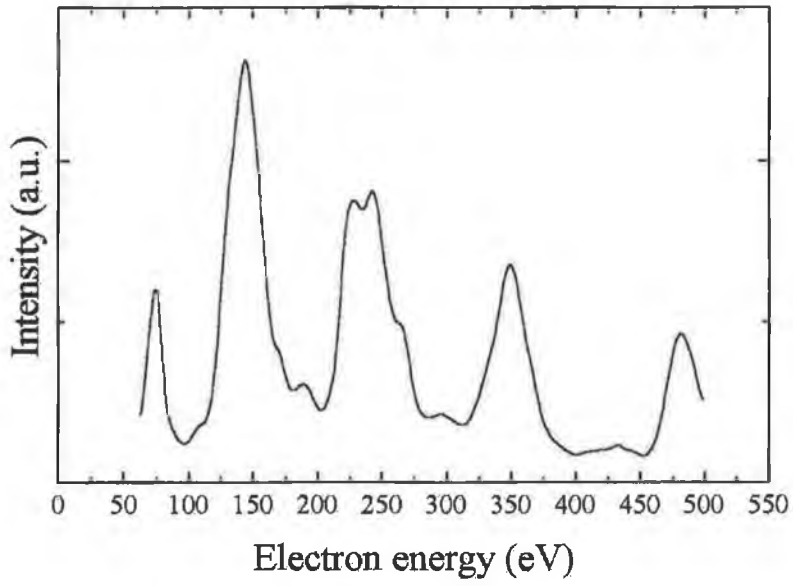

Figure 2.13: Averaged and 5-point smoothed LEED I(V) of the (1,0) beam from clean Cu{100}.

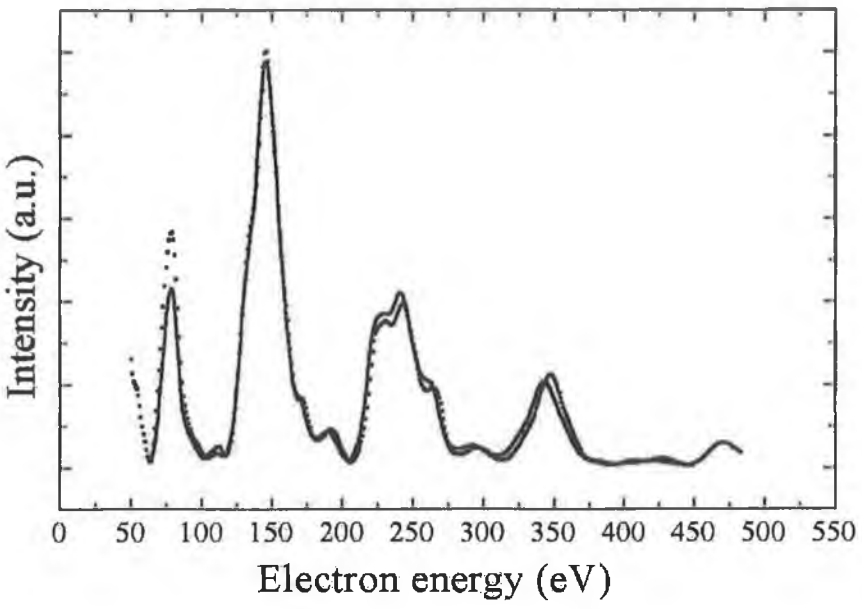

Figure 2.14: The final "analysis-ready" LEED I(V) spectrum of the (1,0) beam for clean Cu{100}. The dotted line spectrum is the LEED I(V) spectrum of the (1,0) beam from clean Cu{100} measured at room temperature and normal incidence by Adams [14].

2.9 Temperature-Programmed Desorption (TPD)

One of the fundamental surface kinetic processes is the desorption of adsorbed atoms/molecules from solid surfaces. These surface reactions are best followed by temperature-programmed desorption techniques. There is a range of techniques for studying atomic/molecular adsorption /desorption and surface reactions on surfaces that utilise temperature programming the sample to discriminate between processes with different activation parameters. Of these, the most useful for single crystal studies is Temperature-Programmed Desorption (TPD). TPD is also known as Thermal Desorption Spectroscopy (TDS). When the technique is applied to a system in which the adsorption process is, at least in part, irreversible and temperature-programming leads to surface reactions, then this technique is known as Temperature Programmed Reaction Spectroscopy (TPRS). As a surface analysis technique, TPD was first introduced by Apker in 1948 [16].

In TPD, atomic/molecular species are adsorbed onto the crystal surface. Then a temperature ramp is applied to the crystal where the rate of desorption of certain fragments of fixed charge to mass ratio (m/e) from the solid surface back into the gas phase is followed as a function of temperature. To facilitate quantitative data interpretation, a linear heating rate (β) is usually applied to the crystal that satisfies the equation

$$T(t) = T_o + \beta.t \qquad (2.13$$

where T is the crystal temperature, t the heating time and T_o is the initial crystal temperature. Experimentally, heating rates (β) may take values as low as 0.01 Ks^{-1} [17] or as high as 100 Ks^{-1} [18]. Flash desorption uses very high β values whilst most TPD experiments are usually done at β of around 1-10 Ks^{-1}.

A quadrupole mass spectrometer (QMS) is used to detect and record the desorption of pre-set fragment masses under computer control with the possibility of quasi-simultaneous monitoring of a large number of possible products.

The sample is oriented close to the QMS filament, typically around 1-3 cm. Such an arrangement maximises the signal obtained. The QMS signal of a certain fragment is directly proportional to its partial pressure, and hence this signal is a direct quantitative representation of the amount of that fragment evolved from the sample surface.

The data obtained from such an experiment consists of the partial pressure of each recorded mass fragment as a function of temperature. The resulting graph is called the TPD spectrum from which information about the binding energies of different adsorbates may be deduced.

As adsorbate molecules may decompose into a range of products of differing mass, this experiment often requires the simultaneous monitoring of several masses. This can be achieved by allowing the mass spectrometer to switch between several

detected masses as the temperature is increased. Thus, while truly simultaneous 7monitoring is not possible, a quasi-continuous output is recorded.

For example, in the decomposition of the formate intermediate (HCOO), adsorbed on Cu{100} which decomposes to CO_2 and H_2 via cleavage of the C-H bond can be investigated by monitoring the masses of carbon dioxide (m/e=44), hydrogen (m/e=2) and the molecular formic acid (HCOOH) (m/e=46) (formed via re-combination of atomic hydrogen with formate) as the crystal temperature is increased. Figure 2.15 shows a typical TPRS spectrum resulting from adsorption of HCOOH onto Cu{100} crystal at 305K. In the spectrum, mass 44 amu (CO_2) is recorded as a function of the sample temperature.

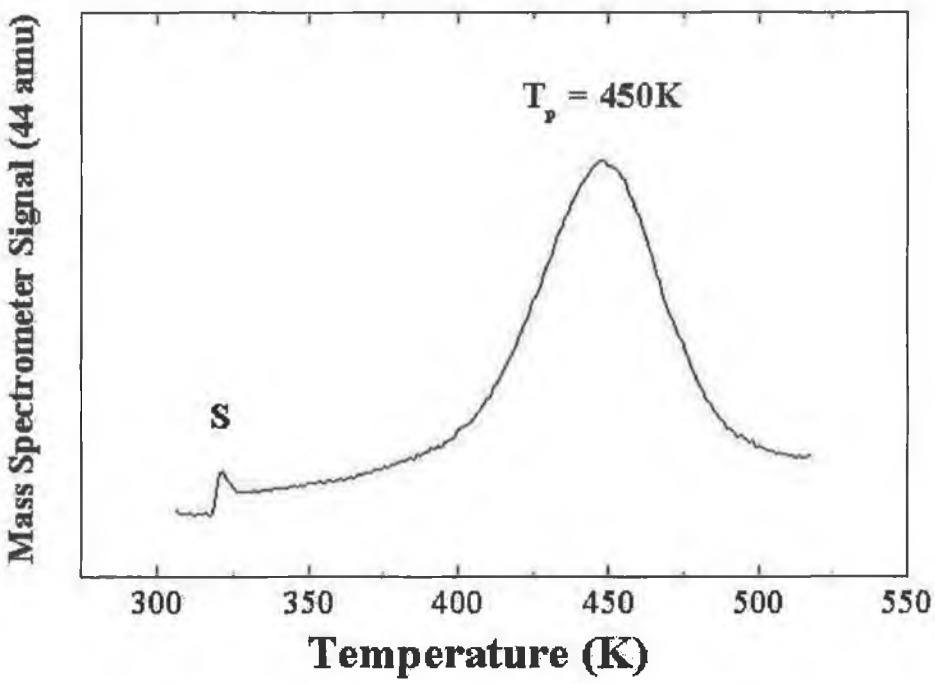

Figure 2.15: A typical TPRS spectrum of HCOOH adsorbed on Cu{100} locked into mass 44 (a decomposition product of the formate HCOO intermediate). The feature "S" is desorption from the sample support wires.

The shape of the TPRS spectrum originates from the product of two temperature-dependent physical parameters: the increasing rate of desorption versus temperature and the decreasing surface coverage as the temperature is increased. Figure 2.16 shows schematically the TPD spectrum (red line) as a product of changes in surface coverage and rate constant as a function of temperature.

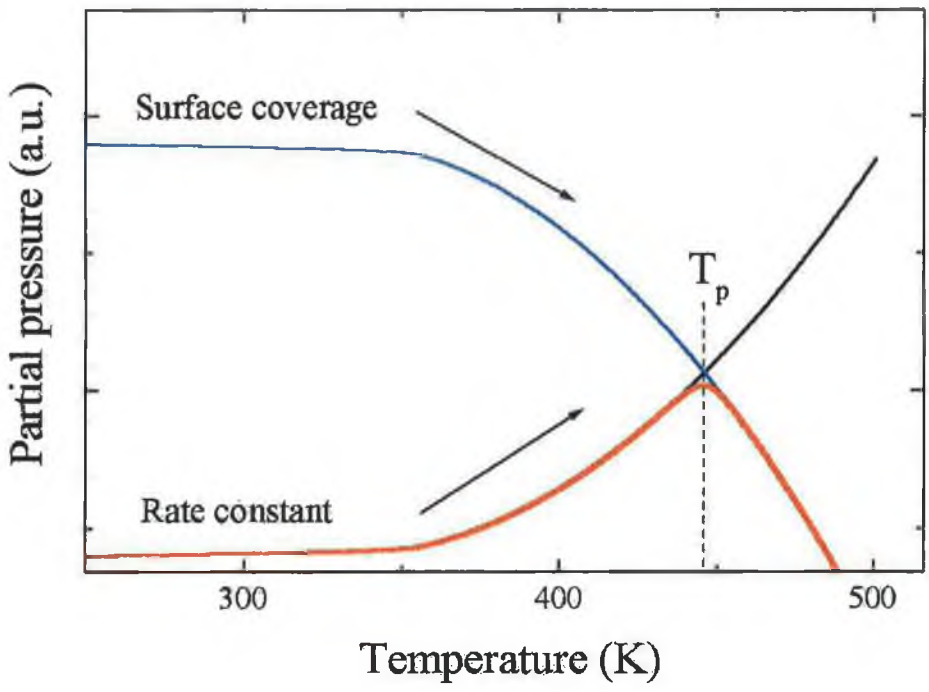

Fig 2.16: The rate of desorption (red curve) as a product of changes in surface coverage and rate constant as a function of temperature [19].

The sensitivity of TPD technique is considered high due to the use of mass spectrometric detection. Detection limits below 0.1% of a monolayer of adsorbate are deemed attainable [20].

The rate of desorption per unit surface area may be described by:

$$-dN/dt = k_d.N^m \qquad (2.14$$

where m is the order of desorption and N is the number of adsorbed particles [19]. The desorption rate constant, k_d, obeys an Arrhenius dependency and shows an exponential increase with temperature given by equation (2.15):

$$k_d = A \exp(-E_d/RT) \qquad (2.15$$

where E_d is the activation energy for the desorption process, A is a pre-exponential factor and R is the ideal gas constant (8.314 $Jmol^{-1}K^{-1}$).

For a first order desorption process, A is assumed to be of the same order of magnitude as the molecular vibration frequency and is often assumed to be 10^{13} s^{-1} for diatomic molecules [19]. Actual values, measured by other techniques such as Molecular Beam Relaxation Spectroscopy (MBRS), however, may differ from this value by as much as 10^5.

Substituting for k_d and the heating rate $\beta = dT/dt$ into equation (2.14) yields a representation of dN as a function of temperature (T):

$$-dN/dT = N^m (A/\beta) \exp(-E_d/RT) \qquad (2.16$$

The rate of desorption reaches a maximum when $T=T_p$ and then the second derivative $d^2N/dT^2 = 0$ (the desorption maximum in figure 2.16). Hence, by differentiating equation (2.16) with respect to T and equating to zero, a general equation relating T_p, E_d and N can be derived:

$$E_d/R(T_p)^2 = (A/\beta)\, m\, N^{m-1} \exp(-E_d/RT_p) \qquad (2.17$$

Thus, as β and T_p are experimentally measured parameters, the activation energy E_d may be evaluated.

For a first order desorption process (m=1), equation 2.17 can be simplified to:

$$E_d/R(T_p)^2 = (A/\beta) \exp(-E_d/RT_p) \qquad (2.18$$

By assuming a first order desorption process, Redhead postulated a simple and direct equation to calculate the activation energy by knowing only the experimentally measured values T_p and β:

$$E_d = RT_p [\ln (AT_p/\beta)-3.46] \qquad (2.19)$$

For example, for formate desorption from Cu{100} shown in figure 2.15, the TPRS spectrum shows T_p at 450K. Using a heating rate of $\beta = 2.5\ Ks^{-1}$ and assuming a pre-exponential factor $A=10^{13}\ s^{-1}$, the activation energy can be calculated as follows:

$$E_d = (8.314\ Jmol^{-1}K^{-1})(450K)[\ln ((10^{13}\ s^{-1})(450K)/2.5Ks^{-1})-3.46]$$

$$= 118\ kJmol^{-1}$$

Note that T_p is variable for desorption processes with orders different from unity. King showed that T_p is dependent on the initial coverage N for desorption orders higher than unity. For adsorbates with no lateral interaction an asymmetric curve for first-order desorption is predicted while a symmetric curve in a second order desorption process is obtained [21].

A TPD spectrum can provide valuable information about the relative surface coverage. To practically make use of the TPD data for relative coverage evaluations, several assumptions must be made. For example when evaluating relative coverage via integration, the pumping speed of the UHV system is assumed constant. If this is the case, the area under the TPD curve is directly proportional to the surface coverage. Hence, a simple integration of the area under the curve allows a direct measurement of the relative coverage. Furthermore, if there is more than one binding state for a molecule on a surface (and these have significantly different adsorption enthalpies), multiple peaks will generally be observed in the TPD spectrum. Figure 2.17 shows data from a TPD experiment following adsorption of NO on Pt{331} at 300 K [22]. The pt{331} surface contains two distinct sites {111}

"terrace sites" and step-edge sites. Clearly, two desorption peaks at high NO exposures are observed which implies the presence of more than one binding state for the NO molecule. In this case it seems logical to assign two distinct desorption states to desorption from terrace and step sites.

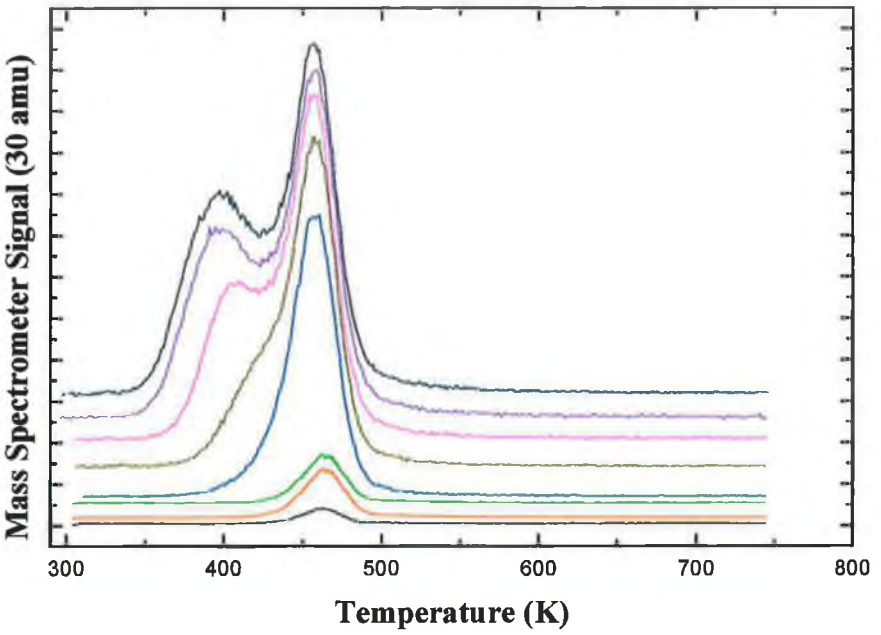

Fig 2.17: TPD spectra of NO (30 amu) adsorbed on Pt{331} at room temperature as a function of NO exposure. The exposures correspond to: (a) 0.05; (b) 0.1; (c) 0.2; (d) 0.3; (e) 0.4; (f) 0.5; (g) 0.6 and (h) 0.75 L. (a) corresponds to the lower spectrum and (h) corresponds to the upper curve.

It should be noted that care should be exercised in assigning multiple peaks to distinct adsorption sites. In some adsorption systems exhibiting first order kinetics, increasing exposure leads to the desorption peak maximum temperature shifting to a lower value. Furthermore, low temperature additional peaks can often appear at the highest exposure. The existence of multiple desorption peaks and coverage-dependent shifts in peak maxima may arise from:

1. The presence of more than one distinct binding site with different activation energies for adsorption (e.g. hollow, atop, bridge);
2. Coverage-dependent lateral interactions between adsorbates [19].

References:

[1] P.W. Atkins, Physical Chemistry, Oxford University Press, Oxford, 1982.

[2] M.A. Van Hove, W.H. Weinberg, C.M. Chan, LEED:Experiment, Theory and Surface Structure Determination, Springer Verlag, 1986, Springer Series in Surface Sciences Volume 6.

[3] L.J. Clarke, Surface Crystallography, Wiley&Sons, New York, 1985.

[4] J.M. MacLaren, J.B. Pendry, P.J. Rous, D.K. Saldin, G.A. Somorjai, M.A. Van Hove, and D.D. Vedensky, Surface Crystallographic Information Service, A Handbook of Surface Structures, D. Reidel Publishing, 1987.

[5] K. Heinz and L. Hammer, Z. Kristallogr. 213 (1998) 615.

[6] S. Walter, V. Blum, L. Hammer, S. Muller, K. Heinz and M. Giesen, Surf. Sci. 458 (2000) 155.

[7] P.M. Marcus and F. Jona, Determination of Surface Structure by LEED, Plenum Press, 1984, The IBM Research Symposia Series.

[8] M.P. Seah and W.A. Dench, Surface and Interface Analysis, 1 (1979) 2.

[9] J.B. Pendry, J. Phys. C 13 (1980) 937.

[10] M.A. Van Hove and S.Y. Tong, Surface Crystallography by LEED:Theory, Computation and Structural Results, Springer Verlag, 1979, Springer Series in Chemical Physics Volume 2.

[11] A. Barbieri and M.A. Van Hove, private communication.

[12] J.B. Pendry, LEED: The Theory and its Application to Determination of Surface Structure, Academic Press, 1974, Techniques of Physics Volume 2.

[13] F. Jona, J.A. Strozier, W.S. Yang, Rep. Prog. Phys. 45 (1982) 527; Y.S. Li, J. Quinn, F. Jona, and P.M. Marcus, Phys. Rev. B 46 (1992) 4830; Z.Q. Wang, C.K.C. Lok, J. Quinn, Y.S. Li and F. Jona, J. Phys. C , 21 (1988) 653; Z.Q. Wang, Y.S. Li, C.K.C. Lok, J. Quinn and F. Jona, Solid State Commun. 62 (1987) 181

[14] J.R. Noonan and H.L. Davis, J. Vac. Sci. Technol. 17 (1980) 194.

[15] D. Adams, private communication.

[16] L. Apker, Ind. Eng. Chem 40 (1948) 846.

[17] T. P. Clair, J.M. Rested and T. Oyama, J. Mater. Res, 13 (1998) 1430.

[18] D. V. Andreev, A. Yu. Biryukov, L. S. Danelyan, N. G. Elistratov, V. M. Gureev, M. I. Guseva, B. N. Kolbasov, Yu. Ya. Kurochkin, V. N. Nevzorov, O. V. Stativkina and A. M. Zimin , Fusion Engineering and Design, 39 (1998) 465.

[19] G. Attard and C.J. Barnes, Surfaces, Oxford University Press, 1998.

[20] R. Nix, http://www.qmw.ac.uk/surfaces/scc/, 1996.

[21] D.A. King, Surf. Sci., 47 (1975) 384.

[22] E. Timothy, private communication.

CHAPTER 3

Coverage and Temperature Dependent Structural Transitions in the Cu{100}/Pd Surface Alloy System

Early Stages of Surface Alloy Formation:

A Diffuse LEED I(V) Study

C. J. Barnes[a], E. AlShamaileh[a], T. Pitkänen[b] and M. Lindroos[b]

[a] School of Chemical Sciences, Dublin City University, Dublin 9, Ireland
[b] Institute of Physics, Tampere University of Technology, Tampere, Finland

Abstract

The technique of diffuse low energy electron diffraction (DLEED) *I*(*V*) analysis is shown to be a useful quantitative probe of the structure of surface alloys in the early stages of growth before long-range order develops.

The Cu{100}/Pd system has been studied in the Pd coverage range 0.10-0.55 ML. We demonstrate the Pd adsorbs at all coverages primarily by substitutional replacement of top layer copper atoms forming a two-dimensional Cu_xPd_{1-x} surface alloy. At low coverages a quasi-random substitutionally disordered two-dimensional alloy is formed with local order detected by LEED developing at Pd coverages above 0.25 ML. The surface geometry is not strongly coverage dependent with top layer Cu and Pd atoms almost coplanar and the first interlayer spacing slightly expanded (3%) with respect to the bulk value.

1. Introduction

Investigation of the structure of low coverages of disordered adsorbates has proved a difficult problem to solve. Local probes such as photo-electron diffraction, surface extended X-ray absorption fine structure and more recently X-ray standing wave techniques have in many cases been successfully applied [1,2]. However, while yielding accurate surface geometries their use necessitates access to synchrotron radiation facilities.

Of the laboratory based surface crystallographic tools, low energy electron diffraction (LEED) is highly successful for the study of systems possessing a high degree of long range order. The introduction of diffuse LEED by Pendry, Heinz and co-workers [3-6] opened the way for study of low coverage disordered systems in which adsorbates occupy well defined sites as in the lattice gas model. A variant of this technique, diffuse LEED $I(V)$ involves the measurement of the diffuse background intensity as a function of beam energy as in traditional LEED $I(V)$ analysis [7-10].

Adsorption of Pd on Cu(100) at 300 K leads to formation of an ordered c(2×2) overlayer alloy [11]. Lu et al. demonstrated by LEED $I(V)$ analysis that the c(2×2) periodicity originated from formation of a CuPd surface alloy with approximately 0.5 ML of Pd substitutionally replacing Cu atoms within the outermost layer with Pd atoms slightly rippled outwards by 0.02±0.03 Å [12,13]. The same structure has been re-examined by LEED $I(V)$ analysis [14] confirming the geometry initially proposed by Lu et al. Pope et al. using medium energy ion scattering favoured a geometry with Pd atoms rippled outwards with a slightly larger amplitude between 0.04 and 0.08 Å [15]. However, in the latter case it was implicitly assumed that first and second layer copper atoms remained in bulk truncated positions. Finally, embedded atom method calculations favoured a geometry with the first copper interlayer spacing contracted by 3% with Pd atoms buckled outwards by 0.12 Å [16]. In contrast, little is known about the structure below Pd coverages of 0.5 ML. The only work to date is the STM study of Murray et al. [17], which indicates that surface alloy formation occurs even at low Pd coverages with a quasi-random

substitution of Pd into the outermost layer with preference for Pd atoms to occupy second nearest neighbour sites. In this short contribution we illustrate the power of the diffuse LEED $I(V)$ technique to provide structural information about the early stages of Pd adsorption on Cu(100).

2. Experimental

The experimental $I(V)$ spectra were acquired with an energy increment of 1 eV and were symmetry averaged to reduce error due to sample mis-alignment [18] and residual electrostatic and magnetic fields and normalised to constant incoming beam current. In the case of partially ordered and disordered overlayers, an identical tracking path was used as that for the (1/2,1/2) beam from the ordered Cu(100)-c(2×2)-Pd phase at maximum perfection.

In the case of the diffuse $I(V)$ data, a careful background subtraction of the diffusely scattered intensity from clean Cu(100) under identical experimental conditions was applied to remove diffuse spectral structure from defects in the Cu(100) sample and phonon related diffuse scattering. This procedure is similar to that successfully adopted in previous diffuse $I(V)$ studies [9, 10].

Palladium was evaporated from a well outgassed 0.3 mm diameter tungsten filament around which was wrapped high purity 0.125 mm diameter Pd wire (Goodfellow Metals Ltd.). Coverages were calibrated by measurement of spot profiles as a function of evaporation time to determine the time required to bring the (1/2,1/2) beam to maximum intensity. Pope et al. have previously determined by Rutherford backscattering spectroscopy (RBS) that the (1/2,1/2) beam reaches maximum intensity at a Pd coverage of 0.55±0.1 ML [14, 15]. Coverages below 0.25 ML yielded p(1×1) LEED patterns with increased background intensity. Diffuse circular c(2×2) beams were observed for Pd coverages above 0.25 ML which became increasingly sharp and bright in the coverage range 0.25–0.55 ML. The observation of diffuse circular beams at coverages 0.25 ML suggests islanding in small c(2×2) domains with spot broadening due to finite size effects. The Cu(100)-c(2×2)-Pd surface alloy at a Pd coverage of 0.55 ML yielded bright and sharp fractional order beams.

3. Calculations

LEED calculations were performed using the Barbieri/Van Hove symmetrised automated tensor LEED package [19]. Up-to 10 phase shifts generated from the potentials of Moruzzi et al. [20] were used. Other non-structural parameters used included bulk Debye temperatures (275 K for Pd and 335 K for Cu) [21] and an energy independent imaginary part of the inner potential of 5 eV. Along with the structural parameters (the co-ordinates of the Cu and Pd atoms in the outermost layer), the real part of the inner potential was varied in the tensor LEED search routine. The theory–experiment agreement was tested using the Pendry *R*-factor [22].

4. Results and discussion

Fig. 1 illustrates the LEED $I(V)$ spectrum from the (1/2,1/2) beam from an ordered Cu(100)-c(2×2)-Pd surface alloy formed by deposition of 0.55 ML of Pd at room temperature. This spectrum is in excellent agreement with the measurements of Valden et al. [23] from the same system and also in good agreement with earlier studies of Lu et al. [12], Wu et al. [13] and Pope et al. [16]. Also shown are the equivalent diffuse $I(V)$ spectra from long range disordered overlayers of Pd coverages of 0.10, 0.15 and 0.20 ML and from partially ordered overlayers exhibiting diffuse c(2×2) beams for coverages of 0.25 and 0.30 ML. The diffuse $I(V)$ spectra have been normalised by $1/E$ to account for the increase in the area of reciprocal space sampled with increasing energy [9].

Clearly the spectra at all Pd coverages are highly similar in terms of spectral structure and peak positions. This strongly suggests that the local geometry surrounding the Pd adsorbate is coverage independent i.e. surface alloys are formed at all coverages studied with similar Cu–Pd nearest neighbour bond lengths.

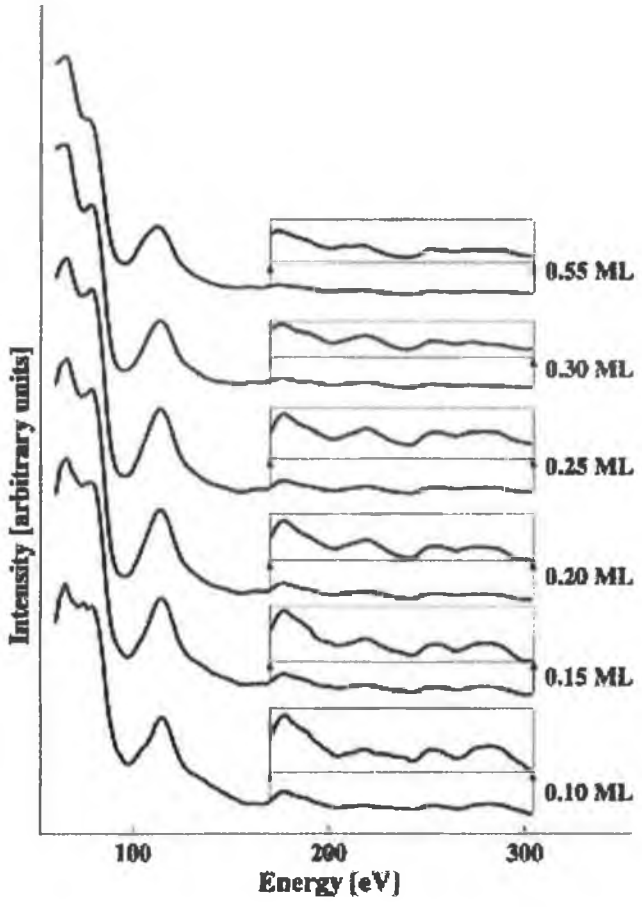

Fig. 1: Normal incidence symmetry averaged and beam current normalised $I(V)$ spectra from the (1/2,1/2) position for different Pd coverages marked in the figure. A single 13 point smoothing has been applied to all spectra.

In order to examine the effect of Pd coverage and lateral distribution within the outermost mixed CuPd alloy layer on LEED $I(V)$ spectra, a series of model calculations were performed for ordered surface alloys producing diffracted beams in the (1/2,1/2) position. Fig. 2 illustrates $I(V)$ spectra from c(4×4) Fig. 2(A) and p(2×4) Fig. 2(B) (θ_{Pd}=0.125 ML), p(2×2) Fig. 2(C) (θ_{Pd}=0.25 ML) and c(2×2) Fig. 2(D) (θ_{Pd}=0.50 ML) surface alloys. In each case all structural and non-structural parameters were held fixed with the surface geometry corresponding to that obtained by Lu et al. for the Cu(100)-c(2×2)-Pd structure [12,13]. The high level of similarity in the calculated $I(V)$ spectra for widely different Pd coverages and lateral distributions clearly illustrates that at normal incidence the spectral structure in the (1/2,1/2) beam is relatively insensitive to the exact Pd coverage/lateral distribution, suggesting that events involving multiple scattering between two or more Pd atoms

is weak even for a strong scatterer such as Pd. The structure in all spectra is extremely similar, only very small changes occur involving mainly changes in peak relative intensities. The most significant change is in the peak at 140 eV which exhibits a large decrease in intensity with increasing Pd coverage. Model calculations (not shown) were also performed for the (3/2,1/2) and (3/2,3/2) beams, the results confirmed the similarity demonstrated for the (1/2,1/2) beam.

Also shown in Fig. 2 (curve *E*) is a model calculation for a p(2×2) Pd overlayer, with Pd adatoms adsorbed in fourfold hollow sites above the outermost copper plane with a copper-palladium interlayer spacing of 1.945 Å, equal to the bulk interlayer spacing in Pd(100). This structure yields a significantly different $I(V)$ spectrum from that of the surface alloy, and much poorer agreement with the experimental $I(V)$ spectra of the Cu/Pd surfaces illustrated in Fig. 1. While it is possible that the copper-palladium interlayer spacing varies from that of bulk Pd, it is unlikely to do so by more than 10%. An overlayer model for all physically reasonable surface geometries yields poor agreement when compared to the experimental data of Fig. 1. This allows us to rule out overlayer formation at low Pd coverages and suggests that surface alloy formation occurs throughout the coverage range studied.

Finally, as the coverage and lateral distribution of Pd appears to be relatively unimportant, diffuse and partially ordered $I(V)$ data may be analysed using model calculations for ordered overlayers which yield a diffracted beam in the region of k-space for which the diffuse $I(V)$ spectrum was acquired.

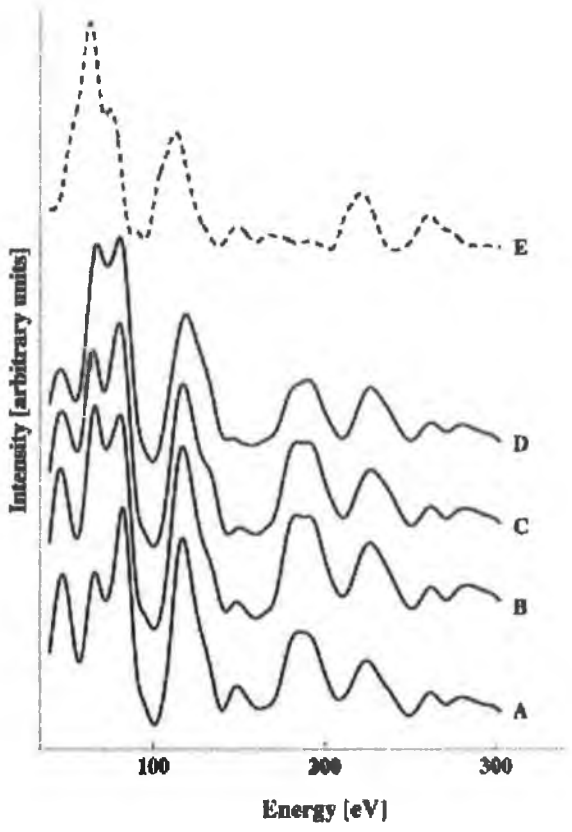

Fig. 2: Calculated normal incidence $I(V)$ spectra for ordered surface alloys including: (A) c(4×4) (θ_{Pd}=0.125 ML); (B) p(2×4) (θ_{Pd}=0.125 ML); (C) p(2×2) (θ_{Pd}=0.25 ML) and (D) c(2×2) (θ_{Pd}=0.50 ML). In all cases the surface geometry corresponds to that of Lu et al. [12] and Wu et al. [13]. The dotted line (E) shows a calculation for a p(2×2) overlayer with Pd adatoms in fourfold hollow sites and a copper-palladium interlayer spacing of 1.945 Å.

Fig. 3 illustrates the optimal theory-experiment agreement and corresponding Pendry R-factors for the diffuse $I(V)$ spectra of Pd coverages of 0.15, 0.25 and 0.55 ML respectively using calculations for a perfect top layer c(2×2) CuPd alloy. For the purpose of the fitting, all structural parameters in second and deeper layers were frozen at their bulk values. The only structural parameters which were allowed to vary were the first interlayer spacing and the rippling within the composite CuPd alloy layer along with a rigid shift in the real part of the inner potential. Freezing of the atomic positions in second and deeper layers appears a good approximation based on the results of the LEED $I(V)$ analysis of the Cu(100)-c(2×2)-Pd ordered alloy by Lu et al. [12] and Wu et al. [13]. The favoured geometries are summarised in Fig. 3 and consist of an almost coplanar mixed layer with the first interlayer spacing slightly expanded by up-to 0.06 Å (d_{z12}=3%). Optimal geometries were also

obtained for the 0.25 and 0.15 ML data using calculations based on p(2×2) and c(4×4) overlayers respectively yielding geometries identical to within a few hundredths of an Angstrom to those obtained with a c(2×2) model calculation with Cu and Pd again coplanar. The analysis confirms the observation that the similar nature of the diffuse $I(V)$ spectra imply a highly similar local geometry.

The only previous geometric study of Cu(100)/Pd surfaces below 0.5 ML coverage is the STM study of Murray et al. [17]. Their work indicates that even at the lowest coverage studied (0.2 ML), formation of a surface alloy is favoured with substitution of Pd into the outermost copper layer. As the Pd coverage is increased Pd atoms adsorbing in the vicinity of alloyed Pd atoms avoid occupation of nearest neighbour sites, forming locally microscopic areas of c(2×2) periodicity. The diffuse LEED results are thus in full agreement and independently support the STM work of Murray and co-workers that surface alloying occurs with Pd atoms occupying fourfold hollow sites within the outer monolayer at low coverages.

Our results agree rather well with those of Lu et al. [12] and Wu et al. [13] and indicate that the copper and palladium atoms are close to coplanar at all coverages. However, it is important to note that the Cu atoms within the outermost layer, particularly at the lower Pd coverages, may exist in a range of slightly different local geometries dependent on the number of nearest and next nearest Pd neighbours. Hence an analysis based on a c(2×2) or p(2×2)/c(4×4) outer layers is strictly incorrect. In reality a range of slightly different local geometries may exist. Thus the best an analysis of the type presented here can achieve is to give an *average* picture of the top layer geometry. The situation is further complicated by the existence of Pd in sub-surface layers [11, 16, 17, 23 and 24]. While the exact percentage of deposited Pd atoms located in the second layer varies from study to study, it would appear that the amount is in the range 15% to 40% of the total quantity of Pd deposited at maximum perfection of the ordered Cu(100)-c(2×2)-Pd phase. The STM study of Murray et al. [17] indicates that at Pd coverages of 0.20 and 0.35 ML (as calibrated by RBS) between 20% and 25% of Pd atoms are sub-surface. While the scattering from top layer atoms will dominate, both due to their higher concentration and to the additional loss of intensity from second layer atoms due to inelastic scattering by the outer CuPd monolayer, their presence may lead to small

systematic errors in the recovered geometry of top layer atoms. While for a semi-quantitative analysis based on the (1/2,1/2) beam alone it is not realistic to include this additional complexity, the presence of second layer Pd should be accounted for in a full quantitative study based on a larger data base. Collection of $I(V)$ spectra from integral order beams at low Pd coverage (e.g. 0.2 ML) and analysis assuming a top layer substitutionally disordered alloy applying the average T-matrix approximation (ATA) may allow more accurate geometric determination and yield further insight in-to the concentration of Pd in sub-surface sites. Work along these lines is presently underway and will be reported in a future and more comprehensive article.

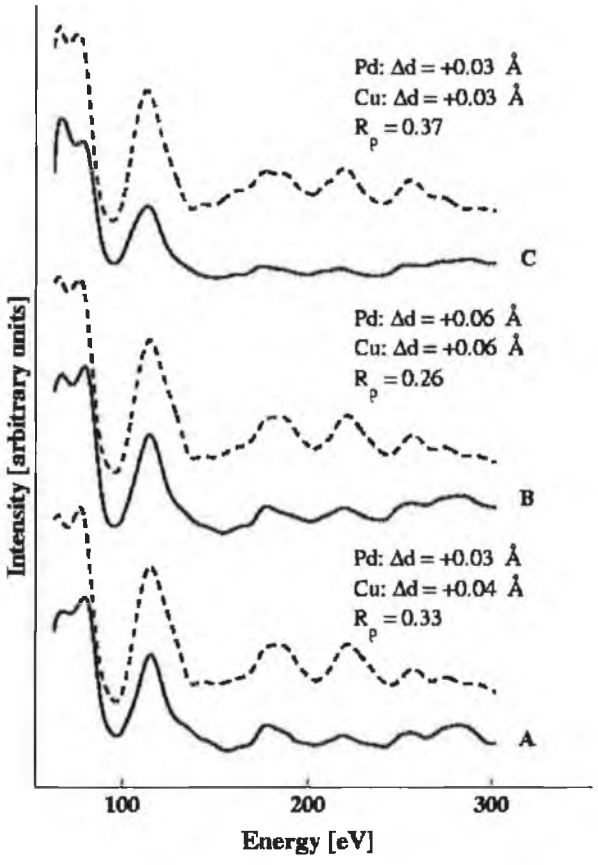

Fig. 3: Theory-experiment agreement for palladium coverages of (A) 0.15 ML; (B) 0.25 ML and (C) 0.55 ML. Calculated spectra shown as dashed lines. The Pendry *R*-factors along with the optimal geometry in terms of shifts in the Cu and Pd atoms in the outermost layer away from bulk truncated positions (Δd) is shown (positive values indicate expansions).

Most common metal adsorbates such as transition metals are strong scatterers and form monolayers whose atomic density are similar to that of the substrate and thus provide sufficient diffusely scattered intensity that DLEED $I(V)$ spectra can easily be collected for coverages as low as 0.10 ML using a standard CCD camera and display type LEED optics. In the case of the Cu(100)/Pd system reported here, the 0.10 ML data was collected without significant difficulty at 300 K. The use of liquid nitrogen cooling should enhance further the diffuse $I(V)$ data quality, hence we can envisage that in principle, coverages as low as 0.05 ML could be studied. The diffuse $I(V)$ technique could thus yield quantitative structural determinations of accuracy approaching that of LEED analyses from ordered overlayers by collection of diffuse $I(V)$ spectra from a range of regions of k-space along with integral beams coupled with application of the Average T-matrix Approximation (ATA) analysis.

5. Conclusions

The technique of diffuse LEED $I(V)$ analysis has been applied to study the earliest stages of surface alloy formation during the room temperature growth of Pd on Cu(100).

We demonstrate that even for strong scatterers such as Pd, multiple scattering between two or more Pd atoms is weak for conditions normally applied in $I(V)$ analysis (normal incidence, energy range 50-300 eV) provided adsorbates are coplanar. Thus, a quantitative analysis of the surface geometry of lattice gas disordered overlayers is possible combining diffuse LEED $I(V)$ measurements and calculations from ordered phases producing LEED beams in regions of k-space at which diffuse $I(V)$ measurements were performed.

For Pd adsorption on Cu(100) at 300 K in the coverage range 0.1 to 0.55 ML:

(a) the local geometry at all coverages corresponds to a Cu_xPd_{1-x} surface alloy with adsorbate atoms predominantly substituting into the outermost copper monolayer occupying substitutional lattice sites,

(b) the local surface geometry is coverage independent within the resolution of the analysis and corresponds to an approximately coplanar CuPd outer monolayer and an expanded (3%) first to second interlayer spacing.

References

1. D.P. Woodruff. *Prog. Surf. Sci.* **57** (1998), p. 42.
2. D.P. Woodruff and A.M. Bradshaw. *Rep. Prog. Phys.* **57** (1994), p. 1029.
3. J.B. Pendry and D.K. Saldin. *Surf. Sci.* **145** (1984), p. 33.
4. L. Heinz, D.K. Saldin and J.B. Pendry. *Phys. Rev. Lett.* **55** (1985), p. 2312.
5. K. Heinz, Vacuum 41 (1990) 328 and references therein.
6. U. Starke, K. Heinz and J.B. Pendry. *Prog. Surf. Sci.* **52** 2 (1996), pp. 53-124.
7. W.S. Yang, F. Jona and P.M. Marcus. *Phys. Rev. B* **27** (1983), p. 6397.
8. P. Hu, C.J. Barnes and D.A. King. *Phys. Rev. B* **45** (1992), p. 13595.
9. K. Heinz, U. Starke and F. Bothe. *Surf. Sci. Lett.* **243** (1991), pp. L70-L73.
10. C.J. Barnes, A. Wander and D.A. King. *Surf. Sci.* **281** (1993), p. 33.
11. G.W. Graham. *Surf. Sci.* **171** (1986), p. L432.
12. S.H. Lu, Z.Q. Wang, S.C. Wu, C.K.C. Lok, J. Quinn, Y.S. Li, D. Tian, F. Jona and P. Marcus. *Phys. Rev. B* **37** (1988), p. 4296.
13. S.C. Wu, S.H. Lu, Z.Q. Wang, C.L.C. Lok, J. Quinn, Y.S. Li, D. Tian, F. Jona and P.M. Marcus. *Phys. Rev. B* **38** (1988), p. 5363.
14. T.D. Pope, M. Vos, H.T. Tang, K. Griffiths, I.V. Mitchell, P.R. Norton, W. Liu, Y.S. Li, K.A.R. Mitchell, Z.-J. Tian and J.E. Black. *Surf. Sci.* **337** (1995), p. 79.
15. T.D. Pope, G.W. Anderson, K. Griffiths, P.R. Norton and G.W. Graham. *Phys. Rev. B* **44** (1991), p. 11518.
16. T.D. Pope, K. Griffiths and P.R. Norton. *Surf. Sci.* **306** (1994), p. 294.
17. P.W. Murray, I. Stensgaard, E. Laegsgaard and F. Besenbacher. *Surf. Sci.* **365** (1996), p. 591.
18. F. Jona, Surf. Sci. 192 (1987) 398, and references therein.
19. M.A. Van Hove, W. Moritz, H. Over, P.J. Rous, A. Wander, A. Barbieri, N. Materer, U. Starke and G.A. Somorjai. *Surf. Sci. Rep.* **19** (1993), p. 191.
20. V.L. Moruzzi, J.F. Janak and A.R. Williams. *Calculated Electronic Properties of. Metals*, Pergamon Press, New York (1978).

21. N.W. Ashcroft and N.D. Mermin. *Solid State Physics*, CBS Publishing, Japan (1981).

22. J.B. Pendry. *J. Phys. C: Solid State Phys.* **13** (1980), p. 937.

23. M. Valden, J. Aaltonen, M. Pessa, M. Gleeson and C.J. Barnes. *Chem. Phys. Lett.* **228** (1994), p. 519.

24. G.W. Graham, P.J. Schmitz and P.A. Thiel. *Phys. Rev. B* **41** (1990), p. 3353.

The Kinetics of Formation and Structure of an Underlayer Alloy: The Cu(100)-c(2×2)-Pd System

C. J. Barnes[a], E. AlShamaileh[a], T. Pitkänen[b], P. Kaukasoina[b] and M. Lindroos[b]

[a] School of Chemical Sciences, Dublin City University, Glasnevin, Dublin 9, Ireland
[b] Institute of Physics, Tampere University of Technology, P.O. Box 692, FIN-33101 Tampere, Finland

Abstract

The kinetics and mechanism of an irreversible overlayer to underlayer transition in the Cu(100)-c(2×2) surface alloy has been investigated by LEED. The activation energy for Pd site switching from the outermost layer to sub-surface (second layer) sites has been estimated to be 109±12 kJ mol^{-1} (1.13±0.12 eV).

The structure of the underlayer alloy has been examined quantitatively by tensor LEED. The Cu(100)-c(2×2) underlayer is demonstrated to have its origin in substitution of approximately 0.5 ML of Pd into the second layer to form a c(2×2) CuPd underlayer alloy capped by a copper monolayer (R_p=0.28). A mixed third layer c(2×2) CuPd layer capped by a copper double layer may be ruled out. Incorporation of sub-surface Pd into the Cu(100) surface leads to significant expansion of both the first and second interlayer spacings of dz_{12}=+3.3% (0.06 Å) and Dz_{23}=+6.6% (0.12 Å) relative to the bulk Cu(100) interlayer spacing (1.805 Å) leading to a net expansion of the outermost three layer slab of 0.18 Å.

1. Introduction

The early stages of epitaxial growth are often dominated by interfacial mixing resulting in surface alloy formation [1]. Surface alloys consisting of a mixed monolayer two-dimensional alloy or an interfacial mixed region several monolayers thick are of great interest as they provide ideal templates to study the effect of alloying on surface electronic structure, catalytic activity and magnetic properties. One of the most fundamental questions that must be answered about a surface alloy, is the detailed nature of the surface geometry including the exact location of adsorbate atoms within the selvedge and bond lengths within the mixed outermost layers. Low energy electron diffraction (LEED) is an ideal probe of the geometry of surface alloys as it possesses the required sensitivity to both surface and sub-surface aspects of the mixed interface.

The Cu(100)-c(2×2)-Pd surface alloy formed by deposition of sub-monolayer coverages of Pd on Cu(100) at 300 K is one of the most extensively studied examples of surface alloy formation. Graham was the first to study in detail the adsorption of Pd on Cu(100), observing formation of an intense c(2×2) LEED pattern over a range of sub-monolayer coverages [2]. The geometric structure was subsequently solved by Lu et al. [3] and Wu et al. [4] using LEED $I(V)$ analysis, and was shown to be due to a mixed CuPd monolayer formed by substitution of 0.5 ML of Pd into the outermost copper monolayer in a c(2×2) array. The copper and palladium were found to be almost coplanar with Pd rippled outwards by 0.02±0.03 Å and the outermost interlayer spacings close to the bulk value. Subsequently, the basic geometry resulting from a top layer mixed CuPd compound was confirmed by Pope et al. [5] using LEED and Rutherford backscattering spectroscopy (RBS) [5, 6 and 7].

Early studies of the Cu(100)-c(2×2)-Pd surface alloy already pointed to additional complexity as the Pd coverage which was determined to be required to yield the best developed c(2×2) LEED pattern varied from the RBS determination of Pope et al. [6, 7] of 0.55±0.1 ML upto a value of 0.8 ML determined by Auger Electron Spectroscopy (AES) by Graham et al. [2, 8]. A deficiency in Pd in the outermost layer was reported [2-8] using desorption spectroscopy with CO as probe molecule

and low energy ion scattering spectroscopy (LEISS). Valden et al. using CO desorption spectroscopy combined with polar X-ray photo-electron diffraction demonstrated that the top layer was heterogeneous with domains of pure copper co-existing with areas of c(2×2) CuPd alloy with significant quantities of Pd located in the second layer [9]. The non-ideal nature of the surface alloy was most recently further confirmed by Murray et al., who using STM, illustrated that formation of the most microscopically ideal top layer c(2×2) occurred somewhat later than the optimisation in intensity of half order LEED beams with excess Pd being present in sub-surface sites [10]. The surface structure corresponding to maximum intensity in half order LEED beams was demonstrated to consist of significant areas of pure copper in the outermost layer co-existing with domains of CuPd c(2×2) alloy. Most recently, Shen et al. [11], using a calibrated quartz crystal microbalance determined that the best quality c(2×2) LEED pattern occured at a palladium coverage of 0.58±0.06 ML. Furthermore, using LEISS the authors were able to determine that at this coverage approximately three quarters of the Pd atoms were localised in the outermost layer with the remaining 25% sub-surface [11].

The question of the thermal stability of the Cu(100)-c(2×2)-Pd top layer alloy has been addressed by Graham et al. [8] who report rapid incorporation of Pd into sub-surface sites at 440 K using LEISS as a probe of surface composition. The LEED pattern was reported to remain c(2×2) upon annealing leading to the suggestion of incorporation of Pd into subsurface layers in an ordered array. Subsequent work by Andersen et al. [12, 13] using AES in combination with LEED, work function measurements and desorption of probe molecules (CO) confirmed a temperature induced c(2×2) overlayer to underlayer transition occurs and followed the kinetics of the transition by LEED/AES at 353 K. Their kinetic data suggested that the transition was complete at this temperature over a time period of approximately 60 min. Koyman et al. [14] using Positron annihilation induced Auger spectroscopy studied the overlayer to underlayer transition at the higher temperature of 423 K. Heating to 423 K led to the rapid disappearance of the positron induced Pd Auger transitions, allowing Koyman et al. to infer that Pd atoms move to sites only one atomic layer below the surface.

In this article we examine quantitatively the kinetics of the transition between a Cu(100)-c(2×2)-Pd top layer surface alloy to an ordered underlayer alloy. In addition, the geometric structure of this phase has been probed by tensor LEED to extract the detailed geometry of the Cu(100)-c(2×2)-Pd underlayer, including the effect of Pd on the outermost interlayer spacings of the Cu(100) substrate and to examine the extent of rippling in the mixed CuPd underlayer due to the large size difference (7.8%) between copper and palladium.

2. Experimental

All experiments were performed in an ion and titanium sublimation pumped ultra-high-vacuum chamber with a base pressure of 1×10^{-10} Torr. The chamber was equipped with four-grid reverse view LEED optics for display of diffraction patterns, which could also be used as a retarding field analyser for AES. A quadrupole mass spectrometer was also available for residual gas analysis and as a detector for thermal desorption spectroscopy (TDS).

The Cu(100) sample was mounted on a high precision goniometer with facilities for sample rotation and incorporating a tilt mechanism for accurate attainment of normal incidence conditions. The sample temperature could be measured with a chromel–alumel thermocouple.

The sample was cleaned in situ by cycles of argon ion bombardment and annealing to 800 K until no contaminants could be observed above the AES noise level and the sample exhibited normal incidence LEED $I(V)$ spectra of the (1,0) beam in excellent agreement with literature reports [15].

Normal incidence was attained by adjustment of the sample rotation and tilt until the (1,0), (-1,0), (0,1) and (0,-1) beams where identical to within the standards typically attained in LEED studies [15].

LEED I-V spectra were acquired with a CCD video camera (Hitachi-Denshi KP-M1E/K) with software supplied by Data Quire Corporation. The software allowed

acquisition of LEED beam spot profiles for study of surface phase transformations and automatic tracking of a user selectable number of beams for collection of LEED $I(V)$ spectra.

In the case of the Cu(100)-c(2×2)-Pd underlayer, five non-symmetric beams were collected, providing a normal incidence total energy range of 1039 eV. The low intensity of half order beams other than the (1/2,1/2) prevented reliable acquisition. Each beam was individually background subtracted and symmetry equivalent beams were then averaged to improve the signal-to-noise level and to compensate for any small remaining deviations from normal incidence and stray magnetic and electrostatic fields. All beams were normalised to constant incoming beam current and smoothed prior to data analysis.

Palladium was evaporated from a 0.3 mm tungsten filament around which was wrapped high purity 0.125 mm Pd wire. The evaporator was heated by a constant current power supply. The evaporation rate was calibrated by monitoring LEED beam profiles through the (1/2,1/2) beam as a function of evaporation time and locating the time required for the (1/2,1/2) beam to reach maximum intensity. As mentioned earlier, Pope et al. [6, 7] have reported using RBS in combination with LEED that the Pd coverage at which the (1/2,1/2) beam reaches optimal intensity is 0.55±0.10 ML. All coverages are quoted based on this calibration.

The Cu(100)-c(2×2)-Pd underlayer alloy structure on which LEED $I(V)$ analysis performed was created from a top layer c(2×2) alloy of coverage 0.5 ML by heating of the top layer alloy to 550 K at a linear heating rate of 5 K s^{-1}. Upon cooling to 300 K a sharp c(2×2) LEED pattern persisted but with fractional order beams of significantly lower intensity relative to integral order beams. Chemical probes of the surface including CO desorption and decomposition of a formate catalytic intermediate indicated penetration of the majority of Pd from top layer to sub-surface sites with only small amounts of Pd (0.05 ML) remaining in the top layer.

3. Theoretical considerations

LEED calculations were performed with the Barbieri/Van Hove symmetrized automated tensor LEED package [16]. Up to 12 phase shifts were used generated from the potentials of Moruzzi et al. [17]. Other non-structural parameters used were a bulk Debye temperature of 315 K for copper and an energy independent imaginary part of the inner potential of 5 eV. A Debye temperature of 275 K was used in the case of Pd [18]. The energy independent real part of the inner potential was allowed to vary in the LEED calculations with theory-experiment agreement tested using the Pendry *R*-factor [19].

4. Results and discussion

4.1. The Cu(100)-c(2×2)-Pd overlayer to underlayer transition: kinetics and mechanism

Fig. 1(a) illustrates a normal incidence LEED $I(V)$ spectrum of the (1/2,1/2) beam from a Cu(100)-c(2×2)-Pd overlayer of 0.5 ML coverage deposited at 315 K (lower curve). This spectrum is virtually identical to that reported by Valden et al. [9]. The data is also in good agreement with earlier measurements of Lu et al. [3, 4] and Pope et al. [5]. The c(2×2) underlayer alloy was then formed by thermal activation and the $I(V)$ spectrum of the (1/2,1/2) beam was re-measured upon cooling to room temperature and is also shown in Fig. 1(a) (upper curve). Significant changes occur upon annealing. While at low energies the spectra are rather similar, an intense peak is observed around 250 eV from the annealed c(2×2) which is clearly absent in the directly deposited top layer alloy spectrum. In addition, the broad peak at around 220 eV from the top layer c(2×2) alloy corresponds closely to a minimum in the annealed surface spectrum. A further general feature appears to be the larger relative intensity of the $I(V)$ peaks at higher beam energies from the thermally activated surface. Clearly these changes signal that a significant structural rearrangement occurs upon annealing. This hypothesis is confirmed by the CO thermal desorption data shown in Fig. 1(b). Saturation of a Cu(100)-c(2×2)-Pd top layer alloy with CO (100 L) led to a broad desorption peak (T_p=360 K). As CO does not adsorb on copper at temperatures of 300 K, we assign this desorption state to CO bound to surface Pd

atoms. Upon cooling the surface to room temperature, the surface was again re-saturated with CO and a second desorption spectrum acquired with identical sample position and mass spectrometer settings. The CO desorption signal was drastically reduced as illustrated in the lower spectrum of Fig. 1(b).

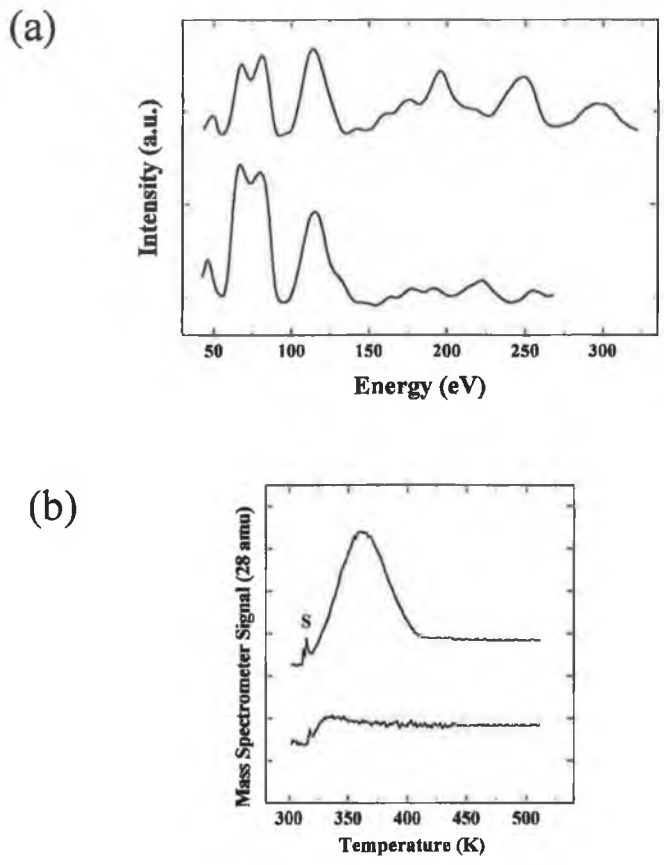

Fig. 1: (a) Symmetry averaged normal incidence $I(V)$ spectra from the (1/2,1/2) beam of the Cu(100)-c(2×2)-Pd top layer alloy (lower curve) and the Cu(100)-c(2×2)-Pd alloy formed by annealing to 550 K (upper curve). The spectra have not been normalised to incoming beam current in order to artificially emphasise higher energy diffraction features. (b) Mass 28 (CO) desorption spectra acquired with a linear heating rate of 5 K s^{-1} from the Cu(100)-c(2×2)-Pd top layer alloy (upper curve) and after heating and re-cooling to room temperature (lower curve). Both surfaces were dosed with a saturation CO exposure (100 L). The sharp feature S corresponds to desorption from the sample support wires.

In order to probe the kinetics of the transition, LEED spot profiles through the (1,0), (0,1) and (1/2,1/2) beams were collected as a function of time for a range of temperatures. Fig. 2 illustrates the variation of the (1/2,1/2) intensity with time for independently prepared top layer c(2×2) CuPd surface alloys recorded at three different temperatures at a primary beam energy of 117 eV. The half order intensity decreases monotonically and non-linearly as a function of time as the overlayer to underlayer transition is activated with the half order intensity reaching a constant value of approximately 65% of that of the top layer alloy when the transition is complete. Fig. 3 illustrates selected beam profiles at chosen times during the transition, illustrating that the c(2×2) reflexes remain sharp.

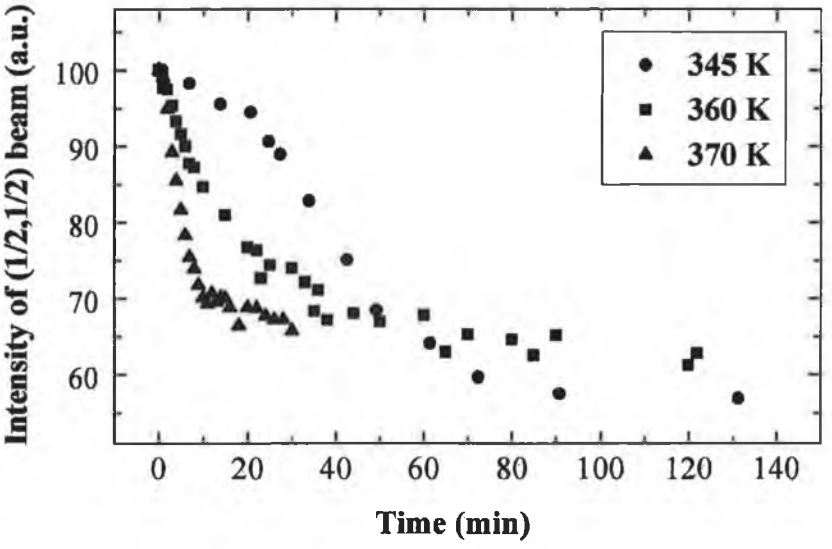

Fig. 2: Variation of the (1/2,1/2) beam intensity as a function of time for substrate temperatures of 345, 360 and 370 K at a primary beam energy of 117 eV.

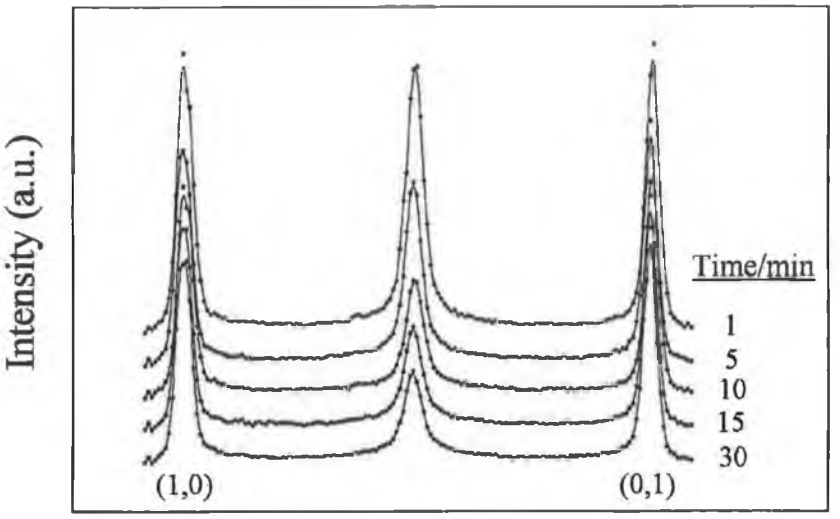

Fig. 3: Selected spot profiles at chosen stages in the overlayer to underlayer transition at temperature of 365 K.

First order kinetic plots using the (1/2,1/2) beam intensity variation, assuming that the (1/2,1/2) beam intensity is directly related to the concentration of second layer c(2×2) yield good linearity. An example of a first order plot is shown in Fig. 4 (experimental data illustrated in the inset). Fig. 5 illustrates an Arrhenius plot, using a standard chemical kinetics approach fitting the data to Eq. (1):

$$\ln k(T) = \ln A - \Delta E/RT \qquad (1)$$

where $\ln k(T)$ is the natural logarithm of the temperature dependent rate constant and ΔE represents the activation energy barrier for transport of Pd from the outermost to sub-surface layers. This yielded an activation energy barrier of 109±12 kJ mol^{-1} (1.13±0.12 eV).

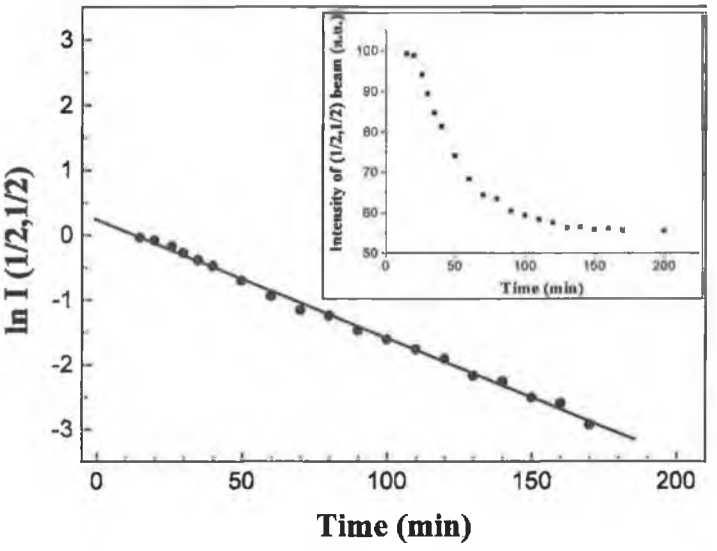

Fig. 4: A first order kinetic plot of the transition data illustrated in the figure inset. The data was recorded at a temperature of 343 K.

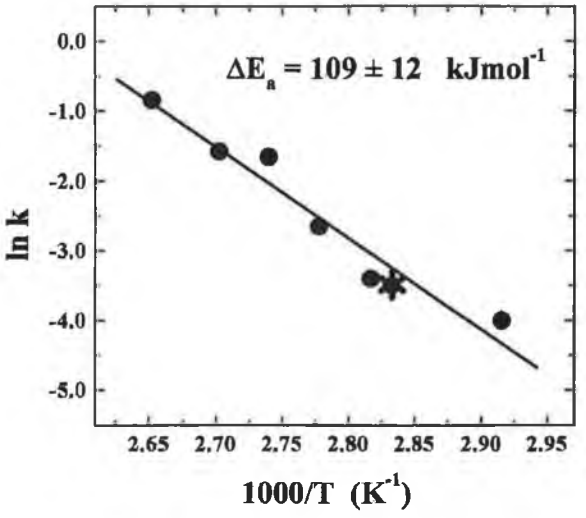

Fig. 5: Arrhenius plot for the overlayer to underlayer transition. The starred point represents data of Anderson et al. [12].

This activation barrier is higher than the 0.88 eV determined by Pope et al. [20] for alloying of Pd into the outermost layer in a c(2×2) array, yet considerably lower than

that for bulk interdiffusion which has been determined to be 2.1 eV by Goupper et al. [21] using X-ray diffraction from a $Cu_{85}Pd_{15}$ bulk alloy. A recent study of the kinetics of a top layer to underlayer transition for 0.5 ML of Pd deposited on a vicinal Cu(1,1,11) surface, consisting of (100) terraces of five unit cells width using He scattering determined an activation barrier of 1.0±0.1 eV for substitution of Pd into second layer sites, in good agreement with the value determined here for the atomically flat Cu(100) surface [21]. However, there is some indication from the He scattering data of Goupper et al., which is reflected in the slightly lower activation barrier determined, that the top layer to underlayer transition occurs faster on the high step density surface, implicating steps may play some role in the transition mechanism.

The form of the variation of the (1/2,1/2) intensity and half width with time does allow some qualitative conclusions to be drawn with respect to the mechanism of the overlayer to underlayer transition. A mechanism by which top layer Pd atoms "randomly" exchange with second layer Cu atoms may be expected to conform closely to first order kinetics. However, such a mechanism would be predicted to lead to almost complete disappearance of the (1/2,1/2) beam intensity and a marked increase in the full-width-at-half-maximum mid way through the transition. As the long range order in the top layer is gradually broken up due to top layer Pd atoms exchanging into layer 2, the intensity scattered into half order positions would rapidly decay. The second layer c(2×2) diffracted intensity would not be expected to give a significant intensity until a large amount of Pd is present in the second layer. Hence, such a mechanism would generate a rapid loss in half order beam intensity, reaching a minimum when approximately half of the top layer atoms have penetrated sub-surface. This would be followed by an increase in intensity with the ordering increasing in layer two as the Pd coverage approaches the optimal Pd concentration of 0.5 ML. Reference to Fig. 2 and Fig. 3 illustrate that this is clearly not the case.

A second mechanism would be one in which a place exchange of a Pd atom in the top layer destabilises nearest neighbour Pd atoms in the top layer, thus making them more likely to subsequently undergo transport into layer 2. This would lead to a mechanism where top layer Pd atoms exchanging with second layer atoms form

nucleation centres which subsequently grow laterally with time, leading to formation of both top layer Cu two-dimensional islands and likewise patches of second layer c(2×2) CuPd alloy. This would manifest itself in a delay period in which the half order beam intensity changes extremely slowly. This mechanism would not be expected to follow first order kinetics as the rate of the transformation would be expected to depend strongly on the island edge area, which itself would depend on the island shape and two-dimensional density of nucleation centres.

Finally, a simple mechanism exists invoking the participation of step edges in the overlayer to underlayer transition. This involves copper atoms at step edges detaching themselves and diffusing away to cover exposed CuPd top layer alloy. The newly exposed Pd atoms at the receeding step edge then undergo place exchange with a copper atom in the layer below, thus forming newly exposed Cu step-edge atoms which may in turn diffuse away and further cover existing areas of CuPd. Such a simple receeding step-edge mechanism would be predicted to follow zero order kinetics as the step edge is regenerated and would thus predict a linear decrease in the (1/2,1/2) beam intensity with time, in disagreement with experimental observation. Thus, such a simplistic step related mechanism may be ruled out. An STM study would be invaluable to allow a detailed microscopic insight into the mechanism of the overlayer to underlayer transition.

4.2. The structure of the Cu(100)-c(2×2)-Pd underlayer alloy

The surface structure of Cu(100) has been the subject of a number of quantitative structural studies by LEED [22-26], medium energy ion scattering (MEIS) [27, 28] along with semi-empirical [29, 30] and first principles [31] calculations. All results lead to a first layer contraction (dz_{12}) between -1.1 and -3.0%. The most recent analysis is that of Walter et al. [26], who have examined the geometry of Cu(100) in some detail, including allowing the real part of the inner potential to take an energy dependent form according to the Hedin-Lunquist local density approximation. A contraction of the first interlayer spacing of -1.9% (0.035 Å) and a small second layer expansion of +0.6% (0.01 Å) was found assuming the real part of the inner potential to be energy independent. In the case of allowing the real part of the inner potential to become energy dependent a first interlayer contraction of -2.5% (0.045

Å) and second interlayer expansion of +0.3% (0.005 Å) was recovered. Thus, a contraction of 0.025 Å (-0.7%) and 0.04 Å (-1.1%) of the outermost three layer slab results. We will use the average of the two latter values i.e. a contraction of 0.0325 Å (-0.9% of 3.61 Å three layer slab) as our reference structure for the clean surface.

Data sets were collected from the top layer Cu(100)-c(2×2)-Pd surface alloy formed by room temperature deposition of 0.5 ML of Pd i.e. the precursor structure to the thermally activated underlayer alloy. Visual comparison of our own data with previously published LEED $I(V)$ spectra collected from this phase [3-5] indicated the data to be almost indistinguishable from previous reports. This technique of "fingerprinting" $I(V)$ spectra ensures that the structures formed independently in different laboratories are highly similar. The visual inspection led us to believe that full LEED analysis of this data would retrieve an essentially identical structure to that obtained by other groups [3, 4].

Fig. 6 illustrates an underlayer c(2×2) alloy based on a mixed CuPd second layer. The major structural parameters varied within the analysis are illustrated which include the first, and second interlayer spacings (dz_{12}, dz_{23}). Large variations were allowed due to the significantly larger lattice constant of Pd (3.89 Å) compared to Cu (3.61 Å). Placing Pd in a two-dimensional array with nearest neighbour separation corresponding to the copper lattice constant would represent a 16% increase in two-dimensional density, hence it may be expected that such a situation may lead to significant changes in the outermost interlayer spacings to compensate for the increase of the in-plane Pd density. Other structural variables include the rippling between copper and palladium atoms in the second layer (δ_2). Rippling was also allowed in layer 4 (δ_4). Symmetry constraints rule out the buckling in the outermost copper monolayer and layer 3 as all Cu atoms are in identical environments and thus experience identical forces.

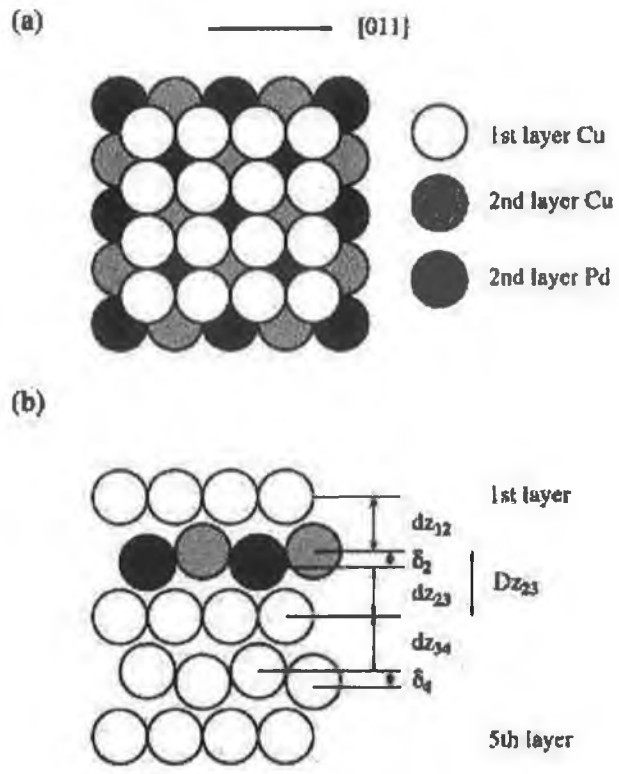

Fig. 6: Model of the Cu(100)-c(2×2)-Pd underlayer alloy. (a) Top view. (b) Side view. The structural parameters varied within the analysis are outlined including the first, second and third interlayer spacings (dz_{12}, dz_{23} and dz_{34}), rippling with the mixed CuPd layer and fourth copper layer (δ_2 and δ_4) and the distance between second and third layer Cu atoms Dz_{23}.

Fig. 7 illustrates the optimum theory-experiment agreement resulting in a minimum Pendry *R*-factor of 0.28. This compares with a minimum *R*-factor of 0.8 for a model of a top layer c(2×2) alloy with identical geometry as determined by Lu et al. [3, 4]. In the case of the top layer alloy model, geometric parameters allowed to vary included rippling within the outermost mixed CuPd layer and the third layer (again rippling in layer 2 is forbidden by symmetry). The first three interlayer spacings were also allowed to vary. The minimum *R*-factor obtained for a top layer model was 0.4, and allowed this model to be ruled out.

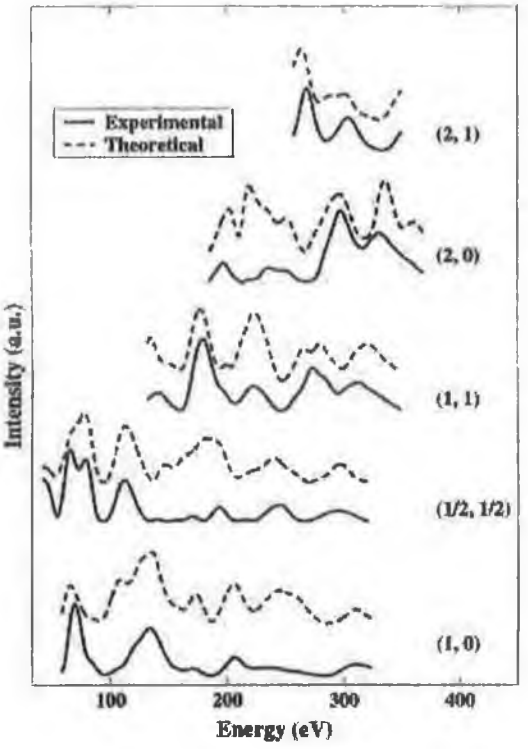

Fig. 7: Optimal theory-experiment agreement at normal incidence for the Cu(100)-c(2×2)-Pd underlayer alloy. Experimental data is shown as full lines and theory as dotted lines.

A structure in which the c(2×2) mixed CuPd slab was located in layer 3 was also tested. In this case the geometric parameters that were varied included rippling in layers 1 and 3 and the first three interlayer spacings. This model yielded a minimum *R*-factor of 0.37. In all cases the range of the variations considered were commensurate with variations expected due to the difference in metallic radii of Cu and Pd and the effective increase in the two-dimensional density encountered by constraining Pd within a Cu lattice.

Both LEED *I*(*V*) analysis and the kinetic/desorption data definitively rule out a top layer CuPd alloy structure for the annealed surface. A third layer bimetallic CuPd alloy gives a higher *R*-factor than its second layer counterpart. Furthermore, it may be expected that site switching from layer 1 to 3 may be kinetically inhibited at the annealing temperatures for which the overlayer to underlayer transition occurs, further mitigating in favour of a mixed CuPd second layer capped by a copper monolayer.

Fig. 8 illustrates the variation of the Pendry *R*-factor with the first and second interlayer spacings and with the degree of rippling in the second layer. The first copper interlayer spacing expands by +3.3% (0.06 Å) while the second layer copper interlayer spacing (Dz_{23} in Fig.7) also expands by +6.6% (0.12 Å). Thus, there exists a net expansion of 0.18 Å which corresponds to a 5% expansion in the outermost three layer slab relative to bulk copper and 0.21 Å corresponding to an 6% increase relative to clean Cu(100) taking into account the clean surface layer relaxation. Substitution of Pd into layer 2 leads to an average increase in the Cu-Pd nearest neighbour distances of 0.06 Å relative to those in bulk or 0.08 Å relative to the clean Cu(100) surface. A small rippling in the composite second layer occurs of amplitude 0.07±0.05 Å with Pd atoms rippled inwards away from the solid-vacuum interface.

The analysis also indicates a significant rippling in layer 4 with an amplitude of 0.2±0.1 Å, with fourth layer Cu atoms directly below second layer Pd rippled upwards leading to a Pd-Cu separation of 3.58 Å, which represents an 0.08% contraction relative to the sum of Pd and Cu metallic radii. While it is physically reasonable that the Pd does produce buckling in layer 4, we regard the magnitude retrieved as surprisingly large. Attempts to artificially inhibit buckling in layer 4 led to a marked increase in R_p to 0.38, thus the layer 4 buckling does appear to be required in obtain a good level of theory-experiment agreement. It should be noted that the spacing of the second three layer copper slab, consisting of layers 3-5 is 3.63 Å, very close to that in bulk Cu (3.61 Å). Thus, while rippling occurs in layer 4, the interlayer spacing below the third layer remain close to that in clean Cu(100).

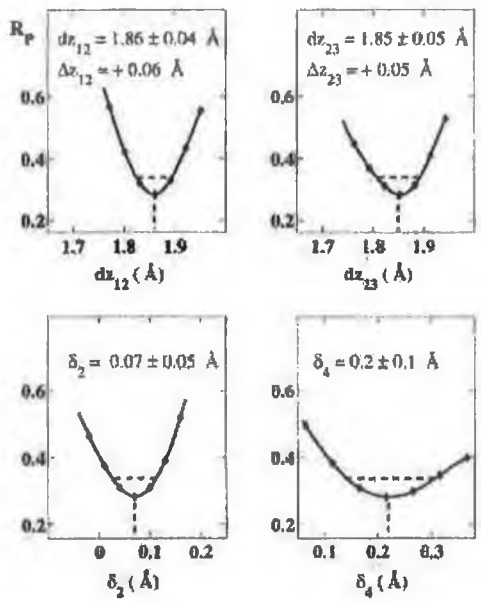

Fig. 8: Variation of the Pendry *R*-factor with: the first interlayer spacing (dz_{12}), the second interlayer spacing (dz_{23}); the rippling in the mixed CuPd layer and the fourth layer (δ_2 and δ_4 respectively).

We do not place a large emphasis on the large layer 4 rippling as the lack of half order beam data, which is the most sensitive to aspects of the geometry leading to the c(2×2) periodicity such as the chemical ordering in layer 2 and rippling in layer 4, will lead to a difficulty in assigning movements in deep lying layers which contribute weakly to the *I*(*V*) spectra due to inelastic damping. The retrieved rippling on layer 4 may be a compensation for aspects of the actual geometry and Pd composition profile not correctly modelled (for example the presence of small amounts of Pd in layers 1 and 3). It should be noted that no rigorous effort was made to optimise the layerwise Pd concentration in this work. It thus remains a possibility that deviation from the ideal 50:50 concentration of Cu and Pd in layer 2 occurs and that the 0.5 ML of Pd deposited is actually partitioned between layers 1, 2 and 3 with dominant concentration in layer 2. Consideration of this possibility may lead to an improved level of theory-experiment agreement and to a modification of the retrieved geometry in terms of interlayer spacings and buckling amplitudes. This is presently being investigated using an enhanced experimental data base including both normal and off-normal incidence *I*(*V*) spectra for both the Cu(100)-c(2×2)-Pd underlayer alloy and the corresponding precursor Cu(100)-c(2×2)-Pd top layer surface alloy.

The overall level of agreement obtained for the Cu(100)-c(2×2)-Pd underlayer is degraded relative to that of the clean Cu(100)-(1×1) surface. Experimental data sets were measured on several separate occasions from freshly prepared c(2×2) underlayer alloys indicating consistent $I(V)$ spectra for the beams illustrated in Fig. 7. This suggests that the underlayer alloy may be formed reproducibly. While it is a characteristic even of the ordered overlayers that a larger R-factor is retrieved compared to the clean Cu(100) surface, the size of the increase in the Pendry R-factor in this case is suggestive of imperfections in the c(2×2) underlayer structure. For example, recent studies in our laboratory of a Cu(100)-c(2×2)-Bi overlayer yielded a Pendry R-factor of 0.20 indicating that for a rather perfect structure, a significantly better level of theory-experiment agreement than that obtained for the c(2×2) CuPd underlayer is possible. The most likely reason is heterogeneity in the Cu(100)-c(2×2)-Pd underlayer arising from deviation in the Pd surface coverage from the exact value of 0.50 ML required and the presence of minority Pd in layer 1 (and perhaps layer 3).

Evidence indicates that the Pd coverage at which the half order beams reach maximum intensity upon Pd deposition at room temperature is between 0.55 and 0.60 ML [7, 11] and that approximately 25% of the deposited Pd already exists in layer 2 [11]. Regions of clean Cu(100) are known to be present near step edges even close to maximal perfection [10]. It appears likely, given the accepted growth mechanism of the top layer c(2×2) surface alloy, that regions exist on the surface of the underlayer alloy with Pd both in the top and second layers upon room temperature deposition as well as areas of clean copper. Thus, it is likely that annealing this top layer alloy will create a somewhat heterogeneous underlayer structure consisting of the major proportion of the surface corresponding to an ideal Cu-capped CuPd underlayer along with minority regions of c(2×2) underlayer with excess Pd atoms remaining in layer 1 possibly leading to areas of double layer CuPd surface along with small areas of clean copper. Copper capping of areas with high local Pd concentration in both layers 1 and 2 would become difficult as it requires transport of Pd into layer 3 or deeper layers. This process would be expected to be characterised by a high activation energy preventing the capping by Cu without destruction of the c(2×2) CuPd underlayer via loss of Pd into the bulk of the sample.

A limited number of calculations using the average T-matrix approximation (ATA) have been performed to model the effect of 0-50% Pd remaining in the outermost layer in a random distribution above a homogeneous c(2×2) alloy. For structural models identical to that retrieved for a pure Cu layer outermost, insertion of Pd in layer 1 led to an increased *R*-factor. However, calculations with upto 20% Pd in layer 1 were performed in which the first three layer spacings and the rippling in layers 2 and 4 were allowed to vary, in an attempt to investigate whether a similar level of theory-experiment agreement than with pure Cu surface layer could be obtained without such a large buckling in layer 4. Results indicated that the optimum geometry was essentially the same as with a pure copper surface layer and buckling in layer 4 was still required to achieve a good level of theory-experiment fit.

The CO thermal desorption data indicates that small amounts of Pd may remain in the outermost layer. The surface geometry (including the outermost interlayer spacings) of areas of structure with high local Pd concentration in both top and second layers is likely to be significantly different from the majority Cu-capped c(2×2) CuPd underlayer. Top layer Pd may also artificially lead to retrieval of the large Cu buckling in layer 4. A set of $I(V)$ spectra were also measured from a Pd coverage of 10% below that required to bring the top layer c(2×2) to maximal perfection. However, similar experimental $I(V)$ spectra were recovered to those shown in Fig. 7, suggesting that even at net Pd coverages below the ideal 0.50 ML required to form a "perfect" underlayer alloy, there are imperfections in the structure.

Embedded atom method calculations by Pope et al. [5] for the Cu(100)-c(2×2)-Pd system at 0.5 ML Pd coverage predict that an underlayer alloy is unstable with respect to a top layer alloy by 0.17 eV per Pd atom. This is in disagreement with the results obtained here, which illustrate that upon thermal activation, an irreversible switch from predominantly top layer to second layer sites occurs, implying that the underlayer alloy is the more stable structure. The c(2×2) top layer alloy is then metastable with Pd atoms simply kinetically frozen in the outermost layer. Based on surface energy considerations, there is a considerable driving force for the system to

form a copper capped geometry as the copper surface energy (1.85 J m^{-2}) is considerably lower than that of Pd (2.05 J m^{-2}) [32, 33].

Formation of underlayer CuPd alloys have been identified during room temperature growth of Pd on Cu(110) at 300 K by Murray et al. [34] and Ruban et al. [35]. STM imaging at low Pd coverages illustrated domains of p(2×1) CuPd alloy capped by Cu islands. A second STM study at higher Pd coverages by Reilly et al., confirmed that copper capping of a p(2×1) CuPd alloy occurs both in the low and higher coverage regime [36]. Thus, for the related Cu(110)-Pd system it is also clear that the formation of an ordered CuPd alloy underlayer is a more stable situation that Pd located within an outermost mixed layer.

The composition profile of the Cu(100)-c(2×2)-Pd underlayer alloy reported here based on the assumption that all evaporated Pd resides in layer 2 closely resembles that of the top three layer slab of a bulk $Cu_{0.85}Pd_{0.15}$(1 1 0) alloy, which exhibits a p(2×1) LEED pattern, due to a chemically ordered mixed CuPd second layer below a Cu rich surface layer [37-39]. This structure has been subjected to LEED *I*(*V*) analysis, indicating a Pd induced lattice expansion in which the clean Cu(1 1 0) surface, which itself undergoes a net compression of -7% (0.09 Å) in the outermost three layer slab when clean [40 and 41], reverts to an expansion of 4% (0.05 Å) with Pd substituted in the second layer. This resulted in a net expansion of 0.14 Å (5.5%) relative to clean Cu(110) similar to that obtained for Cu(100)-c(2×2)-Pd (6%). The surface structure of the same $Cu_{0.85}Pd_{0.15}$(110) alloy has been studied by Newton et al. [42] using polar X-ray photo-electron diffraction monitoring emission from both Pd $3d_{5/2}$ and Cu $2p_{3/2}$ core levels. Their results interpreted both by geometric arguments based on shifts in the observed emission angles of forward scattering diffraction features relative to clean Cu(110) and by single and double scattering modelling [43], also favoured a lattice expansion in the outermost three layer slab. Weightman et al. [44] have studied extensively the local geometry surrounding dilute bulk Pd impurities in CuPd polycrystalline alloys by EXAFS. At very low Pd concentrations (1 at. %) a small Pd-induced expansion in nearest neighbour bond lengths of 0.05±0.01 Å was deduced. This compares with the average local nearest neighbour bond length increase determined here (0.08 Å) in the case of surface localised Pd for the eight Cu nearest neighbours in the plane above and below the

mixed CuPd layer. However, in the case of the Cu(100)-c(2×2)-Pd underlayer alloy the situation is somewhat more complex compared to the bulk alloy as the four nearest neighbour Cu-Pd distances in the (100) surface plane are fixed at the value of the nearest neighbour separation in Cu(100) of 2.55 Å. This in-plane compression of Pd is compensated by a large increase in the Cu-Pd nearest neighbour separation to layer 1 Cu atoms (0.12 Å) and a smaller increase (0.03 Å) to layer 3 Cu atoms.

5. Conclusions

A thermally activated transition from a Cu(100)-c(2×2)-Pd top layer surface alloy to an ordered c(2×2) underlayer alloy consisting of a CuPd mixed second layer capped by a copper monolayer has been shown to occur. An activation energy of 109±12 kJ mol^{-1} (1.13±0.12 eV) has been estimated for this transition.

A tensor LEED *I*(*V*) analysis has been performed on a Cu(100)-c(2×2)-Pd underlayer alloy. Substitution of approximately 0.5 ML of Pd into the second layer leads to a significant modification of the first two copper interlayer spacings:

(a) the first interlayer spacing which is contracted in the case of clean Cu(100) undergoes an expansion of +3.3% upon insertion of Pd;

(b) the second interlayer spacing which is slightly expanded in clean Cu(100) undergoes an expansion of +6.6% upon substitution of Pd;

(c) the composite CuPd underlayer is rippled with a amplitude of 0.07±0.05 Å with Pd atoms being rippled inwards away from the solid-vacuum interface.

Insertion on approximately 0.5 ML of Pd into the second layer leads to a considerable lattice expansion of 0.18 Å relative to bulk Cu(100) in the outermost three monolayer slab. This expansion occurs in response to the elastic lattice strain due to the substitution of the larger Pd atoms into the smaller Cu lattice. The absolute value is considerably smaller (6%) than that predicted to be required to maintain Pd at constant density equal to that of bulk (16%).

References

1. U. Bardi *Rep. Prog. Phys.* **57** (1994), p. 939.

2. G.W. Graham *Surf. Sci* **171** (1986), p. L432.

3. S.H. Lu, Z.Q. Wang, S.C. Wu, C.K.C. Lok, J. Quinn, Y.S. Li, D. Tian, F. Jona and P.M. Marcus *Phys. Rev. B* **37** (1988), p. 4296.

4. S.C. Wu, S.H. Lu, Z.Q. Wang, C.L.C. Lok, J. Quinn, Y.S. Li, D. Tian, F. Jona and P.M. Marcus *Phys. Rev. B* **38** (1988), p. 5363.

5. T.D. Pope, M. Vos, H.T. Tang, K. Griffiths, I.V. Mitchell, P.R. Norton, W. Liu, Y.S. Li, K.A.R. Mitchell, Z.-J. Tian and J.E. Black *Surf. Sci.* **337** (1995), p. 79.

6. T.D. Pope, G.W. Anderson, K. Griffiths, P.R. Norton and G.W. Graham *Phys. Rev. B* **44** (1991), p. 11518.

7. T.D. Pope, K. Griffiths and P. Norton *Surf. Sci.* **306** (1994), p. 294.

8. G.W. Graham, P.J. Schmitz and P.A. Thiel *Phys. Rev. B* **41** (1990), p. 3353.

9. M. Valden, J. Aaltonen, M. Pessa, M. Gleeson and C.J. Barnes *Chem. Phys. Lett.* **228** (1994), p. 519.

10. P.W. Murray, I. Stensgaard, E. Laegsgaard and F. Besenbacher *Surf. Sci.* **365** (1996), p. 591.

11. Y.G. Shen, A. Bilic, D.J. O'Connor and B.V. King *Surf. Sci. Lett.* **394** (1997), p. L131.

12. G.W. Andersen, K.O. Jensen, T.D. Pope, K. Griffiths, P.R. Norton and P.J. Schultz *Phys. Rev. B* **46** (1992), p. 12880.

13. G.W. Andersen, T.D. Pope, K.O. Jensen, K. Griffiths, P.R. Norton and P.J. Schultz *Phys. Rev. B* **48** (1993), p. 15283.

14. A.R. Koymen, K.H. Lee, G. Yang, K.O. Jensen and A.H. Weiss *Phys. Rev. B* **48** (1993), p. 2020.

15. F. Jona *Surf. Sci.* **192** (1987), p. 398.

16. M.A. Van Hove, W. Moritz, H. Over, P.J. Rous, A. Wander, A. Barbieri, N. Materer, U. Starke and G.A. Somorjai *Surf. Sci. Rep.* **19** (1993), p. 191.

17. V.L. Moruzzi, J.F. Janak, A.R. Williams, Calculated Electronic Properties of Metals, Pergamon Press, New York, 1978.

18. N.W. Ashcroft, N.D. Mermin, Solid State Physics, CBS Publishing, Japan, 1981.

19. J.B. Pendry *J. Phys. C: Solid State Phys.* **13** (1980), p. 937.

20. T.D. Pope, K. Griffiths, V.P. Zhdanov and P.R. Norton *Phys. Rev. B* **50** (1994), p. 18553.

21. S. Goupper, L. Barbier and B. Salanon *Surf. Sci.* **409** (1998), p. 81.

22. H.L. Davis and J.R. Noonan *J. Vac. Sci. Technol.* **20** (1982), p. 842.

23. D.M. Lind, F.B. Dunnings, G.K. Walters and H.L. Davis *Phys. Rev. B* **35** (1987), p. 9037.

24. R. Mayer, C.S. Zhang, K. Glynn, W.E. Frieze, F. Jona and P.M. Marcus *Phys. Rev. B* **35** (1987), p. 3102.

25. F. Jona *Surf. Sci.* **192** (1987), p. 398.

26. S. Walter, V. Blum, L. Hammer, S. Muller, K. Heinz and M. Giesen *Surf. Sci.* **458** (2000), p. 155.

27. P.F.A. Alkemade, W.C. Turkenburger and W.F. van der Weg *Nucl. Instr. Meth. B* **15** (1986), p. 126.

28. T. Jiang, P. Fenter and T. Gustaffson *Phys. Rev. B* **44** (1991), p. 5773.

29. S.M. Foiles, M.J. Baskes and M.J. Daw *Phys. Rev. B* **33** (1986), p. 7983.

30. T. Ning, Q. Yu and Y. Ye *Surf. Sci.* **201** (1988), p. L857.

31. Th. Rodach, K.P. Bohnen and K.M. Ho *Surf. Sci.* **286** (1993), p. 66.

32. F.R. De Boer, R. Boom, W.C.M. Mattens, A.R. Miedema, A.K. Niessen, in: F.R. DeBoer, D.G. Pettifor (Eds.), Cohesion in Metals: Transition Metal Alloys, Elsevier, Amsterdam, 1998.

33. L.Z. Mezey and J. Giber *Jpn. J. Appl. Phys.* **21** (1982), p. 1569.

34. P.W. Murray, S. Thorshaug, I. Stensgaard, F. Besenbacher, E. Laegsgaard, A.V. Ruban, K.W. Jacobsen, G. Kopidakis and H.L. Skriver *Phys. Rev. B* **55** (1997), p. 1380.

35. A.V. Ruban, I.A. Abrikosov and H.L. Skiver *Phys. Rev. B* **51** (1995), p. 12958.

36. J.P. Reilly, C.J. Barnes, N.J. Price, R.A. Bennett, S. Poulston, P. Stone and M. Bowker *J. Phys. Chem. B* **103** (1999), p. 816.

37. D.J. Holmes, D.A. King and C.J. Barnes *Surf. Sci.* **227** (1990), p. 179.

38. M. Lindroos, C.J. Barnes, M. Bowker, D.A. King, in: S.Y. Tong, M.A. Van Hove, K. Takagana, X.D. Xie, The Structure of Surfaces III, Springer, Berlin, 1991, p. 287.

39. M.A. Newton, S.M. Francis, Y. Li, D. Law and M. Bowker *Surf. Sci.* **259** (1991), p. 45.

40. R.H. Bergmans, M. Van der Grift, A.W. Denier van der Gon, H.H. Brongersma, S.M. Francis and M. Bowker *Nucl. Instr. Meth. B* **85** (1994), p. 435.

41. R.H. Bergmans, M. Van der Grift, A.W. Denier van der Gon and H.H. Brongersma *Surf. Sci.* **345** (1996), p. 303.

42. M. Newton, Ph.D. Thesis, University of Liverpool, 1995.

43. M. Bowker, M. Newton, S.M. Francis, M. Gleeson and C.J. Barnes *Surf. Rev. Lett.* **1** (1994), p. 569.

44. P.W. Weightman, H. Wright, S.D. Waddington, D. Van der Marel, G.A. Sawatzky, G.P. Diakun and D. Norman *Phys. Rev. B* **36** (1987), p. 9098.

A SATLEED Study of the Geometric Structure of Cu{100}-Pd Monolayer Surface Alloys

K.Pussi[a], M.Lindroos[a], E.AlShamaileh[b] and C.J.Barnes[b]

[a]Institute of Physics, Tampere University of Technology, Tampere, Finland.
[b]School of Chemical Sciences, Dublin City University,Dublin 9, Ireland.

Abstract

The structure of a Cu{100}-p(2x2) surface alloy formed by deposition of 1ML of Pd on Cu{100} at room temperature has been studied by Symmetrised Automated Tensor LEED (SATLEED).

The favoured model from the wide range tested consists of a double layer ordered c(2x2) CuPd alloy with p(2x2)-p2gg symmetry introduced into the outermost layer via clock rotation of the CuPd monolayer with the p(2x2) vertices centred over second layer Pd atoms (R_p =0.21). Lateral shifts of the top layer Cu and Pd atoms are determined to be 0.25±0.12Å. Substitution of 0.5ML of Pd in both layers 1 and 2 leads to a significant expansion of the outermost two interlayer spacing to 1.93±0.02Å (+6.6±1.1%) and 1.90±0.03Å (+5.3±1.7%) and a rippling of Pd and Cu atoms in the outermost layer of 0.06±0.03Å with top layer Pd atoms rippled outwards. This model is in keeping with previous ion scattering studies of a Cu:Pd stoichiometry of 1:1 in the outermost two layers.

A second mode of film growth consisting of adsorption of 0.5ML of Pd on a copper capped Cu{100}-c(2x2)-Pd underlayer alloy leads to a structure which retains a simpler c(2x2) periodicity, clearly illustrating that growth of the p(2x2)-glide line phase requires a c(2x2) CuPd outermost template.

1. Introduction

Adsorption of Pd on Cu{100} at room temperature leads to a structural phase transition as observed by Low Energy Electron Diffraction (LEED) in which a c(2x2) surface alloy consisting of a mixed ordered CuPd outermost layer (Θ_{Pd} = 0.5 ML) transforms to a p(2x2) phase with systematic absences in the (0, n+1/2) and (m+1/2, 0) positions as the Pd coverage is increased towards and beyond the monolayer point consistent with a p4g or p2gg space group [1]. While the structure of the c(2x2) phase is now considered to be solved [2-5], the p(2x2)-glide line phase has been the centre of considerable debate. Three independent research groups, using different primary surface probes have attempted to solve the geometry with differing conclusions [6,7,8,9]. While all groups appear to agree that the sub-surface layer is a mixed c(2x2) CuPd alloy layer, no clear consensus has been reached on the top layer structure and composition. The four top layer models suggested to date are briefly summarised below (in each case unless explicitely stated, the second layer is assumed to be c(2x2) of composition CuPd and the pure top layer Pd regions to exhibit a p(2x2)-p4g clock rotated structure):

(a) 80% clock rotated Pd{100} islands (fig 1(a)) mixed with 20% c(2x2) CuPd regions (fig 1(b)) (Θ_{Pd}= 1.30ML) suggested by Pope et al based on a combined Medium Energy Ion Scattering (MEIS)/Low Energy Electron Diffraction (LEED) I-V analysis [6];

(b) a randomly intermixed top layer clock rotated Cu-Pd monolayer suggested by Yao and co-workers using Low Energy Ion Scattering Spectroscopy (LEISS) [8];

(c) a homogeneous p(2x2) outermost layer of composition CuPd with a 50% decrease in surface layer atomic density above a clock rotated c(2x2) CuPd underlayer (fig 1(c)) suggested by Murray et al based on Scanning Tunnelling Microscopy (STM) observations (Θ_{Pd}=0.75ML) [7] ;

(d) 30% clock rotated Pd{100} (fig 1(a)) and 70% p(2x2) Cu_3Pd phase suggested by Shen and co-workers using LEISS (fig 1(d)) (Θ_{Pd}= 1.0ML) [9].

The LEISS study of Yao et al [8] accurately determined the average composition to be 53 at % Cu: 47 at % Pd in the outermost layer and 58 at % Cu: 42 at % Pd in layer 2 with about 90% of the deposited Pd residing in layers 1 and 2 and the

residual Pd in third and deeper layers. Shen et al [9] have also reported that the top layer composition is very close to the ideal CuPd stoichiometry with a top layer Pd concentration of 53±4% (Li^+ ions) and 51±3% (He^+ ions) with an outermost layer atomic density similar to that of Cu{100}. This information was utilised by Shen and co-workers to rule out the models of Pope at al [6] and Murray et al [8] which were found to be inconsistent with the top layer Pd atomic density and surface coverages as measured by LEISS.

The model of co-existing areas of p(2x2)-p4g clock rotated Pd and p(2x2) Cu_3Pd alloy was preferred over the earlier suggestion of a top layer consisting of a random substitutionally disordered clock rotated CuPd alloy as it provided an explanation of an observation reported by Shen and co-workers that the LEED pattern exhibits non zero intensities in p(2x2) superlattice positions which are symmetry forbidden for a p(2x2)-p4g phase alone. This structural model also provides a satisfactory theory-experiment agreement of theoretical modelling of the ion scattering process with measured LEISS data both in the form of kinetic energy scans and azimuthal ion distributions. An R-factor analysis allowed extraction of the Pd displacement from 4-fold hollow sites of 0.25±0.07Å within the clock rotated Pd domains and a fractional surface coverage of p(2x2)-p4g Pd domains of 30%.

A major discrepancy remains unexplained: STM images an essentially homogeneous non clock rotated p(2x2) outermost layer with a high density of defects such as anti-phase domain boundaries at a Pd coverage of 1.3ML [7]. At lower Pd coverages (1.1ML) STM images indicated formation of a heterogeneous surface with c(2x2) periodicity in large areas of the surface[7]. LEED indicates a p(2x2) periodicity throughout the coverage regime 1.0 to 1.3ML with systematic absences indicating p4g or p2gg symmetry.

Symmetrised Automated Tensor LEED (SATLEED) has been demonstrated to be a technique ideally suited to full determinations of ordered structures with large and complex surface unit cells [10,11,12]. While in the case of the Cu{100}-p(2x2)-1ML- Pd structure , the surface unit cell is not particularly large, the possibility of a heterogeneous surface consisting of two areas with their own composition and geometry increases significantly the complexity of the LEED structural search.

The primary aim of this study, utilising an independently measured and enhanced experimental data base compared to the early LEED study of Pope et al [6], is to apply SATLEED to test the full range of models suggested to date to describe the geometry of the Cu{100}-p(2x2)-1ML-Pd structure. We demonstrate that none of these models provide a satisfactory level of theory-experiment agreement. Instead we propose an alternative model with the two outermost layers consisting of c(2x2) CuPd layers, with the p(2x2) periodicity introduced via a clock rotation of the outermost CuPd layer rotating in an alternate clockwise-anticlockwise motion centred on second layer Pd atoms. This model yields the correct top layer stoichiometry as well as being the only model tested to give a satisfactory level of theory-experiment agreement in the SATLEED analysis (R_p=0.21). A detailed picture of the surface geometry is provided, including the degree of clock rotation in the outermost CuPd monolayer, the buckling amplitudes in the outermost and second mixed CuPd layers and the outermost three interlayer spacings.

Finally, we examine an alternative mode of preparation of the Cu{100}-1ML-Pd phase involving deposition of 0.5ML of Pd on to a Cu(100)-c(2x2)-Pd "underlayer alloy" consisting of a mixed c(2x2) CuPd second layer capped by a pure copper monolayer [13], unambiguously demonstrating that formation of the p(2x2) phase requires a c(2x2) CuPd top layer alloy template.

2. Experimental

All experiments were performed in an ion and titanium sublimation pumped ultra-high-vacuum chamber of base pressure $2x10^{-10}$ torr equipped with facilities for LEED, Auger electron spectroscopy (utilising the LEED optics as a retarding field analyser) and a quadrupole mass spectrometer for residual gas analysis. The Cu{100} sample was that used in previous studies [13] and was cleaned in-situ by repeated cycles of argon ion bombardment and annealing to 800K until the surface was clean as judged by AES analysis and by careful comparison of the I(V) spectrum of the (1,0) LEED beam at normal incidence with previous reports [14]. At this stage the sample exhibited a sharp and low background p(1x1) LEED pattern.

Palladium was evaporated from a 0.125mm Pd wire (99.99%) wrapped around a 0.3mm tungsten filament. The Pd coverage was calibrated by determining the evaporation time required for room temperature deposition to maximise the intensity of the (1/2,1/2) LEED beam at a primary beam energy of 125eV via acquisition of spot profiles through the (1,0), (1/2,1/2) and (0,1) beams and setting this evaporation time to a coverage of 0.55ML using the well established Rutherford Backscattering/LEED calibration of Pope at al [5]. The Cu{100}-p(2x2) structure was formed by evaporation of below 1ML of Pd with the sample held at room temperature, followed by stepwise addition of small amounts of Pd until the p(2x2) structure appeared visually to attain optimal intensity. A Pd coverage of 1.0±0.1ML of Pd was required, which compares with previous reports of Pope et al of 1.1±0.06ML calibrated via Rutherford Backscattering Spectroscopy (RBS) [6] and by Shen and co-workers of 1.2±0.1ML using a calibrated quartz crystal microbalance [9]. The structure formed was observed visually to have negligible intensity scattered in-to the (0,n+1/2) and (m+1/2,0) positions under conditions of normal incidence of the incoming electron beam. Gentle annealing of the Cu{100}-p(2x2) phase has previously been reported to improove the surface crystal quality in the form of the sharpening of superlattice diffraction features [6]. Yao et al [8] indicate that annealing up-to 425K for short periods does not lead to significant changes in the top layer stoichiometry. It would thus seem likely that a short anneals between 350 and 425K should generate a surface with enhanced crystal quality for SATLEED analysis. In order to gauge the effect of gentle annealing prior to collection of I(V) data, we acquired LEED I(V) spectra from the (1,0) and (1/2,1/2) beams at normal incidence for room temperature deposited film and from the same surface after annealing to 350K for several minutes. No significant changes in spectral structure or peak positions were detected and we thus conclude that Cu{100}-p(2x2)-Pd surfaces formed by direct deposition and after thermal activation essentially have identical structures as sensed by LEED.

LEED I(V) spectra were measured at room temperature from a film thermally activated to 350K for several minutes under conditions of normal incidence of the primary electron beam, determined by variation of the angular alignment until the four (1,0) beams were identical in terms of spectral structure and peak positions to a level typically acceptable for LEED I(V) analysis [14]. The I(V) spectra were

measured with a high sensitivity CCD camera connected to a microcomputer which was equipped with data acquisition software allowing automatic tracking of a user defined number of beams. Typically one full set of symmetry equivalent beams would be acquired in a single "run", allowing full symmetry averaging to increase the signal to noise level and compensate for any remaining deviation of the angular alignment. Each beam was individually background corrected by fitting an empirical smoothly increasing background to selected minima in the I(V) curve before symmetry addition was performed and normalised to constant incoming beam current prior to R-factor analysis.

The data set utilised for the Cu{100}-p(2x2)-1ML Pd structure consisted of a normal incidence data base of total energy range of 1496eV including six symmetry inequivalent beams ((1,0), (1,1), (2,0), (0.5,0.5), (1,0.5) and (1.5,0.5)) measured in an energy range of 50-450eV .

3. Theoretical Analysis

All calculations were performed with the Barbieri/Van Hove Symmetrized Automated Tensor LEED package [15]. Atomic potentials for Cu and Pd were characterised by up-to 9 phase shifts obtained from the Barbieri/Van Hove phase-shift package. Initially the thermal vibration properties of Cu and Pd were characterised by their bulk Debye temperatures of 315 and 275K respectively [16]. Other non-structural parameters utilised included an imaginary part of the optical potential of magnitude -4eV while the real part of the inner potential was assumed to be energy independent and was allowed to rigidly shift to obtain optimal theory-experiment agreement as is standard practice in LEED I(V) analysis. Theory-experiment agreement was tested using the Pendry reliability factor [17] and error bars calculated using the Pendry RR-factor. Normal incidence LEED is generally relatively insensitive to distortions within the plane of the surface such as lateral shifts. However, in this particular case, the extent of lateral movement in clock rotated models may be determined with a reasonable degree of accuracy as the (1,0.5) beam is created as a result of these systematic in-plane movements within a p4g or p2gg surface model. In the case of models in which the outermost layer is

heterogeneous and consists of two domains of differing composition and geometry the following procedure was adopted:

Step 1: The I-V spectra were initially calculated independently for both domains with all atoms in Cu{100} bulk positions. The geometry of the first domain (domain 1) was then optimised by varying the relevant geometric parameters. The I-V spectra utilised consisted of addition of intensities from domain 1 and bulk-like domain 2, with intensities being added in accordance with the percentage of each domain within the structure;

Step 2: The geometry of the second domain (domain 2) was then optimised. The I-V spectra utilised consisted of addition of intensities from the optimal domain 1 structure obtained in step 1 to those of domain 2 ;
Step 3: Stages 1 and 2 were repeated until the structure within both domains converged.

4. Results and Discussion

(a) The Cu{100}-p(2x2)-p4g/p2gg-1ML Pd Phase:

Figure 1 illustrates top views of models previously suggested including: (a) a Pd clock rotated p(2x2)-p4g structure; (b) a c(2x2) CuPd alloy ;(c) a p(2x2) CuPd outermost layer with a 50% decrease in atomic density relative to Cu{100} above a clock rotated CuPd underlayer having p2gg symmetry [7]; (d) a p(2x2) Cu_3Pd alloy . The structures (a), (b) and (d) are supported on a second layer c(2x2) CuPd alloy.

The structures illustrated in figure 1 are the basic building blocks of previously suggested heterogeneous surface models including the MEIS/LEED based model of Pope et al [6] which combines structures illustrated in figures 1(a) and (b) in an 80:20% ratio and that of Shen et al [9] which combines structures outlined in figures 1(a) and 1(d) in a 30:70% ratio.

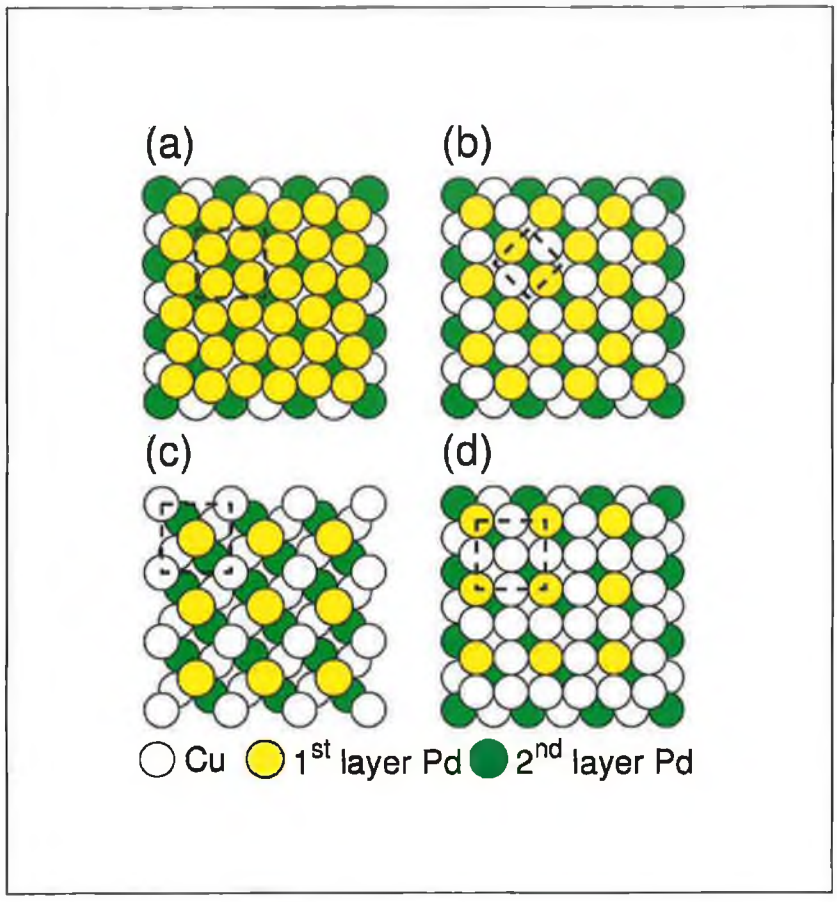

Figure 1: Top view of models of structures previously suggested for the Cu{100}-p(2x2)-1ML Pd phase including: (a) a p(2x2)-p4g clock rotated Pd monolayer; (b) a c(2x2) CuPd monolayer; (c) a p(2x2) CuPd outermost layer with 50% decrease in atomic density above a clock rotated CuPd underlayer and (d) a p(2x2) Cu_3Pd outermost layer. In all cases the outermost two atomic layers only are shown. Top layer unit cells are denoted by dotted lines.

In the initial phase of the analysis, atoms in layer 3 and deeper layers were assumed to be copper and were frozen at their bulk truncated positions since their contribution to the measured LEED intensities is relatively small compared to that of the outermost two monolayers. The geometric parameters varied for each model are summarised in table 1 and defined in the table caption. Table 1 also illustrates the minimum Pendry R-factor obtained in this initial screening stage of the analysis and the available experimental energy range per geometric parameter optimised. In all models exhibiting p2gg symmetry, calculations were performed for two energetically equivalent domains rotated by 90° co-added in a 1:1 ratio. At this stage of the analysis no effort was made to optimise non-structural parameters.

The STM model of Murray et al [7] yielded a rather poor level of theory-experiment agreement (R_p=0.54) as did the heterogeneous surface model of Pope et al [6] (R_p=0.59). Neither of these models yield the level of agreement expected for a satisfactory solution of a surface structure. Of the previously suggested models, only the model of Shen et al yielded a reasonable level of agreement (R_p=0.36).

To investigate whether allowing the top layer domain composition to vary led to an improovement in theory-experiment agreement, the percentage of p(2x2)-p4g Pd domains was allowed to change in 10 at% steps for the model of Pope et al [6]. A minimum Pendry R-factor of 0.41 was obtained for 10% p(2x2)-p4g Pd and 90% c(2x2) CuPd in the outermost layer yielding a total Pd coverage of 1.05ML and a top layer coverage of 0.55ML. Increasing the percentage of p(2x2)-p4g-Pd islands not only led to an increase in R_p, but also yielded top layer Pd coverages well in excess of that determined by LEISS. While increasing the percentage of model 1(b) within the heterogeneous surface leads to an increased level of agreement, areas consisting of two adjacent c(2x2) CuPd layers would not generate beams in p(2x2) positions and small concentrations of p(2x2)-p4g Pd such as that most favoured ((R_p=0.41) for 10% p(2x2)-p4g Pd) would not yield sufficient intensity in p(2x2) positions to explain experimental observations.

Table 1: Summary of the structures examined in the first phase of the analysis along with the minimum Pendry reliability factors (R_p) obtained for each structure. The structural parameters optimised in each case along with the experimental data range available per structural parameter are listed. The theoretical Pd coverage in the outermost layer and total Pd coverage is also given for each individual model. The lateral shifts of first and second layer atoms away from four-fold hollow sites are denoted by σ_1 and σ_2 respectively. Interlayer spacing dz_{12} and dz_{23} are quoted with respect to Cu atoms in layers 1,2 and 3 accepting for models with a top layer p(2x2)-p4g Pd phase where dz_{12} represents the spacing between top layer Pd and second layer Cu atoms. The buckling amplitudes Δ_1 and Δ_2 represent the rippling between Pd and Cu atoms in layers 1 and 2 respectively.

Model	Ref.	Top layer Pd coverage (ML)	Total Pd coverage (ML)	Structural parameters varied	Energy range per structural parameter (eV)	R_P
STM model: Murray et al	[7]	0.25	0.75	dz_{12}, dz_{23}, Δ_1, Δ_2, σ_2	334	0.54
Pope et al: 80% p(2×2)-p4g Pd and 20% c(2×2)	[6]	0.9	1.3	dz_{12}, dz_{23}, Δ_1, Δ_2	167	0.59
Shen et al: 30% p(2×2)-p4g Pd and 70% p(2×2)-Cu_3Pd	[9]	0.48	0.98	dz_{12}, dz_{23}, $\Delta_1(\times 2)$, Δ_2	150	0.36
A p(2×2)-p2gg CuPd layer above a c(2×2) mixed CuPd 2nd layer Domain A Domain B	This work	0.5	1.0	dz_{12}, dz_{23}, Δ_1, $\Delta_2(\times 2)$, σ_1	278	 0.34 0.39
A c(2×2) mixed CuPd layer above a p(2×2)-p2gg CuPd 2nd layer Domain A Domain B	This work	0.5	1.0	dz_{12}, dz_{23}, $\Delta_1(\times 2)$, Δ_2, σ_2	278	 0.52 0.43

However, the tendency for an enhanced level of agreement as the surface becomes increasingly dominated by the double layer c(2x2) structure prompted the trial of a range of models not previously discussed for the Cu{100}/Pd system that adhere to the measured top layer stoichiometry of Cu:Pd of 1:1 in the outermost two atomic layers and a LEED pattern with symmetry p(2x2)-p4g or p(2x2)-p2gg consistent with experimental observations. Figure 2 illustrates a simple homogeneous surface model consisting of two mixed CuPd alloy layers. The sub-surface layer is a CuPd c(2x2) while the outermost mixed CuPd monolayer represents a p(2x2) clock rotated

structure yielding a p2gg space group. In this particular case two non-energetically degenerate translated domains exist, depending on whether the vertices of the p(2x2) clock rotated outermost layer are centred on second layer Pd as illustrated in figure 2 (domain A) or second layer Cu atoms (domain B). As these domains exhibit different structures and bonding it is to be expected that one domain will be energetically preferred. Thus, calculations were performed from each translated domain independently and table 1 gives the minimum Pendry R-factor in each case. The lowest R-factor was obtained for domain type A (R_p=0.34) in which the vertices of the p(2x2) clock rotated outer monolayer are centred above second layer Pd atoms compared to 0.39 for domain type B in which the vertices are located above second layer Cu atoms. The geometry corresponding to the minimum R-factor for domain type B also contained an unusually small second to third interlayer spacing of 1.68Å, along with an interatomic separation of only 2.33Å between top and second layer Pd atoms (a compression of 15% relative to the bulk nearest neighbour separation in Pd). Taking into account the large in-plane compressive strain of Pd atoms substituted in-to a smaller copper lattice, further compression in the growth direction is highly unlikely. The geometry retrieved for domain type B is considered to be physically unreasonable in addition to yielding a poorer level of theory-experiment agreement and was rejected.

A model consisting of a mixed c(2x2) outermost CuPd layer above a clock rotated p(2x2)–p2gg second layer was also tested as it would be in keeping with the inability of STM to resolve the clock-rotation for the Cu{100}-p(2x2)-Pd system. However, as indicated in table 1, this model yields significantly higher R-factors than its counterpart in which the clock-rotation exists in the outermost mixed CuPd layer. At this stage of the analysis, a variance of 0.04 allows all models other than the structure corresponding to the model of Shen et al [9] and a p(2x2)-p2gg clock rotated CuPd surface layer supported on a c(2x2) CuPd underlayer (figure 2) to be ruled out.

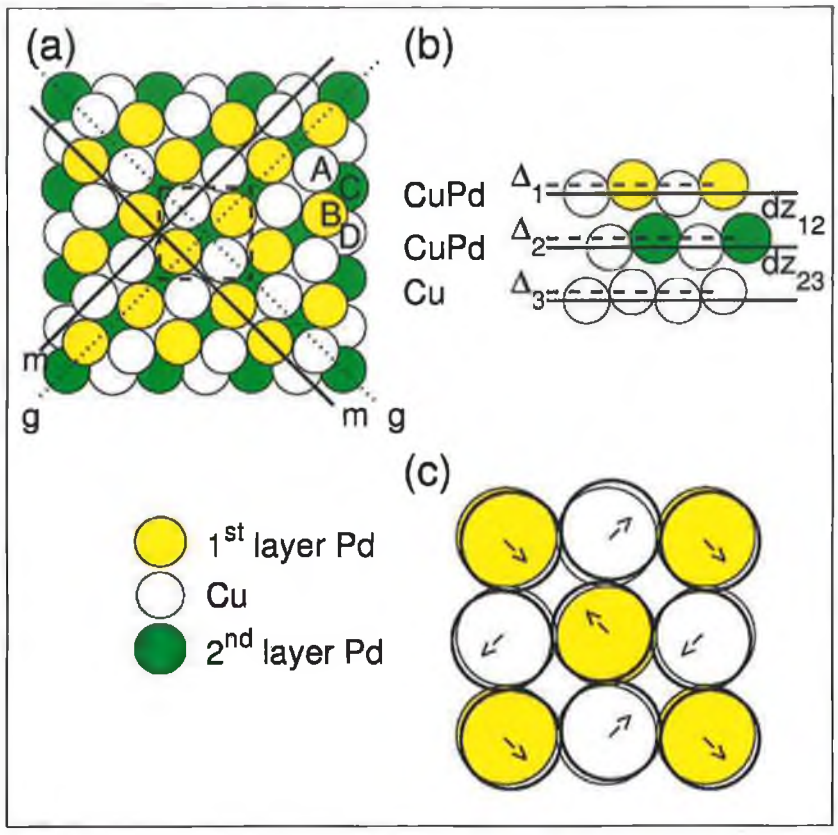

Figure 2: Top and side views of a double layer CuPd alloy consisting of a c(2x2) underlayer and a clock rotated p(2x2)-p2gg CuPd outer layer including: (a) top view: the symmetry elements including two orthogonal mirror planes (m) and glide lines (g) are illustrated. The black dotted line denotes the p(2x2) unit cell; (b) side view: the main geometric parameters varied within the analysis are labelled; (c) the clock-rotation of top layer Cu and Pd atoms illustrated in more detail.

These two models were selected for further refinement, including variation of the third (dz_{34}) and fourth (dz_{45}) interlayer spacings and allowing buckling in layers 3 and 4. In this second stage, the Pd and Cu phase shifts utilised were re-calculated specifically for the structural model investigated. Non structural parameters were also optimised including the imaginary part of the inner potential and the Cu and Pd Debye temperatures.

In the case of the model of Shen et al, a number of top layer domain compositions were tested. The composition originally suggested by Shen and co-workers (30% p4g-Pd and 70% Cu_3Pd) which corresponds to a top layer Pd coverage 0f 0.48ML and a total Pd loading of 0.98ML yielded a R_p value of 0.30. Increasing the proportion of p4g-Pd led to both an increase in R_p and a top layer Pd composition in excess of that favoured by LEISS analysis. Reducing the proportion of top layer p4g-Pd to 20% led to a small decrease in R_p to 0.28, however the corresponding top layer Pd coverage of 0.40ML has already decreased to a value inconsistent with LEISS analysis. The large proportion of p(2x2) Cu_3Pd top layer (80%) would again lead to considerable scattering in-to the systematic absence positions, inconsistent with our experimental observations.

The Pendry R-factor for the model illustrated in figure 2 was reduced to 0.21: the RR-value of 0.04 allows selection of this model rather than the heterogeneous surface model of Shen and co-workers [9]. The optimised non-structural parameters for this model include an imaginary part of the inner potential of –4eV and Debye temperatures for Cu and Pd of 315 and 255K respectively.

Figure 3 illustrates the level of theory-experiment agreement obtained corresponding to a Pendry R-factor of 0.21 with individual beam R-factors quoted. Figure 4 illustrates the sensitivity of the analysis to the key geometric variables, including the lateral displacement of top layer atoms from four-fold hollow sites (σ_1), the buckling amplitude in top layer CuPd layers (Δ_1) and the outermost two copper interlayer spacings (dz_{12} and dz_{23}). In each case the variation of the Pendry R-factor is calculated with all other structural and non structural parameters held at their optimal values. The favoured value for each parameter along with its calculated error is shown at the top of each panel within figure 4.

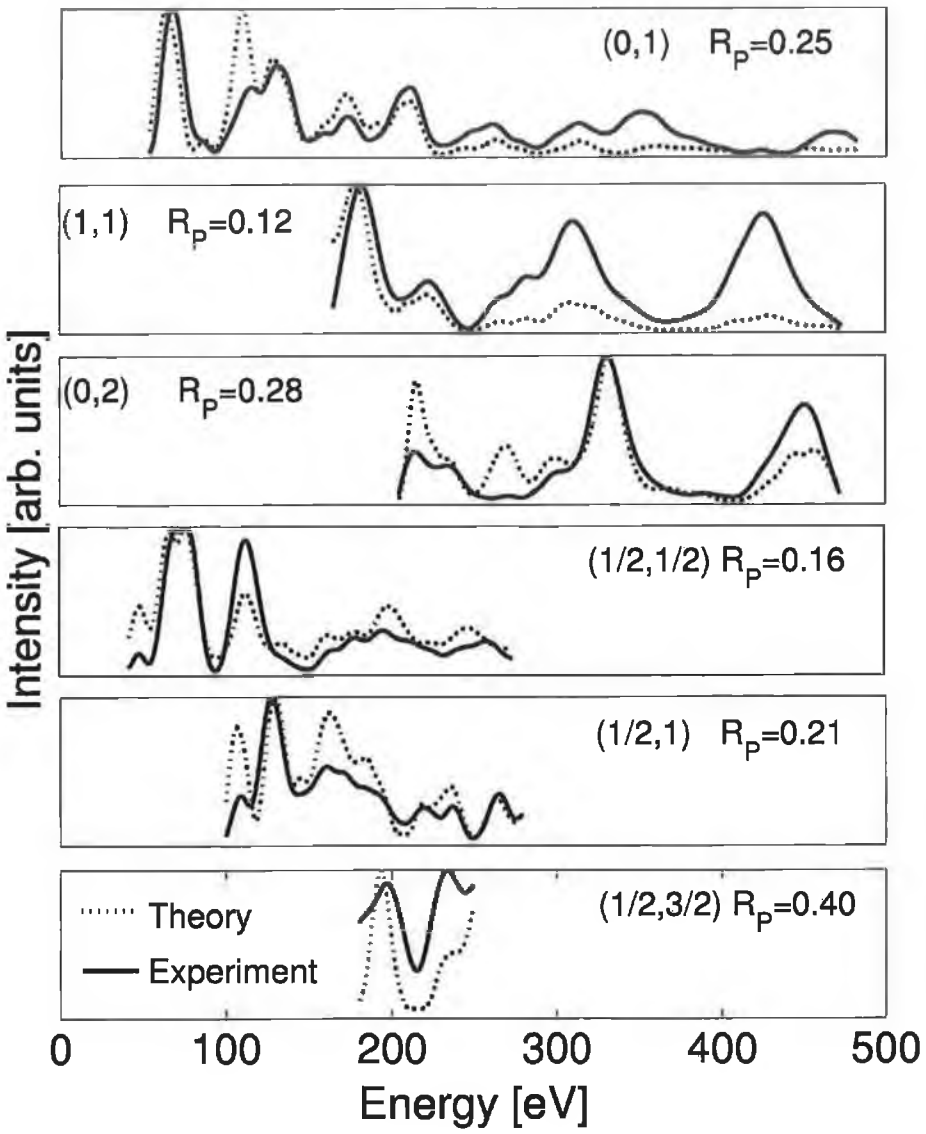

Figure 3: Optimal theory-experiment agreement. Experimental data is shown as full lines and theory as dotted lines.

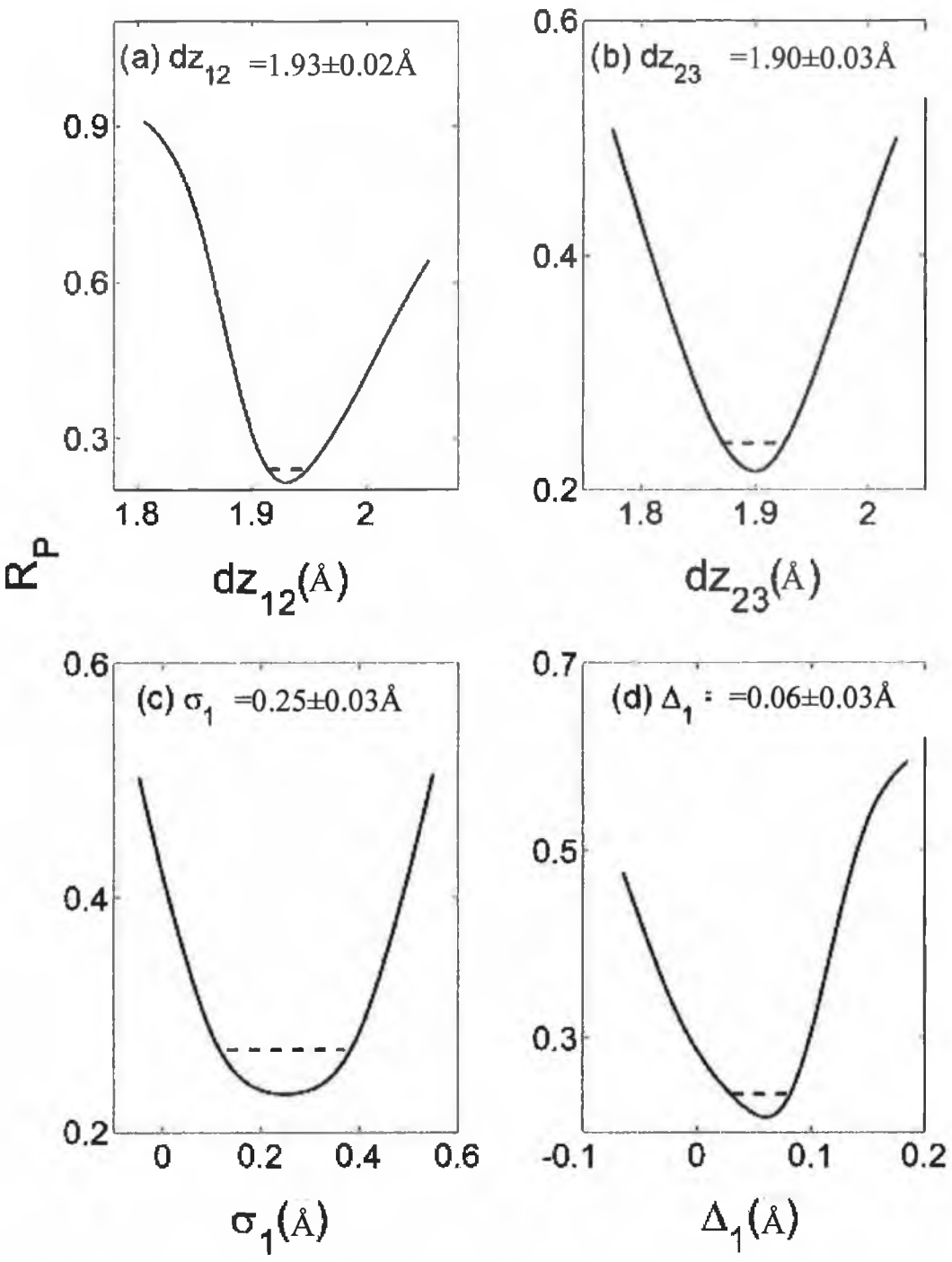

Figure 4: Variation of the Pendry R-factor with the key structural parameters within the favoured model illustrated in figure 2 including: (a) the first interlayer spacing between outermost and second layer Cu atoms (dz_{12}) ; (b) the second interlayer spacing (dz_{23}); (c) the lateral shift of top layer Cu and Pd atoms within the clock-rotated outer CuPd monolayer (σ_1); (d) the buckling amplitude in the outermost monolayer (Δ_1). Favoured values for each parameter along with associated errors are shown at the top of each panel.

Table 2 summarises the structural parameters along with those deduced from both the MEIS/LEED study of Pope et al [6] and the LEISS study of Shen et al [9].

Table 2: Favoured structural parameters along with their associated errors. The second layer buckling amplitudes Δ_{2_1} and Δ_{2_2} refer to the rippling of Pd atoms relative to the two symmetrically inequivalent Cu atoms within the second layer 2D unit cell. Geometric parameters obtained by Shen et al and by Pope et al for the p(2x2)-p4g Pd domains are also shown for comparative purposes. Also included are the spacings between Cu and Pd atoms in layers 1 and 2 in the favoured geometry. The nearest neighbour Pd-Pd spacings in bulk Pd{100} is also tabulated for comparative purposes. The atom pairs may be identified using key in figure 2.

Structural parameter	Optimal value (Å)	Shen et al [9]	Pope et al [6]
dz_{12}	1.93 ±0.02		2.03
dz_{23}	1.90 ±0.03		1.84
dz_{34}	1.80 ±0.03		
dz_{45}	1.83 ±0.03		
σ_1	0.25 ±0.12	0.25±0.07	0.28
Δ_1	0.06 ±0.03		
Δ_{2_1}	0.02 ±0.06		0.14
Δ_{2_2}	0.03 ±0.05		
Atom pair	Spacing (Å)		
A-A	3.11 / 3.61		
B-B	4.11 / 3.61		
A-B	2.58		
B-C	2.67		
B-D	2.51		
Pd{100}	2.75		

SATLEED geometry retrieved is consistent with studies of the lower coverage Cu{100}/Pd surface alloys [2,3,13] and previous structural work on the Cu{100}-p(2x2) 1ML Pd phase [6,8,9]. A lateral shift of top layer Pd and Cu atoms within the p2gg clock rotated layer of 0.25±0.12Å agrees remarkably well with the lateral displacements of top layer Pd atoms of 0.25±0.07Å determined by Shen et al [9] and 0.28Å by Pope and co-workers [6]. The agreement is all the more remarkable considering that the top layer models used in previous studies correspond to lateral shift of Pd atoms within p(2x2)-p4g pure Pd islands. A large expansion in the first interlayer spacing to 1.93±0.02Å was also found in the LEED study of Pope et al [6] where an even larger value of 2.03Å is preferred (in this case it must be remembered that the spacing corresponds to the spacing between an outermost pure Pd monolayer and second layer Cu atoms). Rippling of Cu and Pd atoms in layer 2 is 0.06±0.03Å while a larger value of 0.14Å is favoured by Pope et al within the c(2x2) domain illustrated in figure 1(b) [6], in both cases with Pd atoms rippled towards the solid-vacuum interface. As expected, substitution of 0.5ML of Pd in-to layers 1 and 2 leads to a significant expansion of the outermost two interlayer spacings. The first two interlayer spacings are increased by 0.125±0.02Å (+6.6±1.1%) and 0.10±0.03Å (+5.3±1.7%) respectively, yielding a net expansion of the outermost three layer slab of 0.23Å (+6.4%). A recent study of a Cu{100}-c(2x2)-Pd underlayer alloy in which 0.5ML of Pd was substituted into the second copper layer also led to significant expansion of the outermost three layer slab of 0.18Å [13]. The larger metallic radius of Pd means that Pd atoms substituted into the smaller copper lattice are under considerable compressive in-plane strain, which may be relieved by expansion of the interplanar spacings normal to the Cu{100} surface. The effect is strongest for Pd atoms substituted in second or deeper layers which experience a higher co-ordination and lack the freedom of first layer Pd atoms to relax perpendicular to the surface. For example, substitution of 0.5ML of Pd into the outermost layer in a Cu{100}-c(2x2) surface alloy leads to a structure with an outermost interplanar spacing equal to that of bulk Cu{100} [2,3], which represents only a very weak Pd-induced expansion of about 0.02Å (+1.2%) relative to the clean Cu{100} surface. A small top layer rippling of amplitude 0.06±0.03Å with Pd atoms rippled outwards is similar to that obtained in the Cu{100}-c(2x2)-Pd top layer surface alloy at a Pd coverage of 0.5ML [2,3] in which a small outward rippling of 0.02±0.03Å occurs.

The most attractive explanation for the occurrence of the clock rotation within the outermost CuPd monolayer is that it is a response to the high level of compressive stress experienced by Pd atoms forced to remain in the four-fold hollow sites provided by the underlying c(2x2) CuPd alloy which itself is commensurate with the Cu{100} substrate. Palladium atoms remaining at a separation dictated by the Cu{100} periodicity would be forced to adopt nearest neighbour Cu-Pd separations of 2.55Å, compared to a favoured in-plane spacing of 2.65Å based on the sum of the Cu and Pd metallic radii. Calculated in plane Pd-Cu nearest neighbour distances in the favoured clock rotated structure along with the corresponding first to second layer Pd-Pd and Pd-Cu separations are listed in table 2. The combined effect of the clock rotation and buckling serves to increase the nearest neighbour in-plane Cu-Pd separation in the outermost layer slightly from 2.55 to 2.58Å, while the nearest neighbour Pd-Pd separation between top and second layer Pd atoms is 2.67Å, intermediate between a bulk Cu-Cu separation of 2.55Å and Pd-Pd separation of 2.75Å.

The model proposed has both first and second layer compositions of CuPd, as suggested by the LEISS studies of Yao et al and Shen et al [8,9] and is able to naturally explain the systematic absences in the experimentally observed LEED pattern.

One surprising aspect based on the model obtained here for the Cu{100}-p(2x2)-Pd-1ML phase is the inability of STM to image the clock rotation [7]. This has previously been successfully achieved by Kishi et al [18] from a clock rotated outer Pd monolayer of p(2x2)-p4g symmetry above a highly buckled c(2x2) PdAl underlayer in a Pd{100}-p(2x2)-p4g-Al surface alloy. The structure is characterised by a large bimetallic buckling in layer 2 of 0.25±0.07Å with Pd buckled outwards and large lateral movement of top layer Pd atoms of 0.57±0.1Å within the outer monolayer [19,20]. The clock rotation has also been imaged by STM in the related Ni{100}-p(2x2)-p4g carbon structure, a classic example of lateral "clock-type" reconstruction [21] where a lateral in-plane shift of top layer Ni atoms of 0.45Å is favoured with a 0.16Å buckling amplitude of second layer Ni atoms [22]. We note that in both cases where a clock rotation has successfully been imaged by STM, the

degree of lateral motion of top layer atoms was considerably larger than is the case for the Cu{100}-p(2x2)-1ML-Pd phase. In the Cu{100}-p(2x2)-Pd system there is a much smaller buckling in layer 2. It is possible these two features combine to prevent the STM from resolving the clock rotation in the Cu{100}/Pd system.

The overall level of theory-experiment agreement obtained (R_p=0.21) compares well with a Pendry R-factor of 0.22 obtained by Onishi and co-workers for the Pd{100}-p(2x2)-p4g-Al structure [19]. A similar level of theory-experiment agreement was obtained in the most recent LEED analysis of the Ni{100}-p(2x2)-p4g reconstructed surface formed by carbon adsorption [22]. The structure of the Cu{100}-p(2x2)-Pd phase at 1.3ML Pd is imperfect, with a high concentration of domain boundaries and other defects imaged by STM [7]. Disorder is also imaged for the lower Pd coverage of 1.1ML [7]. This is reflected in the quality of the LEED pattern, which exhibits a higher diffuse background intensity than the clean Cu{100} sample. It is thus likely that the lower crystal quality of the Cu{100}-p(2x2)-p2gg-1ML-Pd surface is a contributing factor to the slightly lower level of overall agreement obtained compared to the clean Cu{100}-(1x1) phase (R_p = 0.15). It should also be noted that for Pd coverages utilised in our measurements (1.0ML), the STM studies of Murray et al [7] indicate that the Cu{100}/Pd surface is heterogeneous with large areas of c(2x2) periodicity imaged by STM. While it appears that areas of heterogeneity exist within the surface structure from which the I(V) data was acquired, the exact nature and extent of the heterogeneity is unknown at present. However, I(V) data measured at a higher Pd coverage (1.2ML) are practically identical to those illustrated in figure 3, indicating that the structure as sensed by LEED is not strongly dependent on the exact Pd coverage deposited in the range 1.0 to 1.3ML. This suggests that either the heterogeneous regions do not play a major role in scattering in-to the measured LEED beams or alternatively that the local structure within these regions is similar to that modelled in the favoured p(2x2)-p2gg structure illustrated in figure 2.

(b) The Cu{100}-c(2x2)-1ML-Pd Phase:

A second alternative mode of preparation of the Cu{100}/Pd-1ML phase was investigated within this study. In this case, 0.5ML of Pd was evaporated on-to a clean Cu{100} substrate at room temperature forming a Cu{100}-c(2x2)-Pd top layer alloy. This structure was then converted by controlled thermal activation into a c(2x2) underlayer CuPd alloy consisting of a mixed CuPd second layer capped by a copper monolayer slab as recently reported by Barnes and co-workers [13]. A further 0.5ML of Pd was then evaporated to give a total Pd coverage of 1.0ML. In this case no p(2x2) phase was observed despite the fact that the total Pd coverage was similar to that employed in the direct deposition method. Instead the periodicity remained c(2x2) with good crystal quality even after gentle annealing . In order to probe the geometry of this Cu{100}-c(2x2)-Pd-1ML structure, the I(V) spectra of the (1,0) and (1/2,1/2) LEED beams were measured at normal incidence from both the Cu{100}-c(2x2)-Pd underlayer alloy and after addition of the excess 0.5ML of Pd. Figure 5 illustrates the results. The I(V) spectra after addition of the excess 0.5ML Pd while not undergoing radical change do exhibit clear differences from those of the underlayer alloy both in terms of peak position and spectral structure.

Figure 6 illustrates possible idealised models for the Cu{100}-c(2x2)-Pd-1ML structure. Figure 6(a) illustrates a double layer c(2x2) model in which the additional 0.5ML of Pd substitutes into the outermost Cu layer to form a second c(2x2) CuPd alloy layer without clock rotation. As 50% of top layer Cu atoms are expelled during this process the surface must be heterogeneous, consisting of 50% c(2x2) CuPd double layer alloy and 50% double layer c(2x2) CuPd alloy capped by a Cu monolayer. Figure 6(b) illustrates a second possibility where Pd adsorbs as a pseudomorphic p(1x1) epitaxial film above the outermost copper monolayer. Again the surface formed will be heterogeneous, consisting of 50% of Cu{100}-c(2x2)-Pd underlayer alloy and the remaining 50% capped by a Pd-monolayer.

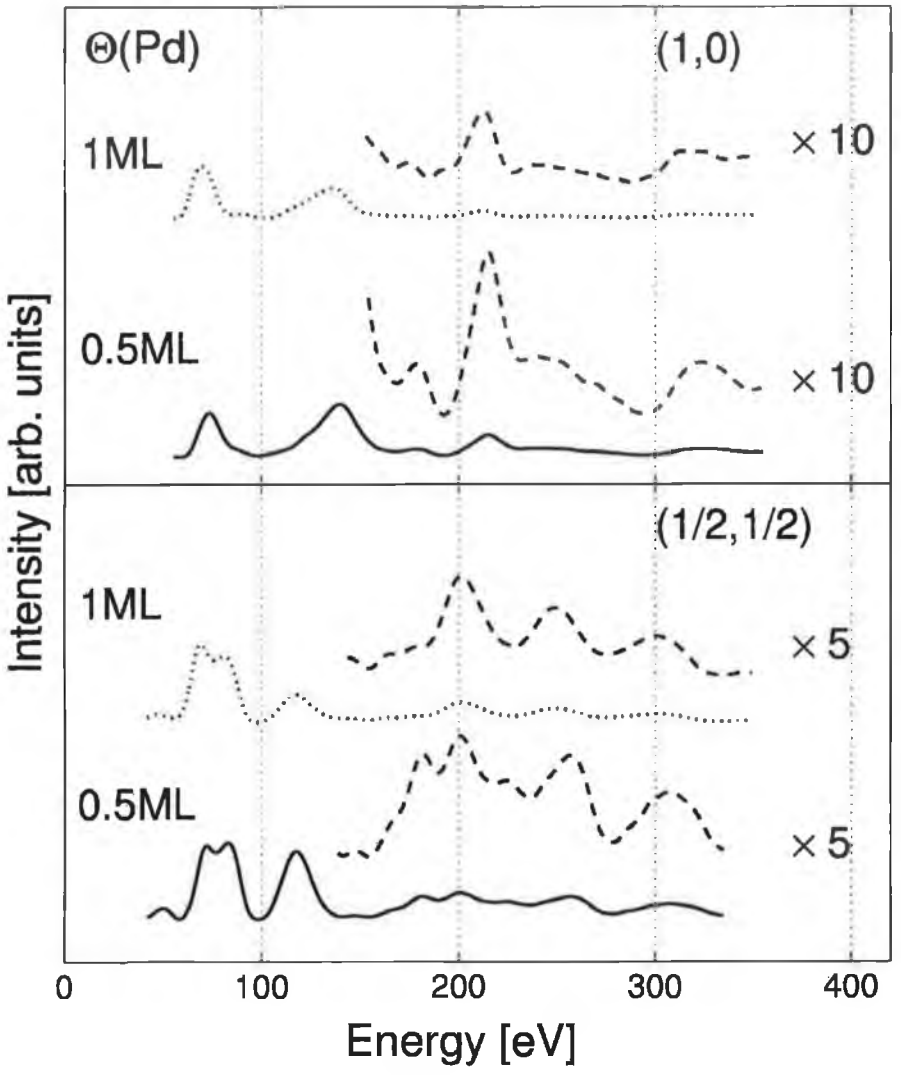

Figure 5: Experimental normal incidence I(V) spectra from the (1,0) and (1/2,1/2) beams from a Cu{100}-c(2x2)-Pd underlayer alloy formed by deposition of 0.5ML of Pd and thermal processing to 550K (lower curves=full lines) and after deposition of a further 0.5ML (upper curves=dotted lines). In both cases the energy region between 150 and 350eV is also shown on an expanded scale (heavy dashed lines) in order to allow a more detailed visual comparison.

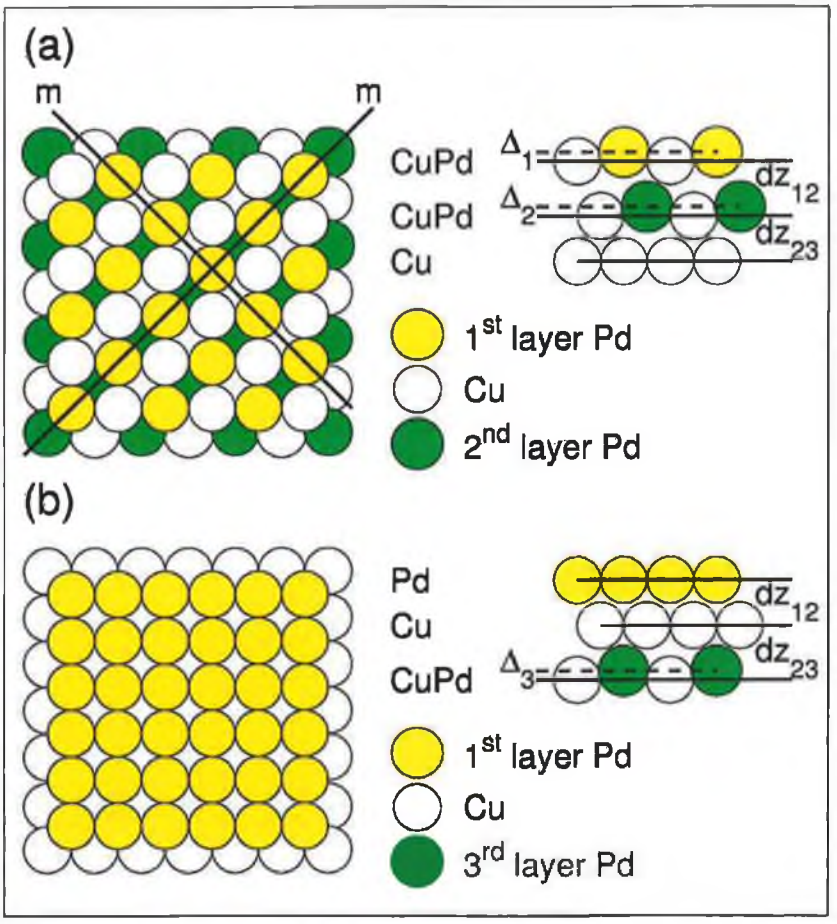

Figure 6: Top and side view of possible models for the Cu{100}-c(2x2)-Pd-1ML structure including: (a) a double layer c(2x2) CuPd alloy ; (b) p(1x1) Pd clusters above a copper capped c(2x2)-CuPd underlayer alloy. The geometric parameters varied within the analysis are indicated in each case within the side views.

In order to test which of these models provided the best agreement, a limited set of SATLEED calculations were made. The case of the model shown in figure 6(b) was easier as the surface geometry of 50% of surface corresponding to the Cu{100}-c(2x2)-Pd underlayer alloy with local Pd coverage of 0.5ML may be frozen at that previously determined by Barnes et al [14]. This should be a good approximation provided the Pd island size is large. The geometric parameters varied in the 50% of the surface covered by a Pd monolayer included: the interlayer spacing between the Pd monolayer and the underlying Cu layer (dz_{12}), the spacing between the pure Cu second layer and Cu atoms in the third mixed c(2x2) CuPd layer (dz_{23}) and finally the buckling amplitude within this mixed layer (Δ_3). The theoretical LEED I(V) spectra were then formed for each geometry by a 1:1 addition of computed intensities from the two domains. The minimum Pendry R-factor obtained was 0.44. The high Pendry R-factor suggests this scenario may be discarded.

In the case of the double layer c(2x2) alloy, a minimum Pendry R-factor of 0.31 was obtained. The geometry of both the double layer c(2x2) and the Cu capped double layer were allowed to vary. In the case of the double layer domain, the outermost interlayer spacing and buckling in the outermost CuPd layer (dz_{12} and Δ_1 in figure 6(a)) were optimised. The favoured geometry in the double layer c(2x2) alloy corresponds to a first interlayer spacing of 1.99Å (+11%) and a buckling amplitude of 0.02Å in the outermost mixed CuPd layer with Pd rippled outwards. The favoured geometry for the Cu-capped double layer c(2x2) CuPd alloy correponded to an interlayer spacing between the outermost Cu monolayer and Cu atoms in the first mixed CuPd layer of 1.84Å (+2%) and a buckling of 0.04Å in the first sub-surface CuPd layer with Pd rippled downwards. It is likely that further parameter optimisation for this structure would lead to an increase in the level of agreement yielding a similar level obtained for the Cu{100}-p(2x2)-p2gg-1ML-Pd structure. Such a search would require a larger data base to extract with confidence the detailed geometry of the two heterogeneous patches.

It should be noted that if this model does represent the surface geometry/composition formed, a puzzle remains as to why the 50% of the surface adopting the double layer c(2x2) CuPd geometry does not adopt a clock rotated p(2x2)-p2gg structure similar to that of a directly deposited 1ML Pd film. Many

other possibilities remain untested for the Cu{100}-c(2x2)-Pd-1ML phase. For example, if intermixing of the second 0.5ML of Pd with the outermost Cu is kinetically inhibited it may be expected that Pd will grow as clusters due to the higher surface energy of Pd relative to Cu combined with the interfacial strain induced by the smaller Cu lattice spacing. It is thus also possible that Pd adsorbs in the form of multilayer epitaxial clusters covering a much smaller fraction of the surface than 50%.

Clearly further work using SATLEED and a larger experimental data base combined with chemical probes of the nature of the top layer composition will be required before a definitive answer regarding the structure of the Cu{100}-c(2x2)-Pd-1ML phase is obtained.

Despite the uncertainty regarding the exact structure and compositional profile of the Cu{100}-c(2x2)-Pd-1ML phase two definite conclusions may be reached:

(a) A simple model consisting of a heterogeneous surface with a 50% coverage of epitaxial p(1x1) Pd overlayer above a Cu capped c(2x2) CuPd underlayer alloy and 50% pure Cu capped underlayer alloy may be ruled out;
(b) This second mode of preparation of the Cu{100}-1ML Pd surface provides definitive evidence that a top layer c(2x2) CuPd alloy is required as a template to form the p(2x2) clock-rotated CuPd structure .

5. Conclusions

The Cu{100}-p(2x2) structure formed by deposition of 1ML of Pd on Cu{100} at room temperature has been re-analysed by Symmetrized Automated Tensor LEED (SATLEED). A wide range of models suggested by MEIS/LEED,STM and LEISS along with selected new models in keeping with the accurately determined LEISS layerwise elemental composition have been tested.

Of the previously suggested models, the SATLEED analysis shows a preference for the structure based on low energy ion scattering spectroscopy consisting of a

heterogeneous surface with the outermost layer consisting of domains of pure clock rotated p(2x2)-p4g Pd and p(2x2) Cu_3Pd alloy consisting of 30% p4g Pd and 70% Cu_3Pd with a top layer Pd coverage of 0.5ML and a total Pd loading of 1ML (R_p=0.30) .

However, the favoured model among those tested consists of a p(2x2) clock rotated ordered CuPd monolayer of symmetry p2gg above a c(2x2) ordered CuPd underlayer (R_p=0.21). Top layer Cu and Pd atoms are laterally shifted by 0.25±0.12Å from four-fold hollow sites in an alternate clockwise and anti-clockwise fashion with the vertices of the p(2x2) clock rotation centred over second layer Pd atoms. Substitution of a high concentration of Pd into the outermost two atomic layers leads to a significant expansion of the outermost two interlayer spacings to 1.93±0.02Å and 1.90±0.03Å.

A second mode of preparation of the Cu{100}/Pd-1ML phase has been investigated consisting of adsorption of 0.5ML of Pd at room temperature onto a Cu{100}-c(2x2)-Pd underlayer alloy consisting of a mixed c(2x2) CuPd second layer capped by a copper monolayer. In this case, the structure retains c(2x2) periodicity. This clearly implicates top layer c(2x2) CuPd as the required template for formation of regions of p(2x2) clock rotated phase.

References

[1] G.W.Graham, Surf.Sci 171 (1986) L432.

[2] S.H.Lu, Z.Q.Wang, S.C.Wu, C.K.C.Lok, J.Quinn, Y.S.Li, D.Tian, F.Jona and P.M.Marcus, Phys.Rev.B 37 (1988) 4296.

[3] S.C.Wu, S.H.Lu, Z.Q.Wang, C.K.C.Lok, J.Quinn, Y.S.Li, D.Tian, F.Jona and P.M.Marcus, Phys.Rev.B 38 (1988) 5356.

[4] G.W.Graham, P.J.Schmitz and P.A.Thiel, Phys.Rev.B 41 (1990) 3353.

[5] T.D.Pope, G.W.Anderson, K.Griffiths, P.R.Norton and G.W.Graham, Phys.Rev.B 44 (1991) 11518.

[6] T.D.Pope, M.Vos, H.T.Tang, K.Griffiths, I.V.Mitchell, P.R.Norton, W.Liu, Y.S.Li, K.A.R.Mitchell, Z.J.Tian and J.E.Black, Surf.Sci 337 (1995) 79.

[7] P.W. Murray .I.Stensgaard, E.Laegsgaard and F.Besenbacher Phys.Rev.B 52 (1995) R14404; P.W.Murray, I.Stensgaard, E.Laegsgaard and F.Besenbacher, Surf.Sci 365 (1996) 591.

[8] J.Yao, Y.G.Shen, D.J.O'Connor and B.V.King, Surf.Sci 359 (1996) 65.

[9] Y.G.Shen, A.Bilic, D.J.O'Connor and B.V.King, Surf.Sci 394 (1997) L131-137.

[10] M.A.Van Hove in "Solving Complex and Disordered Surface Structures with Electron Diffraction" in "Chemistry and Physics of Solid Surfaces VII", Editors R.F.Howe and R.Vanselow, Springer Series in Surface Science 10 (1988) 513.

[11] P.J.Rous, Prog.Surf.Sci 39 (1992) 3

[12] K.Pussi, M.Lindroos and C.J.Barnes, Chemical Physics Letters 341 (2001) 7.

[13] C.J.Barnes, E.AlShamaileh, T.Pitkanen, P.Kaukasoina and M.Lindroos, Surface Science 492 (2001) 55.

[14] H.L.Davis and J.R.Noonan, J.Vac.Technol 20 (1981) 842 ; F.Jona, Surf.Sci 192 (1987) 398.

[15] M.A.Van Hove, W.Moritz, H.Over, P.T.Rous, A.Wander, A.Barbieri, N,Materer, U.Starke and G.A.Somorjai, Surf.Sci.Rep 19 (1993) 191.

[16] N.W.Ashcroft and N.D.Mermin, Solid State Physics, CBS Publishing, Japan, 1981.

[17] J.B.Pendry, J.Phys.C:Solid State Physics 13 (1980) 937.

[18] K.Kishi, A.Oka, N.Takagi, M.Nishijima and T.Aruga, Surf.Sci 460 (2000) 264.

[19] H.Onishi, H.Sakama, T.Aruga, A.Kawazu and Y.Iwasawa, Surf.Sci 444 (2000) 7.

[20] Y.G.Shen, J.Yao, D.J.O'Connor, B.V.King and R.J.Mac-Donald, Phys.Rev.B 56 (1997) 9894.

[21] C.Klink, L.Olesen, F.Besenbacher, I.Stensgaard, E.Laegsgaard and N.D.Lang, Phys.Rev.Lett 71 (1993) 4350.

[22] Y.Gauthier, R,Baudoing-Savois, K.Heinz and H.Landskron , Surf.Sci 251/252 (1991) 493.

CHAPTER 4

Cu{100}-c(2x2)-Pt Surface Alloy: Structural Analysis As a Function of Pt Loading

Formation of a Cu-capped Cu{100}-c(2x2)-Pt Underlayer Alloy: a SATLEED analysis

E. AlShamaileh and C.J. Barnes

School of Chemical Sciences and National Centre for Plasma Science and Technology (NCPST), Dublin City University, Dublin 9, Ireland.

Abstract

The room temperature deposition of 0.5 ML Pt on Cu{100} followed by annealing to 525 K results in a sharp c(2x2) LEED pattern. SATLEED analysis for this phase shows that it consists of an ordered c(2x2) Cu-Pt second layer capped with a pure Cu layer. The first and second interlayer spacings are found to be expanded by +5.1±1.7 % and +3.5±1.7%, respectively (relative to the bulk Cu interlayer spacing of 1.807 Å) due to the insertion of the 8% larger Pt atoms into the second layer. The ordered mixed layer is found to be rippled by 0.08±0.06 Å with Pt atoms rippled outwards towards the solid-vacuum interface. A smaller rippling of 0.03±0.11 Å in the fourth pure Cu layer was also detected with Cu atoms directly underneath Pt atoms rippled towards the second layer Pt resulting in a Pt-Cu bond length of 2.52 Å which compares to the sum of metallic radii of 2.67 Å.

1. Introduction

The incorporation of catalytically active metals into the top few surface layers of another metal is an area of growing physical and chemical interest [1-5]. The Cu-Pt combination is of particular importance due to the many applications of both Pt and Cu in heterogeneous catalysis including oxidation of CO and NO gases over Pt [6-8] and methanol and ammonia production [9,10].

In contrast to the Cu{100}/Pd bimetallic combination, little work has appeared to date on the Cu{100}/Pt system. Using He^+ and LEISS, Graham et al. have reported that the room temperature deposition of 0.5 ML Pt film on Cu{100} followed by annealing to 525 K produces an essentially Cu-terminated surface [11]. On the contrary, Shen et al. suggested that at this coverage with annealing to 453 K for 10 minutes results in a surface alloy with 38 at. % in the outermost layer and 10 at. % in the second layer [12]. The different top layer compositions may be attributed to the differing thermal activation procedures employed.

Recently, Reilly et al. [13] have studied the formation kinetics of the Cu{100}-c(2x2)-Pt by deposition of Pt at room temperature and monitoring the intensity and full-width-at-half-maximum of (1,0) and (1/2,1/2) LEED beams as a function of temperature and time. It was found that annealing to 550K for 30 seconds produced the maximum (1/2,1/2) beam intensity indicating a state of optimal ordering of the c(2x2) phase. Using CO titration to probe the surface Pt concentration, Reilly et al. reported a considerable reduction in saturation CO uptake after annealing the room temperature deposited Pt to 550K. This was interpreted as due to the formation of a Cu{100}-c(2x2)-Pt underlayer alloy with an almost pure copper layer outermost. The authors excluded the possibility of top layer surface alloy formation based on studies of CO adsorption on Cu_3Pt bulk alloys [13].

In this paper, the structure of the Cu{100}-c(2x2) 0.5 ML Pt phase is determined by Symmetrised Automated Tensor LEED (SATLEED) testing both a surface alloy model where the mixed layer is located in the outermost layer and the underlayer alloy model with the mixed layer sandwiched in the second layer along with overlayer models with Pt occupying four-fold hollow, bridge and atop sites.

2. Experimental

The details of the LEED ultra-high vacuum has already been published [14]. In this study, the base pressure was 2 x 10^{-10} Torr. Platinum was evaporated via resistively heating of a well outgassed 0.25 mm diameter W wire (99.99%, Goodfellow Metals Ltd.) around which was wrapped high purity 0.125 mm diameter Pt wire (99.999 %, Goodfellows Metals, UK). The evaporation rate was calibrated measuring the (1/2,1/2) beam-intensity and full-width at half-maximum. The deposition time needed to maximise the (1/2,1/2) beam intensity was assigned to a Pt coverage of 0.60 ML according to a recent study by Reilly et al. [15]. From the calibration curve constructed for the measured (1/2,1/2) beam intensity versus deposition time, we estimate the Pt coverage to be 0.50±0.10 ML.

Deposition of 0.5 ML Pt at room temperature results in a weak and diffuse high background c(2x2) LEED pattern. Annealing this phase to 525 K for 30 seconds produced a good quality c(2x2) LEED pattern.

LEED I(V) data were collected at close to room temperature using a CCD camera interfaced with a minicomputer for data acquisition. All spectra used in this study were collected at normal incidence. One set of data measured for the same phase on the same day was used in the calculations.

Five non-symmetric beams (three integral: (1,0), (1,1), (2,0) and two fractional: (1/2,1/2), (3/2,1/2)) were used in the analysis corresponding to a total energy range of 1300 eV. Beams were individually back-ground subtracted and symmetry-equivalent beams were averaged to minimise errors ensuing from small deviations from normal incidence or residual magnetic fields. The beams were then normalised to constant incoming beam current and finally smoothed by a 5-point adjacent-averaging prior to analysis.

3. Theoretical Considerations

Theoretical LEED I(V) spectra were calculated using the SATLEED package [16]. Nine phase shifts for both Pt and Cu were used in the calculations and were generated by the phase shifts package of Barbieri/van Hove [16]. Initially, bulk Debye temperatures of Cu and Pt of 343 K and 240 K, respectively were used in the analysis [17]. A fixed value of – 5.0 eV for the energy independent imaginary part of the inner potential was used in the initial phase of the analysis while the energy independent real part was allowed to be optimised (vary) in the course of the calculations. The Pendry R-factor (R_p) was used to test theory-experiment agreement [18].

4. Results and discussion

Fig. 1 illustrates possible models for the Cu{100}-c(2x2) 0.5 ML Pt phase. Extensive LEED calculations were carried out for each model involving optimisation of structural and non-structural parameters seeking the lowest R_p factor. At this stage of the analysis, only the first two interlayer spacings were allowed to vary (d_{12} and d_{23} are measured from 1st layer Cu atoms to 2nd layer Cu atoms in the alloy models). The ranges of variation for each model are indicated in table 1, which also shows the lowest total R_p for the tested models. In the alloy models where mixing of Pt and Cu takes place, a buckling of about 0.3 Å was allowed for Pt atoms buckled in either vertical direction.

The results clearly indicate that the underlayer CuPt alloy yields the best theory-experiment agreement and all other structures fell outside the RR-value of 0.05. Hence, the underlayer model was considered for further optimisation excluding all other models. This refinement process involved the optimisation of all structural and non-structural parameters yielding an optimal Pendry R-factor of 0.27.

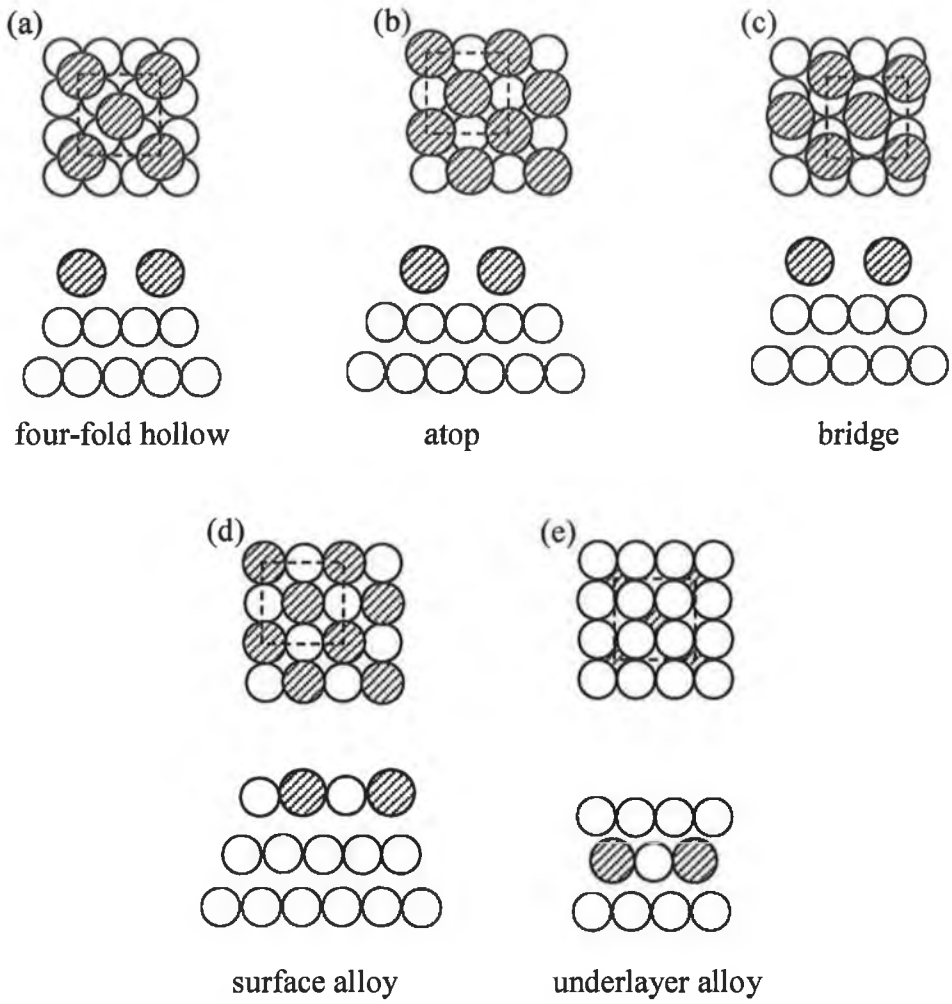

Fig. 1: Possible models for the Cu{100}-c(2x2)-Pt phase including: (a) four-fold hollow overlayer; (b) atop overlayer; (c) bridge overlayer; (d) surface alloy and (e) underlayer alloy.

Table 1: Optimal Pendry R-factors for models shown in Fig. 1.

Model	d_{12} and d_{23} tested ranges Å	R_p
Four-fold hollow overlayer	1.65-2.25	0.56
Atop overlayer	2.50-2.90	0.62
Bridge overlayer	2.00-2.55	0.52
Surface alloy	1.65-2.25	0.40
Underlayer alloy	1.65-2.25	0.32

Fig. 2 shows a side view of the model detailing the favoured geometric parameters. Fig. 3 illustrates the comparison of experimental and calculated (best-fit) LEED I(V) spectra for the favoured underlayer structure. The dependence of Pendry R-factor on the first and the second interlayer spacings and the rippling in the mixed CuPt layer and the fourth Cu layer are shown in Fig. 4.

The favoured model consists of a mixed CuPt underlayer capped with a pure Cu layer. The first and second interlayer spacings were found to be d_{12} =1.90±0.03 Å and d_{23}=1.87±0.03 Å, respectively, corresponding to an expansion of 5.1±1.7 % and 3.5±1.7 %, respectively (relative to the bulk Cu value of 1.807 Å). The third interlayer spacing experienced a small expansion of 0.3±1.7 %. A small buckling of 0.08±0.05 Å was detected in the mixed underlayer with Pt atoms rippled outwards towards the solid-vacuum interface.

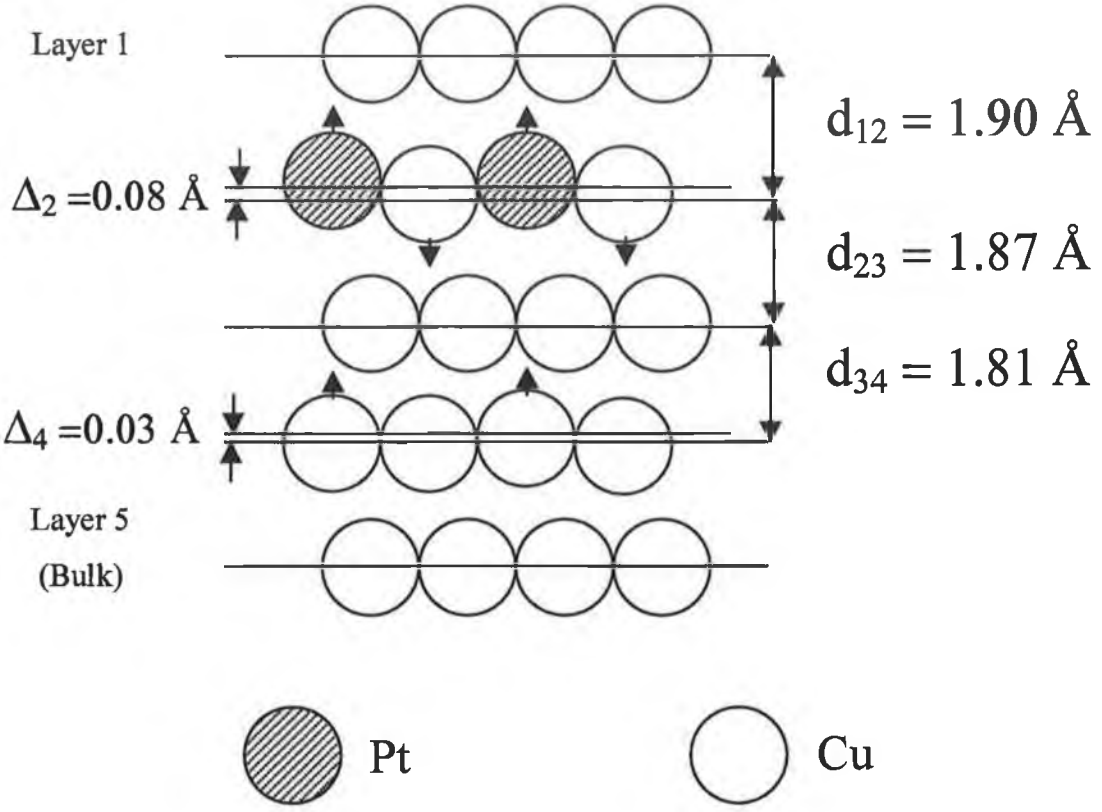

Fig. 2: Side view along [011] direction of the favoured model showing the best-fit geometrical parameters.

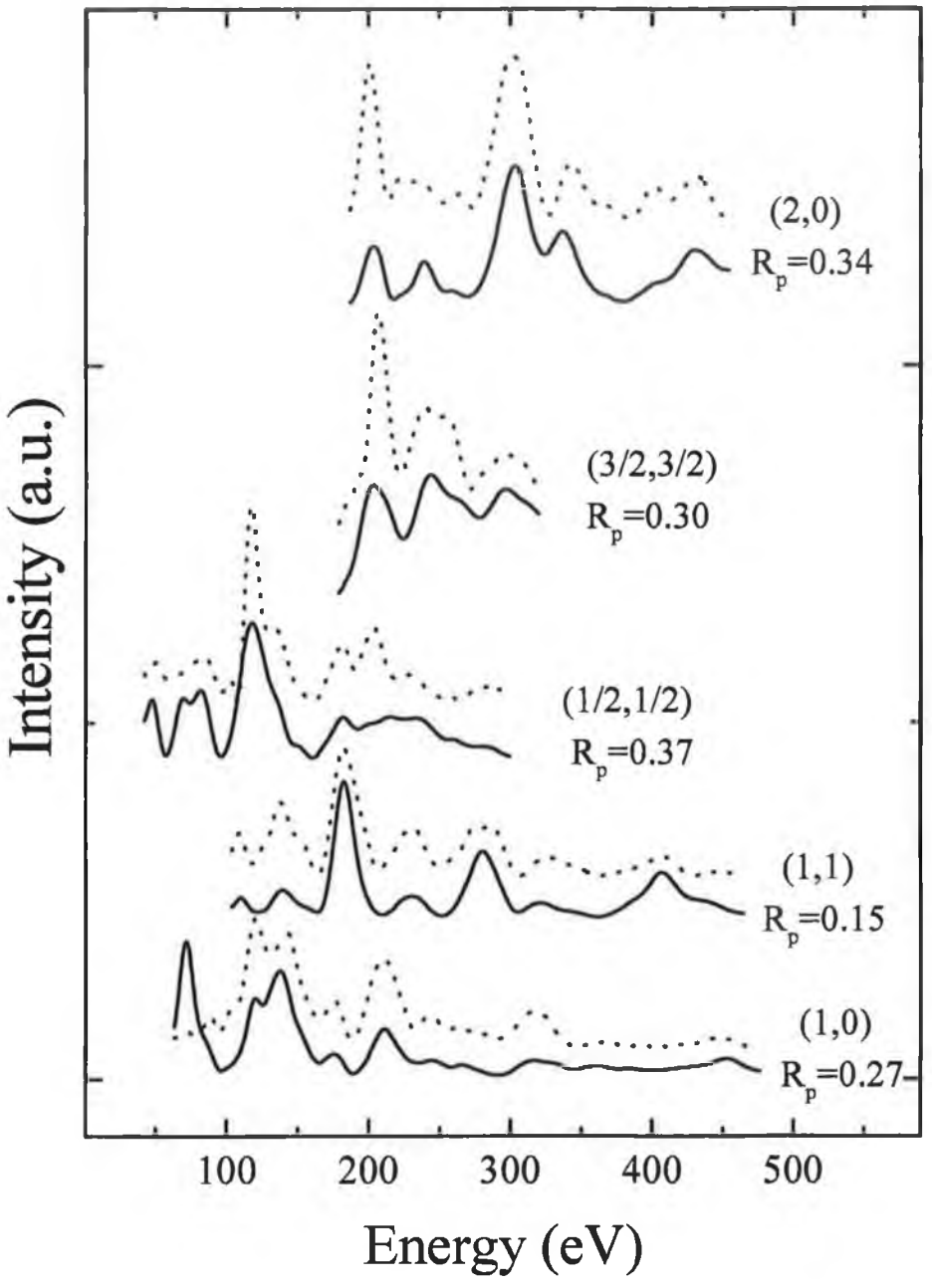

Fig. 3: Comparison of experimental (solid lines) and calculated (dotted lines) LEED I(V) spectra for the favoured Cu{100}-c(2x2)-Pt underlayer structure.

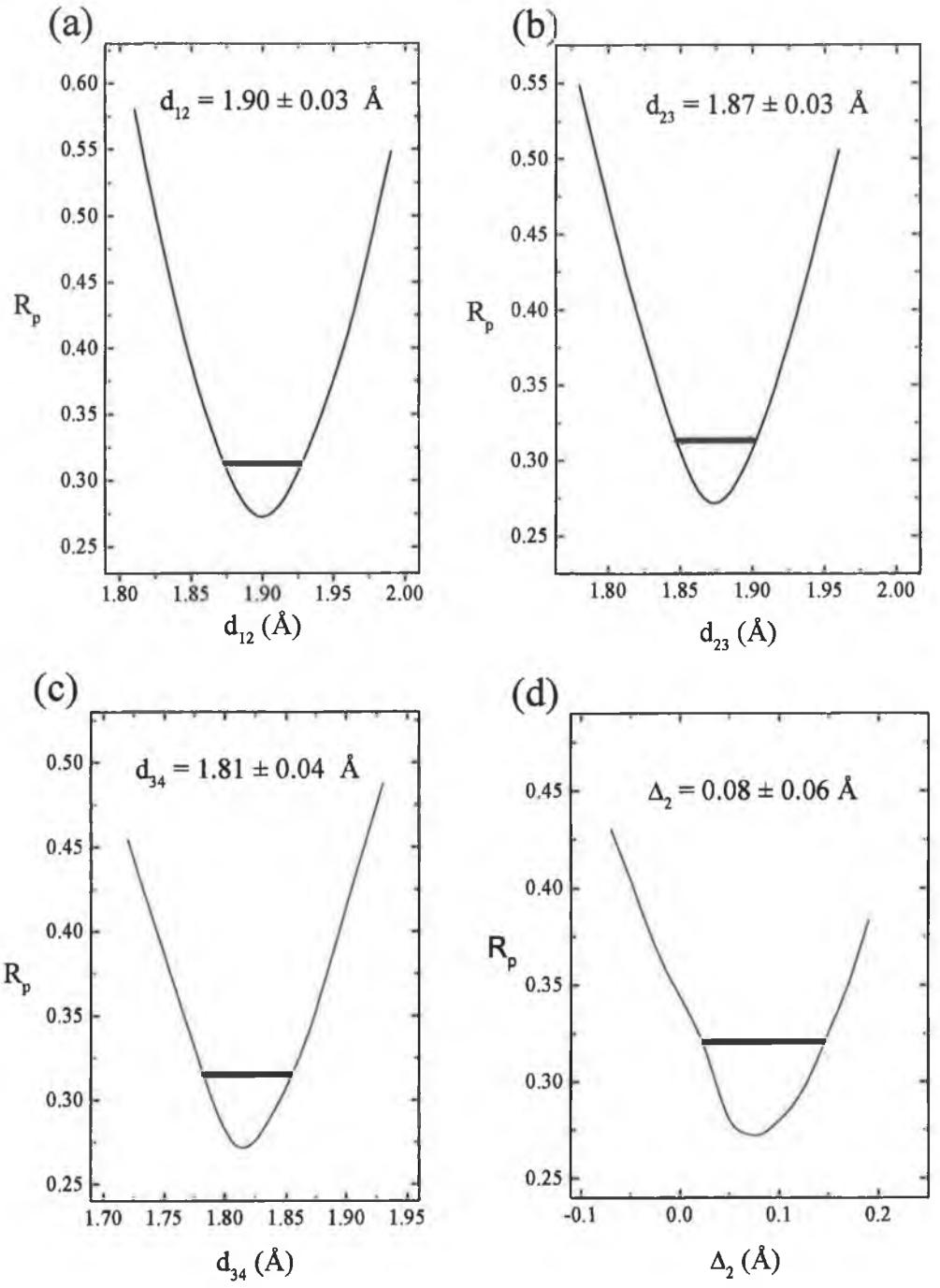

Fig. 4: The dependence of Pendry R-factor on (a) the first interlayer spacing (d_{12}); (b) the second interlayer spacings (d_{23}); (c) third interlayer spacings (d_{34}) and (d) the buckling in the mixed CuPt layer (Δ_2). The optimal value for each variable is shown at the top of each panel along with the associated error. Horizontal lines indicate the variance.

It is interesting to compare the structure obtained in this analysis to the corresponding Cu{100}-c(2x2)-Pd underlayer alloy analysed recently by LEED I(V) calculations [14]. It was found that Pd forms a mixed CuPd underlayer when a top layer surface alloy formed by deposition of 0.5 ML Pd is thermally treated [14]. Two major differences with our results can be noticed: firstly, in the mixed underlayer, Pd atoms are rippled inward while Pt atoms in the mixed underlayer are rippled outward towards the solid-vacuum interface. Secondly: in the Pd system, a greater buckling was detected in the fourth Cu layer (0.2±0.1 Å) while in the Pt system a much smaller value is favoured (0.03±0.11 Å).

On the other hand, the two systems display similar general structure where the first and second interlayer spacings are expanded relative to the Cu bulk values. The net expansion of the outermost three layer slab is found to be 0.18 Å and 0.15 Å for the Cu{100}/Pd and Cu{100}/Pt underlayer alloys, respectively. This similarity may be attributed to the almost identical sizes of Pd (12-coordinate metallic radius=1.38 Å) and Pt (12-coordinate metallic radius=1.39 Å) and may also be extended to the similarity of their electronic/bonding properties since they belong to the same group in the periodic table.

When Pt atoms replace every second Cu atom in the second layer, the Cu-Pt bond length calculated between 1st layer Cu atoms and 2nd layer Pt atoms is found to be 2.56 Å. This value corresponds to a 4.1% contraction of the sum of the 12-coordinate metallic radii of Cu and Pt of 2.67 Å. It is interesting to note that the sum of the first and second interlayer spacings in the Cu{100}-c(2x2)-Pt undelayer is 8.6% which is very similar to the size mismatch between Cu and Pt atoms of 8.1%. The apparent contraction of Pt atoms is a result of co-ordination with Cu atoms while the expansion in the 1st and 2nd interlayer spacings comes from the incorporating of the larger Pt atoms into the second layer of the selvedge.

The structure retrieved in this study is in accordance with that suggested by Reilly et al. based on CO titration results. The authors also suggested that the top layer may contain some Pt atoms (about 10% of the deposited Pt) [13]. In our study, we have modelled a relatively perfect distribution of Pt atoms in the system represented by considering a pure top Cu layer, a 50:50 mixed CuPt underlayer and pure Cu layers

underneath. It is possible that the experiment-theory agreement can be improved if the Average T-matrix Approximation (ATA) technique is used to model imperfections such as low Pt concentration in layers 1 and 3. This should lead to an enhanced level of theory-experiment agreement and a detailed picture of the layerwise compositional profile along with small changes in surface geometric parameters to those obtained here based on assumption of a somewhat idealised layerwise compositional profile.

Finally, it is worthy of note that the {100} surface of a Cu_3Pt bulk alloy prefers a c(2x2) mixed CuPt underlayer capped with a pure Cu layer as determined by ion scattering studies [19]. The tendency for preference of Cu termination occurs due to the significantly lower surface energy of Cu (2.09 Jm^{-2}) compared to Pt (2.48 Jm^{-2}) [20].

5. Conclusions

SATLEED has been used to determine the structure of Cu{100}-c(2x2)-Pt underlayer alloy formed by thermal activation of 0.5 ML Pt adsorbed on Cu{100}. The analysis retrieved a structure that consists of an ordered c(2x2) Cu-Pt second layer capped with a pure Cu layer.

(a) The first and second interlayer spacings are found to be expanded by +5.1±1.7 % and +3.5±1.7%, respectively (relative to the bulk Cu interlayer spacing of 1.807 Å) as a result of insertion of the ~8% larger Pt atoms into the second layer.

(b) The ordered mixed layer is found to be rippled by 0.08±0.06 Å with Pt atoms rippled outwards towards the solid-vacuum interface.

References

[1] U.Bardi, Rep.Prog.Phys 57 (1994) 939.
[2] P.Praserthdam and T.Majitnapakul, Appl.Catal.A 108(1) (1994) 21.
[3] J.Yoshinbu and M.Kawai, J.Chem.Phys 103 (1995) 3220.

[4] G.W.Graham, P.J.Schmitz and P.A.Thiel, Phys.Rev.B 41 (1990) 3353.

[5] R.Belkhou, J.Thiele and C.Guillot, Surface Science 377-379 (1997) 948.

[6] J.P.Reilly, D.O'Connell and C.J.Barnes, J.Phys: Condensed Matter 11 (1999) 8417.

[7] H.L.Davis and J.R.Noonan, J.Vac.Sci.Technol 20 (1981) 842 ; F.Jona, Surf.Sci 192 (1987) 398.

[8] M.P.Seah and W.R.Dench, Surface and Interface Analysis

[9] M.A.Van Hove, W.Moritz, H.Over, P.T.Rous, A.Wander, A.Barbieri, N.Materer, U.Starke and G.A.Somorjai, Surf.Sci.Rep 19 (1993) 191.

[10] N.W.Ashcroft and N.D.Mermin, Solid State Physics , CBS Publishing, Japan, 1981.

[11] G. W. Graham, P.J. Scmitz and P. A. Thiel, Phys. Rev. B 41 (1990) 3353.

[12] Y.G. Shen, J. Yao, D. J. O'Connor, B. V. King and R. J. MacDonald, Solid State Comm, 100 (1996) 21.

[13] J.P. Reilly, D. O'Connell and C. J. Barnes, J. Phys.: Cond. Matt. 11 (1999) 8417.

[14] C.J. Barnes, E. AlShamaileh, T. Pitkänen, P. Kaukasoina and M. Lindroos, Surface Science 492 (2001) 55.

[15] M. Valden, J. Aaltonen, M. Pessa, M. Gleeson and C.J. Barnes *Chem. Phys. Lett.* 228 (1994) 519.

[16] A. Barbieri and M.A. Van Hove, private communication.

[17] C. Kittel, Introduction to Solid State Physics, John Wiley & Sons, New York, 1986, p. 110

[18] J.B. Pendry, J. Phys. C. 13 (1980)937.

[19] J.S. Tsay, T. Mangen and K. Wandelt, Thin Solid Films 397 (2001) 152.

[20] L.Vitos, A.V.Ruban, H.LSkriver and J.Kollar, Surf.Sci 411 (1998) 186.

A Tensor LEED Determination of the Structure and Compositional Profile of a Cu{100}-c(2x2)-Pt Surface Alloy

E.AlShamaileh[a], H. Younis[a], C.J.Barnes[a,b], K.Pussi[c] and M.Lindroos[c]

[a] School of Chemical Sciences, Dublin City University, Dublin 9, Ireland.
[b]National Centre of Plasma Science and Technology (NCPST), Dublin City University, Dublin, Ireland.
[c] Institute of Physics, Tampere University of Technology, Tampere, Finland.

Abstract

The geometric structure and compositional profile of a Cu{100}-c(2x2)-Pt surface alloy formed by thermal activation of a monolayer Pt film has been determined by tensor LEED. A wide range of models have been tested. The favoured model consists of an ordered c(2x2) CuPt underlayer below a Cu terminated surface. Models involving a mixed ordered CuPt layer outermost may be definitively ruled out. The average T-matrix approximation (ATA) has been applied allowing variable Pt concentrations to be introduced in-to both the outermost layer and deeper in-to the selvedge (layers 3 and 4) in the form of a random substitutionally disordered Cu_xPt_{1-x} alloy. The favoured concentration profile corresponds to an almost pure outermost Cu monolayer (Θ_{Pt} =10±10 at%) with Pt concentrations of 20±20 at% and 30±30 at% in layers 3 and 4 respectively. Introduction of Pt into the surface layers induces a significant expansion of the selvedge yielding modification of the outermost three interlayer spacings to 1.84±0.02Å (Δdz_{12}= +1.9±1.1%), 1.91±0.03Å (Δd_{23}=+5.8±1.7 %) and 1.89±0.03Å (Δd_{34}=+4.7±1.7 %). The rippling in the first mixed CuPt monolayer is small and of amplitude 0.03±0.04 Å with Pt rippled outwards towards the solid-vacuum interface.

1. Introduction

The bimetallic combination Cu{100}/Pd is one of the best studied examples of surface alloy formation [1]. In contrast, the closely associated Cu{100}/Pt system has recieved much less attention, despite the application of Cu_xPt_{1-x} alloys as a working catalyst for both CO oxidation [2] and hydrocarbon reforming reactions [3].

The earliest study of the Cu{100}/Pt system was carried out by Graham, Schmitz and Thiel [4] using Auger Electron Spectroscopy (AES), Low Energy Ion Scattering Spectroscopy (LEISS) and Low Energy Electron Diffraction (LEED) illustrating that Pt grows at room temperature in a somewhat disordered overlayer as Pt clusters with some intermixing with the underlying Cu substrate. Auger spectroscopy was used to calibrate the Pt surface coverage via comparison of the AES intensities of Pt and Cu to those of Au and Cu from the Cu{100}-c(2x2)-Au surface alloy (Θ_{Au}=0.5ML)*. Formation of a weak diffuse c(2x2) LEED pattern was reported for coverages 0.8ML and above for room temperature deposition. Annealing of the Cu{100}/Pt interface to 525K at a Pt coverage of 0.8ML was indicative of strong copper segregation and formation of a well ordered c(2x2) LEED pattern. Graham et al determined that for Pt coverages up-to 1ML, annealing to 525K leads to surfaces with a pure or almost pure Cu layer outermost [4]. In contrast, Shen and co-workers, using a combination of He^+ and Li^+ LEISS, report that thermal activation of a 1ML Pt film to the slightly lower temperature of 450K for 10 minutes led to formation of a c(2x2) structure with adjacent layers with Pt concentrations of 46 at% and 41 at% in layers 1 and 2 respectively [5]. Clearly the compositional profile of the Cu{100}-c(2x2)-Pt surface alloy with Pt loading of around 1ML is highly sensitive to the thermal treatment utilised. It would appear that "low temperature" thermal activation ($\langle$450K) lead to surfaces with considerable Pt content in the outermost layer, while "high temperature" ($\rangle$525K) annealing leads to surfaces with a pure or almost pure Cu termination at low Pt loadings. Thermal processing at temperatures above 600 K leads to rapid destruction of the c(2x2) superstructure due to Pt interdiffusion into the bulk of the Cu{100} sample. Hence, the Cu{100}-c(2x2)-Pt surface alloys reported by Graham et al [4] and Shen et al [5] correspond to kinetically trapped

* This calibration method is approximate due to differences in the growth mechanism of Pt and Au on Cu{100} and the assumption of identical cross sections for the Pt and Au for the Auger transitions monitored.

meta-stable states with face-centred-cubic dilute substitutional $Cu_{1-x}Pt_x$ alloys being the true thermodynamically favoured structure. Nevertheless, once formed, the Cu{100}-c(2x2)-Pt alloy is stable for prolonged operation temperatures below 500K and as such is useful to probe the effect of surface alloying of Cu and Pt on a range of reactions including hydrocarbon reforming, CO oxidation and methanol synthesis. For example, in a recent study of the Cu{100}-c(2x2)-Pt system, Reilly et al reported that Cu{100}-c(2x2)-Pt surface alloys formed by "high temperature" (550K) thermal activation of a Pt films of loadings of 1 to 1.5ML led to significant changes in the decomposition kinetics of a formate catalytic intermediate [6] .

To date no quantitative structural work has been carried out on the Cu{100}/Pt bimetallic interface. The Cu/Pt system is a favourable bimetallic combination to utilise the technique of tensor LEED (TLEED) in combination with the average T-matrix approximation (ATA) to determine **both** the surface geometric structure and the layerwise compositional profile. In this paper we report the results of a TLEED-ATA analysis of a Cu{100}-c(2x2)-Pt surface alloy formed by "high temperature" thermal activation of Pt films of monolayer coverage, illustrating that the c(2x2) periodicity arises from chemical ordering in a mixed CuPt underlayer with an essentially Cu-terminated surface with a concentration profile similar to the outer bilayer of a Cu_3Pt{100} bulk alloy surface which adopts a Cu terminated $L1_2$ structure consisting of alternate layers of pure Cu and c(2x2) mixed CuPt [7].

2. Experimental

All experiments were performed in an ion and titanium sublimation pumped ultra-high vacuum chamber with facilities for LEED, AES and thermal desorption spectroscopy and a base pressure of $1x10^{-10}$ torr. The Cu{100} sample was cleaned by standard procedures involving argon ion bombardment and annealing to 800K until no contaminants were observed in AES and LEED I(V) spectra from the clean Cu{100}-(1x1) surface were in excellent agreement with previous literature reports [8]. Platinum was evaporated from ultra-high-purity (99.99%) 0.125mm Pt wire wrapped around a shrouded and collimated 0.3mm tungsten filament. The platinum

evaporation rate was estimated using the method of Reilly et al [6] which consisted of periodic monitoring of the intensity and full-width-at-half-maximum (f.w.h.m) of the (1,0) and (1/2,1/2) LEED reflexes as a function of Pt evaporation time. Spot profiles were collected at constant temperature (~330K) with the surface being briefly thermally activated to 550K using a temperature ramp of $2.5Ks^{-1}$ after each Pt dose in order to promote c(2x2) surface alloy formation. Reilly et al have argued that the co-incident maximum in the intensity and minimum in f.w.h.m of the (1/2,1/2) beam corresponds to formation of a well ordered c(2x2) CuPt underlayer (θ_{Pt}=0.5ML). Titration experiments with CO indicated that a small (0.1ML) coverage of Pt remained in the outermost layer, hence the evaporation time required to reach a maximum in the (1/2,1/2) beam intensity and minimum in f.w.h.m was set to a Pt coverage of 0.6ML. This method was adopted rather than traditional methods of coverage calibration such as construction of Auger signal versus deposition time plots, as it is known that the room temperature growth mode for the Cu{100}/Pt bimetallic combination involves Pt clustering and surface alloy formation making definitive coverage calibration by Auger spectroscopy difficult.

The Cu{100}-c(2x2)-Pt structure was formed by deposition of 1ML of Pt onto Cu{100} with the sample held at room temperature, resulting in a high background LEED structure with weak broad c(2x2) reflections. The procedure adopted to determine the optimal thermal treatment to form a well ordered c(2x2) surface alloy was as follows: a 1ML Pt film was evaporated on-to a clean Cu{100} surface at room temperature and a spot profile across the (1,0), (1/2,1/2) and (0,1) beams was recorded. The surface was then heated to increasing temperature in increments of between 20 and 25K with the crystal held at the anneal temperature for 1 minute duration before cooling to a constant temperature and acquiring a spot profile. The optimal annealing temperature was decided by plotting both the integrated intensity and f.w.h.m of the (1/2,1/2) reflex as a function of annealing temperature: the optimal anneal temperature of 550K was that required to bring the (1/2,1/2) beam to a co-incident maximum intensity and minimum f.w.h.m. Annealing to temperatures above 600K led to destruction of the c(2x2) due to interdiffusion of Pt deep in-to the Cu{100} sample.

The LEED I(V) measurements were made at room temperature under conditions of normal incidence using a CCD video camera and collecting data by automatic spot tracking. Normal incidence was attained by variation of the sample alignment until the four (1,0) beams had identical spectral structure and highly similar relative intensities over the energy range 50-350eV. Symmetry equivalent beams were co-added to reduce effects of residual sample misalignment. Prior to symmetry addition, each beam was individually background subtracted by fitting an exponential background to chosen minima in the I(V) curves. The data was then normalised to constant incoming beam current. The data set utilised in the analysis corresponded to a total energy range of 1260eV.

3. Theoretical Analysis

LEED calculations were performed with the Barbieri/Van Hove Symmetrized Automated Tensor LEED package [9]. Up-to 9 phase shifts were used for both copper and platinum initially taken from the Van Hove/Barbieri phase shift package. Other non-structural parameters included bulk Debye temperatures of 315K for Cu and 233K for Pt [10]. In the initial stage of analysis these values where fixed while in the final optimisation of the favoured structures both the Pt and Cu Debye temperatures were allowed to vary in order to obtain optimal theory-experiment agreement. An energy independent imaginary part of the inner potential of -5eV was utilised throughout the initial stage of the analysis with this parameter again being optimised in the final refinement stage. The energy independent real part of the inner potential was allowed to vary via a rigid shift in the LEED calculations with theory-experiment agreement being tested with the Pendry R-factor [11]. Error bars were calculated based on the variance of the Pendry R-factor using the standard prescription [11].

4. Results and Discussion

The initial models tested were limited by the following assumption that the c(2x2) structure observed upon thermal activation was due to chemical ordering of Cu and Pt in c(2x2) sub-layers with composition CuPt. Based on the structure of the {100} surface of a bulk Cu_3Pt $L1_2$ alloy, a natural suggestion for the structure of the surface alloy would be alternate CuPt and Cu layers initially confined to the in-plane Cu{100} periodicity [7]. To test this structure, we allowed up-to 3 layers of CuPt stoichiometry to be distributed within the selvedge. Inclusion of one , two and three c(2x2) CuPt layers would lead to creation of top two, four and six layer slabs respectively of average stoichiometry Cu_3Pt. As LEED is insensitive to deeper lying layers, a 6 layer slab should correctly model to a good level of approximation the entire LEED probing depth as a distorted Cu_3Pt $L1_2$ type structure. In each case, two possibilities exist in which the surface terminates either in a mixed CuPt layer or a pure Cu layer. Structures were also tested in which two or three ordered CuPt sub-planes (Θ_{Pt}=1 and 1.5ML respectively) were stacked in adjacent layers. Again terminations with either a mixed CuPt layer or pure Cu layer outermost were tested. The structural parameters allowed to vary included the first five interlayer spacings and rippling within mixed CuPt layers and in pure Cu layers (when allowed by symmetry). The range of rippling amplitudes considered was ±0.2Å which is in excess of the difference in metallic radius between Pt and Cu of 0.11Å. Layer spacings were also allowed to vary by ±0.3Å from the bulk Cu value of 1.805Å, which represents a variation of 17% with respect to the bulk interlayer spacing. To preserve the experimentally observed 4-fold rotational symmetry observed in the LEED pattern, calculations were performed for two domains rotated by 90^0 and co-added where appropriate.

Table 1 illustrates the results of this screening stage of the analysis. The results collated in table 1 clearly illustrate that the favoured model consists of a mixed c(2x2) CuPt underlayer capped by a pure Cu monolayer (R_p=0.25). Of all models tested, only two give a comparable level of agreement and consist of Cu_3Pt $L1_2$ like structures with the ordered CuPt layers extending deeper in-to the selvedge. Slabs of Cu_3Pt like structure of four and six atomic layers thick both yield Pendry R-factors of 0.29, which lie just on the limit of acceptable structures based on the RR-value

for the favoured structure of 0.04. The four layer thick Cu_3Pt slab has what initially appears to be an advantage: it corresponds to a net Pt loading of 1.0ML, in agreement with the experimental coverage calibration. However, as the favoured model based on the Cu/CuPt/Cu/Cu/Cu stacking sequence contains only 0.5ML Pt, hence there exists the potential to further increase the level of agreement by distributing additional Pt as a substitutionally disordered alloy within Cu layers within the LEED probing depth .

Table 1: Minimum Pendry R-factors for stacking patterns tested in the initial screening stage of the analysis. In each case the total Pt loading is given. All mixed CuPt layers were assumed to be chemically ordered with a c(2x2) periodicity.

Θ_{Pt}(ML)	Stacking pattern	R_P
0.5	PtCu / Cu / Cu / Cu / Cu	0.51
0.5	Cu / PtCu / Cu / Cu / Cu	0.25
1	PtCu / Cu / PtCu / Cu / Cu	0.53
1	Cu / PtCu / Cu / PtCu / Cu	0.29
1	PtCu / PtCu / Cu / Cu / Cu	0.51
1	Cu / PtCu / PtCu / Cu / Cu	0.45
1.5	PtCu / Cu / PtCu / Cu / PtCu / Cu	0.53
1.5	Cu / PtCu / Cu / PtCu / Cu / PtCu	0.29
1.5	PtCu / PtCu / PtCu / Cu / Cu / Cu	0.55
1.5	Cu / PtCu / PtCu / PtCu / Cu / Cu	0.46

Two structures were selected for final structural optimisation corresponding to stacking sequences Cu/CuPt/Cu/Cu/Cu/Cu (model A) and Cu/CuPt/Cu/CuPt/Cu/Cu (model B). The modelling of Pt atoms in the disordered substitutional alloy layers was achieved through application of the ATA approximation [12]. In this final refinement stage the Pt and Cu phase shifts utilised were also re-calculated for a models consisting of an ordered c(2x2) CuPt underlayer alloys. Total Pt loadings in the coverage range between 0.50 and 1.8 ML were considered, with the excess Pt distributed in layer 1, 3 and 4 in steps of 10 at % (model A) and in layers 1 and 3 (model B) again in steps of 10 at %. For each compositional profile tested, the tensor LEED allowed a full geometrical optimisation. Addition of extra Pt within the model B structure did not lead to any significant decrease in R_p below the value of 0.29 obtained for the ideal stacking sequence. In contrast the R-factor for model A was reduced from 0.25 to 0.20 leaving this model alone as the clearly favoured structure.

Figure 1 illustrates schematically the favoured geometry and layerwise compositional profile and corresponds to a Pt coverage of 1.1±0.6ML. Figure 2 illustrates the level of theory-experiment agreement obtained, corresponding to a Pendry R-factor of 0.20. Non structural parameters included Debye temperatures of 155K for Pt and 300K for Cu and an imaginary part of the inner potential of -5eV.

Incorporation of such large quantities of Pt in-to the outermost four atomic layer slab yields an average stoichiometry close to Cu_3Pt. Due to the larger metallic radius of Pt, it is possible that Pt induces an in-plane lateral expansion, however no experimental evidence was found for Pt-induced in-plane expansion. Sharp circular LEED spots were always obtained with the in-plane periodicity of the c(2x2) surface alloy being identical to that of Cu{100} within the resolution of the measurements. In order to further examine whether lateral relaxation leads to an increased level of theory-experiment agreement, a series of calculations were performed in which the in-plane spacing was increased in steps of 0.03Å (≈1% of the Cu-Cu in-plane nearest neighbour separation). While small (1%) expansions yielded no significant change in R_p expansions of 2% or more led to a monotonic increase in the R-factor, with expansions in equal to or in excess of 3% being outside the Pendry RR value of 0.04. Thus, any Pt-induced lateral expansion must be below 2% (≈0.05Å).

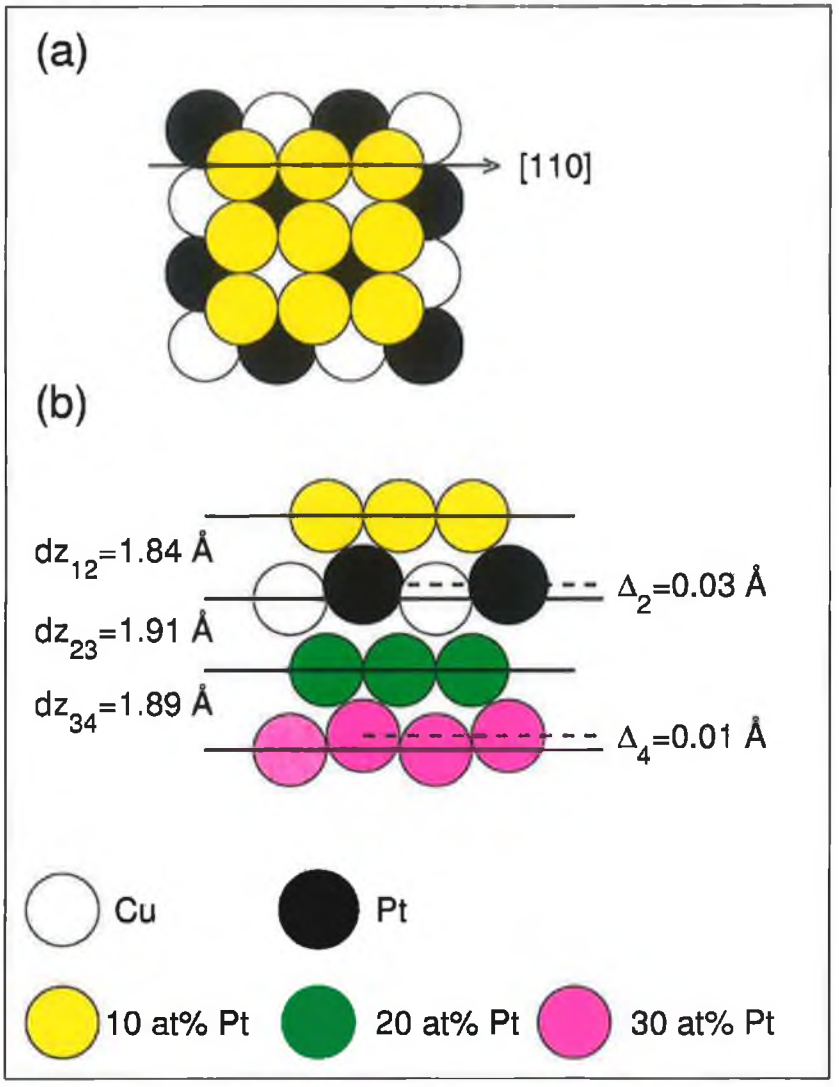

Figure 1: Model of the favoured geometry for the Cu{100}-c(2x2)-Pt surface alloy : (a) top view (outermost two layers only shown); (b) side view along the [110] azimuth defining the major geometric parameters varied within the analysis (the buckling in layers 2 and 4 is over-emphasised for clarity as is the z-spacing between adjacent layers). Note that the second and fourth layers are out of plane with respect to the pure copper layers.

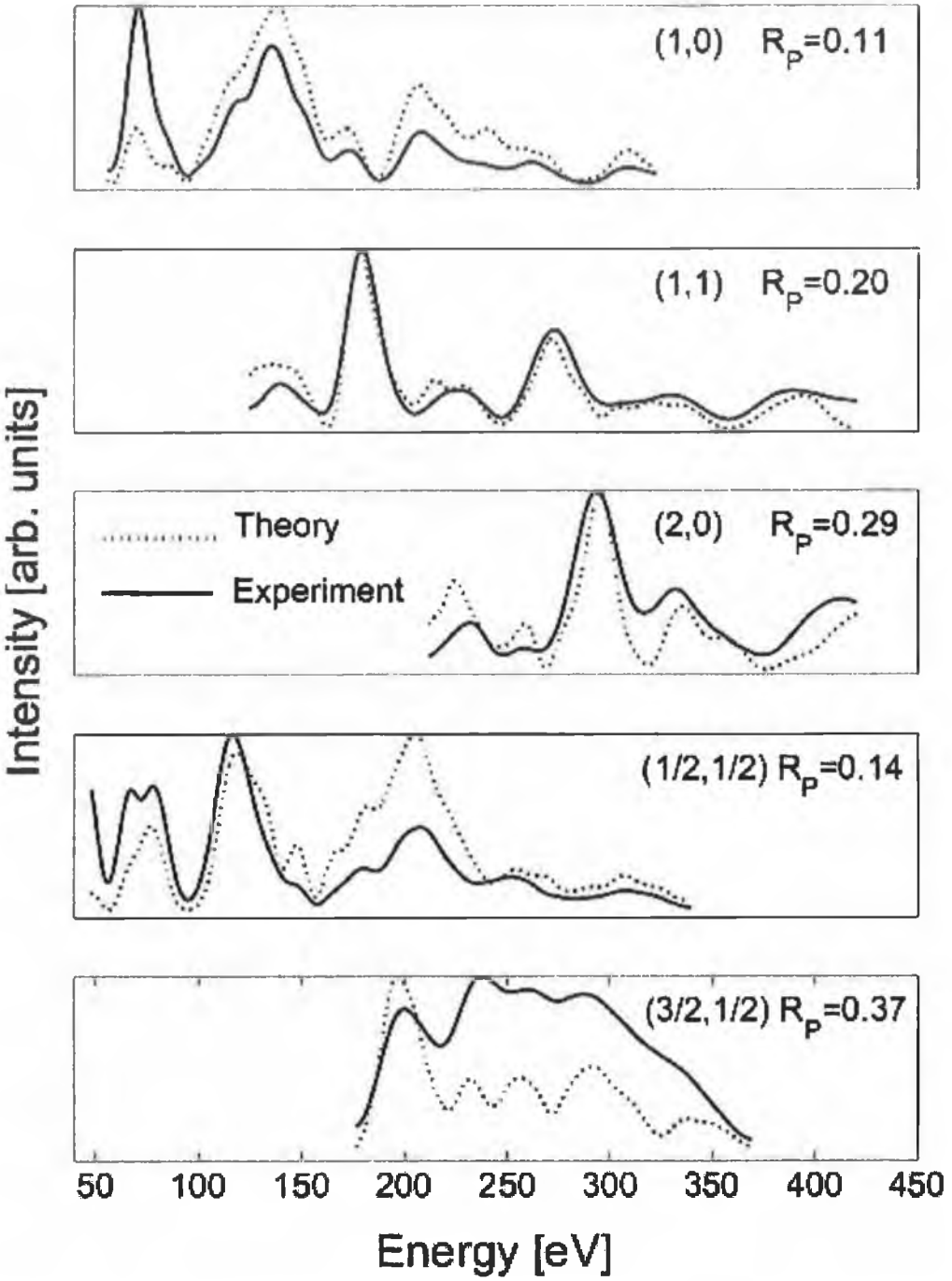

Figure 2: Optimal theory-experiment agreement. Experimental data is shown as full lines and theory as dotted lines.

Figure 3 illustrates the response of the Pendry R-factor to the main geometric variables, including the first three interlayer spacings and the buckling within the mixed CuPt monolayer (layer 2) with all other structural and non-structural variables held at their optimal values.

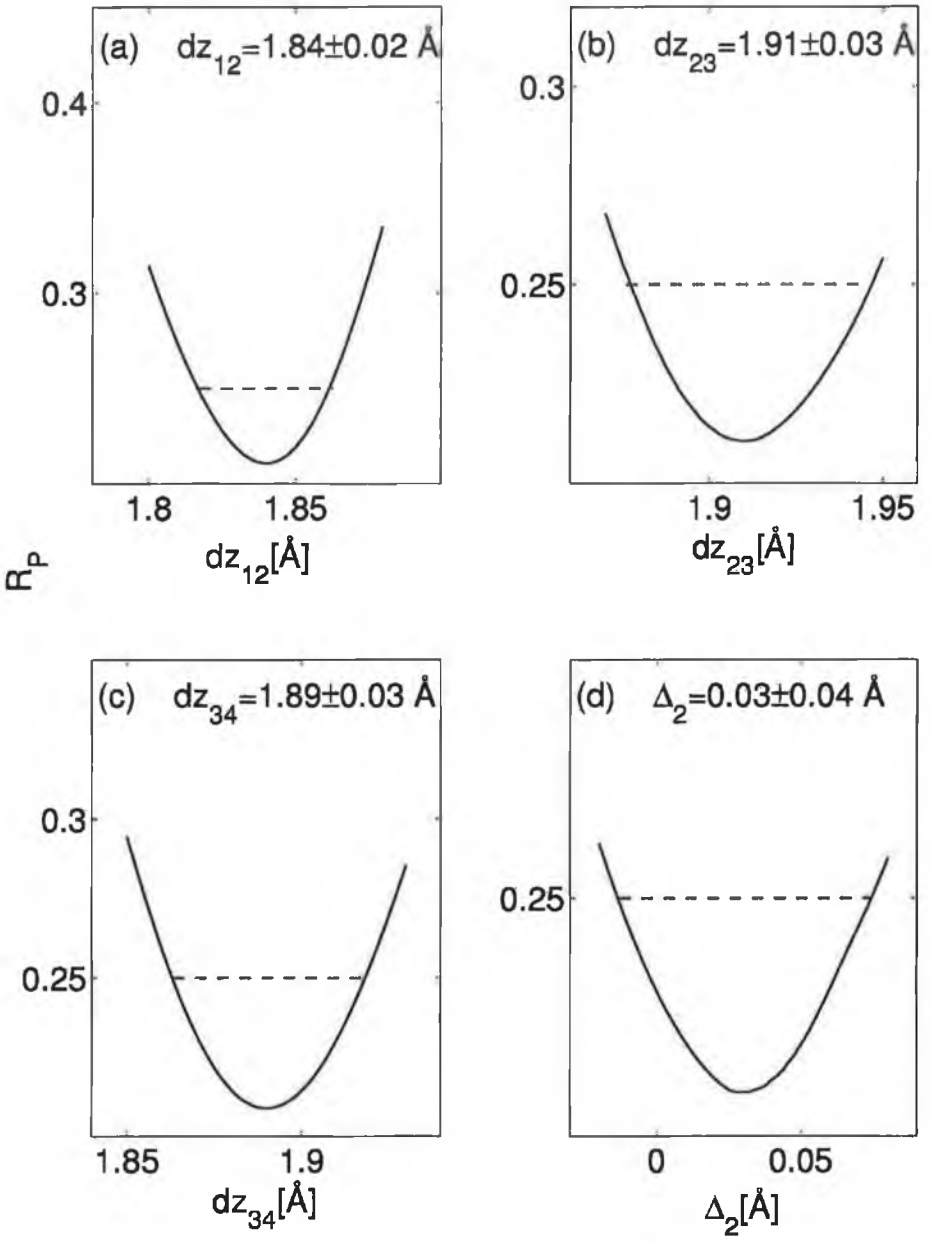

Figure 3: Variation of the Pendry R-factor with the first three interlayer spacings and buckling in the mixed CuPt second layer. Positive buckling amplitudes correspond to Pt atoms rippled outwards towards the solid-vacuum interface. The optimal value for each parameter along with the associated error is given at the top of each panel.

The optimal value for each parameter is given at the top of each panel along with the estimated error. Substitution of Pt into the outermost four atomic layers leads to a significant expansion of the outermost three interlayer spacings, particularly dz_{23}, which is expanded to 1.91 Å (+5.8%). A small Cu-Pt buckling amplitude of 0.03±0.04Å occurs in the ordered mixed c(2x2) CuPt underlayer, with Pt rippled outwards towards the vacuum interface.

The layer spacings within the surface alloy are strongly modified from those of pure copper: the structure of the clean Cu{100}-(1x1) surface determined for the same Cu{100} sample used in this study yielded a first layer contraction of −1.0±1.5% and a second layer expansion of +1.2±1.5% with third and deeper layers at their bulk truncated positions (R_p=0.15) [13]. Confining Pt two-dimensionally to a Cu{100} lattice leads to a 17% increase in the effective Pt two-dimensional density. The surface alloy may be expected to relieve the lattice strain by an expansion of the layer spacing in the z-direction. This effect would be expected to be considerably less than 17%, as such a large interlayer spacing increase would lead to significant Cu-Cu bond weakening. A compromise will be adopted, as was recently found in the case of a Cu{100}-c(2x2)-Pd underlayer alloy structure [14]. In the case of the Cu{100}-c(2x2)-Pd underlayer alloy a net expansion relative to clean Cu{100} of the outermost three layer slab of 0.18Å (6%) resulted [14], compared to the value of 0.14Å (8%) in the case of Cu{100}-c(2x2)-Pt-1ML structure.

The composition profile adopted appears to be driven by the tendency of the system to form a layerwise composition profile similar to that of the {100} surface of a Cu_3Pt $L1_2$ bulk alloy which consists of alternate pure Cu and mixed c(2x2) CuPt layers with a Cu terminated surface [7]. While layers 2 (50 at%) and layer 4 (30±30 at%) have high Pt concentrations and layer 1 a very low Pt content (10±10 at%) as expected, a considerable quantity of Pt is located in layer 3 (20±20 at%) which would correspond to a pure Cu layer in a Cu_3Pt{100} bulk alloy. Formation of the surface alloy requires interdiffusion of significant quantities of Pt from the Cu/Pt interface through many copper layers. It is thus perhaps not unsurprising that quantities of Pt are kinetically trapped in layer 3. As transport of Pt from layer 3 to 4 corresponds to a bulk interdiffusion process, minimising the Pt concentration in layer 3 competes with loss of Pt from layer 4 deeper into the bulk of the sample, thus

making it extremely difficult to prepare a Cu{100}-c(2x2)-Pt surface alloy with a perfect layerwise composition. While the favoured Pt loading determined by ATA analysis of 1.1±0.6ML agrees rather well with the experimental estimated of 1ML based on the methodology of Reilly et al [6], the relative insensitivity of LEED to layerwise composition even for a relatively favourable bimetallic combination such as Cu and Pt leads to a correspondingly large uncertainty in the exact Pt loading.

Figure 4 illustrates a plot of the Pendry R-factor as a function of the concentration of Pt in layers 3 and 4, demonstrating this rather weak sensitivity of the analysis to the layerwise composition. In order to test the reliability of the analysis to the details of the layerwise composition, a second experimental data set was collected. The experimental data consisted of the same beams as the original analysis and a slightly larger data range of 1500eV. The layerwise composition, geometric parameters and non-structural parameters were optimised based on the favoured model illustrated in figure 1. Table 2 illustrates the results of the two analyses. There is excellent agreement both in terms of structural parameters such as interplanar spacings and buckling amplitudes and the layerwise Pt concentration extracted via ATA analysis. The only significant difference is in outermost layer composition for which analysis of the second data set favours a pure Cu layer outermost, although both analyses fall within the estimated error of 10 at% for the outermost layer composition. This appears to suggest that the structure and compositional profile of the Cu{100}-c(2x2)-Pt-1ML alloy may be formed rather reproducibly.

A copper capped geometry is in full agreement with the ion scattering studies of Graham et al [5] who have determined the surface of a Cu{100} doped with Pt and thermally processed to 525K to be essentially copper terminated up-to Pt loadings of 1ML. Copper capping is clearly favoured based on surface energy considerations due to the significantly lower surface energy of Cu{100} (2.17 Jm^{-2}) compared to that of Pt{100} (2.73 Jm^{-2}) [15]. This difference is further enhanced if the surface energy per surface Cu or Pt atom is considered due to the higher atomic density adopted by Cu{100} compared to Pt{100}.

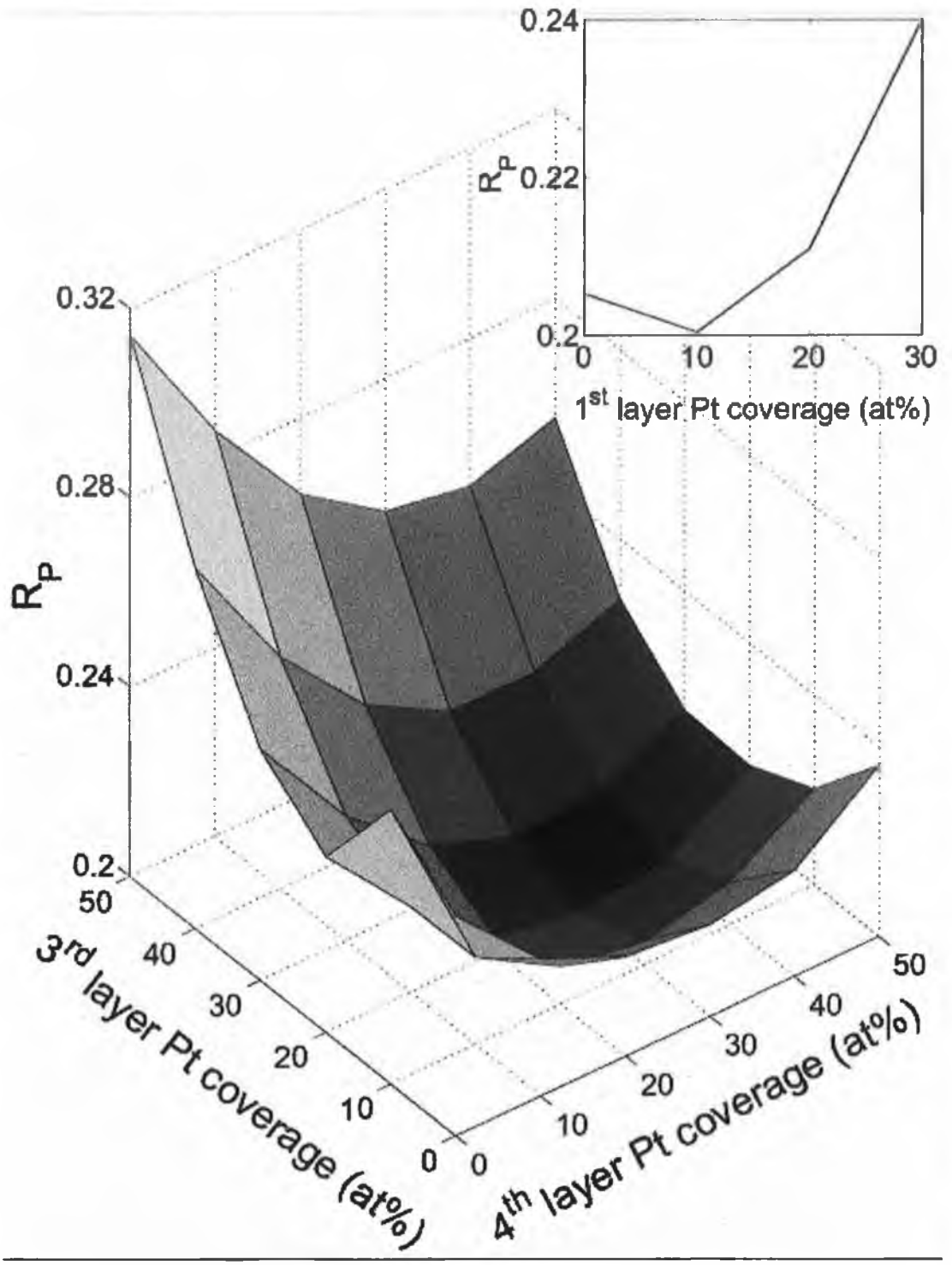

Figure 4: Variation of the Pendry R-factor with layerwise Pt concentrations in layer 3 and 4 with all structural parameters held at their favoured values and the first layer concentration held at the optimal value of 10 at%. The inset at the top of the figure illustrates the response of the Pendry R-factor to the outermost layer composition, again with all structural parameters held at their optimal values and third and fourth layer Pt compositions at 20 and 30 at% respectively.

Table 2: Comparison of geometric parameters and layerwise Pt concentration for the favoured model illustrated in figure 1 obtained from two independently prepared Cu{100}-c(2x2)-Pt (1ML) surfaces. Layer spacings are quoted with respect to copper atom positions in mixed CuPt layers.

Parameter	Data set 1	Data set 2	Average
dz_{12}(Å)	1.84	1.86	1.85
dz_{23}(Å)	1.91	1.91	1.91
dz_{34}(Å)	1.89	1.86	1.88
Δ_2(Å)	0.03	0.03	0.03
$(\Theta_{Pt})_1$(at%)	10	0	5
$(\Theta_{Pt})_3$(at%)	20	20	20
$(\Theta_{Pt})_4$(at%)	30	30	30

Reports of formation of a Cu{100}-c(2x2)-Pt surface alloy with Pt loading of 1ML via annealing to the lower temperature of 450K in which significant quantities of Pt are present in both layer 1 (46 at%) and layer 2 (41 at%) clearly indicate the possibility of formation of a second metastable ordered surface alloy [5] consisting of two adjacent c(2x2) CuPt layers with a mixed CuPt termination. However the primary technique involved in this study was LEISS which is primarily sensitive to atomic composition, it is also possible that the structure corresponds simply to a heterogeneous surface consisting of domains of Cu terminated c(2x2) CuPt underlayer co-existing with areas of Pt clusters in the correct ratio to yield the measured top layer composition. Further work is required using both TLEED-ATA and chemical probes of the top layer local composition to establish the identity of the intermediate Cu{100}-c(2x2)-Pt phase reported by Shen and co-workers [16].

5. Conclusions

A Cu{100}-c(2x2)-Pt surface alloy structure formed by deposition of 1ML of Pt and thermal processing to 550K is shown to correspond to a copper capped bimetallic surface localised alloy with a sub-surface ordered c(2x2) CuPt layer. The layerwise compositional profile has been extracted via ATA modelling resulting in an almost pure outermost copper monolayer with only a small Pt impurity concentration (10±10 at%). Layers 3 and 4 contained higher Pt concentrations of 20±20 and 30±30 at% respectively.

Substitution of platinum into the selvedge results in a significant expansion in the surface interlayer spacings relative to clean Cu{100} and switches the weak oscillatory relaxation of clean Cu{100} to a strongly and non-uniformly expanded interlayer separation. The outermost three interlayer spacings are strongly expanded by 1.84±0.02Å (+1.9±1.1%), 1.91±0.03Å (+5.8±1.7%) and 1.89±0.03Å (+4.7±1.7%) respectively. A slight rippling in the c(2x2) CuPt underlayer of amplitude 0.03±0.04Å, with Pt atoms rippled outwards towards the vacuum interface within the composite layer occurs.

References

[1] U.Bardi, Rep.Prog.Phys 57 (1994) 939.

[2] P.Praserthdam and T.Majitnapakul, Appl.Catal.A 108(1) (1994) 21.

[3] J.Yoshinbu and M.Kawai, J.Chem.Phys 103 (1995) 3220.

[4] G.W.Graham, P.J.Schmitz and P.A.Thiel, Phys.Rev.B 41 (1990) 3353.

[5] Y.G.Shen, J.Yao, D.J.O'Connor, B.V.King and R.J.MacDonald, Solid State Commun, 100 (1996) 21.

[6] J.P.Reilly, D.O'Connell and C.J.Barnes, J.Phys: Condensed Matter 11 (1999) 8417.

[7] Y.G.Shen, D.J.O'Connor and K.Wandelt, Surf.Sci. 406 (1998) 23.

[8] H.L.Davis and J.R.Noonan, J.Vac.Sci.Technol 20 (1981) 842 .

[9] M.A.Van Hove, W.Moritz, H.Over, P.T.Rous, A.Wander, A.Barbieri, N.Materer, U.Starke and G.A.Somorjai, Surf.Sci.Rep 19 (1993) 191.

[10] N.W.Ashcroft and N.D.Mermin, Solid State Physics , CBS Publishing, Japan, 1981.

[11] J.B.Pendry, J.Phys.C:Solid State Physics 13 (1980) 937.

[12] Y.Gauthier and R.Baudoing, in "Segregation and Related Phenomena" Editors: P.Dowben and A.Miller, CRC Press, Boca Raton (1990) p169.

[13] E.AlShamaileh and C.J.Barnes, submitted to Phys.Rev.B.

[14] C.J.Barnes, E.AlShamaileh, T.Pitkanen, P.Kaukasoina and M.Lindroos, Surface Science 492 (2001) 55.

[15] L.Vitos, A.V.Ruban, H.L.Skriver and J.Kollar, Surf.Sci. 411 (1998) 186.

[16] C.J.Barnes and E.AlShamaileh, work in progress.

CHAPTER 5

Adsorption of Semi-Metals on Cu{100}: LEED Structural Studies of the Cu{100}/Bi and Cu{100}/Sn Systems

LEED Investigation of the Alloying/De-alloying Transition in the Cu{100}/Bi system

E. AlShamaileh and C.J. Barnes

School of Chemical Sciences and National Centre for Plasma Science and Technology (NCPST), Dublin City University, Dublin 9, Ireland

Abstract

The surface structures formed by deposition of 0.25 ML and 0.50 ML Bi on Cu{100} at room temperature have been determined quantitatively using the Symmetrised Automated Tensor Low Energy Electron Diffraction (SATLEED). At θ_{Bi}=0.25 ML, Bi forms a partially ordered p(2x2) surface alloy with the Bi atoms located 0.56±0.06 Å with respect to centre of gravity of the buckled outermost Cu layer (buckling amplitude=0.11 Å). The interlayer spacing in the first three substrate layers are found to be: d_{12}=1.71±0.06 Å, d_{23}=1.82±0.06 Å, d_{34}=1.81±0.06 Å (d_{bulk}=1.807 Å). The first and the third Cu layers are found to be buckled by 0.11±0.06 Å and 0.05±0.06 Å, respectively. At higher Bi coverage, de-alloying of Bi atoms occurs culminating in formation of a well ordered c(2x2) overlayer at θ_{Bi}=0.50 ML. Bi atoms occupy the four-fold hollow sites with a vertical Bi-Cu interlayer separation of d_{Bi-Cu}=2.17±0.06 Å above a slightly perturbed substrate. The interlayer spacing in the first four substrate layers are found to be: d_{12}=1.82±0.03 Å, d_{23}=1.80±0.03 Å and d_{34}=1.84±0.03 Å. A small buckling of 0.02±0.02 Å is detected in the second Cu layer in which Cu atoms below Bi atoms are rippled outwards. The structures obtained by LEED are compared to those evaluated recently for the same system by surface X-ray diffraction.

1. Introduction

The room temperature adsorption of Bi on Cu{100} has been the subject of several studies using different techniques [1-5]. Delamare and Rhead first observed four ordered superstructures in the submonolayer Bi coverage regime [1]. The structures were designated p(2x2), c(2x2), c(9√2x√2) and (√41x√41) corresponding to Bi coverages of 0.25, 0.50, 0.56 and 0.60 ML respectively. While the three higher coverage phases may be reproducibly prepared, the low coverage, p(2x2) phase was not reported in some later studies [2,4]. Blum et al. have also observed a p(2x2) LEED pattern at low Bi coverage for room temperature adsorption which they interpreted as the result of the coexistence of c(2x4) and c(4x2) domains with a small fraction of the c(2x2) phase [3].

Recently, the surface geometric structure of Cu{100}/Bi system was studied by surface X-ray diffraction (SXRD) [4]. The study reported that Bi forms a substitutionally disordered Bi/Cu surface alloy up-to a coverage of ~0.35 ML, while Bi de-alloying takes place above this coverage leading to the formation of a well ordered Cu{100}-c(2x2)-Bi overlayer structure at 0.50 ML. At Bi coverages below ~0.35 ML, Bi atoms substitute into the Cu atoms located at 0.61±0.01 Å above the surface causing a 3-4% expansion of the first Cu interlayer spacing. At the higher Bi coverage of 0.50 ML, Bi is found to adsorb in the four-fold hollow sites above the Cu{100} surface with Cu-Bi vertical interlayer separation of 2.18±0.08 Å and a contraction of 1.5% in the first Cu interlayer spacing.

Dynamical LEED I(V) analysis is considered as one of the most accurate and widely used techniques of surface structure determination [6-7]. Most recently, the applications of Symmetrised Automated Tensor Low Energy Electron Diffraction (SATLEED) calculations have proved to be fast and reliable for structure determination often involving rather complex structures [8-10].

In the present study, we used SATLEED to determine the surface structures of the c(2x2) and the p(2x2) phases of Cu{100}/Bi, investigating the room temperature alloying/de-alloying phenomena and including the possibility of Bi-induced substrate distortions.

2. Experimental

The measurements were carried out in an ion and titanium sublimation pumped ultrahigh vacuum chamber with base pressure ≤ $2x10^{-10}$ Torr described in more detail elsewhere [11]. The system was equipped with facilities for low-energy electron diffraction (LEED), Auger electron spectroscopy (AES), and thermal desorption spectroscopy (TDS).

The Cu sample of dimensions 15x10x1.5 mm was cut to within 0.5° of the {100} plane. The sample mounting and cleaning procedure have been described elsewhere [11]. High purity bismuth (6N) was enclosed in a tantalum boat wrapped with a tungsten coil for resistive heating. The bismuth evaporator was equipped with a quartz crystal thickness monitor for monitoring the Bi deposition rate. The deposition of Bi onto the substrate, held close to room temperature, resulted in LEED patterns in excellent agreement with those reported in the literature [1,3]. The Bi coverage was calibrated by monitoring the intensity of the (1/2,1/2) fractional-beam and the (1,0) integral-beam during evaporation at a fixed beam energy of 70 eV. The evaporation time required to bring the c(2x2) to maximum perfection is determined from the time needed to maximise the half-order beam intensity and this coverage is set to 0.50 ML. This technique has been successfully applied to coverage monitoring of various systems [23,24]. The transition from the c(2x2) phase to the complex c(9√2x√2)R45° phase occurs in the narrow coverage window of 0.50-0.56 ML [5]. Hence, it was straightforward to obtain a coverage calibration upon assumption of coverage-independent sticking probability at room temperature. This assumption has been used earlier for this system for the same purpose [1]. The Bi deposition rate used was ~0.05 ML per minute giving an estimated Bi coverage error of ±0.02 ML. The LEED pattern of the p(2x2) phase exhibited very weak and diffuse fractional order diffraction beams with a noticeably high background.

LEED I(V) spectra were collected at room temperature using a CCD camera and a data acquisition system supplied by Data Quire Corporation. All spectra used in calculations were measured at normal incidence, which was attained by careful visual comparison of (1,0) symmetrically equivalent beams, in the electron energy range of 40-480 eV. For all systems studied, two independent sets of data were collected and compared to ensure reproducibility while one complete set only was used in the analysis.

Six non-symmetric beams were used in the analysis giving a total energy range of 1380 eV for the Cu{100}-c(2x2)-Bi phase and 1356 eV for the Cu{100}-p(2x2)-Bi phase. The total energy range for the clean Cu{100} was 1250 eV. Beams were individually background-subtracted and symmetry-equivalent beams were averaged to reduce errors resulting from small deviations from normal incidence and residual magnetic fields. In case of the diffuse I(V) data, a careful background subtraction of the diffusely scattered intensity from clean Cu{100} under identical experimental conditions was applied to remove diffuse spectral structure from defects in the Cu{100} sample and phonon related diffuse scattering. This procedure is similar to that successfully adopted in previous diffuse I(V) studies [26-28]. In this case, no 1/E scaling of experimental spectra was performed to account for the increase in the area of reciprocal space sampled with increasing energy as the p(2x2) was considered "semi-ordered" rather than being truly disordered [26]. Finally, the beams were normalised to constant incoming beam current and smoothed by a 5-point adjacent-averaging prior to analysis.

3. Theoretical Considerations

The LEED calculations were performed with the Barbieri/Van Hove automated tensor LEED package [13]. Ten phase shifts calculated with the Barbieri/Van Hove phase shift package [14] were used for both copper and bismuth. The use of 10 phase shifts was deemed sufficient as calculations based on a or greater number of phase shifts resulted in an identical structure without significant improvement of the Pendry reliability factor (R_p-factor) which was used to judge the theory-experiment fit [15]. The error bars quoted were estimated using the Pendry double reliability RR-factor [15].

The energy-independent real part of the inner potential ($V_{o,r}$) was optimised during the course of the theory-experiment fit. The best-fit imaginary part ($V_{o,i}$) was found to be -5.0, -6.5 and –5.5 eV for the Cu{100}-c(2x2)-Bi phase, the Cu{100}-p(2x2)-Bi phase and the clean Cu{100}, respectively.

Debye temperatures for Cu ($\theta_{D,Cu}$) and Bi($\theta_{D,Bi}$) were assumed to take the bulk values of $\theta_{D,Cu}$= 343K and $\theta_{D,Bi}$= 119K [17] in the initial analysis procedure. In the final stage of

the analysis (i.e. for the geometry optimised for the favoured adsorption sites for the c(2x2) and the p(2x2) phases) both Cu and Bi Debye temperatures were allowed to vary in order to obtain the best-fit Debye temperatures. The final Debye temperatures corresponding to the best-fit structures were found to be $\theta_{D,Cu}$=330±30 K and $\theta_{D,Bi}$=95±20 K for the c(2x2) phase and $\theta_{D,Cu}$=330±30 K and $\theta_{D,Bi}$=80±20 K for the p(2x2) phase.

4. Results and Discussion

(a) The clean Cu{100} surface

As a first step, LEED I(V) spectra were measured at room temperature for the clean Cu{100}-(1x1) substrate and the structure determined by SATLEED. Good agreement with previous literature reports was achieved represented by a best-fit Pendry R_p factor of 0.18 and similar trends of relaxation in the top two interlayer spacings [18-22]. The comparison between experimental and calculated (best-fit) LEED I(V) spectra for the clean Cu{100} is shown in Fig. 1, with the individual R_p-factor for each beam indicated. Relative to the bulk interlayer spacing value d_o=1.807 Å, the structure obtained in this study showed a contraction in the first interlayer spacing by $\Delta d_{12}/d_o$= -1.2±1.7% and an expansion in the second interlayer spacing by $\Delta d_{23}/d_o$= +1.0±1.7%. Third and subsequent interlayer spacings adopted the bulk value. Table 1 shows some previous experimental determinations of $\Delta d_{12}/d_o$ and $\Delta d_{23}/d_o$.

Table 1: Changes of the first ($\Delta d_{12}/d_{bulk}$) and second ($\Delta d_{23}/d_{bulk}$) interlayer spacings and for clean Cu{100} evaluated by LEED.

$\Delta d_{12}/d_{bulk}$	$\Delta d_{23}/d_{bulk}$	Ref.
-1.1	+1.7	[18]
-1.2	+0.9	[19]
-1.5	+0.8	[20]
-2.4	-0.1	[21]
-1.0	0.0	[22]
-1.2	+1.0	present

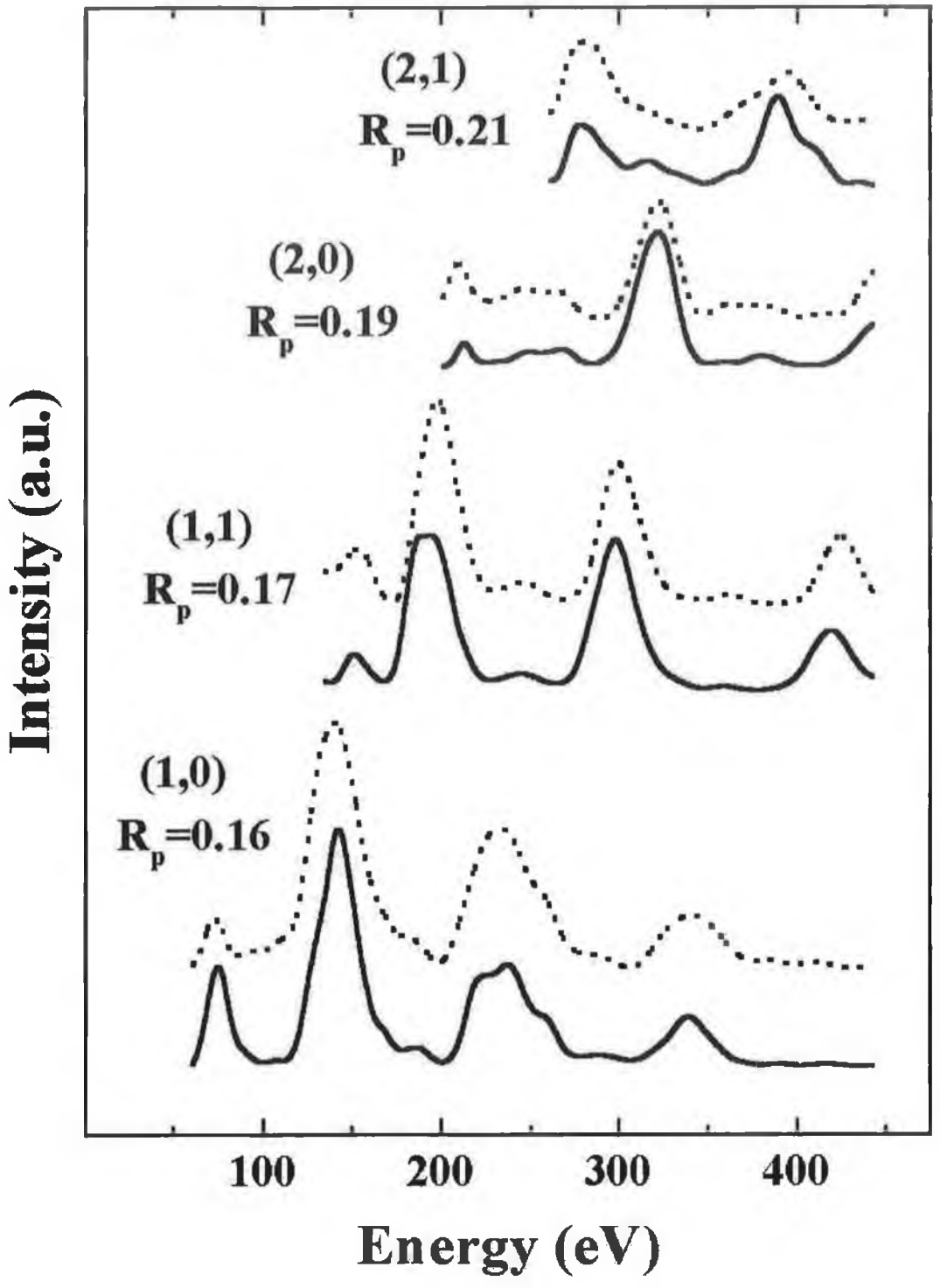

Fig. 1: Best fit comparison of experimental (solid lines) and calculated (dashed lines) LEED I(V) spectra for clean Cu{100}. Individual R_p-factor values are shown for each beam.

(b) The Cu{100}-c(2x2)-Bi structure (θ_{Bi}=0.50 ML)

The structure determination procedure for the Cu{100}-c(2x2)-Bi phase was started by comparing the experimental LEED I(V) spectra with those calculated for four different possible high symmetry adsorption sites. Fig. 2 shows a schematic of the sites tested, namely: atop, bridge, four-fold hollow, and a four-fold substitutional surface alloy site. The preliminary search was done by allowing the z-atomic co-ordinates of Bi and Cu atoms in the first four layers to be optimised with Cu interlayer spacings and in-plane separations initially fixed at bulk values. The ranges of Bi-Cu interlayer spacing investigated are indicated in table 2. Non-structural parameters other than the real part of the inner potential were kept constant for all models in the course of the initial search. As shown in Table 2, the four-fold hollow site gave a significantly better R_p-factor than all the other sites tested and hence was chosen for further refinement including allowing variation in non-structural parameters and re-optimisation of atomic positions and allowing buckling within deeper Cu layers.

Table 2: Optimum Pendry R-factors for the four Cu{100}-c(2x2)-Bi structural models shown in fig. 2. The d_{Bi-Cu} range is the vertical Bi-Cu distance limits within which the search was performed.

Adsorption site	Vertical d_{Bi-Cu} range (Å)	Optimal vertical d_{Bi-Cu} (Å)	R_p
Atop	2.50 to 3.10	2.79	0.46
Bridge	2.00 to 2.80	2.52	0.68
4-fold hollow (overlayer)	1.43 to 2.60	2.17	**0.20**
4-fold substitutional (surface alloy)	-0.10 to 0.80	0.10	0.52

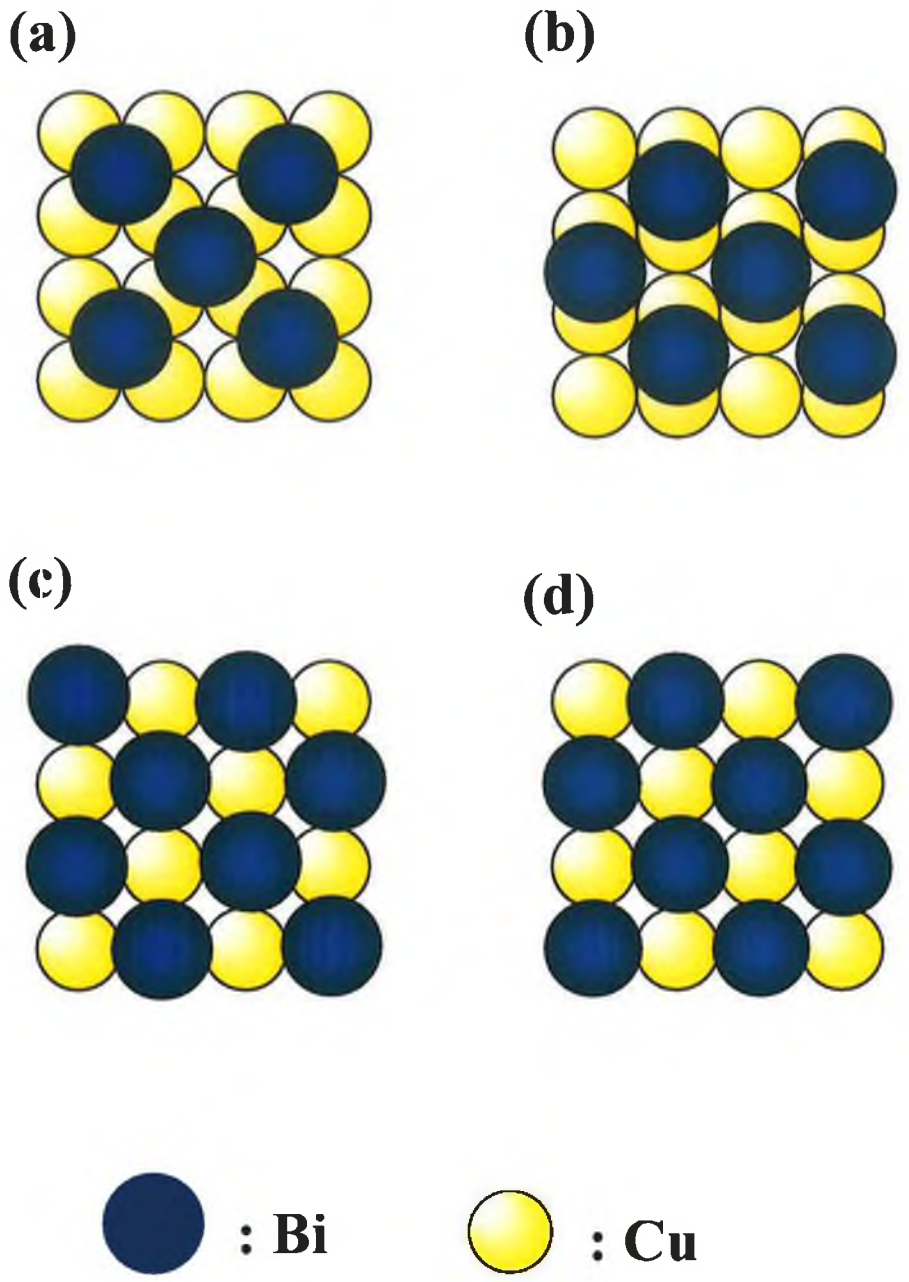

Fig. 2: Schematic diagram of four models for Cu{100}-c(2x2)-Bi structure including: (a) four-fold hollow overlayer; (b) bridge overlayer; (c) atop overlayer and (d) four-fold substitutional surface alloy. Filled circles represent Bi atoms,

Fig. 3 illustrates the comparison of experimental and calculated (best-fit) LEED I(V) spectra for the Cu{100}-c(2x2)-Bi structure using the optimum structural and non-structural parameters summarised in Table 3, yielding a minimum Pendry R-factor of 0.20. Fig. 4 illustrates the response of the Pendry R-factor to the variation of the main geometric variables, including the Bi-Cu interlayer spacing and the first three Cu interlayer spacings with all other structural and non-structural parameters held at their optimal values. The optimal value for each variable is shown at the top of each panel along with the associated error.

Table 3: Best-fit parameters for the final structure of Cu{100}-c(2x2)-Bi four-fold hollow overlayer.

Structural			
	Co-ordinates[a]		
Atom[b]	X (Å)	Y (Å)	Z[c] (Å)
Bi	1.278	1.278	-2.17 ± 0.06
Cu_1	0.000	0.000	0.00 ± 0.03
Cu_2	1.278	1.278	1.81 ± 0.03
Cu_2	-1.278	1.278	1.83 ± 0.03
Cu_3	0.000	2.556	3.62 ± 0.03
Cu_4	-1.278	1.278	5.46 ± 0.02
Cu_4	1.278	1.278	5.46 ± 0.02
Cu_5	0.000	0.000	7.27
Non-structural			
$\theta_{D,Cu}$ (K)[d]	330±30		
$\theta_{D,Bi}$ (K)	95±20		
Inner potential (eV)	-6.5 + 5 i		

[a] Values without error bars indicate that the value was not refined in the analysis but held at bulk position.

[b] Cu atom numbers correspond to substrate layer number. Note that, by symmetry, there may exist two Cu atoms exhibiting different heights in layers 2 and 4.

[c] Positive values indicate displacement towards the bulk.

[d] θ_D = Debye Temperature.

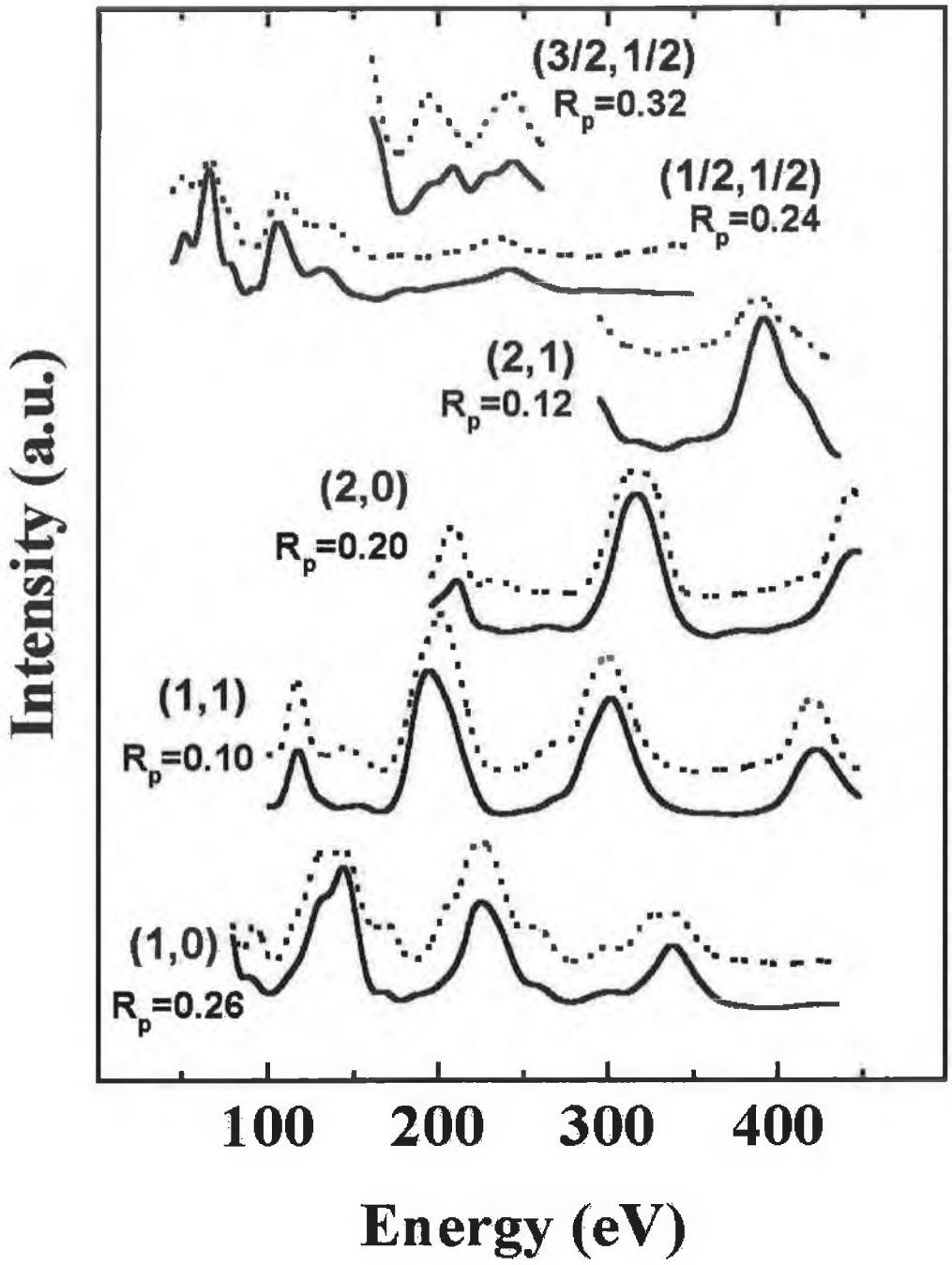

Fig. 3: Best fit comparison of experimental (solid lines) and calculated (dashed lines) LEED I(V) spectra for the Cu{100}-c(2x2)-Bi four-fold hollow overlayer model. Individual R_p-factor values are shown for each beam.

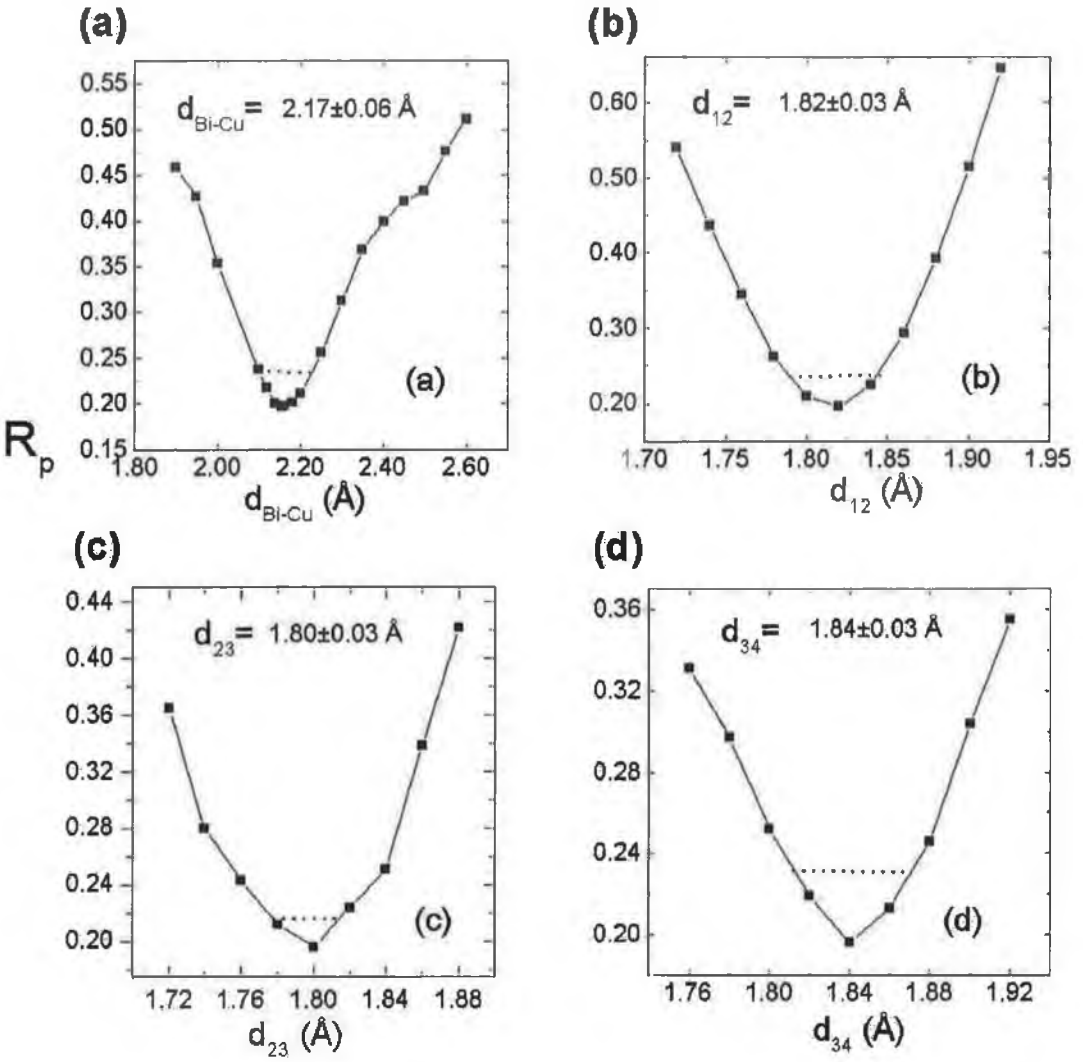

Fig. 4: Variation of the Pendry R-factor as a function of: (a) Bi-Cu interlayer spacing (d_{Bi-Cu}); (b) first Cu interlayer spacing (d_{12}); (c) second Cu interlayer spacing (d_{23}); (d) third Cu interlayer spacing (d_{34}) for the Cu{100}-c(2x2)-Bi. The optimal value for each variable is shown at the top of each panel along with the associated error.

The present model determined by full dynamical LEED I(V) analysis corresponds to an overlayer of Bi atoms adsorbed in four-fold hollow sites of a slightly perturbed Cu{100} surface. Bismuth is found to adsorb at a height above the first copper plane of 2.17±0.06 Å. The calculations show a very small rippling in the second Cu layer of 0.02±0.02 Å in which Cu atoms beneath the top layer Bi atoms are rippled outward towards the vacuum. The change of the first three Cu interlayer spacing relative to the bulk are Δd_{12}=+0.7±1.6%, Δd_{23}=-0.4±1.6%, and Δd_{34}=+1.8±1.6%.

Using SXRD, Meyerheim et al. [4] studied the c(2x2) Cu{100}/Bi phase and reported that Bi reside in the hollow site at 2.18±0.08 Å above the surface with 1.5% contraction of the first Cu interlayer spacing. Our results for the c(2x2) phase at θ_{Bi}=0.50 which give a Bi-Cu height of 2.17±0.06 Å is in excellent agreement with the SXRD result. However, the observed contraction of the first interlayer spacing was not confirmed and instead an expansion of +0.7±1.6% was retrieved which is between combined error bars. In fact it may be expected that the LEED value with its enhanced sensitivity with respect to substrate interlayer spacings provides the more accurate value in this case.

It should be noted that our c(2x2) phase was prepared by direct deposition of 0.50 ML Bi at room temperature while the SXRD c(2x2) phase was made by deposition of large amount of Bi (≥1 ML) and subsequent annealing to 500°C for 5 min. LEED I(V) data collected from phases prepared using procedures involving direct deposition at room temperature and via desorption of higher Bi coverages seemed indistinguishable, however, the data analysed in this study were taken using the room temperature direct deposition approach.

Based on a hard sphere model and assuming a Cu radius of 1.278 Å, the effective Bi radius in the c(2x2) overlayer is calculated to be 1.55±0.09 Å. The crystal structure of solid Bi is rohmbohedral, but Bi becomes more closely packed on melting with an anomalous density increase. Our result for the Bi radius comprises a 9% reduction compared to the 12-fold co-ordinate metallic radius of 1.70 Å [25]. The effective radius compares well with the literature rohmbohedral bulk Bi-Bi shortest nearest-neighbour distance of 3.10 Å [17].

The best-fit Debye temperatures (θ_D) for the c(2x2) model were found to be $\theta_{D,Bi}$=95±20 K and $\theta_{D,Cu}$=330±30 K. Fig. 5 shows the dependence of Pendry R-factor on $\theta_{D,Bi}$. From the exponential decay of the (1/2,1/2) spot intensity with sample temperature for the c(2x2) Bi/Cu{10θ} phase, Delamare and Rhead calculated a $\theta_{D,Bi}$ of 110±20 K [1] which is consistent within the error limits with our $\theta_{D,Bi}$ for the same phase. Our $\theta_{D,Cu}$ is in excellent agreement with recent LEED calculations (e.g. $\theta_{D,Cu}$=328±20 K [22]).

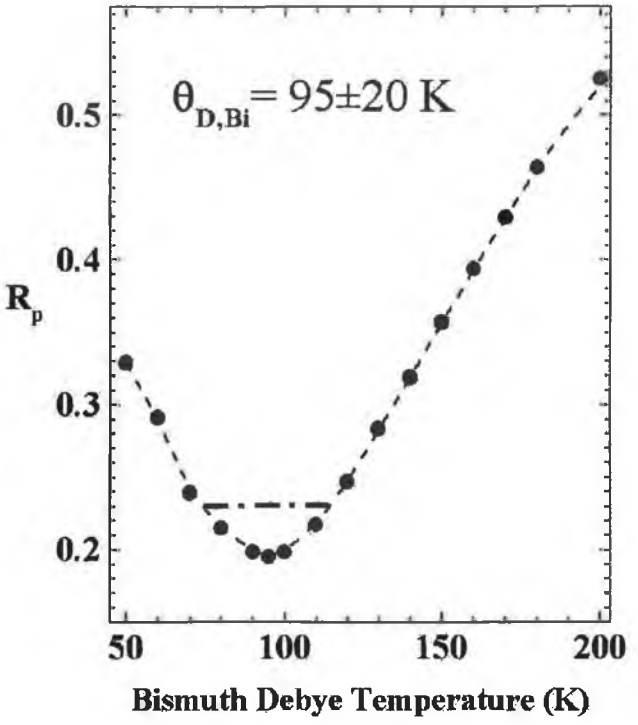

Fig. 5: Variation of the Pendry R-factor as a function of the Bi Debye temperature ($\theta_{D,Bi}$) for the Cu{10θ}-c(2x2)-Bi.

(c) The Cu{100}-p(2x2)-Bi structure (θ_{Bi}=0.25 ML)

For the p(2x2) phase, the weak (1/2,1/2) diffraction beam has an I(V) spectrum very different from the corresponding spectrum measured from the c(2x2) phase as illustrated in figs. 3 and 6. This suggests a strong variation in the local geometry surrounding the Bi adsorbate. LEED I(V) data were measured from two independently prepared p(2x2) phases by depositing 0.25 ML. Several high symmetry models of Cu{10θ}-p(2x2)-Bi have been tested allowing only the first four z-atomic co-ordinates to vary. Interestingly

and as shown in Table 4, only a surface alloy model gave good theory-experiment fit and hence further refinement of the analysis for this structure only was considered. The comparison of experimental and calculated (best-fit) LEED I(V) spectra for the Cu{100}-p(2x2)-Bi is shown in Fig. 6. The best structure retrieved is illustrated in Fig. 7. The structure found in this study by LEED I(V) analysis has a Bi-Cu vertical distance of 0.56±0.06 Å which agrees very well with the corresponding value of 0.61±0.01 Å found by SXRD [3]. The insertion of Bi atoms into the top Cu surface causes a significant rippling of 0.11±0.06 Å in the first Cu layer. A small rippling of 0.05±0.06 Å in the third Cu layer was detected in which Cu atoms underneath the surface Bi atoms are rippled away from the Bi atoms. The major relaxation was observed in the first substrate interlayer spacing and found to be a contraction of −5.3±2%.

Table 4: Pendry R-factors for the four models tested for the Cu{100}-p(2x2)-Bi low-coverage structure.

Adsorption site	Vertical d_{Bi-Cu} range (Å)	Optimal d_{Bi-Cu} (Å)	R_p
Atop	2.50 to 3.10	2.62	0.40
Bridge	2.00 to 2.80	2.80	0.59
4-fold hollow overlayer	1.43 to 2.60	2.15	0.52
4-fold substitutional surface alloy	-0.10 to 0.80	0.56	**0.29**

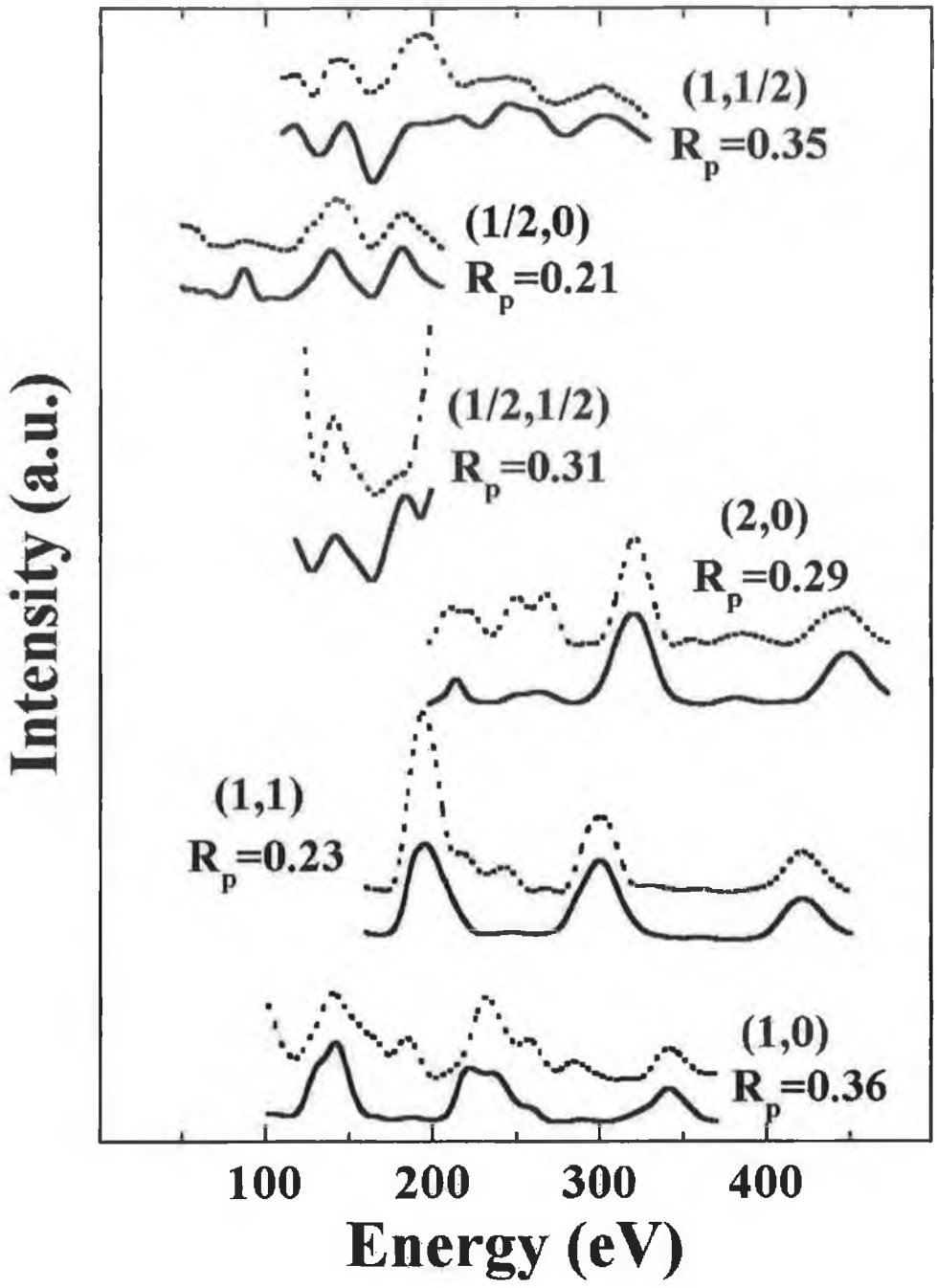

Fig. 6: Best fit comparison of experimental (solid lines) and calculated (dashed lines) LEED I(V) spectra for the Cu{100}-p(2x2)-Bi substitutional surface alloy. Individual R_p-factor values are shown for each beam.

(a)

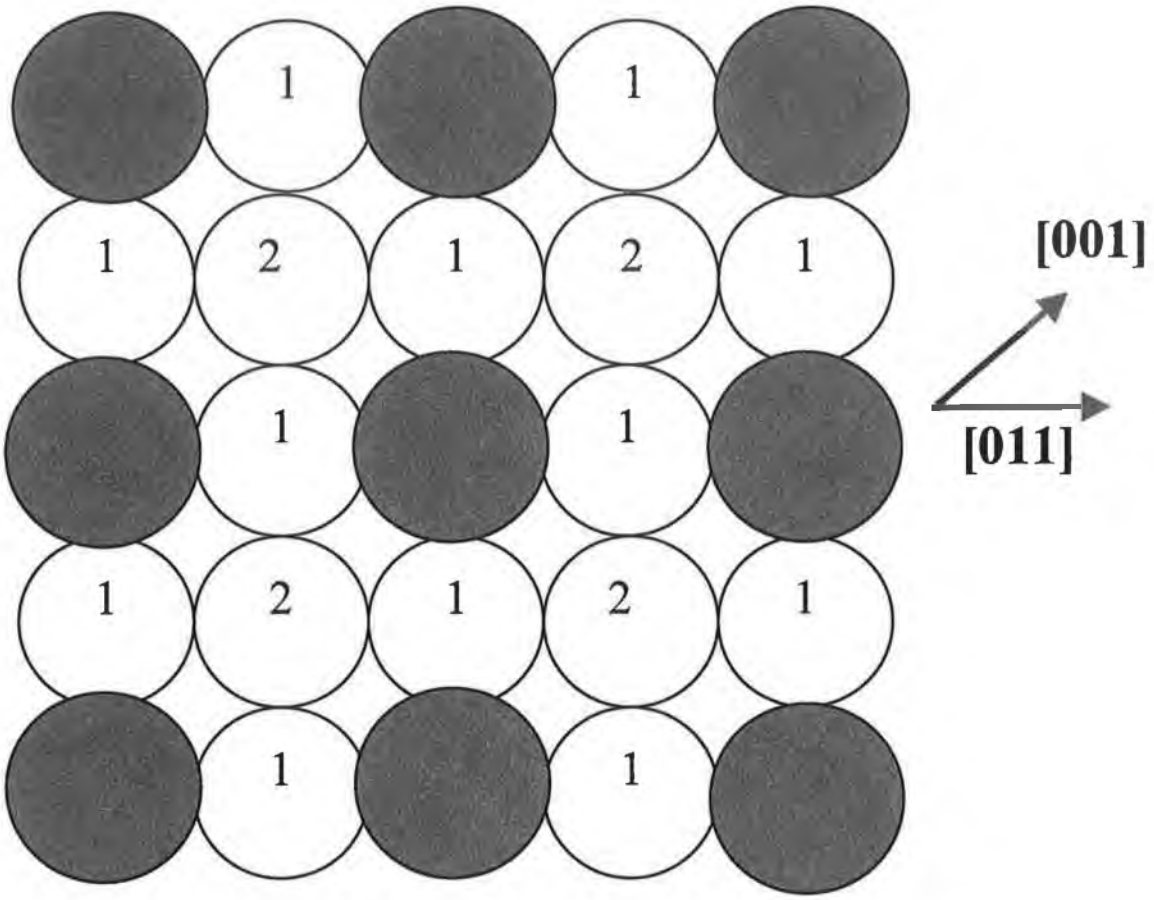

Fig. 7 (a): Top view structural model for the Cu{100}-p(2x2)-Bi substitutional surface alloy with inequivalent Cu atoms numbered.

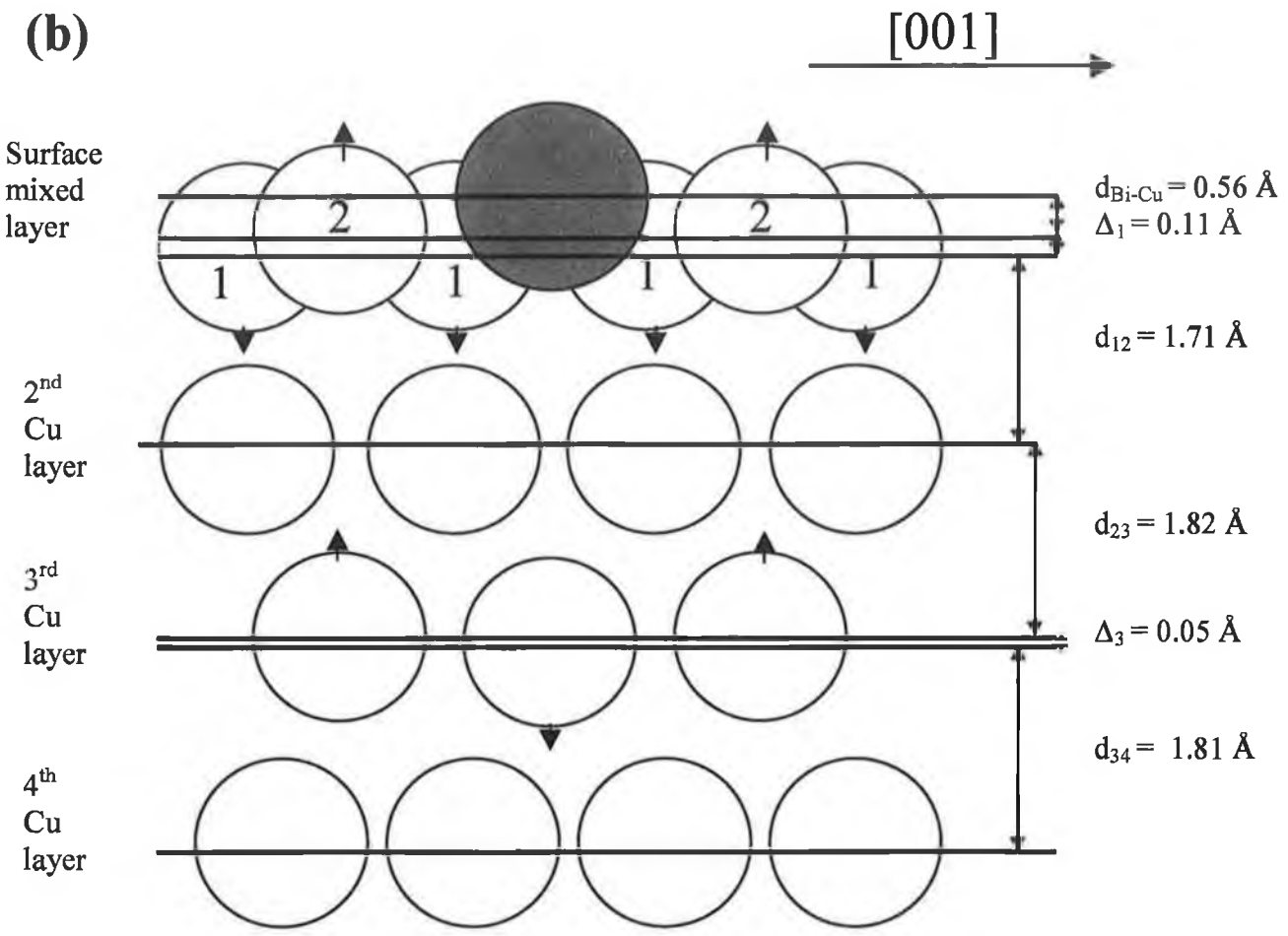

Fig. 7 (b): Side view structural model for the Cu{100}-p(2x2)-Bi substitutional surface alloy showing the best-fit geometrical parameters. The arrows indicate the rippling direction of Cu atoms in layers 1 and 3. Filled circles represent Bi atoms.

5. Conclusions

Symmetrised Automated Tensor Low Energy Electron Diffraction (SATLEED) has been used to determine the surface structures of the Cu{100}-c(2x2)-Bi and the Cu{100}-p(2x2)-Bi formed by deposition of 0.50 ML and 0.25 ML Bi on Cu{100} at room temperature. Bismuth was found to form a surface alloy at 0.25 ML with the Bi atoms located 0.56±0.06 Å outwards from the outermost Cu layer. The interlayer spacing in the first three substrate layers are found to be: d_{12}=1.71±0.06 Å, d_{23}=1.82±0.06 Å, d_{34}=1.81±0.06 Å. With increasing Bi coverage, de-alloying of Bi atoms occurs until a well-ordered c(2x2) overlayer is formed with Bi atoms occupying the four-fold hollow site with a vertical Bi-Cu interlayer separation of 2.17±0.06 Å above a slightly perturbed substrate structure. The interlayer spacing in the first four substrate layers were found to be: d_{12}=1.82±0.03 Å, d_{23}=1.80±0.03 Å, d_{34}=1.84±0.03 Å and d_{45}=1.81±0.02 Å. The structures of both the low and high coverage Cu{100}/Bi obtained in this study are in good agreement with those evaluated recently for the same system by surface X-ray diffraction and provide an enhanced precision for Bi induced relaxation with the Cu selvedge.

Acknowledgements

We would like to thank Prof. Iggy McGovern (Physics Department, The University of Dublin-Trinity College) for the loan of the Bi evaporator used in this study. E.A. would like to acknowledge the National Centre for Plasma Science and Technology (NCPST) for financial support.

References

[1] F. Delamare and G.E. Rhead, Surf. Sci., 35 (1973) 172.

[2] C. Argile and G.E. Rhead, Surf. Sci. 78 (1978) 115.

[3] B. Blum, E.W. Plummer, H.L. Davis and D.M. Zehner, J. Vac. Sci. Technol. A9 (1991) 1703.

[4] H.L. Meyerheim, H. Zajonz, W. Moritz and I.K. Robinson, Surf. Sci. Lett. 381 (1997) L551.

[5] H.L. Meyerheim, M. De Santis, W. Moritz and I.K. Robinson, Surf. Sci. 418 (1998) 295.

[6] J. B. Pendy: Low Energy Electron Diffraction, Academic Press, London, 1974.

[7] M.A. Van Hove, W.H. Weinberg, C.-M. Chan, in: Low-Energy Electron Diffraction: Experiment, Theory and Structural Determination, Springer Series in Surface Sciences, Vol. 6, Springer-Verlag, Berlin, 1986.

[8] M.A. Van Hove, W. Moritz, H. Over, P.J. Rous, A. Wander, A. Barbieri, N. Materer, U. Starke and G.A. Somorjai, Surf. Sci. Rep. 19 (1993) 191.

[9] M. Saidy and K.A.R. Mitchell, Surf. Sci. 441 (1999) 425.

[10] I. Zasada and M.A. Van Hove, Surf. Sci. Lett. 457 (2000) L421.

[11] C.J. Barnes, E. Alshamaileh, T. Pitkanen, P. Kaukasoina and M. Lindroos, Surf. Sci. 492 (2001) 55.

[13] M.A. Van Hove and A. Barbieri, Symmetrized Automated Tensor LEED Package; http://electron.lbl.gov/leedpack/ leedpack.html.

[14] A. Barbieri and M.A. Van Hove, Phase Shift Program Package; http://electron.lbl.gov/leedpack/leedpack.html.

[15] J.B. Pendry, J. Phys. C. 13(1980)937.

[16] B. Narloch and D. Menzel, Surf. Sci. 412/413(1998)562.

[17] C. Kittel, Introduction to Solid State Physics (John Wiley & Sons, New York, 1986).

[18] H.L.Davis and J.R. Noonan, J. Vac. Sci. Technol. 20 (1982) 842.

[19] D.M. Lind, F.B. Dunning, G.K. Walters and H.L. Davis, Phys. Rev. B 35 (1987) 9037.

[20] F. Jona, Surf. Sci. 192 (1987) 398; F. Jona, P. Jiang and P.M. Marcus, Surf. Sci. 192 (1987) 414.

[21] S. Muller, A. Kinne, M. Kottcke, R. Metzler, P. Bayer, L. Hammer and K. Heinz, Phys. Rev. Lett. 75 (1995) 2859.

[22] A. Mikkelsen and D.L. Adams, Phys. Rev. B 60 (1999) 2040.

[23] M. Valden, J. Aaltonen, M. Pessa, M. Gleeson and C.J. Barnes, Chem. Phys. Lett. 228(1994)519.

[24] J.P. Reilly, Ph.D. thesis, Dublin City University (2000).

[25] N.W. Alcock, Bonding and structure: structural principles in inorganic and organic chemistry, Ellis Horwood, New York, 1990.

[26] K. Heinz, U. Starke and F. Bothe, Surf. Sci. Lett. 243(1991)L70.

[27] C. J. Barnes, A. Wander and D.A. King, Surf. Sci. 281(1993)33.

[28] C. J. Barnes, E. AlShamaileh, T. Pitkanen and M. Lindroos, Surf. Sci. 482(2001)1425.

A Re-Interpretation of the Cu{100}/Sn Surface Phase Diagram

E. McLoughlin[a], A.A.Cafolla[a,c,*], E.AlShamaileh[b] and C.J.Barnes[b,d,]

[a] School of Physical Sciences,

[b] School of Chemical Sciences,

[c] National Centre for Sensor Research (NCSR),

[d] National Centre for Plasma Science and Technology (NCPST),

Dublin City University, Glasnevin, Dublin 9, Ireland.

Abstract

The coverage dependent structural phase transitions of Sn on Cu{100} have been re-examined by Low Energy Electron Diffraction (LEED). Double scattering LEED pattern simulations have been applied both to a range of possible new models and to previously suggested structures with the aim of identifying the most likely surface geometries throughout the sub-monolayer coverage regime. A model consistent with both the Sn surface coverage and the complex split beam LEED pattern observed has been suggested for the low coverage (θ_{Sn} = 0.21 ML) ordered phase based on a p(2×2) structure with "light" antiphase domain walls. We also demonstrate that higher coverage p(2x6) (θ_{Sn} = 0.37 ML) and p(3√2×√2)R45^0 (θ_{Sn} = 0.50 ML) structures based on c(2×2) local periodicity yield a consistent explanation of the higher coverage LEED data. While the simulations identify likely structures, the limitations of this approach mitigate against definitive structural assignments. However Simulations for models based on c(2×2) structures incorporating defects in the form of periodic density modulations combined with substrate reconstruction lead to an enhanced agreement with observed LEED data compared to overlayer models previously suggested.

1. Introduction

The adsorption of metal submonolayers, monolayers and multilayers to form modified bimetallic surfaces and thin films with differing lattice constants and/or crystal structures is an area receiving increasing attention [1]. These systems are potentially important in fields as diverse as heterogeneous catalysis and magnetic data storage [2]. Increasingly, it is being revealed that intermixing between film and substrate takes place in many systems in the earliest stages of film growth leading to surface alloy formation [3].

The Cu/Sn system is an excellent example of a complex bimetallic combination. Copper adopts a face centred cubic structure of lattice constant 3.61Å. Tin is metallic at 300K adopting a tetragonal structure. For room temperature growth a large mismatch exists in the 12-fold coordinate metallic radii of 26% [5]. The Cu/Sn system has a highly complex bulk phase diagram with alloys forming throughout the composition range including a range of intermetallic compounds [6]. While Sn diffusion into copper is kinetically limited at 300K in bulk alloys, diffusion of Cu into Sn occurs via an interstitial mechanism with a small activation barrier of approximately 0.3eV, hence interdiffusion may be significant even at 300K [7]. Thus, surface alloy formation is quite possible for room temperature growth of Sn on Cu{100}.

The adsorption of Sn on Cu{100} was first studied by Argile and Rhead [8] using Auger spectroscopy in combination with LEED. Four ordered phases were discovered in the submonolayer regime, namely, Phase I: a "complex" pattern with unidentified unit cell; Phase II: a rotated domain p(2×6); Phase III: a rotated domain $p(3\sqrt{2}\times\sqrt{2})R45°$ and Phase IV: a $p(2\sqrt{2}\times2\sqrt{2})R45°$ monolayer at a tin coverage of 0.625 ML with respect to the Cu{100}-(1×1) density of 1.538×10^{15} atoms cm^{-2}. Phases II-IV have been explained in terms of overlayer structures consistent with the determined surface coverages and symmetry/periodicity of the LEED patterns.

For phases II and III it has been observed that the LEED beams in the c(2×2) positions are significantly brighter over a wide energy range than the other

superlattice reflexes. A possible explanation of this observation is that phases II and III originate from a c(2×2) superstructure with additional weaker reflexes arising from a longer range modulation in the c(2×2) due for example, to strain in the adlayer-substrate combination or anti-phase domain boundaries which offers a different interpretation to the structural models presented by Argile and Rhead. One obvious suggestion for the origin of a c(2×2) structure would thus be a surface alloy formed by substitution of 0.5 ML of Sn into the outermost copper layer. This structure has been identified for a number of transition metal adsorbates on Cu{100} including Pd, Au, Mn, Pt and Rh [9-12]. Evidence for surface alloy formation in the Cu{100}/Sn system has been provided by Abel *et al.* [13] using Rutherford Backscattering Spectroscopy (RBS).

In this paper we re-examine the Cu{100}/Sn system by LEED providing further insight into the surface phases formed and their coverage dependent transitions. We present data supporting the assertion that Sn adsorption leads to significant perturbation of the copper selvedge, consistent with adsorbate induced reconstruction/surface alloy formation. A range of new models are suggested for structures I-III which are shown to be in good agreement with double scattering simulations of the LEED patterns.

2. Experimental

The experiments were performed in an ultra-high-vacuum chamber operated at a base pressure of 1×10^{-10} torr. The system was equipped with 4-grid reverse view LEED optics (VG Microtech). The Cu{100} sample of dimensions 15 × 10 × 1.5mm (Metal Crystals and Oxides, Ltd.) was polished mechanically to a mirror finish. The specimen was cleaned *in-situ* by cycles of argon ion bombardment and annealing to 800K, as monitored by a chromel-alumel thermocouple. The atomically clean sample yielded a sharp well contrasted p(1×1) LEED pattern with I-V spectra in excellent agreement with literature reports [14].

Deposition of tin on room temperature Cu{100} was carried out using a water cooled Knudsen cell evaporator (WA Technology) which provided a constant tin

flux of approximately 0.015 ML min^{-1} with the chamber base pressure remaining below 3×10^{-10} torr. The LEED patterns obtained were in excellent agreement with the report of Argile and Rhead [8], in terms of the symmetry and periodicity observed. Coverage assignments were made by monitoring LEED spot profiles as a function of evaporation times. This analysis indicated that phases I to IV reached maximal perfection at Sn coverages of 0.21, 0.37, 0.50 and 0.70 ML respectively based on the assumption that the coverage at which phase III reaches maximum perfection is that of a perfect c(2×2) i.e. 0.50 ML and a coverage independent sticking probability. These coverages compare with values of 0.42, 0.50 and 0.625 for phases II, III and IV determined by Argile and Rhead [8] based on their own postulated structure for phase II. The apparent disagreement for the monolayer coverage (Phase IV) may be explained by the fact that in this work we assume a coverage independent sticking probability for the tin and scale our coverages according to evaporation time. In the work of Argile and Rhead [8] a decrease in the sticking probability close to monolayer formation was indicated by a non-linearity in Auger uptake measurements. The spot profiles indicate that the transition between phases occurs by phase co-existence rather than sharp coverage dependent phase switching and consists of nucleation of domains of the higher coverage structure within the lower coverage phase.

Diffraction data was acquired with a high sensitivity CCD camera (Hitachi Denshi KP-M1E/K) interfaced to a micro-computer. Spot profiles and I-V spectra were acquired with software provided by Data-Quire Corporation (Stony Brook, New York).

3. Results

LEED I-V spectra were collected for beams common to all phases, including the p(1×1) beams and fractional order beams in c(2×2) positions (other than phase I where these beams are split into quartets centred on the c(2×2) positions). Figure 1(a) illustrates the symmetry averaged (1,0) beam at normal incidence from clean Cu{100} and for phases I to IV. Adsorption of Sn leads to very significant changes in the I-V spectrum of the (1,0) beam for phases II, III and IV.

(a)

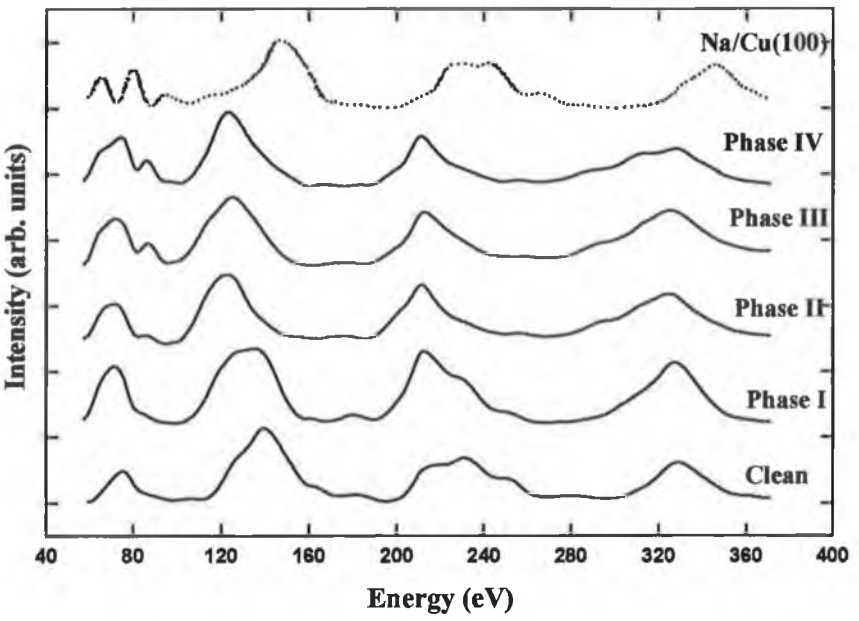

(b)

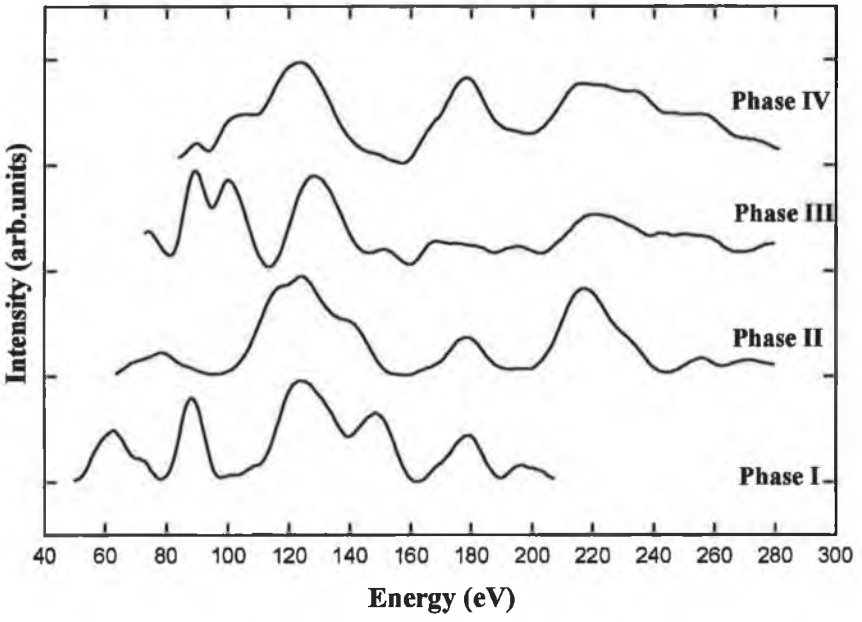

Figure 1: (a) Symmetry averaged and beam current normalised normal incidence LEED I-V spectra from the (1,0) beam from clean Cu{100} and Sn phases I to IV and LEED I-V spectra from the Cu{100}-c(2×2)-Na phase [15]. (b) Symmetry averaged and beam current normalised normal incidence LEED I-V spectra from the (1/2, 1/2) beam for Sn phases I to IV.

A number of I-V analyses of simple ordered c(2×2) metallic overlayers on Cu{100} in which the adsorbate leads to a small perturbation of the Cu{100} selvedge structure are available in literature. Perhaps the most relevant is a recent study of the structure of a simple c(2×2)-Na overlayer on Cu{100} in which Na atoms sit in four-fold hollow sites of an essentially structurally unmodified Cu{100} substrate [15] . Sodium has a larger 12-fold coordinate metallic radius than tin {1.91 Å (Na) versus 1.62 Å (Sn) [5]} which both differ substantially from that of copper (1.275 Å). Thus, if both adsorbates adopted a simple overlayer structure without significant modification of the substrate structure, a similar level of modification of the spectral structure of integral order beams may be expected. Comparison of the integral beam I-V spectra from this phase and clean Cu{100} illustrate changes as shown in figure 1(a) (dotted line). However, the Sn phases II, III and IV have integral order I-V spectra modified to a greater degree than was the case for Na, including substantial shifts of Bragg peaks. This suggests that adsorption of Sn may lead to a reconstructive modification of the copper surface structure [8]. This hypothesis is further enhanced by noting that both Argile and Rhead and Abel *et.al.* observed that Sn adsorption at a substrate temperature below 200K inhibited formation of phases I-IV and instead only a diffuse p(1×1) was observed [8,13]. The LEED patterns for the ordered phases only became apparent upon warming to between 250 and 350K. Surface diffusion coefficients for metal adatoms on Cu{100} are sufficient even at 200K to allow ordered overlayer formation and local displacive substrate reconstruction [4]. The I-V spectra of the (1/2,1/2) beams for phases I to IV illustrated in figure 1(b) differ strongly, suggesting that the local surface geometry giving rise to the dominant c(2 × 2) periodicity is different for all four phases. In the case of phase I, the c(2×2) beams shown correspond to the integrated intensity of the four split beams.

To simulate the expected LEED patterns the double scattering LEED simulation program of Panagiotides *et al.* was utilised [16]. The program uses only s-waves, producing the correct symmetry and periodicity but not quantitatively reliable intensities in the LEED pattern. The patterns were simulated in the energy range 100-200eV in 5eV steps, with the resulting patterns being co-added to provide an overview of the LEED pattern over a reasonable energy range. The geometric structure for all models is based on the clean surface structure of Cu{100} with tin

atom positions determined by distances calculated geometrically based on the 12-fold coordinate radius of tin.

(a) Phase I: No structure has yet been proposed for this phase, which produced the complex LEED pattern shown in figure 2, although it has been suggested that the spot splitting may be a result of domain walls [8]. Given that the tin coverage is 0.21 ML (according to our calibration) when the pattern reaches maximum intensity and that the centre of gravity of the split beams are centred on positions of a p(2×2) superstructure which would reach maximum perfection at a coverage of 0.25 ML, it is reasonable to suggest that phase I may be explained in terms of a p(2×2) periodicity with "light" domain walls. Measurement of the splitting of the (m, n/2) and (m/2, n) beams relative to the reciprocal lattice vector of the substrate in the [011] and $[01\bar{1}]$ directions indicate the domain wall structure adopts a periodicity that is 11 times that of the real space lattice unit cell in the [011] and $[01\bar{1}]$ directions as can be seen in figure 2.

The models giving the best agreement with experimental observations is illustrated in figure 2 and consists of small units of p(2×2) structure, with rows of copper atoms separating them in both the [011] and $[01\bar{1}]$ directions. These models correspond to a tin coverage of 0.18 ML. Figures 2(b) and 2(d) illustrate the LEED patterns generated, which are in excellent agreement with observations, producing (m,n/2) and (m/2,n) beams split into doublets and (m/2,n/2) centred beams split into quartets. Models based on both overlayers and surface alloys in which Sn atoms penetrate into the outermost copper layer yield similar LEED patterns which may not be easily differentiated without a full dynamic I-V analysis.

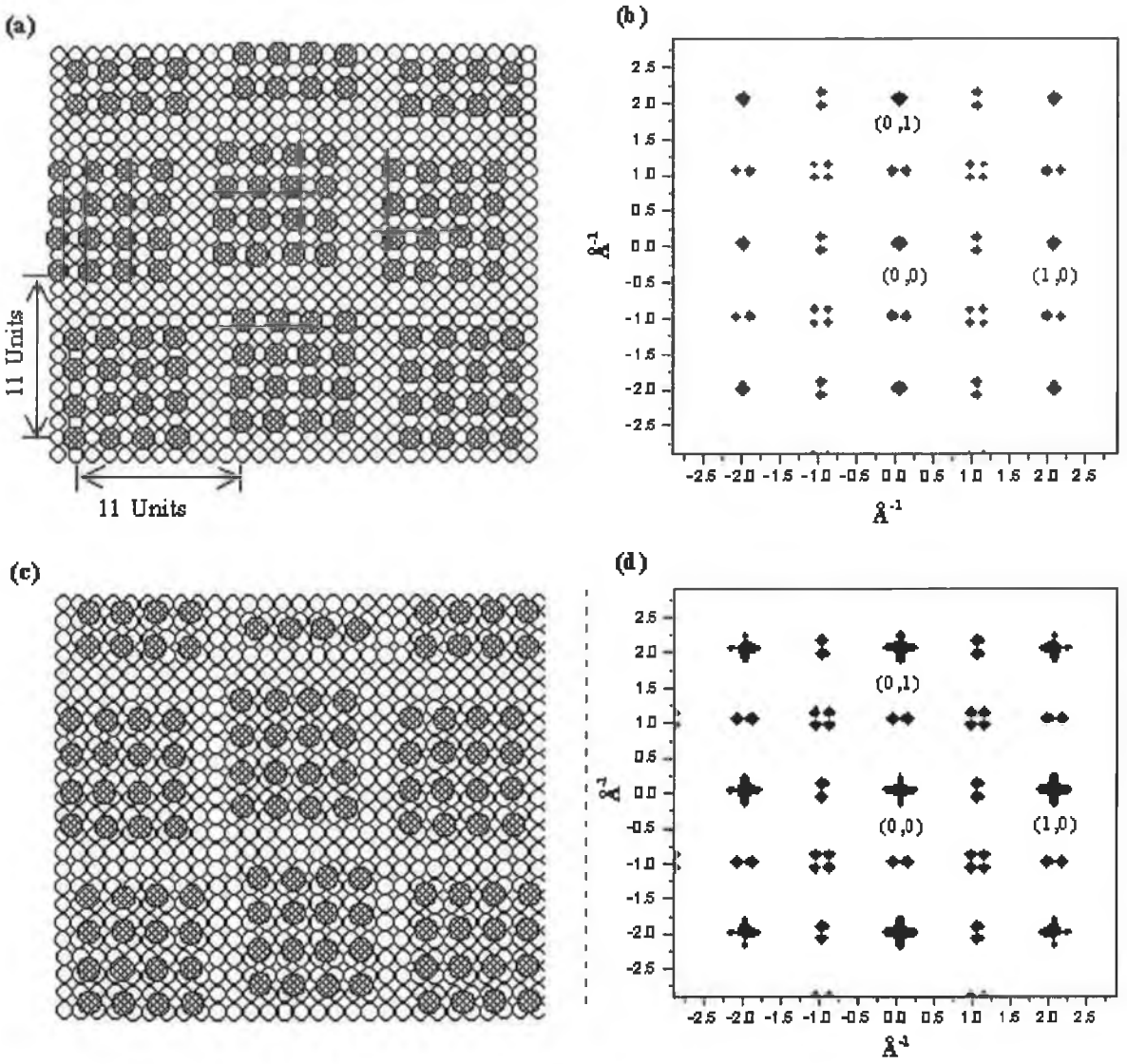

Figure 2: (a) Single domain structural model for a p(2×2) Cu{100}-Sn surface alloy with "light" antiphase domain walls; (b) simulated LEED pattern for (a) averaged over the energy range 100-200eV; (c) as (a) but for an overlayer model; and (d) the simulated LEED pattern for (c).

(b) Phase II: Figure 3(a) illustrates a single domain of the p(2×6) model suggested by Argile and Rhead, consisting of a coincidence mesh with 5 Sn atoms fitting into six copper interatomic spacings in the $[01\bar{1}]$direction. While this model is entirely consistent with the p(2×6) periodicity observed with a Sn coverage of 0.42 ML, it would not necessarily be expected to produce (m/2,n/2) beams with considerably higher intensity than other superlattice beams as has been observed experimentally. As illustrated in figure 3(b), the simulations confirm this expectation. We suggest that phase II, has its origin in a mixed c(2×2)/p(2×2) structure. A model capable of reproducing the LEED observations and yielding a Sn coverage of 0.42 ML is shown in figure 3(c). This structure consists of domains of c(2×2) CuSn surface alloy of two unit cells width, separated by a p(2×2) unit cell, leading to sixth order periodicity in the [011] and $[01\bar{1}]$ directions for the two monoenergetic rotated domains. Figure 3(d) illustrates the LEED pattern generated by this model which exhibits dominant (m/2,n/2) beams from the local c(2×2) structure within these narrow domains. A second possibility, shown in figure 3(e), is a p(2×6) unit cell consisting of a single c(2×2) unit cell with two p(2×2) unit cells on either side, yielding a coverage of 0.33 ML. The simulated LEED pattern, figure 3(f), is not dissimilar to that shown in figure 3(d), the only difference (as expected) is an increase in (m/2,n) and (m,n/2) beams relative to their c(2×2) counterparts. Hence it is quite possible that phase II consists of a mixture of domains of the structures illustrated in figures 3(c) and (e).

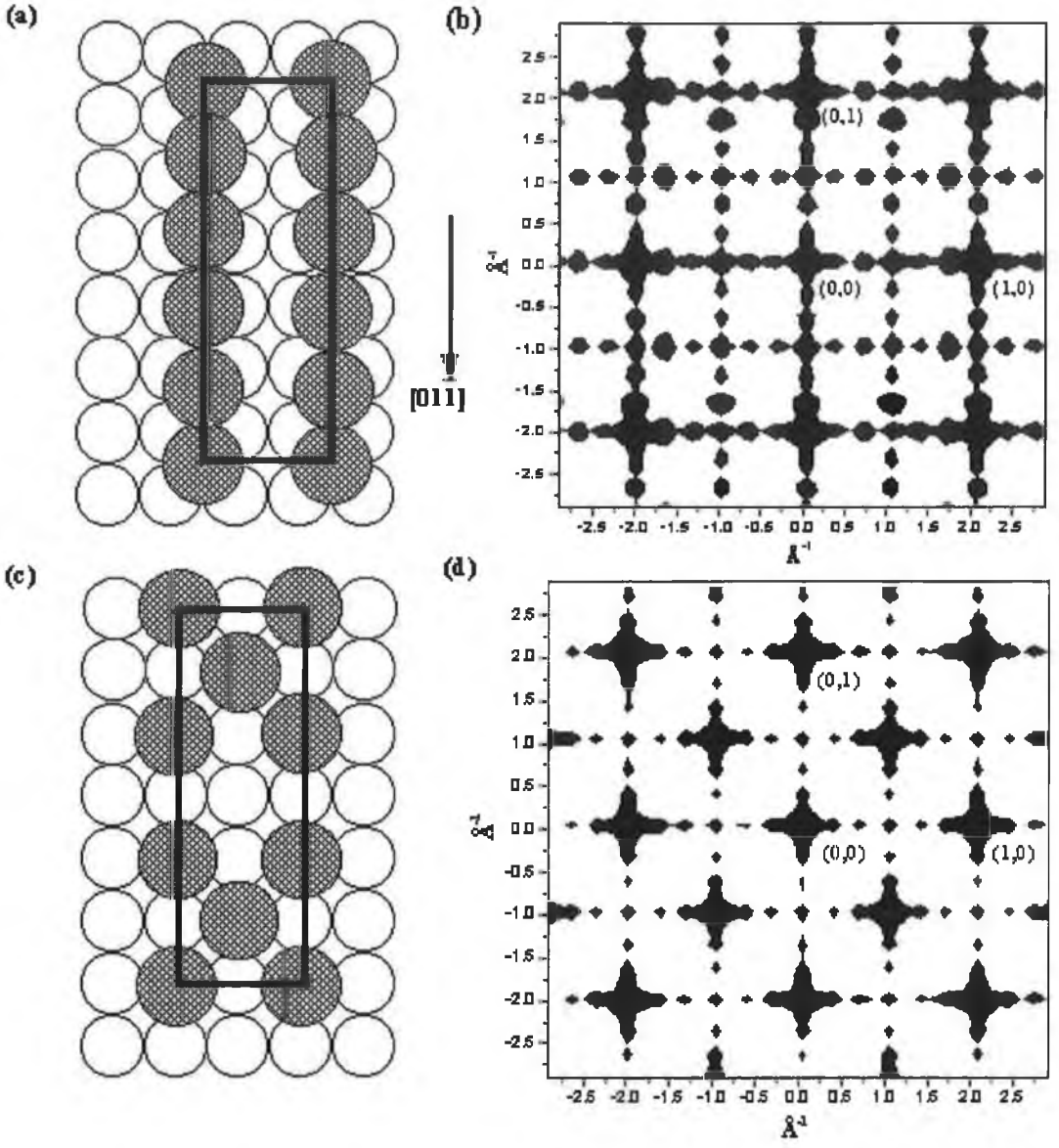

Figure 3: Single domain structural models for a single rotated domain p(2×6) structure (phase II) and the simulated energy averaged LEED patterns including : (a), (b) the Argile and Rhead overlayer structural model; (c), (d) the surface alloy model based on domains of c(2×2) surface alloy separated by p(2×2) unit cells

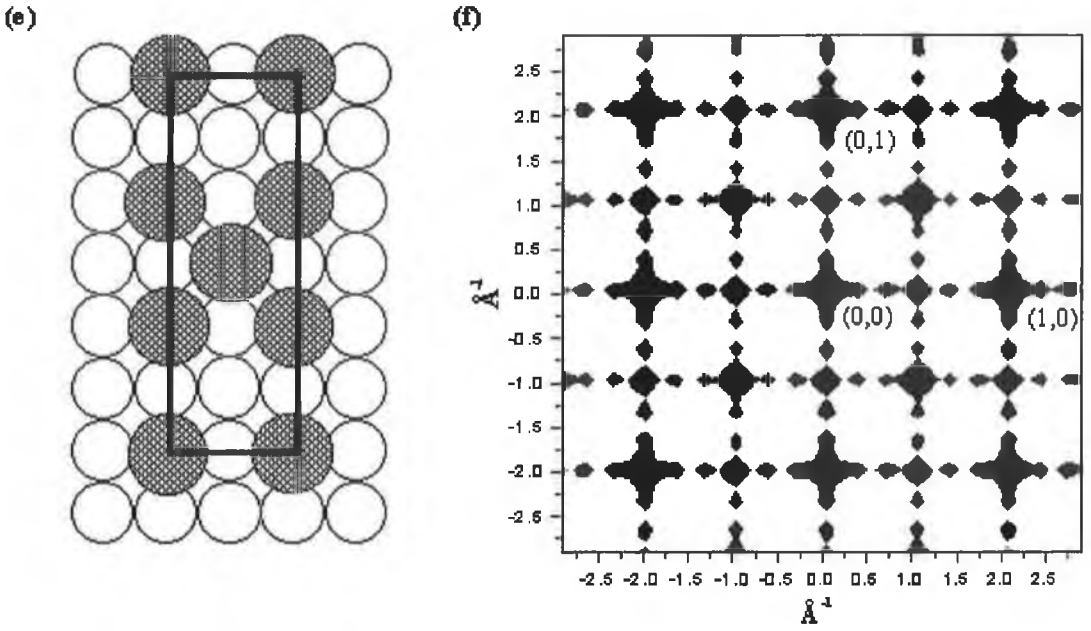

Figure 3: (cont'd) (e), (f) p(2×2) micro-domains separated by a single c(2×2) unit cell. Simulation of the overlayer models present similar LEED patterns.

(c) Phase III The transition between phase II and III is a most dramatic one in terms of the observed periodicity of the LEED pattern given that this transition is completed by addition of only an extra ~0.10 ML of Sn. The structural model suggested by Argile and Rhead along with the simulated LEED pattern is shown in figures 4(a,b) which generates the correct periodicity but dominant (m/2,n/2) beams were not predicted [8]. Based on the structural models proposed for phase II, clearly the obvious location of the additional Sn atoms is to fill the vacancy in the centre of the p(2×2) unit cells separating the c(2×2) domains and yield the observed Sn coverage of 0.50 ML. Simple substitution of Sn atoms into the c(2×2) sites in the vacant copper rows would lead to a perfect c(2×2) structure rather than the p(3√2×√2)R45° structure observed. Due to the large metallic radius of Sn, a simple c(2×2) structure with Sn and Cu coplanar within a surface alloy model would lead to significant strain along the [010] directions. We thus propose that this strain is relieved by buckling and/or small lateral displacements of Sn and Cu atoms. To model this, figure 4(c) shows a c(2×2) overlayer with pairs of Sn atoms "pinched"

together. While clearly this is one of many possibilities for which combined lateral and perpendicular motion of Cu and Sn atoms yield a p(3√2×√2)R45° unit cell it serves to illustrate the principle that a model based on a c(2×2) overlayer with minor modifications may lead to the observed periodicity. In such models the magnitude of the lateral displacement of copper atoms controls the relative intensities of the c(2×2) beams at (m/2,n/2) positions and the remaining superlattice beams with larger displacements tending to increase the intensity of the non c(2×2) superlattice beams. Figures 4(d)-(f) illustrate the simulated LEED patterns for varying degree of lateral shifting of Cu and Sn atoms indicating that a lateral shift of approximately 0.4Å (figure 4e) yields the best qualitative agreement with the observed LEED intensities.

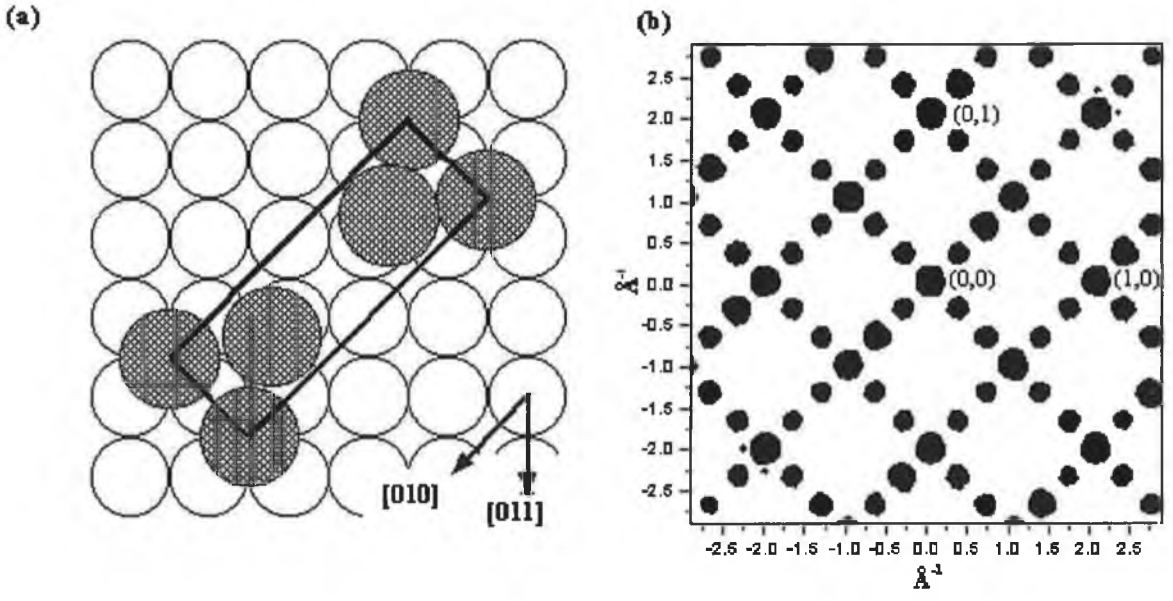

Figure 4: Single domain structural models for a single domain p(3√2×√2)R45^0 structure (phase III) and simulated energy averaged LEED patterns including: (a) and (b) the Argile and Rhead overlayer model, respectively.

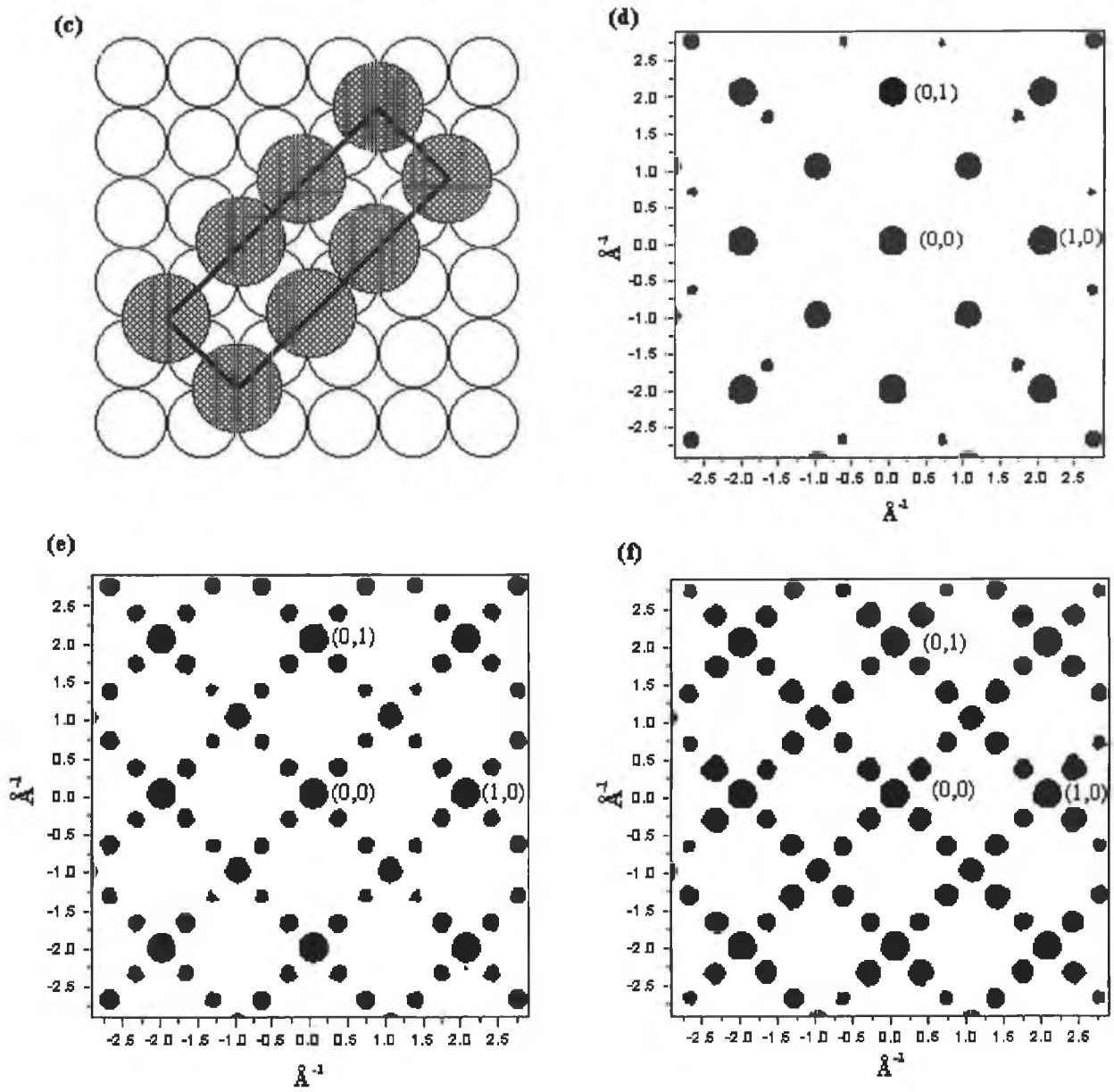

Figure 4: (cont'd) (c)-(f) the c(2×2) surface overlayer model with substrate reconstruction with lateral displacements of surface Cu atoms of (d) 0.2Å ; (e) 0.4 Å and (f) 0.6 Å respectively. Simulation of surface alloy models present similar results.

4. Discussion

The double scattering LEED simulations have enabled us to suggest a possible model based on an antiphase domain p(2×2) structure for phase I which are consistent with both the Sn surface coverage and the observed complex split beam LEED pattern. Furthermore, we have demonstrated that phases II and III are readily explainable in terms of c(2×2) structures containing local density modulations and substrate reconstruction. The double scattering simulations for these models are in better agreement with the observed LEED patterns than the original structures suggested by Argile and Rhead.

Previous work with similar large atoms such as Cu{100}/Bi and Cu{100}/Pb indicate that at coverages well below 0.5 ML surface alloys form [17]. In the case of Bi a disordered or partially ordered p(2 × 2) phase forms around θ_{Bi} = 0.25 ML which has been demonstrated to be a surface alloy by grazing incidence X-ray diffraction [17]. Dealloying occurs as the coverage is increases forming a c(2× 2) Bi overlayer at θ_{Bi} = 0.50 ML, with Bi atoms located in four-fold hollow sites above the first copper layer [17]. Bismuth is slightly lager than Sn having a 12-fold coordinate radius of 170 pm versus 162 pm for Sn. A similar scenario holds for Pb. At a coverage of 0.375 ML a c(4 × 4) structure is formed which consists of a surface 2D alloy which upon raising the coverage to 0.50 ML leads to the formation of a c(2× 2) structure, identified as an overlayer as in the case of Bi[18].

If a similar behaviour were followed in the case of Cu{100}/Sn, Phase I would represent a surface alloy, while Phase III at θ_{Sn} = 0.50 ML would be an overlayer. The intermediate phase (Phase II) exists in the intermediate regime where the transition from a surface alloy to an overlayer occurs. The large changes in the IV spectra of the (1/2,1/2) and (1,0) beams for phases I and II would be qualitatively in keeping with a gross structural rearrangement such as that of a surface alloy switching to a dealloyed surface overlayer structure.

Abel *et al.* [13] report a p(1×1) LEED pattern for the adsorption of 0.33 ML of Sn at 170K, while a p(2×2) LEED pattern appears upon warming to 250K. The origin of the formation of the split p(2×2) upon deposition at 300K and an unsplit p(2×2) by

adsorption at low temperature followed by controlled annealing is unknown at present. Most interestingly, submonolayer Sn deposition was found to lead to an **increase** in the Cu RBS surface peak, a result which would not be expected from overlayer growth, and the authors suggest that Cu atoms are displaced from their regular lattice sites and that each Sn atom displaces one copper substrate atom, i.e. surface alloy formation. The related Cu{111}/Sn system also forms a surface alloy upon deposition of 0.33 ML of Sn as demonstrated by alkali ion scattering spectroscopy [19]. The $\sqrt{3}\times\sqrt{3}R30°$ structure has Sn atoms rippled outwards by approximately 0.4Å with respect to the outermost copper plane. No quantitative information is available to date on changes in the outermost interlayer spacings induced by incorporation of Sn or possible Sn induced buckling in sub-surface layers [19].

5. Conclusions

We have re-examined by LEED the Cu{100}/Sn bimetallic system by double scattering LEED simulation as a function of adsorbate coverage for a range of model structures.

(i) A model for the low coverage ordered phase has been suggested based on a "light" antiphase domain wall p(2×2) structure;

(ii) We have suggested alternative explanations for the structures of phases II and III which yield better agreement with the relative intensities of superlattice beams in the LEED patterns compared to previous explainations of Argile and Rhead [8]. A possible explanation of the transition to the p(2×6) structure involves formation of narrow domains of c(2×2) CuSn structure of two unit cells width separated by a p(2×2) unit cell yielding sixth order periodicity in [011] and $[01\bar{1}]$ directions. The $p(3\sqrt{2}\times\sqrt{2})R45°$ phase is suggested to have its origin in a c(2×2) structure with elastic strain due to the large metallic diameter of Sn leading to displacive reconstruction within the outer layer(s) ;

(iii) The transition between phases occurs by nucleation of domains of the higher coverage phase within the lower coverage structure with concomitant density modulations across the surface.

Clearly further quantitative structural work both by LEED I-V analysis and STM is required to validate the proposed models and to differentiate between surface alloy and overlayer structures.

References

[1] C.T.Campbell, Ann. Rev. Phys. Chem 41 (1990) 775.

[2] P.Houdy, Met. Multilayers Trans. Pub 59/60 (1990) 581.

[3] U.Bardi, Rep. Prog. Phys. 57 (1994) 939.

[4] M.Breeman and D.O.Boermas, Phys. Rev. B46 (1992) 1703.

[5] N.W.Alcock in Bonding and Structure, Ellis Horwood (1990)

[6] M.Hansen, Constitution of Binary Alloys, McGraw-Hill, New York, (1958).

[7] B.F.Dyson, T.R.Anthony and D.Turnbull, J.Appl.Phys. 38 (1967) 3408.

[8] G.Argile and G.E.Rhead, Thin Solid Films 87 (1982) 265; G.E.Rhead, C.Argile and M-G.Barthes, Surf. Interface Anal. 3 (1981) 165; G.Argile and G.E.Rhead, Surf.Sci. 135 (1983) 18.

[9] P.W.Murray, I.Stensgaard, E.Laegsgaard and F.Besenbacher, Surf.Sci. 365 (1996) 591.

[10] D.Brown, T.C.Q.Noakes, D.P.Woodruff, P.Bailey and Y.LeGoaziou, J.Phys.Condens.Matter 11 (1999) 1889.

[11] J.P.Reilly, D.O'Connell and C.J.Barnes, J. Phys. Condens. Matter 11 (1999) 8417.

[12] G.W.Graham, P.J.Schmitz and P.A.Thiel, Phys. Rev. B 41 (1990) 3353.

[13] F.Abel, C.Cohen, J.A.Davies, J.Moulin and D.Schmaus, Appl.Surf.Sci. 44 (1990) 17.

[14] F.Jona, Surf. Sci. 192 (1987) 398 and references therein.

[15] A. Mikkelsen and D.L.Adams, Phys.Rev.B 60 (1999) 2040.

[16] N.Panagiotides, D.R.Batchelor and D.A.King, Chem. Phys. Lett. 177 (1991) 419.

[17] H.L.Meyerheim, H.Zajonz, W.Moritz and I.K.Robinson, Surf. Sci. 381 (1997) L551 and references therein.

[18] G.L.Kellogg and R.Plass, Surf. Sci. Lett. 465 (2000) L777.

[19] S.H.Overbury and Yi-sha Ku, Phys. Rev. B 46 (1992) 7868.

CHAPTER 6

Conclusions

The technique of diffuse LEED $I(V)$ analysis has been applied to study the earliest stages of surface alloy formation during the room temperature growth of Pd on Cu{100}. For Pd adsorption on Cu{100} at 300 K in the coverage range 0.1 to 0.55 ML, the local geometry at all coverages corresponds to a Cu_xPd_{1-x} surface alloy with adsorbate atoms predominantly substituting into the outermost copper monolayer occupying substitutional lattice sites. The local surface geometry is found to be coverage independent within the resolution of the analysis and corresponds to an approximately coplanar CuPd outer monolayer and a slightly expanded first to second interlayer spacing (+3%).

At a coverage of 0.5 ML, a thermally activated transition from a Cu{100}-c(2×2)-Pd top layer surface alloy to an ordered c(2×2) underlayer alloy consisting of a CuPd mixed second layer capped by a copper monolayer has been shown to occur.

A tensor LEED $I(V)$ analysis has been performed on a Cu{100}-c(2×2)-Pd underlayer alloy. Substitution of approximately 0.5 ML of Pd into the second layer leads to a significant modification of the first two copper interlayer spacings. The first interlayer spacing which is contracted in the case of clean Cu{100} undergoes an expansion of +3.3% upon insertion of Pd while the second interlayer spacing which is slightly expanded in clean Cu{100} undergoes an expansion of +6.6% upon substitution of Pd. The composite CuPd underlayer is rippled with Pd atoms being relaxed inwards away from the solid-vacuum interface. Insertion of approximately 0.5 ML of Pd into the second layer leads to a considerable lattice expansion relative to bulk Cu{100} in the outermost three monolayer slab. This expansion occurs in response to the elastic lattice strain due to the substitution of the larger Pd atoms into the smaller Cu lattice. The absolute value is considerably smaller (6%) than that predicted to be required to maintain Pd at constant density equal to that of bulk (16%).

The Cu{100}-p(2x2) structure formed by deposition of 1ML of Pd on Cu{100} at room temperature has been re-analysed by SATLEED using an enhanced normal incidence data base. A wide range of models suggested by MEIS/LEED, STM and LEIS along with selected new models in keeping with the layerwise elemental composition determined by LEIS have been tested.

The favoured model consists of a p(2x2) clock rotated ordered CuPd monolayer of symmetry p2gg above a c(2x2) ordered CuPd underlayer. Top layer Cu and Pd atoms are laterally shifted from four-fold hollow sites in an alternate clockwise and anti-clockwise fashion with the vertices of the p(2x2) clock rotation centred over second layer Pd atoms. The displacement of the top layer Cu and Pd atoms is found to be 0.25±0.12Å. Substitution of a high concentration of Pd into the outermost two atomic layers leads to a significant expansion of the outermost two interlayer spacings.

SATLEED has been used to determine the structure of Cu{100}-c(2x2)-Pt alloy formed by thermal activation to 525 K of 0.5 ML Pt adsorbed on Cu{100}. The analysis retrieved a structure that consists of an ordered c(2x2) Cu-Pt second layer capped with a pure Cu layer. The ordered mixed layer is found to be rippled with Pt atoms rippled outwards (0.08±0.06Å) towards the solid-vacuum interface.

A Cu{100}-c(2x2)-Pt surface alloy structure formed by deposition of a 1 ML Pt and thermal processing to 550 K is shown to correspond to a copper capped bimetallic surface localised alloy with an ordered c(2x2) CuPt underlayer. Excess Pt is distributed in layer 3 (20 ± 20 at. %) and layer 4 (30 ± 30 at. %). The selvedge structure within the LEED probing depth resembles the {100} surface of the $L1_2$ phase of the bulk Cu_3Pt alloy. Substitution of platinum into the selvedge results in a significant expansion in the surface interlayer spacings relative to clean Cu{100} due to the larger metallic radius of Pt and switches the weak oscillatory relaxation of clean Cu{100} to a strongly and non-uniformly expanded interlayer separation.

This new class of materials, namely underlayer alloys may have potential for future use as catalysts: the inclusion of metals such as Pt or Pd in layer 2 will lead to different stability of reactants due to prevention of top layer Cu reconstruction.

The surface structures of a Cu{100}-c(2x2)-Bi and Cu{100}-p(2x2)-Bi phases formed by deposition of 0.50 ML and 0.25 ML Bi respectively on Cu{100} at room temperature have been determined. Bismuth was found to form a surface alloy at 0.25 ML with the Bi atoms located 0.56±0.06 Å outwards from the outermost Cu layer. With increasing Bi coverage, de-alloying of Bi atoms occurs until a well-

ordered c(2x2) overlayer is formed with Bi atoms occupying the four-fold hollow site above a slightly perturbed substrate structure. The structures of both the low and high coverage Cu{100}/Bi obtained in this study are in good agreement with those evaluated recently for the same system by surface X-ray diffraction and provide an enhanced precision for Bi induced relaxation with the Cu selvedge.

Finally, structures of the Cu{100}/Sn bimetallic system has been re-examined by double scattering LEED simulation as a function of adsorbate coverage. A model for the low coverage ordered phase has been suggested based on a "light" antiphase domain wall p(2×2) structure. We have suggested alternative explanations to those previously asserted by Argile and Rhead for the structures of phases II and III which yield better agreement with the relative intensities of superlattice beams in the LEED patterns. A possible explanation of the p(2×6) structure (phase II) involves formation of narrow domains of c(2×2) CuSn structure of two unit cells width separated by a p(2×2) unit cell yielding sixth order periodicity in [011] and $[01\bar{1}]$ directions. The p($3\sqrt{2}\times\sqrt{2}$)R45° phase (phase III) is suggested to have its origin in a c(2×2) structure with elastic strain due to the large metallic diameter of Sn leading to displacive reconstruction within the outer layer(s).

Appendix A

Simulation of LEED I(V) spectra

This section briefly describes the code used in these calculations, namely the Symmetrised Automated Tensor LEED (SATLEED).

A.1 The Symmetrised Automated Tensor LEED (SATLEED)

A.1.1 Search Strategy and Partial Automation Approach

The strategy for solving a particular surface structure can be summarised in the following steps:

1. Testing separately different possible surface models which have to be chemically and physically logical.

2. For each model, guess reasonable starting co-ordinates for all atoms. This is called the reference structure.

3. For each reference structure, the LEED program (TLEED1) is run to compute accurate dynamic LEED intensities, and to compute tensors related to possible atomic displacements from the positions assumed in the reference structure.

4. The second LEED program (TLEED2) is run using the results from TLEED1 to optimise the atomic positions. TLEED2 varies atomic positions, computes approximate LEED intensities at these modified positions, compares these intensities with experiment, updates atomic positions based on the result of the comparison, and iterates until convergence of the co-ordinates is achieved. The comparison between theory and experiment is made through one or more R-factors, which quantify the misfit between calculation and experiment.

R-factors are then minimised to produce modified structures ready for further testing and refinement. These modified structures are called "trial structures".

5. Iterating the last step (TLEED2) with different starting structures, near the reference structure, to make sure that a proper R-factor minimum is found and the structure obtained does not have multiple minima. The occurrence of multiple minima near an optimum structure usually indicates that more atomic co-ordinates should be fit to the experimental data, i.e. that some co-ordinates were kept fixed that should be allowed to vary.

6. Iterating the TLEED1 step once or twice with updated optimised atomic co-ordinates, i.e. with new reference structures (especially if the TLEED2 search has shifted atoms by more than about 0.1Å), followed by a new optimisation with TLEED2.

7. Repeating as necessary to reduce the possibility of being trapped in a "local minimum", rather than in the "global minimum". There exists no failsafe procedure for locating the global minimum, and therefore an exhaustive search approach should be conducted.

8. Repeating the same procedure for other models. However, iterations are only necessary for models that look promising or competitive with the best one.

9. The best structure may be further refined with improved phase shifts and perhaps if necessary an increased number of phase shifts. Different values of other non-structural parameters, such as the imaginary part of the inner potential and the atomic vibration properties may help the final structure determination.

A.1.2 Structural Models: Reference Structures and Trial Structures

Normally, there are several possible qualitatively different models possible for the surface structure to be determined. Examples are different adsorbate sites, different

reconstruction types, different molecular rearrangements, etc. Each model will have to be tested independently against experiment with separate LEED calculations. For each model, a full dynamical LEED calculation will be necessary (using program TLEED1), using physically and chemically reasonable starting co-ordinates.

Whenever co-ordinates are specified for a given model and a dynamical LEED calculation is performed using TLEED1, we speak of a reference structure. TLEED2 will then explore trial structures that deviate from the reference structure. In general, if two models differ in any atomic co-ordinate by 0.2 Å or more, then separate TLEED1 calculations will be required for the two reference structures. This is because the automated search algorithm cannot be guaranteed to locate the correct structure when started from more than about 0.2 Å away. The calculations should lead to the desired global minimum in the reliability factor rather than a local minimum that might lead to the wrong structure.

A.1.3 Composite Layers

The LEED programs assume all atoms to be arranged either in simple layers (Bravais-lattice layers) which contain 1 atom per 2D unit cell, or in composite layers which contain more than 1 atom per 2D unit cell. These layers may be coplanar or not. The assignment of atoms to these two types of layers is very important for reducing computer requirements: memory and time. Principally, matrix dimensions should be minimised to save storage requirements and to speed up mathematical and matrix operations.

Atoms of trial structures are arranged in terms of simple and composite layers in the SATLEED programs. This arrangement must be input into the calculation. Whenever possible, simple layers are preferred over composite layers in terms of computing efficiency. However, it is not often possible to avoid having to combine simple layers into composite layers. The reason is that simple layers that have a small mutual interlayer spacing give rise to divergences in the LEED theory, a situation which is difficult to produce convergence. Any surface will thus be composed of a "surface region" with a number of simple and/or composite layers, followed by a "bulk" with simple layers and/or composite layers.

Given a specific surface structure model, one starts by considering all atoms to be arranged in simple planes of atoms parallel to the surface. These planes usually contain only one atom per 2D unit cell (whether it is the (1x1) cell of bulk layers or the supercell of surface layers). Thus, any bulk atom will define a simple plane with (1x1) periodicity, while a surface atom (e.g. in an overlayer) may define another simple plane with a 2D superlattice periodicity.

Composite layers are formed by combining simple planes that are closely separated, as follows: any two simple atomic planes which are spaced less than 1 Å apart (perpendicular to the surface, measured between nuclear planes) MUST be combined into one composite layer. A composite layer then contains two or more atoms per unit cell, one each from each simple layer. Several composite layers may be created in this way. Simple planes that do not become part of a composite layer are simply called layers.

Most important is that different composite layers must therefore be spaced by at least about 1Å. Thus, no atomic plane in one composite layer may come closer than 1 Å to any atomic plane in another composite layer. A composite layer must also be spaced by at least 1 Å from a simple layer. Simple layers must be spaced at least 1 Å apart. It is allowed to let a composite layer contain spacings larger than 1 Å, i.e. it could alternatively be split into separate composite layers, but this arrangement is computationally wasteful.

A good example of a composite layer is a buckled layer, in which atoms lie in slightly separate planes. Another example is an adatom in a deep hollow site, such that the adatom plane is less than 1Å from the nearest substrate atomic plane. Many molecules also must be arranged into composite layers. Bulk layers in a compound often also must be grouped into composite layers.

A surface model to be analysed must thus first be sliced into one or more composite layers and any remaining simple layers. For simple substrates, the bulk will be composed of well-spaced simple layers, which are treated as such. For example, in low-Miller-index fcc and bcc crystal surfaces, bulk layers are simple and well-spaced.

Composite layers require much more computer memory and time than simple layers. Also, the computer requirements will rise steeply with the number of atoms per 2D unit cell in a composite layer. Thus, the use of composite layers should be minimised within the following constraints:

1. All atoms whose coordinates are to be determined while solving for the structure should form part of a composite layer; thus, one normally treats the entire surface region, in which atomic coordinates are to be determined, as one or more composite layers.

2. All composite layers and any remaining simple layers should be mutually spaced by at least about 1Å.

3. Whenever possible, it is best to split a composite layer into thinner, well-spaced composite layers, and to split off any well-spaced simple layers.

4. When a simple layer with supercell lies so close to a simple layer with (1x1) periodicity that they should be combined into a composite layer (such as with an overlayer lying nearly coplanar with a simple bulk layer), those layers must be combined into a composite layer which takes the supercell periodicity. One thereby loses the potential calculational benefit of the (1x1) periodicity but gains the benefit that one may relax the (1x1) layer structure such that it breaks the (1x1) periodicity.

5. Composite layers should be planned taking into account plausible atomic displacements that will occur in the automated search, i.e. displacements of up to about 0.5 Å.

6. Different models (or different reference structures) generally require different arrangements of atoms into composite layers. For convenience, one therefore often chooses a common arrangement into composite layers, that will satisfy several different models which makes interchanging different layers to produce different models an easier task.

A.1.4 Surface Symmetry

We are here concerned with the possible symmetries of the surface structure itself rather than any symmetry of the diffraction geometry which are discussed in the next section. Structural symmetries in question are axes of rotation, mirror planes, glide planes and combinations thereof.

There are three levels of symmetry to be considered in a SATLEED calculation:

1. The ideal termination (unrelaxed, unreconstructed) of the substrate may possess symmetry. Thus, an ideally terminated fcc(100) surface has a 4-fold rotational axis and 4 mirror planes (passing through suitable points on the surface). This substrate symmetry is labelled S.

2. A reference structure, used in program TLEED1, may possess equal or lower symmetry, labelled S1. For instance, an overlayer on fcc(100) may have a (2x1) superlattice by adsorbing in bridge sites: either of these conditions lowers the symmetry by breaking the 4-fold rotational symmetry and at least 2 of the 4 mirror planes.

3. A structure examined in the course of a structural search, i.e. a trial structure which is used in program TLEED2, may have another symmetry, labelled S2, which must be equal to or lower than S1. Thus, in the course of an automated search, structures having no symmetry whatever might be explored. Note that one can specify that trial structures obey certain symmetries, if so desired.

4. It is normally assumed that a surface structure with symmetry lower than that of the substrate exists on the sample in structurally equivalent, but orientationally different, domains and that these domains have equal areas. Then, the measured intensities are averages over these domains, taken with equal weights. The program TLEED2 makes the same assumption.

   A simple general rule is that a lower-symmetry surface structure can exist in as many domain orientations as the symmetry elements of the ideally terminated

substrate can generate. Thus, on fcc(100), any proposed totally asymmetrical surface structure can exist in four equivalent orientations, i.e. 4 domains, due to the 4-fold rotation and mirror symmetries. But if the proposed structure has some symmetry element itself, such as a mirror plane, some of these 4 domains will be indistinguishable, so that we may end up with just 2 or even 1 domain orientations.

One practical consequence is that we must specify (in an input file) that all beams be calculated which will have to be averaged together in the course of domain-averaging. Thus, we must input a list of all beams that will have to be calculated and subsequently averaged together.

Two codes are input to specify the desired symmetry levels, one (NSYMS) specifying the symmetry S2 that the trial structures must obey during the search, and another (NSYM) which adds the symmetry elements required to recover symmetry S1 from S2.

A.1.5 Diffraction Symmetry

For privileged incidence directions, the diffracted beams exhibit symmetries that reflect the surface structural symmetries, i.e. beam intensities will show corresponding symmetries. Normal incidence produces beam symmetries which are identical to those of the surface structure. Off-normal incidence in a mirror plane of the structure produces beams with a mirror-plane symmetry, and similarly for glide planes. (However, symmetrically-equivalent domains on the surface can increase the apparent symmetry between diffracted beams at normal incidence, often to the symmetry level of the ideally-terminated substrate.)

With the SATLEED programs, such diffraction symmetries can be exploited at all levels of the theory (i.e. both in the plane-wave and in the spherical-wave representations). This yields large savings in computer time for highly symmetric structures. To make use of this capability or to turn it off, the user simply specifies the appropriate symmetry code NSYMS.

A.1.6 Layers and Interlayer Vectors

An important step in preparing a LEED calculation is the assignment of atoms to different simple or composite layers (as described in section A.1.5 above). This section aims at giving an idea about what is possible.

Also, by providing values for the parameters NST1, NST1EFF, IVECT and NLAY for several examples, it is shown how a structure can be entered into the codes.

Sample input files and a more detailed description can be found in Appendix A. Note that there are always several different ways for putting in the structure. These are also described in Appendix A.

In the following examples, the input parameters with which the code would work most rapidly are given.

1. clean surfaces with single layer AB stacking (e.g. fcc(100)-(1x1), fcc(110)-(1x1), bcc(100)-(1x1), hcp(0001)-(1x1))
(a) parameters for the variation of the 1st layer distance: NST1 = 3; NST1EFF = 1; IVECT = 1; NLAY = 1,1,1
(b) parameters for the variation of the 1st and 2nd layer distances: NST1 = 4; NST1EFF = 2; IVECT = 1; NLAY = 1,1,1,1
(c) parameters for the variation of the 1st, 2nd and 3rd layer distances: NST1 = 5; NST1EFF = 3; IVECT = 1; NLAY = 1,1,1,1,1

2) Overlayer structures on surfaces with single layer AB stacking with the registry from A layer to B layer being equal to the registry from B layer to A layer (e.g. fcc(100)-p(2x2)-O, fcc(110)-(1x3)-H, bcc(100)-c(2x2)-N); the examples below are for one adsorbate atom in a p(2x2) overlayer unit cell; more adatoms per unit cell can be handled by increasing the first number in NLAY. Note that ASA has none vanishing y and/or z components in these examples.
(a) parameters for the variation of the adsorbate height over a bulk like substrate: NST1 = 2; NST1EFF = 1; IVECT = 1; NLAY = 1,1

(b) parameters for the variation of the adsorbate height and a 1st substrate layer relaxation: NST1 = 3; NST1EFF = 2; IVECT = 1; NLAY = 1,4,1
(c) parameters for the variation of the adsorbate height and a 1^{st} and 2^{nd} substrate layer relaxation: NST1 = 4; NST1EFF = 3; IVECT = 1; NLAY = 1,4,4,1

A.1.7 Preparing Input Files for Calculations

A specific order for preparing the various files and quantities is proposed that must be set for any particular calculation. Only quantities that require special comments here will be discussed. Details for remaining quantities are explained within the program software. In addition, a sample of the input files and main programs for the system Cu{100}-c(2x2)-Pt system will be attached at the end of this appendix.

It is assumed that a set of appropriate phase shifts to be inserted in file TLEED5.I have been proposed. It is also assumed that the it is decided how to organise the atoms in layers: as simple layers and composite layers discussed previously.

a) Input File: TLEED5.I

This file is read by both TLEED1 and TLEED2. It defines a reference structure and the main diffraction conditions (geometry, energies, etc.). The main input parameters needed in this file are described below.

IDEG: this is the highest rotational structural symmetry common to all "simple" layers, including the simple layers within composite layers, independent of direction of incidence ("simple layers" consist of one layer of atoms while "composite layers" are made of two or more layers of atoms). Possible values are 2, 3, 4 and 6 (any periodic simple layer has at least 2-fold rotational symmetry). Thus, when an overlayer with 2-fold rotational structural symmetry lies on a substrate with 3-fold rotational symmetry, IDEG=2.

NL1, NL2: these are calculated automatically and do not have to be entered. These two integers are chosen such that the lattice points n*ARA1 + m*ARA2 (with

n=0,...,NL1-1 and m=0,...,NL2-1) produce a set of unique points in the superlattice unit cell. Thus, none of these NL1*NL2 lattice points can be translated onto each other by the superlattice translations. For instance, for a $(\sqrt{3}x\sqrt{3})R30^{\circ}$ structure, NL1=3 and NL2=1 (or vice versa: NL1=1, NL2=3). The particular choice of NL1 and NL2 may depend on the particular choice of ARA1, ARA2 and of the corresponding superlattice vectors ARB1, ARB2.

LMAX: The number LMAX+1 (often called the "number of phase shifts") affects the computing effort very much and is thus an important parameter: many matrices have dimensions that depend critically on it, and parts of the computation require times proportional to the 4^{th} or 6th power of LMAX+1. In principle, LMAX should be taken as infinite for full convergence, but LMAX should thus be minimised without damaging the quality of the calculation. LMAX generally grows slowly with increasing Z (atomic number): LMAX=7 is typical for elements in the middle of the periodic table for energies up to about 200 eV. LMAX also grows (roughly linearly) with energy. One should choose LMAX for the worst case in the problem at hand: heaviest atom and highest energy. A trial-and-error approach to determine its optimum value may be used. One may also use a smaller value of LMAX in early stages of a structure determination, and increase it later for higher accuracy.

THDB,AM,FPER,FPAR,DR0: for substrate atoms, one typically uses the bulk Debye temperature for THDB, and FPER=FPAR=1.4 to represent enhanced surface vibration amplitudes, while DR0=0 (zero-point vibration). AM is the atomic mass of the element (e.g. for Cu, AM=63.45 amu). For adsorbed atoms, one often uses a value of THDB calculated to make the vibration amplitudes equal to those of bulk atoms, together with FPER=FPAR=2.0 to represent enhanced surface vibrations. These values are not critical to the structure determination, and may be refined later in a trial-and-error fashion.

Phase shifts: It is important to avoid discontinuities by π as a function of energy, which produce incorrect interpolated phase shifts (the last step in the Barbieri-Van Hove phase shift package specifically removes such discontinuities by π).

ARA1, ARA2: these 2D lattice vectors describe the 2D structure of a "simple" bulk layer. They define the (1x1) lattice. ARA1 and ARA2 should be oriented with care to reflect any desired symmetries and must be consistent with the beam labels (10), (01), etc. Usually, ARA1 is chosen to point in the y-direction (to the right in the surface plane), such that ARA1(2)=0. It is important that the angle between these vectors be consistent with the value of IDEG chosen above (i.e. 360/IDEG, except for IDEG=2, when an angle of 90 degrees rather than 180 degrees should be chosen between ARA1 and ARA2); thus, for a substrate with 3-fold rotational symmetry, the angle between ARA1 and ARA2 can be 120 or 60 degrees, requiring IDEG=3 or 6, respectively.

CAUTION with fcc(111), hcp(0001), diamond(111) and other 3-fold symmetrical substrates: experimentally, one usually does not know the orientation of these substrates within a 180 degrees azimuthal rotation, i.e. rotating the crystal azimuthally by 180 degrees fits the observed pattern equally well (this orientation could be obtained by bulk X-ray diffraction.) In this case, LEED calculations for both orientations are necessary (for all plausible surface structures): the best fit to experiment then decides which is the correct orientation. For off-normal incidence directions, this can be done by changing the incident azimuth by 180 degrees (FI in TLEED5.I) and changing the correspondence between theoretical and experimental beams (see IBP in file RFAC.D). At normal incidence, in principle, a simple relabeling of the already calculated beams is sufficient in place of new calculations.

ARB1, ARB2: these 2D surface vectors are the basic lattice vectors that define the superlattice. The orientations of these 2D superlattice vectors are also important, as they specify one particular domain orientation; their choice implies a particular labeling scheme of the theoretical fractional-order ("extra") beams, relative to the (10) and (01) beams defined by ARA1 and ARA2. Only the beams due to the one domain orientation defined by ARB1 and ARB2 will be calculated. Correspondence with other beams due to other domain orientations should be made through IBP in file RFAC.D.

ASA, ASB: These are the interlayer vectors between different layers as described above.

IFLAG: usually IFLAG=0 is chosen, so that atomic locations in a composite layer are given by 3D vectors. For complex molecules, IFLAG=1 is often convenient, as atomic positions are then defined in terms of bond lengths, bond angles and dihedral angles rather than Cartesian co-ordinates (with the possibility to input only symmetry-inequivalent atoms together with symmetry information to generate the positions of the other symmetry-equivalent atoms).

b) Input File: TLEED4.I

This file is also read by both TLEED1 and TLEED2, but its main use is to direct the search in TLEED2. The main input parameters needed in this file are as floows:

ISTART: set ISTART=1 only when iterating the search by TLEED2, i.e. when restarting TLEED2 with the last trial structure obtained by TLEED2; set ISTART=0 otherwise.

NT0: this is the number of exit beams to be calculated. It should include all the experimentally available beams and those which will have to be averaged to account for different domain orientations.

c) Input File: EXP.D

This file is read by TLEED2 and contains the experimental I-V curves, together with beam-averaging information. The program reads I-V curves for one beam at a time. It requires energy-intensity pairs with a format that the user can choose and must read in explicitly as well (as FMT: formatted Fortran input). The input parameter IAVE indicates which experimental I-V curves are in principle symmetry-equivalent and thus will be averaged together.

c) Input File: RFAC.D

This file is read by TLEED2 and mainly assigns one experimental beam to one or more calculated beams, while specifying how to treat I-V curves such as smoothing

or avergaing and which R-factors to use. The parameter IBP defines the number of symmetrically-inequivalent beams and therefore relates theoretical to experimental beams and hence indicates averaging over theoretical beams, if necessary. For normal incidence, since the theory applies to calculations for only one domain, and since the experiment includes beams for all domain orientations, IBP may be used to relate a theoretical beam calculated for one domain orientation with an equivalent experimental beam measured for another domain orientation.

A.1.8 Input Parameters for the Main Programs

a) TLEED1.for

This program calculates LEED intensities by "exact" multiple- scattering theory for a given "reference structure". Normally only a few parameter statements need be modified from one type of reference structure to another: these are the first few parameter statement lines of the program. Insufficiently large or inconsistent values of the parameters will cause the program to stop with an appropriate warning and explanation.

The parameters: IPNL1, IPNL2, IPLMAX, INLAY, INTAU, INST1, INST2, INT0 and JSMAX should be set equal to the corresponding variables in the input files TLEED5.I and TLEED4.I, namely: NL1, NL2, LMAX, max(NLAY), NEL, NST1, NST1EFF, NT0, LSMAX, respectively. For the other parameters:

IPCLM: use appropriate value NLMS(LMAX) from DATA statement for NLMS in main program TLEED1.

IPCAA: use appropriate value NCA(LMAX) from DATA statement for NCA in main program TLEED1.

IPCUT: a value of 1000 is generally sufficient when no symmetry is used. A much smaller value is appropriate when symmetry is used. The program checks that the input value is sufficient.

NLMB2: use appropriate value from the header of subroutine GAUNT.

NROM: a value of 250 is generally sufficient, but much computer memory is gained by reducing NROM as much as possible. The program checks that the input value is sufficient.

b) TLEED2.for

This program calculates corrected LEED intensities for trial structures that deviate from the reference structure used in program TLEED1, and it optimises the trial structure by iteratively minimising the R-factor(s).

Here also, we need only to modify a few parameter statements from one type of reference structure to another (usually no changes are needed between different runs of TLEED2 for different searches near a given reference structure): these are the first few parameter statement lines of the program.

IPNL1, IPNL2, IPLMAX, INLAY, INTAU, INST1, INT0, JSMAX: should be set equal to corresponding variables in the input files TLEED5.I and TLEED4.I, i.e. just as in program TLEED1 namely: NL1, NL2, LMAX, max(NLAY), NEL, NST1, NT0, LSMAX, respectively.

INLTOT, INLIN, INBED: should be set equal to corresponding variables in the input files TLEED5.I and TLEED4.I, namely: (Σ(NLAY)+number of non-structural parameters), Σ(NLAY) and NTO, respectively.

IPCUT: a value of 1000 is generally sufficient when no symmetry is used. A much smaller value is appropriate when symmetry is used. The program checks that the input value is sufficient.

IINERG: total number of points on calculated energy grid.

IEERG: total number of points of the union of the calculated and measured energy grids, after interpolation onto a common grid with increment EINCR (EINCR is read in from file RFAC.D).

LIMITATIONS:

Currently, this Symmetrised Automated Tensor LEED program

1) does not allow off-normal incidence;

2) is valid for the RFS (Renormalised Forward Scattering) scheme only;

3) does not allow use of glide-plane symmetry.

A.1.9 Example Input Files: The Cu{100}-c(2x2)-Pt Underlayer

TLEED5.I

```
Cu(100)-c(2x2)-Pt   Ehab's phase shifts  underlayer pt3
  4                    IDEG
 20                    NPSI
 0.2000 1.200         FR ASE (the radius??)
 0.0020                TST
 0.00   0.00          THETA FI
  7.50  -5.50          VV VI
  9                    LMAX
  2                    NEL
  1  1                 IT
 315.0000  63.5460   1.0000   1.0000   0.0700   THDB1 AM1 FPER1 FPAR1DR01
 150.0000 195.0900   1.0000   1.0000   0.0700    THDB2 AM2 FPER2FPAR2DR02
 330.0000                                       TI
 0.1838
 3.2623  .0649 -.2036  .0002  .0000  .0000  .0000  .0000
-0.3857-0.0807-1.5018 0.0008 0.0000 0.0000 0.0000 0.0000 0.0000
  .3676
 3.0987  .1302 -.1216  .0024  .0001  .0000  .0000  .0000
-0.6061-0.1776-0.4183 0.0083 0.0003 0.0000 0.0000 0.0000 0.0000
 0.5514
 2.9391  .1596 -.1342  .0087  .0004  .0000  .0000  .0000
-0.7961-0.2712-0.4741 0.0307 0.0015 0.0001 0.0000 0.0000 0.0000
  .7353
 2.7933  .1561 -.1386  .0213  .0013  .0001  .0000  .0000
-0.9659-0.3620-0.5426 0.0764 0.0049 0.0003 0.0000 0.0000 0.0000
 0.9191
 2.6612  .1301 -.1327  .0416  .0030  .0002  .0000  .0000
-1.1200-0.4509-0.6044 0.1531 0.0115 0.0008 0.0001 0.0000 0.0000
 1.4706
 2.3304 -.0085 -.0768  .1559  .0174  .0017  .0001  .0000
-1.5108-0.7065-0.7429 0.5813 0.0636 0.0072 0.0007 0.0001 0.0000
 2.0221
 2.0726 -.1662 -.0205  .3328  .0509  .0070  .0008  .0001
 1.3196-0.9398-0.8429 1.0328 0.1794 0.0273 0.0037 0.0004 0.0000
 2.9412
 1.7486 -.3981  .0069  .6239  .1493  .0307  .0051  .0007
 0.9205-1.2682-0.9961 1.3778 0.4778 0.1065 0.0217 0.0036 0.0005
 4.0441
 1.4641 -.6131 -.0160  .8518  .2920  .0876  .0209  .0040
 0.5638 1.5672-1.1751 1.5401 0.8246 0.2591 0.0762 0.0185 0.0036
 4.9633
 1.2749 -.7558 -.0401  .9872  .3910  .1492  .0456  .0110
 0.3237 1.3616-1.3066-1.5431 1.0652 0.3880 0.1448 0.0451 0.0114
 6.0662
 1.0813 -.9023 -.0674 1.1185  .4805  .2208  .0863  .0267
 0.0763 1.1495-1.4423-1.5200 1.3131 0.5203 0.2334 0.0930 0.0302
 6.9853
  .9400-1.0109 -.0919 1.2042  .5418  .2707  .1237  .0458
-0.1046 0.9924-1.5438-1.5158 1.4796 0.6193 0.3000 0.1391 0.0543
 8.0883
  .7902-1.1277 -.1237 1.2836  .6077  .3195  .1657  .0734
-0.2962 0.8233 1.4842-1.5176-1.5018 0.7304 0.3708 0.1927 0.0899
 9.0074
  .6795-1.2146 -.1500 1.3371  .6566  .3549  .1960  .0977
-0.4382 0.6972 1.3959-1.5243-1.3889 0.8137 0.4266 0.2330 0.1210
 9.9264
  .5795-1.2932 -.1746 1.3836  .6991  .3879  .2221  .1209
-0.5673 0.5826 1.3141-1.5358-1.2900 0.8866 0.4805 0.2698 0.1506
11.0294
  .4708-1.3782 -.2011 1.4320  .7425  .4250  .2499  .1457
-0.7093 0.4571 1.2243-1.5535-1.1893 0.9633 0.5417 0.3122 0.1827
11.9485
  .3876-1.4430 -.2213 1.4664  .7739  .4534  .2715  .1637
-0.8193 0.3600 1.1555-1.5690-1.1187 1.0215 0.5880 0.3474 0.2078
13.0514
  .2950-1.5151 -.2443 1.5006  .8079  .4837  .2965  .1832
-0.9428 0.2507 1.0781 1.5545-1.0457 1.0864 0.6376 0.3883 0.2366
13.9706
  .2228-1.5714 -.2629 1.5241  .8343  .5060  .3164  .1983
```

```
-1.0393 0.1648 1.0168 1.5399-0.9912 1.1363 0.6754 0.4203 0.2609
14.7059
  .1681-1.6141 -.2775 1.5404  .8543  .5222  .3314  .2101
-1.1125 0.0994 0.9695 1.5281-0.9510 1.1729 0.7041 0.4441 0.2802
 2.5560 0.0000            ARA1   (SUBSTRATE LATTICE VECTORS)
 0.0000 2.5560            ARA2
 2.5560 2.5560            ARB1   (OVERLAYER LATTICE VECTORS)
-2.5560 2.5560            ARB2
  1                       IVECT  (NUMBER OF INTERLAYER VECTORS IN INPUT)
 1.8075000  0.0000000  0.00000000     ASA(1,J),J=1,3
  2  1  1                          NST1,NST1EFF,NTENS
  8  1              NLAY(i),i=1,NST1  (1 layer, two, one(bulk))
  0                               IFLAG
  2  1                         NTAU(i),i=1,NST1 (Cu, Cu+Pt, Cu)
  1  1  1  2  1  1  1  1                  LPS(1) (Cu=1)
  1                            LPS(2) (Cu=1, Pt=2)
 -0.0570  0.0000  0.0000    1   (coord.(perp,paral) of atom 1 in lstlayer)
 -0.0610  0.0000  2.5560    2
  1.8400 -1.2780  1.2780    4     CARE!
  1.7600  1.2780  1.2780    3 Pt  Care
  3.7100  0.0000  0.0000    5     asb(2,j),j=1,3
  3.7100  0.0000  2.5560    6
  5.5100  1.2780  1.2780    7
  5.5350 -1.2780  1.2780    8
  1.8075  0.0000  0.0000
    0.50     0.00    -5.00          FRCL(2),VCL(2),VICL(2)
  7.3420   0.0000   0.0000
  1.8075   0.0000   0.0000          asb(3,j),j=1,3
    0.50     0.00    -5.00          FRCL(3),VCL(3),VICL(3)
  40.00  500.0    5.00               EI,EF,DE
```

TLEED4.I

```
1  1  0                    IPR  ISTART LRFLAG
  8  8  0.02 0.20            NSYM NSYMS  STEP   VSTEP
  5  1  4  8                 NT0  NSET   LSMAX  LLCUT
  5                          NINSET(1)
 1.0000 0.0000               BEAM 1
 1.0000 1.0000               BEAM 2
 0.5000 0.5000               BEAM 3
 1.5000 0.5000               BEAM 4
 2.0000 0.0000               BEAM 5
  1                          NDIM
 0.0000 0.0000 0.0000  1     DISP(1,i)  I=1,3  LFLAG
 0.0000 0.0000 0.0000  1     DISP(2,i)  I=1,3  LFLAG
 0.0000 0.0000 0.0000  1
 0.0000 0.0000 0.0000  1
 0.0000 0.0000 0.0000  1
 0.0000 0.0000 0.0000  1
 0.0000 0.0000 0.0000  1
 0.0000 0.0000 0.0000  1
 0.0000  1                  DVOPT, LSFLAG
  2  0  0                   MFLAG, NGRID, NIV
200                         ITMAX
 1.0000 0.5000 2.0000       ALPHA,BETA,GAMMA
 0.001  0.0005              FTOL1,FTOL2
 20  .0050                  NSTEP,STSZ
 1.000  0.000  0.000  0.000  0.000     UDIR
 0.000  1.000  0.000  0.000  0.000     UDIR
 0.000  0.000  1.000  0.000  0.000     UDIR
 0.000  0.000  0.000  1.000  0.000     UDIR
 0.000  0.000  0.000  0.000  1.000     UDIR
```

EXP.D

```
Cu(100)-c(2x2)-
Pt
 5
  1  2  3  4  5
(F6.2,F8.5)
 1.00
(1,0)
433
1.0000E+000
 63.12 3.29253
 64.08 3.78536
 65.04 4.29568
 66.00 5.35402
 66.96 6.43115
 67.92 7.50194
 68.88 8.48091
 69.84 9.25649
 70.80 9.75535
 71.76 9.90028
 72.72 9.70176
 73.68 9.16279
 74.64 8.41114
 75.60 7.49043
 76.56 6.53212
 77.52 5.60356
 78.48 4.81580
 79.44 4.16916
 80.40 3.71034
 81.36 3.38533
 82.32 3.15516
 83.28 2.96692
 84.24 2.79918
 85.20 2.61279
 86.16 2.40574
 87.12 2.19003
 88.08 1.96846
 89.04 1.71876
 90.00 1.47710
 90.96 1.23126
 91.92 0.97959
 92.88 0.75450
 93.84 0.57346
 94.80 0.43945
 95.76 0.36413
 96.72 0.36024
 97.68 0.39770
 98.64 0.46066
 99.60 0.51409
100.56 0.58504
101.52 0.64340
102.48 0.69304
103.44 0.74520
104.40 0.82387
105.36 0.90553
106.32 1.01791
107.28 1.15900
108.24 1.31408
109.20 1.47348
110.16 1.64604
111.12 1.83711
112.08 2.03812
113.04 2.30608
114.00 2.67662
114.96 3.11008
115.92 3.64615
116.88 4.22483
117.84 4.77528
118.80 5.20926
119.76 5.51837
120.72 5.64250
121.68 5.61636
122.64 5.48172
123.60 5.30296
124.56 5.13822
125.52 5.01825
126.48 4.98137
127.44 5.04084
128.40 5.19060
129.36 5.39395
130.32 5.64123
131.28 5.91280
132.24 6.19129
133.20 6.45804
134.16 6.73510
135.12 6.99384
136.08 7.21731
137.04 7.38905
138.00 7.51380
138.96 7.55016
139.92 7.49287
140.88 7.35588
141.84 7.11565
142.80 6.78037
143.76 6.38334
144.72 5.94502
145.68 5.48383
146.64 5.04887
147.60 4.64956
148.56 4.31379
149.52 4.03585
150.48 3.80293
151.44 3.59524
152.40 3.40380
153.36 3.18937
154.32 2.95733
155.28 2.71774
156.24 2.46825
157.20 2.21883
158.16 1.99033
159.12 1.78280
160.08 1.58905
161.04 1.42666
162.00 1.28058
162.96 1.15561
163.92 1.05828
164.88 0.99431
165.84 0.96199
166.80 0.97989
167.76 1.03039
168.72 1.10707
169.68 1.19889
170.64 1.29517
171.60 1.37934
172.56 1.45418
173.52 1.51723
174.48 1.56424
175.44 1.60084
176.40 1.61692
177.36 1.61701
178.32 1.58947
179.28 1.54002
180.24 1.45408
181.20 1.34092
182.16 1.19764
183.12 1.03114
184.08 0.85307
185.04 0.67870
186.00 0.52354
186.96 0.39167
187.92 0.29886
188.88 0.23991
189.84 0.21575
190.80 0.21780
191.76 0.24332
192.72 0.29219
193.68 0.36250
194.64 0.45300
195.60 0.55874
196.56 0.67943
197.52 0.81429
198.48 0.95963
199.44 1.11523
200.40 1.28382
201.36 1.47424
202.32 1.67275
203.28 1.88906
204.24 2.10571
205.20 2.32387
206.16 2.53472
207.12 2.73441
208.08 2.91596
209.04 3.08388
210.00 3.23141
210.96 3.34033
211.92 3.41214
212.88 3.42549
213.84 3.37407
214.80 3.26762
215.76 3.11554
216.72 2.93965
217.68 2.76036
218.64 2.59444
219.60 2.44006
220.56 2.30217
221.52 2.16445
222.48 2.02627
223.44 1.88611
224.40 1.74013
225.36 1.59801
226.32 1.46639
227.28 1.34948
228.24 1.25477
229.20 1.18273
230.16 1.12714
231.12 1.08367
232.08 1.05270
233.04 1.02820
234.00 1.00941
234.96 0.99550
235.92 0.98824
236.88 0.98811
237.84 0.99354
238.80 1.00737
239.76 1.03107
240.72 1.05900
241.68 1.08932
242.64 1.12156
243.60 1.14507
244.56 1.16374
245.52 1.17588
246.48 1.17128
247.44 1.15018
248.40 1.12416
249.36 1.08616
250.32 1.03860
251.28 0.98953
252.24 0.93942
253.20 0.88365
254.16 0.82345
255.12 0.76931
256.08 0.72264
257.04 0.68203
258.00 0.65729
258.96 0.64831
259.92 0.65042
260.88 0.66470
261.84 0.69180
262.80 0.72068
263.76 0.75190
264.72 0.78430
265.68 0.80696
266.64 0.81930
267.60 0.82215
268.56 0.81579
269.52 0.79332
270.48 0.76311
271.44 0.72691
272.40 0.68743
273.36 0.64299
274.32 0.60338
275.28 0.56714
276.24 0.53129
277.20 0.49774
278.16 0.46782
279.12 0.43358
280.08 0.39857
281.04 0.36559
282.00 0.32866
282.96 0.29287
283.92 0.25941
284.88 0.22844
285.84 0.19891
286.80 0.17450
287.76 0.15535
288.72 0.13832
289.68 0.12304
290.64 0.11067
291.60 0.10728
292.56 0.10213
293.52 0.10401
294.48 0.11164
295.44 0.12690
296.40 0.14286
297.36 0.16780
298.32 0.20095
299.28 0.24233
300.24 0.28715
301.20 0.33943
302.16 0.39687
303.12 0.45933
304.08 0.52118
305.04 0.58682
306.00 0.65979
306.96 0.73076
307.92 0.79661
308.88 0.86365
309.84 0.92726
310.80 0.96890
311.76 1.01594
312.72 1.05398
313.68 1.08629
314.64 1.11269
315.60 1.14270
316.56 1.15729
317.52 1.16616
318.48 1.16296
319.44 1.15115
320.40 1.13298
321.36 1.10639
322.32 1.08436
323.28 1.06566
324.24 1.04999
325.20 1.03566
326.16 1.02948
327.12 1.02070
328.08 1.01639
329.04 1.00875
330.00 1.00113
330.96 0.98735
331.92 0.97121
332.88 0.94495
333.84 0.91766
334.80 0.88191
335.76 0.84205
336.72 0.79579
337.68 0.74593
338.64 0.69316
339.60 0.64235
340.56 0.60005
341.52 0.56051
```

342.48 0.53029
343.44 0.50933
344.40 0.49528
345.36 0.48311
346.32 0.48386
347.28 0.49206
348.24 0.50238
349.20 0.51814
350.16 0.55081
351.12 0.58177
352.08 0.61039
353.04 0.64537
354.00 0.67750
354.96 0.69463
355.92 0.71100
356.88 0.72643
357.84 0.73256
358.80 0.73872
359.76 0.75205
360.72 0.76053
361.68 0.76572
362.64 0.76921
363.60 0.76910
364.56 0.75284
365.52 0.73781
366.48 0.71732
367.44 0.69488
368.40 0.66946
369.36 0.64718
370.32 0.62318
371.28 0.60320
372.24 0.58298
373.20 0.56775
374.16 0.55412
375.12 0.54930
376.08 0.54634
377.04 0.54676
378.00 0.55009
378.96 0.55498
379.92 0.56140
380.88 0.56873
381.84 0.57809
382.80 0.58224
383.76 0.58635
384.72 0.58318
385.68 0.57826
386.64 0.56903
387.60 0.56072
388.56 0.55165
389.52 0.53951
390.48 0.52622
391.44 0.51328
392.40 0.49851
393.36 0.48781
394.32 0.47776
395.28 0.46907
396.24 0.46097
397.20 0.45821
398.16 0.45348
399.12 0.45248
400.08 0.45052
401.04 0.45236
402.00 0.45295
402.96 0.46062
403.92 0.46493
404.88 0.47372
405.84 0.48044
406.80 0.48750
407.76 0.48669
408.72 0.48882
409.68 0.49271
410.64 0.49839
411.60 0.50501
412.56 0.51566
413.52 0.52677
414.48 0.53695
415.44 0.54837
416.40 0.56038
417.36 0.57009
418.32 0.58081
419.28 0.59015
420.24 0.59740
421.20 0.60510
422.16 0.61308
423.12 0.62003
424.08 0.63209
425.04 0.64287
426.00 0.65195
426.96 0.66833
427.92 0.68456
428.88 0.69551
429.84 0.70769
430.80 0.71999
431.76 0.72615
432.72 0.73140
433.68 0.73848
434.64 0.74803
435.60 0.76001
436.56 0.77136
437.52 0.79078
438.48 0.81454
439.44 0.83813
440.40 0.86845
441.36 0.90267
442.32 0.93550
443.28 0.96862
444.24 1.01054
445.20 1.05040
446.16 1.08979
447.12 1.12963
448.08 1.16781
449.04 1.19861
450.00 1.22212
450.96 1.23898
451.92 1.25343
452.88 1.26389
453.84 1.27386
454.80 1.27018
455.76 1.26655
456.72 1.24909
457.68 1.22217
458.64 1.17863
459.60 1.13625
460.56 1.08195
461.52 1.02551
462.48 0.96427
463.44 0.90332
464.40 0.84204
465.36 0.78250
466.32 0.72520
467.28 0.67186
468.24 0.62632
469.20 0.58455
470.16 0.55133
471.12 0.51933
472.08 0.49057
473.04 0.46024
474.00 0.43791
474.96 0.41312
475.92 0.39162
476.88 0.37446
477.84 0.35978
(1,1)
378 1.0000E+000
103.44 0.88585
104.40 0.95695
105.36 1.03552
106.32 1.18633
107.28 1.33930
108.24 1.47847
109.20 1.57335
110.16 1.61087
111.12 1.58686
112.08 1.50567
113.04 1.37995
114.00 1.22489
114.96 1.06364
115.92 0.90876
116.88 0.77580
117.84 0.67307
118.80 0.60491
119.76 0.56312
120.72 0.54517
121.68 0.54366
122.64 0.55180
123.60 0.56451
124.56 0.58476
125.52 0.61428
126.48 0.65589
127.44 0.71622
128.40 0.79790
129.36 0.90120
130.32 1.02585
131.28 1.17011
132.24 1.32497
133.20 1.48633
134.16 1.64589
135.12 1.79311
136.08 1.91869
137.04 2.01838
138.00 2.08389
138.96 2.11331
139.92 2.10895
140.88 2.07356
141.84 2.01102
142.80 1.92903
143.76 1.83405
144.72 1.73059
145.68 1.62491
146.64 1.52158
147.60 1.42417
148.56 1.33372
149.52 1.25247
150.48 1.18012
151.44 1.11576
152.40 1.05792
153.36 1.00754
154.32 0.96298
155.28 0.92269
156.24 0.88544
157.20 0.84750
158.16 0.80394
159.12 0.75313
160.08 0.69511
161.04 0.63153
162.00 0.56983
162.96 0.52049
163.92 0.49348
164.88 0.50221
165.84 0.56069
166.80 0.68220
167.76 0.87785
168.72 1.15944
169.68 1.53201
170.64 1.99824
171.60 2.55733
172.56 3.20508
173.52 3.93166
174.48 4.72461
175.44 5.56506
176.40 6.42384
177.36 7.26668
178.32 8.05347
179.28 8.74429
180.24 9.29930
181.20 9.68827
182.16 9.89065
183.12 9.89943
184.08 9.71537
185.04 9.35470
186.00 8.84569
186.96 8.22178
187.92 7.51915
188.88 6.77823
189.84 6.03520
190.80 5.31613
191.76 4.64206
192.72 4.02742
193.68 3.47946
194.64 2.99913
195.60 2.58635
196.56 2.23636
197.52 1.94239
198.48 1.69443
199.44 1.48167
200.40 1.29335
201.36 1.12172
202.32 0.96103
203.28 0.81070
204.24 0.67432
205.20 0.55630
206.16 0.46062
207.12 0.39103
208.08 0.34774
209.04 0.32806
210.00 0.32786
210.96 0.34314
211.92 0.36984
212.88 0.40617
213.84 0.45231
214.80 0.50988
215.76 0.58017
216.72 0.66427
217.68 0.76119
218.64 0.86744
219.60 0.97847
220.56 1.08907
221.52 1.19404
222.48 1.28903
223.44 1.37226
224.40 1.44260
225.36 1.50058
226.32 1.54677
227.28 1.58314
228.24 1.61040
229.20 1.62955
230.16 1.64068
231.12 1.64418
232.08 1.63863
233.04 1.62275
234.00 1.59499
234.96 1.55394
235.92 1.49861
236.88 1.42894
237.84 1.34600
238.80 1.25161
239.76 1.14830
240.72 1.03858
241.68 0.92655
242.64 0.81578
243.60 0.70967
244.56 0.61114
245.52 0.52368
246.48 0.44800
247.44 0.38452
248.40 0.33349
249.36 0.29520
250.32 0.26827
251.28 0.25338
252.24 0.25078
253.20 0.26028
254.16 0.28179
255.12 0.31665
256.08 0.36472
257.04 0.42710
258.00 0.50545
258.96 0.60041
259.92 0.71180
260.88 0.84035
261.84 0.98511
262.80 1.14410
263.76 1.31575

264.72 1.49859
265.68 1.68954
266.64 1.88759
267.60 2.09259
268.56 2.30523
269.52 2.52633
270.48 2.75887
271.44 3.00306
272.40 3.25776
273.36 3.51964
274.32 3.78307
275.28 4.03820
276.24 4.27498
277.20 4.48262
278.16 4.65025
279.12 4.76891
280.08 4.83344
281.04 4.84101
282.00 4.79227
282.96 4.69249
283.92 4.54929
284.88 4.37196
285.84 4.17147
286.80 3.95781
287.76 3.73781
288.72 3.51677
289.68 3.29648
290.64 3.07646
291.60 2.85524
292.56 2.63151
293.52 2.40360
294.48 2.17214
295.44 1.93851
296.40 1.70577
297.36 1.47890
298.32 1.26378
299.28 1.06658
300.24 0.89355
301.20 0.74954
302.16 0.63716
303.12 0.55785
304.08 0.51033
305.04 0.49171
306.00 0.49823
306.96 0.52565
307.92 0.56884
308.88 0.62350
309.84 0.68546
310.80 0.75139
311.76 0.81793
312.72 0.88251
313.68 0.94315
314.64 0.99829
315.60 1.04630
316.56 1.08685
317.52 1.11994
318.48 1.14544
319.44 1.16377
320.40 1.17514
321.36 1.17899
322.32 1.17502
323.28 1.16277
324.24 1.14201
325.20 1.11299
326.16 1.07714
327.12 1.03593
328.08 0.99138
329.04 0.94508
330.00 0.89916
330.96 0.85485
331.92 0.81300
332.88 0.77426
333.84 0.73966
334.80 0.70915
335.76 0.68262
336.72 0.66008
337.68 0.64136
338.64 0.62489
339.60 0.60985
340.56 0.59540
341.52 0.58062
342.48 0.56433
343.44 0.54714
344.40 0.52915
345.36 0.51049
346.32 0.49152
347.28 0.47287
348.24 0.45416
349.20 0.43490
350.16 0.41467
351.12 0.39296
352.08 0.36926
353.04 0.34341
354.00 0.31608
354.96 0.28836
355.92 0.26147
356.88 0.23694
357.84 0.21634
358.80 0.20048
359.76 0.18959
360.72 0.18358
361.68 0.18206
362.64 0.18470
363.60 0.19123
364.56 0.20170
365.52 0.21655
366.48 0.23622
367.44 0.26050
368.40 0.28971
369.36 0.32394
370.32 0.36246
371.28 0.40437
372.24 0.44954
373.20 0.49715
374.16 0.54639
375.12 0.59730
376.08 0.65030
377.04 0.70536
378.00 0.76294
378.96 0.82346
379.92 0.88694
380.88 0.95300
381.84 1.02075
382.80 1.08877
383.76 1.15571
384.72 1.22032
385.68 1.28165
386.64 1.34013
387.60 1.39676
388.56 1.45341
389.52 1.51238
390.48 1.57624
391.44 1.64660
392.40 1.72571
393.36 1.81428
394.32 1.91267
395.28 2.02089
396.24 2.13939
397.20 2.26651
398.16 2.40119
399.12 2.54120
400.08 2.68303
401.04 2.82139
402.00 2.95169
402.96 3.06811
403.92 3.16542
404.88 3.23954
405.84 3.28771
406.80 3.30836
407.76 3.30164
408.72 3.26884
409.68 3.21223
410.64 3.13550
411.60 3.04147
412.56 2.93383
413.52 2.81618
414.48 2.69156
415.44 2.56208
416.40 2.43164
417.36 2.30288
418.32 2.17831
419.28 2.06082
420.24 1.95291
421.20 1.85541
422.16 1.76882
423.12 1.69355
424.08 1.62873
425.04 1.57337
426.00 1.52642
426.96 1.48730
427.92 1.45464
428.88 1.42772
429.84 1.40583
430.80 1.38852
431.76 1.37475
432.72 1.36355
433.68 1.35377
434.64 1.34427
435.60 1.33370
436.56 1.32098
437.52 1.30559
438.48 1.28721
439.44 1.26566
440.40 1.24056
441.36 1.21194
442.32 1.17978
443.28 1.14400
444.24 1.10482
445.20 1.06316
446.16 1.01976
447.12 0.97514
448.08 0.92987
449.04 0.88435
450.00 0.83868
450.96 0.79287
451.92 0.74756
452.88 0.70340
453.84 0.66122
454.80 0.62181
455.76 0.58608
456.72 0.55390
457.68 0.52573
458.64 0.50120
459.60 0.47997
460.56 0.46159
461.52 0.44620
462.48 0.43245
463.44 0.41977
464.40 0.40764
465.36 0.39533
(1/2,1/2)
270 1.0000E+000
42.00 2.85987
42.96 2.93879
43.92 3.22269
44.88 3.61878
45.84 4.10063
46.80 4.51194
47.76 4.72958
48.72 4.65004
49.68 4.27270
50.64 3.65924
51.60 2.92265
52.56 2.18766
53.52 1.53583
54.48 1.02046
55.44 0.66515
56.40 0.46020
57.36 0.38329
58.32 0.42528
59.28 0.58380
60.24 0.84518
61.20 1.18635
62.16 1.59526
63.12 2.06821
64.08 2.59099
65.04 3.14451
66.00 3.68300
66.96 4.15059
67.92 4.47992
68.88 4.64038
69.84 4.63414
70.80 4.51672
71.76 4.35234
72.72 4.21217
73.68 4.12940
74.64 4.11800
75.60 4.17156
76.56 4.28473
77.52 4.44337
78.48 4.63463
79.44 4.83746
80.40 5.01968
81.36 5.14671
82.32 5.18049
83.28 5.10211
84.24 4.89102
85.20 4.55833
86.16 4.11404
87.12 3.59811
88.08 3.03844
89.04 2.48328
90.00 1.95879
90.96 1.49664
91.92 1.10479
92.88 0.79890
93.84 0.57715
94.80 0.44126
95.76 0.38054
96.72 0.39065
97.68 0.46054
98.64 0.58595
99.60 0.75683
100.56 0.97587
101.52 1.24209
102.48 1.56266
103.44 1.94398
104.40 2.39650
105.36 2.92538
106.32 3.52871
107.28 4.19750
108.24 4.90941
109.20 5.64171
110.16 6.37070
111.12 7.08042
112.08 7.74822
113.04 8.35396
114.00 8.87945
114.96 9.30702
115.92 9.62522
116.88 9.82220
117.84 9.90118
118.80 9.86188
119.76 9.71856
120.72 9.47935
121.68 9.16554
122.64 8.79409
123.60 8.38859
124.56 7.95959
125.52 7.51928
126.48 7.08163
127.44 6.66362
128.40 6.27733
129.36 5.93167
130.32 5.62899
131.28 5.36700
132.24 5.13681
133.20 4.93072
134.16 4.73516
135.12 4.53705
136.08 4.31705
137.04 4.06086

138.00 3.75445
138.96 3.39954
139.92 3.00819
140.88 2.60614
141.84 2.22123
142.80 1.88440
143.76 1.61601
144.72 1.42545
145.68 1.30554
146.64 1.24520
147.60 1.22482
148.56 1.22456
149.52 1.22246
150.48 1.20431
151.44 1.15829
152.40 1.08295
153.36 0.98032
154.32 0.86033
155.28 0.73098
156.24 0.60315
157.20 0.48644
158.16 0.39033
159.12 0.32353
160.08 0.29274
161.04 0.30140
162.00 0.34704
162.96 0.42563
163.92 0.53085
164.88 0.66326
165.84 0.81145
166.80 0.96611
167.76 1.11292
168.72 1.24970
169.68 1.37214
170.64 1.49067
171.60 1.62081
172.56 1.77512
173.52 1.95178
174.48 2.14418
175.44 2.34281
176.40 2.53316
177.36 2.70705
178.32 2.86626
179.28 3.00673
180.24 3.11997
181.20 3.19299
182.16 3.22135
183.12 3.19783
184.08 3.12907
185.04 3.02388
186.00 2.90330
186.96 2.77731
187.92 2.65718
188.88 2.54790
189.84 2.45718
190.80 2.39058
191.76 2.34960
192.72 2.33571
193.68 2.34931
194.64 2.38970
195.60 2.44491
196.56 2.50874
197.52 2.57098
198.48 2.62936
199.44 2.67441
200.40 2.70704
201.36 2.72583
202.32 2.74050
203.28 2.75020
204.24 2.76234
205.20 2.77655
206.16 2.80296
207.12 2.83865
208.08 2.88419
209.04 2.93510
210.00 2.99103
210.96 3.04974
211.92 3.10435
212.88 3.15244
213.84 3.18622
214.80 3.20714
215.76 3.20820
216.72 3.19465
217.68 3.16622
218.64 3.13418
219.60 3.09989
220.56 3.07579
221.52 3.05942
222.48 3.05383
223.44 3.05077
224.40 3.05443
225.36 3.05510
226.32 3.05577
227.28 3.05250
228.24 3.05468
229.20 3.05763
230.16 3.06447
231.12 3.07803
232.08 3.09265
233.04 3.10480
234.00 3.10561
234.96 3.09992
235.92 3.08073
236.88 3.05577
237.84 3.02008
238.80 2.97610
239.76 2.91436
240.72 2.83605
241.68 2.74129
242.64 2.63900
243.60 2.53460
244.56 2.43083
245.52 2.32555
246.48 2.21939
247.44 2.11195
248.40 2.00530
249.36 1.90258
250.32 1.81005
251.28 1.73047
252.24 1.66445
253.20 1.61321
254.16 1.58179
255.12 1.57012
256.08 1.57616
257.04 1.59032
258.00 1.60801
258.96 1.61771
259.92 1.61436
260.88 1.59540
261.84 1.56580
262.80 1.52614
263.76 1.47711
264.72 1.42241
265.68 1.36244
266.64 1.30683
267.60 1.25699
268.56 1.21841
269.52 1.18547
270.48 1.16264
271.44 1.14238
272.40 1.12668
273.36 1.11317
274.32 1.10839
275.28 1.10904
276.24 1.11260
277.20 1.11675
278.16 1.11980
279.12 1.11987
280.08 1.11552
281.04 1.11236
282.00 1.10840
282.96 1.10338
283.92 1.09256
284.88 1.07784
285.84 1.05470
286.80 1.02326
287.76 0.98444
288.72 0.94211
289.68 0.89573
290.64 0.84577
291.60 0.79435
292.56 0.74160
293.52 0.68778
294.48 0.63259
295.44 0.58020
296.40 0.53113
297.36 0.48689
298.32 0.45168
299.28 0.42754
300.24 0.41864
(3/2,1/2)
149 1.0000E+000
178.32 1.52326
179.28 1.63470
180.24 1.74305
181.20 1.84124
182.16 2.03578
183.12 2.21991
184.08 2.41023
185.04 2.57609
186.00 2.74818
186.96 2.93422
187.92 3.15555
188.88 3.42077
189.84 3.73751
190.80 4.10304
191.76 4.53705
192.72 5.03007
193.68 5.56319
194.64 6.10850
195.60 6.66211
196.56 7.19443
197.52 7.68714
198.48 8.10741
199.44 8.46186
200.40 8.74839
201.36 8.96209
202.32 9.09590
203.28 9.16679
204.24 9.18149
205.20 9.14968
206.16 9.07305
207.12 8.95755
208.08 8.82914
209.04 8.69694
210.00 8.55207
210.96 8.39026
211.92 8.21414
212.88 8.01785
213.84 7.79731
214.80 7.54320
215.76 7.25713
216.72 6.95751
217.68 6.65086
218.64 6.35198
219.60 6.07467
220.56 5.83168
221.52 5.63150
222.48 5.48585
223.44 5.38730
224.40 5.34218
225.36 5.35114
226.32 5.41398
227.28 5.52102
228.24 5.67712
229.20 5.88267
230.16 6.13488
231.12 6.43128
232.08 6.76220
233.04 7.11350
234.00 7.47771
234.96 7.84889
235.92 8.20384
236.88 8.54204
237.84 8.84486
238.80 9.11355
239.76 9.34786
240.72 9.54754
241.68 9.70215
242.64 9.81889
243.60 9.88326
244.56 9.90036
245.52 9.87224
246.48 9.80003
247.44 9.69514
248.40 9.56540
249.36 9.41082
250.32 9.25056
251.28 9.09442
252.24 8.94565
253.20 8.81524
254.16 8.70181
255.12 8.59867
256.08 8.51408
257.04 8.44361
258.00 8.38871
258.96 8.34495
259.92 8.30732
260.88 8.26753
261.84 8.22523
262.80 8.17489
263.76 8.11950
264.72 8.05768
265.68 7.98796
266.64 7.90917
267.60 7.82064
268.56 7.72515
269.52 7.62013
270.48 7.50864
271.44 7.39692
272.40 7.28455
273.36 7.17297
274.32 7.07279
275.28 6.98460
276.24 6.91455
277.20 6.86658
278.16 6.84049
279.12 6.83818
280.08 6.86414
281.04 6.91420
282.00 6.98908
282.96 7.08958
283.92 7.21165
284.88 7.35171
285.84 7.50758
286.80 7.67283
287.76 7.84375
288.72 8.01623
289.68 8.18184
290.64 8.33942
291.60 8.48231
292.56 8.60601
293.52 8.70998
294.48 8.79405
295.44 8.85058
296.40 8.88174
297.36 8.88451
298.32 8.86150
299.28 8.81761
300.24 8.75714
301.20 8.68444
302.16 8.60772
303.12 8.52629
304.08 8.44279
305.04 8.35407
306.00 8.26974
306.96 8.19119
307.92 8.11623
308.88 8.04716
309.84 7.99168
310.80 7.93587
311.76 7.87991

312.72 7.81962
313.68 7.74803
314.64 7.66753
315.60 7.58234
316.56 7.48725
317.52 7.39409
318.48 7.30737
319.44 7.21622
320.40 7.12102
(2,0)
280 1.0000E+000
186.96 0.15964
187.92 0.19796
188.88 0.28672
189.84 0.42662
190.80 0.61072
191.76 0.84377
192.72 1.09948
193.68 1.40838
194.64 1.74002
195.60 2.09296
196.56 2.44633
197.52 2.83470
198.48 3.21446
199.44 3.54831
200.40 3.80593
201.36 3.98249
202.32 4.10057
203.28 4.14913
204.24 4.16758
205.20 4.14227
206.16 4.09359
207.12 3.96312
208.08 3.74335
209.04 3.40761
210.00 2.97937
210.96 2.47615
211.92 1.94156
212.88 1.43472
213.84 1.00259
214.80 0.68370
215.76 0.47712
216.72 0.37852
217.68 0.35945
218.64 0.39911
219.60 0.46782
220.56 0.54749
221.52 0.62749
222.48 0.70237
223.44 0.76620
224.40 0.83266
225.36 0.89618
226.32 0.95835
227.28 1.01994
228.24 1.08996
229.20 1.17655
230.16 1.28807
231.12 1.43222
232.08 1.61701
233.04 1.85110
234.00 2.12247
234.96 2.40686
235.92 2.67211
236.88 2.88983
237.84 3.04978
238.80 3.12894
239.76 3.14908
240.72 3.09743
241.68 2.99628
242.64 2.82763
243.60 2.62402
244.56 2.39349
245.52 2.16301
246.48 1.93743
247.44 1.72664
248.40 1.53393
249.36 1.35442
250.32 1.20310
251.28 1.08575
252.24 1.01321
253.20 0.97625
254.16 0.96378
255.12 0.96365
256.08 0.97508
257.04 0.99142
258.00 1.01081
258.96 1.02237
259.92 1.02310
260.88 1.00240
261.84 0.96734
262.80 0.91922
263.76 0.86842
264.72 0.81137
265.68 0.75175
266.64 0.68877
267.60 0.62219
268.56 0.57674
269.52 0.55728
270.48 0.56933
271.44 0.59783
272.40 0.64615
273.36 0.69321
274.32 0.75029
275.28 0.82279
276.24 0.92969
277.20 1.06140
278.16 1.21535
279.12 1.38495
280.08 1.56474
281.04 1.75603
282.00 1.96981
282.96 2.22304
283.92 2.51299
284.88 2.83619
285.84 3.18331
286.80 3.54854
287.76 3.92825
288.72 4.31559
289.68 4.72761
290.64 5.16091
291.60 5.61908
292.56 6.08886
293.52 6.57571
294.48 7.05929
295.44 7.53758
296.40 7.99854
297.36 8.44154
298.32 8.83660
299.28 9.17515
300.24 9.45007
301.20 9.66824
302.16 9.81996
303.12 9.90027
304.08 9.89169
305.04 9.78413
306.00 9.57712
306.96 9.26623
307.92 8.87380
308.88 8.41761
309.84 7.93931
310.80 7.44537
311.76 6.95842
312.72 6.48342
313.68 6.04178
314.64 5.62930
315.60 5.24461
316.56 4.88573
317.52 4.56120
318.48 4.27953
319.44 4.03570
320.40 3.83569
321.36 3.68020
322.32 3.57773
323.28 3.52306
324.24 3.51383
325.20 3.54661
326.16 3.62480
327.12 3.74579
328.08 3.89902
329.04 4.07365
330.00 4.26534
330.96 4.46159
331.92 4.65770
332.88 4.83741
333.84 4.99989
334.80 5.12695
335.76 5.21576
336.72 5.25266
337.68 5.23361
338.64 5.15547
339.60 5.03220
340.56 4.86603
341.52 4.67146
342.48 4.45561
343.44 4.22820
344.40 3.98740
345.36 3.74101
346.32 3.48882
347.28 3.23702
348.24 2.98286
349.20 2.73326
350.16 2.49349
351.12 2.27042
352.08 2.06448
353.04 1.88319
354.00 1.72463
354.96 1.58878
355.92 1.46171
356.88 1.34707
357.84 1.24237
358.80 1.14799
359.76 1.05777
360.72 0.97707
361.68 0.91088
362.64 0.85544
363.60 0.81344
364.56 0.77887
365.52 0.75149
366.48 0.71890
367.44 0.68376
368.40 0.63823
369.36 0.58969
370.32 0.53138
371.28 0.47257
372.24 0.41264
373.20 0.36565
374.16 0.32913
375.12 0.30688
376.08 0.29116
377.04 0.28145
378.00 0.26834
378.96 0.25367
379.92 0.24350
380.88 0.24276
381.84 0.25453
382.80 0.27591
383.76 0.31448
384.72 0.36208
385.68 0.42339
386.64 0.48707
387.60 0.55910
388.56 0.62355
389.52 0.68967
390.48 0.75068
391.44 0.81763
392.40 0.88481
393.36 0.95899
394.32 1.03233
395.28 1.10636
396.24 1.18037
397.20 1.25589
398.16 1.32913
399.12 1.39293
400.08 1.44745
401.04 1.49045
402.00 1.52344
402.96 1.54839
403.92 1.57235
404.88 1.59537
405.84 1.61787
406.80 1.63939
407.76 1.66046
408.72 1.68683
409.68 1.72020
410.64 1.76364
411.60 1.81572
412.56 1.87779
413.52 1.95054
414.48 2.03452
415.44 2.12852
416.40 2.23554
417.36 2.35802
418.32 2.49296
419.28 2.63806
420.24 2.79184
421.20 2.95106
422.16 3.11064
423.12 3.26549
424.08 3.41598
425.04 3.55214
426.00 3.66963
426.96 3.76128
427.92 3.82909
428.88 3.86675
429.84 3.87984
430.80 3.87185
431.76 3.85342
432.72 3.82590
433.68 3.79154
434.64 3.74871
435.60 3.69374
436.56 3.63011
437.52 3.55526
438.48 3.47280
439.44 3.37830
440.40 3.28097
441.36 3.17718
442.32 3.07399
443.28 2.96837
444.24 2.87085
445.20 2.78148
446.16 2.70273
447.12 2.63347
448.08 2.57583
449.04 2.53246
450.00 2.49850
450.96 2.47554
451.92 2.45787
452.88 2.44832
453.84 2.43795
454.80 2.42654
455.76 2.40929
456.72 2.38921
457.68 2.36414
458.64 2.33695
459.60 2.30433
460.56 2.26376
461.52 2.21169
462.48 2.14824
463.44 2.07428
464.40 1.99250
465.36 1.90707
466.32 1.81700
467.28 1.72323
468.24 1.62290
469.20 1.52367
470.16 1.42446
471.12 1.33072
472.08 1.23958
473.04 1.15376
474.00 1.06684
474.96 0.98008

```
 475.92 0.89347
 476.88 0.80819
 477.84 0.72639
 478.80 0.64533
 479.76 0.56625
 480.72 0.49811
 481.68 0.44491
 482.64 0.4239
```

RFAC.D

```
1  2  3  4  5  6                  IBP
 0.5                                EINCR
 1.0000 1.0000 1.0000 1.0000 1.0000 1.0000
 0.0000 0.0000 0.0000 0.0000 0.0000 0.0000 0.0000 0.0000 0.0000 1.0000
  5  0  0                           ISMOTH IREN IRGEXP
```